KAUNAS UNIVERSITY OF TECHNOLOGY

NADZEYA A. KUKHTA

DESIGN, SYNTHESIS AND PROPERTIES OF BIPOLAR BRANCHED AND ELECTRON-ACCEPTING BRICK-TYPE COMPOUNDS FOR ORGANIC ELECTRONICS

Doctoral dissertation
Technological sciencies, Materials engineering (08T)

2016, Kaunas

UDK 547-3 + 621.315.5](043.3)

Doctoral dissertation was prepared in Kaunas University of Technology, Faculty of Chemical Technology, Department of Polymer Chemistry and Technology during the period of 2012–2016. The studies were supported by Research Council of Lithuania.

Scientific Supervisor:

Assoc prof. dr. Jolita OSTRAUSKAITĖ (Kaunas University of Technology, Technological sciences, Materials engineering 08T).

Doctoral dissertation has been published in:
http://ktu.edu

Editor:

Armandas Rumšas (Publishing Office “Technologija”)

ISBN 978-609-02-1271-4

KAUNO TECHNOLOGIJOS UNIVERSITETAS

NADZEYA A. KUKHTA

ŠAKOTŲ BIPOLINIŲ IR LINIJINIŲ ELEKTRONŲ AKCEPTORINIŲ ORGANINIŲ PUSLAIDININKIŲ STRUKTŪRŲ KŪRIMAS, SINTEZĖ IR SAVYBĖS

Daktaro disertacija
Technologiniai mokslai, Medžiagų inžinerija (08T)

2016, Kaunas

UDK 547-3 + 621.315.5](043.3)

Disertacija parengta 2012-2016 metais Kauno technologijos universiteto Cheminės technologijos fakultete, Polimerų chemijos ir technologijos katedroje. Mokslinius tyrimus rėmė Lietuvos mokslo taryba.

Mokslinis vadovas:

Doc. dr. Jolita Ostrauskaitė (Kauno technologijos universitetas, Technologijos mokslai, Medžiagų inžinerija 08T).

Interneto svetainės, kurioje skelbiama disertacija, adresas:
http://ktu.edu

Redagavo:

Armandas Rumšas (Leidykla "Technologija")

ISBN 978-609-02-1271-4

LIST OF ABBREVIATIONS

$(piq)_2Ir(acac)$ – bis(1-phenylisoquinolinato)(acetylacetonate)iridium
$(ppy)_2Ir(acac)$ – bis(2-phenylpyridinato-*N*,$C^{2'}$)iridium(III)acetylacetonate
1DPAFO – 2-(4-(diphenylamino)phenyl)-9*H*-fluoren-9-one
2,3,4,6-CzPy – 9,9',9'',9'''-(pyridine-2,3,4,6-tetrayl)tetrakis(9*H*-carbazole)
2,3,5,6-CzPy – 9,9',9'',9'''-(pyridine-2,3,5,6-tetrayl)tetrakis(9*H*-carbazole)
2,3-CzPy – 2,3-di(9*H*-carbazol-9-yl)pyridine
2,4,6-CzPy – 9,9',9''-(pyridine-2,4,6-triyl)tris(9*H*-carbazole)
2,4-CzPy – 2,4-di(9*H*-carbazol-9-yl)pyridine
2,6-CzPy – 2,6-di(9*H*-carbazol-9-yl)pyridine
2,6-DCzPPy – 2,6-bis(3-(carbazol-9-yl)phenyl)pyridine
2BTSi-T – 7,7'-(1,1-dimethyl-3,4-diphenyl-1*H*-silole-2,5-diyl)bis(4-(thiophen-2-yl)benzo[c][1,2,5]thiadiazole)
2BTSi-TPA – 4,4'-((1,1-dimethyl-3,4-diphenyl-1*H*-silole-2,5-diyl)bis(benzo[c][1,2,5]thiadiazole-7,4-diyl))bis(*N*,*N*-bis(4-(octyloxy)phenyl)aniline)
2Cz-PN – 4,5-di(9*H*-carbazol-9-yl)phthalonitrile
2DPAFO – 2,7-bis(4-(diphenylamino)phenyl)-9*H*-fluoren-9-one
3,5-CzPy – 3,5-di(9*H*-carbazol-9-yl)pyridine
3,5-DCzPPy – 3,5-bis(3-(carbazol-9-yl)phenyl)pyridine
3Cz-TRZ – 9'-(4-(4,6-diphenyl-1,3,5-triazin-2-yl)phenyl)-3,3'',6,6''-tetraphenyl-9'*H*-9,3':6',9''-tercarbazole
4Cz-IPN – 2,4,5,6-tetra(9*H*-carbazol-9-yl)isophthalonitrile
ACQ – aggregation caused quenching
ACRFLCN – 10-phenyl-10*H*-spiro[acridine-9,9'-fluorene]-2',7'-dicarbonitrile
AIE – aggregation induced emission
BCP – 2,9-dimethyl-4,7-diphenyl-1,10-phenanthroline
Bis-HFl-NTCDI – *N*,*N*-bis(fluoren-2-yl)-naphthalenetetracarboxylic diimide
BP4mPy – 3,3',5,5'-tetra[(m-pyridyl)-phen-3-yl]biphenyl
BPAPF – 9,9-bis[4-(*N*,*N*-bis-biphenyl-4-yl-amino)phenyl]-9*H*-fluorene
Bphen – 4,7-diphenyl-1,10-phenanthroline
BPTRZ – 3-(carbazol-9-yl)-3′-(4,6-(dicarbazol-9-yl)-1,3,5-triazin-2-yl)-1,1′-biphenyl
CBP – 4,4′-bis(*N*-carbazolyl)-1,1′-biphenyl
CELIV – charge extraction in a linearly increasing voltage
CIE – International Commission on Illumination
CPC – 2,6-di(9*H*-carbazol-9-yl)-4-phenylpyridine-3,5-dicarbonitrile
CT – charge transfer
CV – cyclic voltammetry
CzPP-BT – 4,7-bis(4'-(9-hexyl-9*H*-carbazol-3-yl)-5',6'-diphenyl-[1,1':2',1''-terphenyl]-3'-yl)benzo[c][1,2,5]thiadiazole
CzPP-SD – 3,7-bis(4'-(9-hexyl-9*H*-carbazol-3-yl)-5',6'-diphenyl-[1,1':2',1''-terphenyl]-3'-yl)dibenzo[b,d]thiophene-5,5-dioxide
CzT – 9-(4,6-diphenyl-1,3,5-triazin-2-yl)-9′-phenyl-3,3′-bicarbazole
D–A – donor-acceptor

DBTD-Cz – 2,8-bis(3,6-di-*tert*-butyl-9*H*-carbazol-9-yl)dibenzo[b,d]thiophene-5,5-dioxide
DBTD-DA – 2,8-bis(bis(4-butylphenyl)amino)dibenzo[b,d]thiophene-5,5-dioxide
DBTO-PTZ – 2,8-di(10*H*-phenthiazin-10-yl)dibenzo[b,d]thiophene-5,5-dioxide
DBTO-PXZ – 2,8-di(10*H*-phenoxazin-10-yl)dibenzo[b,d]thiophene-5,5-dioxide
DCV5T-Me – 2,2'-((3",4"-dimethyl-[2,2':5',2":5",2"':5"',2"":quinquethiophene]-5,5""-diyl)bis(methanylylidene))dimalononitrile
DCzIPN – 4,6-di(9*H*-carbazol-9-yl)isophthalonitrile
DCzTrz – 9,9′-(5-(4,6-diphenyl-1,3,5-triazin-2-yl)-1,3-phenylene)bis(9*H*-carbazole)
DDCzIPN – 3,3’,5,5’-tetra(carbazol-9-yl)-[1,1’-biphenyl]-2,2’,6,6’-tetracarbonitrile
DDCzTrz – 9,9′,9″,9‴-((6-phenyl-1,3,5-triazine-2,4-diyl)bis(benzene-5,3,1-triyl)) tetrakis(9*H*-carbazole)
DF – delayed fluorescence
DFT – density functional theory
DMAC-DPS – 10,10'-(sulfonylbis(4,1-phenylene))bis(9,9-dimethyl-9,10-dihydroacridine)
DMAC-TRZ – 10-(4-(4,6-diphenyl-1,3,5-triazin-2-yl)phenyl)-9,9-dimethyl-9,10-dihydroacridine
DMF – dimethylformamide
DMOC-DPS – 9,9'-(sulfonylbis(4,1-phenylene))bis(3,6-dimethoxy-9*H*-carbazole)
DPEPO – bis[2-(diphenylphosphino)phenyl]ether oxide
DPOTPCz – 3-(4,6-diphenoxy-1,3,5-triazin-2-yl)-9-phenyl-9*H*-carbazole
DPO-TXO2 – 9,9-dimethyl-2,7-di(10H-phenoxazin-10-yl)-9*H*-thioxanthene-10,10-dioxide
DPS-CzPTZ – 10-(4-((4-(9*H*-carbazol-9-yl)phenyl)sulfonyl)phenyl)-10*H*-phenothiazine
DPS-PTZ – 10,10'-(sulfonylbis(4,1-phenylene))bis(10*H*-phenothiazine)
DPS-PXZ – 10,10'-(sulfonylbis(4,1-phenylene))bis(10*H*-phenoxazine)
DPTPCz – 3-(4,6-diphenyl-1,3,5-triazin-2-yl)-9-phenyl-9*H*-carbazole
DSC – differential scanning calorimetry
DSFO – 2,7-bis(4-(*tert*-butylthio)phenyl)-fluorenone
DTC-DPS – 9,9'-(sulfonylbis(4,1-phenylene))bis(3,6-di-*tert*-butyl-9*H*-carbazole)
DTPDDA – 5-(4-(4,6-diphenyl-1,3,5- triazin-2-yl)phenyl)-10,10 diphenyl-5,10-dihydrodibenzo[b,e]-[1,4]azasiline
DTPEPO – phenylbis(4-(1,2,2-triphenylvinyl)phenyl)phosphine oxide
EA – electron affinity
EL – electroluminescent
EML – emissive layer
EP – electron photoemission
EQE – external quantum efficiency
ESIPT – excited state intramolecular proton transfer
ET – triplet energy
ETL – electron transport layer
ETM – electron transporting materials
FF – 9',9'-dihexyl-9*H*,9'*H*,9"*H*-[2,2':7',2"-terfluorene]-9,9"-dione

FIrpic – bis[(4′,6′-difluorophenyl)-pyridinato-N,$C^{2'}$]iridium(III)picolinate
HOMO – highest occupied molecular orbital
HTL – hole transport layer
ICT – intramolecular charge transfer
IP – ionization potential
IQE – internal quantum efficiency
IR – infrared
$Ir(ppy)_3$ – fac-tri-(2-phenylpyridinato-N,$C^{2'}$)iridium(III)
ISC – intersystem crossing
ITO – indium tin oxide
JAF – *J*-aggregate formation
LE – locally excited state
LUMO – lowest unoccupied molecular orbital
MBPTRZ – 3-(carbazol-9-yl)-6,6′-dimethyl-3′-(4,6-(dicarbazol-9-yl)-1,3,5-triazin-2-yl)-1,1′-biphenyl
*m*CBP-2CN – 9-(3'-(carbazol-9-yl)-(1,10-biphenyl)-3-yl)-carbazole-3,6-dicarbonitrile
*m*CBP-CN – 9-(3'-(carbazol-9-yl)-(1,10-biphenyl)-3-yl)-carbazole-3-carbonitrile
MCH – methylcyclohexane
mCP – 1,3-bis(*N*-carbazolyl)benzene
*m*CPCN – 9-(3-(9H-carbazol-9-yl)phenyl)-9*H*-carbazole-3-carbonitrile
*m*CPCzCN – 6-(3,5-di(9*H*-carbazol-9-yl)phenyl)-9-ethyl-9*H*-carbazole-3-carbonitrile
m-CzCN – 3,5-bis(3-(9*H*-carbazol-9-yl)phenyl)-1-benzonitrile
m-CzCzCN – 6-(3-(9*H*-carbazol-9-yl)phenyl)-9-ethyl-9*H*-carbazole-3-carbonitrile
m-CzOCN – 8-(3-(9*H*-carbazol-9-yl) phenyl)dibenzo[b,d]furan-2-carbonitrile
m-CzSCN – 8-(3-(9*H*-carbazol-9-yl)phenyl)dibenzo[b,d]thiophene-2-carbonitrile
m-DBPDECZ – 3-(1-(4'-(dimesitylboranyl)-[1,1'-biphenyl]-3-yl)-2,2-diphenylvinyl)-9-ethyl-9*H*-carbazole
m-DPDECZ – 3-(1-(3-(dimesitylboranyl)phenyl)-2,2-diphenylvinyl)-9-ethyl-9*H*-carbazole
Me-THF – 2-methyl-tetrahydrofuran
*m*PCB2Cz – 9-(6-(9*H*-carbazol-9-yl)pyridin-2-yl)-6-(9*H*-carbazol-9-yl)-9*H*-pyrido[2,3-b]indole
NMR – nuclear magnetic resonance
NPD – *N,N′*-di(1-naphthyl)-*N,N′*-diphenyl-(1,1′-biphenyl)-4,4′-diamine
o-CzCN – 3,5-bis(2-(9*H*-carbazol-9-yl)phenyl-1-benzonitrile
o-CzCzCN – 6-(2-(9*H*-carbazol-9-yl)phenyl)-9-ethyl-9*H*-carbazole-3-carbonitrile
o-DCB – *o*-dichlorobenzene
OFET – organic field-effect transistor
OLED – organic light-emitting diode
OPC – (4-(10*H*-phenothiazin-10-yl)phenyl)(4-(9*H*-carbazol-9-yl)phenyl)methanone
OPV – organic photovoltaics
*p*BCb2Cz – 9-(4-(9*H*-pyrido[2,3-b]indol-9-yl)phenyl)-9*H*-3,9’-bicarbazole
PBD – 2-([1,1'-biphenyl]-4-yl)-5-(4-(*tert*-butyl)phenyl)-1,3,4-oxadiazole

PCF – 2,7-bis(diphenylphosphine oxide)-9-(9-phenylcarbazol-3-yl)-9-phenylfluorene
PCz – 9-phenylcarbazole
p-CzCN – 3,5-bis(4-(9*H*-carbazol-9-yl)phenyl)-1-benzonitrile
p-DBPDECZ – 3-(1-(4'-(dimesitylboranyl)-[1,1'-biphenyl]-4-yl)-2,2-diphenylvinyl)-9-ethyl-9*H*-carbazole
p-DPDECZ – (*E*)-4-(2-(4-(dimesitylboranyl)phenyl)-1,2-diphenylvinyl)-*N*,*N*-diphenylaniline
PF – prompt fluorescence
PhOLED – phosphorescent organic light-emitting diode
PIC-TRZ – 2-biphenyl-4,6-bis(12-phenylindolo[2,3-a]carbazole-11-yl)-1,3,5-triazine
PL – photoluminescence
PLQY – photoluminescence quantum efficiency
POCz3 – 3,3′,3″-phosphoryltris(9-phenyl-9*H*-carbazole)
*p*PCB2Cz – 9-(6-(9*H*-carbazol-9-yl)pyridin-3-yl)-6-(9*H*-carbazol-9-yl)-9*H*-pyrido[2,3-b]-indole
ppm – part per million
PPT – 2,8-bis(diphenylphosphoryl)dibenzo[b,d]thiophene
PS – polystyrene
PTZ-TRZ – 10-(4-(4,6-diphenyl-1,3,5-triazin-2-yl)phenyl)-10*H*-phenothiazine
PXZ-DPS – 10,10'-(sulfonylbis(4,1-phenylene))bis(10*H*-phenoxazine)
PXZ-TRZ – 10-(4-(4,6-diphenyl-1,3,5-triazin-2-yl)phenyl)-10*H*-phenoxazine
RIR – restriction of intramolecular rotations
RISC – reversible intersystem crossing
S_n – singlet state
TADF – thermally activated delayed fluorescence
T_g – glass transition temperature
TGA – thermal gravimetric analysis
TICT – twisted intramolecular charge transfer
T_{ID} – initial decomposition temperature
TmPyPB – 1,3,5-tri(*m*-pyrid-3-ylphenyl)benzene
T_n – triplet state
TOF – time-of-flight
TPA – triphenylamine
TPA3TPAN – 2,2',2"-(nitrilotris([1,1'-biphenyl]-4',4-diyl))tris(3,3-diphenylacrylonitrile)
TPA-PRZ$(CN)_2$ – 2,6-bis(diphenylamino)-9,10-dihydro-9,10-[2,3]epipyrazinoanthracene-13,14-dicarbonitrile
TPA-QNX$(CN)_2$ – 8,16-bis(diphenylamino)-6,11-dihydro-6,11-[1,2]benzenobenzo[b]phenazine-2,3-dicarbonitrile
TPB – 1,3,5-triphenylbenzene
TPBi – 1,3,5-tris(phenyl-2-benzimidazolyl)-benzene
TPD – N^4,$N^{4'}$-diphenyl-N^4,$N^{4'}$-di-*m*-tolyl-[1,1'-biphenyl]-4,4'-diamine
TPE – 1,1,2,2-tetraphenylethene

TPEDPO – (*E*,*Z*)-((1,2-diphenylethene-1,2-diyl)bis(4,1-phenylene))bis (diphenylphosphine oxide)
TPE-NB – (*E*)-4-(2-(4-(dimesitylboranyl)phenyl)-1,2-diphenylvinyl)-*N*,*N*-diphenylaniline
TPE-PNPB – (*E*)-4'-(2-(4'-(dimesitylboranyl)-[1,1'-biphenyl]-4-yl)-1,2-diphenylvinyl)-*N*,*N*-diphenyl-[1,1'-biphenyl]-4-amine
TPEPO – diphenyl(4-(1,2,2-triphenylvinyl)phenyl)phosphine oxide
TPSi-F – triphenyl-[4-(9-phenyl-9*H*-fluoren-9-yl)phenyl]silane
TRZ – 2,4,6-triphenyl-1,3,5-triazine
TrzmPCz – 3-(3-(4,6-diphenyl-1,3,5-triazin-2-yl)-2-methylphenyl)-9-phenyl-9*H*-carbazole
TSPO1 – diphenyl-4-triphenylsilylphenyl-phosphine oxide
TTA – triplet-triplet annihilation
TTET – triplet-triplet energy transfer
TTPEPO – tris(4-(1,2,2-triphenylvinyl)phenyl)phosphine oxide
TXO-PCz – 2-(9-phenyl-9*H*-carbazol-3-yl)-9*H*-thioxanthen-9-one-10,10-dioxide
TXO-TPA – 2-(4-(diphenylamino)phenyl)-9H-thioxanthen-9-one-10,10-dioxide
WOLED – white organic light emitting device
ΔE_{ST} – singlet-triplet energy gap
τ – fluorescence lifetime

CONTENTS

1. INTRODUCTION

Since the discovery of the first organic semiconducting compound, polyaniline, by Henry Letheby in 1862, enormous research has been conducted in the field of materials science, resulting in the development of organic electronics and in the industrial production of the first organic diode device several decades ago. Being on par and even outperforming their inorganic analogues, organic semiconductors found wide application in the preparation of such devices as OFETs, OLEDs, and OPVs [1]. Aiming at the fabrication of the ultra-thin, large-area, and flexible devices, researchers are in constant search for low-cost and low-energy consumption procedures. For the sake of achievement of high device performance, many factors should be considered in the development of organic semiconductors. Chemical and thermal stability and durability, charge transport, light absorption, high photoluminescence quantum efficiency, appropriate energy levels and suitable morphological properties can be named as the most important characteristics. Moreover, as the layer of organic semiconductor plays the crucial role in the device, the quality of the thin film should be taken into consideration as well, depending on the type of the target device: while for high performance OLEDs amorphous thin films are preferable, highly ordered crystalline thin films perform better in the OPVs [2]. Consequently, profound understanding of the electronic structure along with the resulting properties of the materials is necessary for the manufacturing of efficient devices and for the design of new compounds.

Most modern devices employ complex multilayer architecture, thus boosting their production cost. Therefore, the design of multifunctional materials proves to be a successful approach for the simplification of fabrication. Bipolar molecular architecture, i.e. combination of electron donating and accepting units, along with the multichromophore feature, leads to a wide range of desirable properties within one molecule, which, in turn, results in the development of a rationalized device. Furthermore, by the variation of the donor and acceptor fluorophores along with the linking pattern significant variation of characteristics can be expected as well.

Bipolar compounds employing fluorene, carbazole and triphenylamine donors and triazine, triphenylbenzene, fluorenone, benzonitrile and naphthalenetetracarboxilic acid dianhydride derivatives as acceptors, have been thoroughly investigated in recent years. Easy functionalization and variation of conjugation strength thus leads to the great diversity of structures, bearing the above-mentioned fragments. Thus, fluorene adducts are well-known deep blue emitters with high photoluminescence efficiency both in solution and solid state [3,4]. In turn, the carbazole unit provides high thermal stability, remarkable hole mobility and considerably high triplet level [5]. The involvement of triphenylamine moiety gives rise not only to excellent charge-transporting materials [6], but also to the AIE active luminogenes due to its propeller shape [7,8]. In recent years, considerable interest in academic research has been devoted to 1,3,5-triazine derivatives due to their strong electronegative nature, high electron mobility, superior thermal stability and interesting photophysical properties [9,10]. Owing to its twisted skeleton and C_3 symmetry, 1,3,5-triphenylbenzene finds application in the preparation of dendritic wide energy gap materials [11]. Incorporation of the

fluorenone acceptor can lead not only to ambipolar charge transport, but also to the emission enhancement, promoted by intermolecular hydrogen bonding [12]. Nitrile-decorated bipolar compounds have gained significant attention as host materials for PhOLEDs and promising emitters for thermally activated delayed fluorescence OLEDs [13,14]. After all, the 1,4,5,8-naphthalenetetracarboxilic dianhydride derivatives are good candidates for the electron transporting layer both in OLEDs and OPVs due to their high electron affinity, planar configuration, excellent electron transport and tunable optical and electrochemical properties [15].

Miscellaneous conjunctions of the above mentioned fragments give rise to bipolar molecules with a wide range of necessary characteristics. In turn, systematic investigation of structure-property relationships aids to predict the performance of the materials in target devices.

The aim of this work is the design, synthesis and investigation of properties of the new bipolar compounds for the application in optoelectronics. Comparison of practically obtained characteristics with the theoretically predicted values is the other goal of the study. Estimation of the applicability of new compounds in optoelectronic devices will be discussed as well.

The following objectives were raised for the achievement of the aim of the thesis:

- Synthesis and investigation of the impact of linking topology on the properties of bipolar star-shaped derivatives of 2,4,6-triphenyl-1,3,5-triazine and 1,3,5-triphenylbenzene.
- Design, synthesis and investigation of optical, photophysical, photoelectrical and thermal characteristics of the boomerang-shaped compounds containing bicarbazolyl moieties.
- Design and synthesis of the multichromophore fluorenone-based compounds, investigation of their optical, photophysical, photoelectrical, thermal, charge transporting characteristics; estimation of the emission behaviour peculiarities of the synthesized materials.
- Design, synthesis and comparison of theoretically simulated and practically determined characteristics of the differently carbazolyl and cyano-substituted 1,3,5-triphenylbenzene derivatives; estimation of the performance in organic light emitting diodes.
- Synthesis and characterization of electron-transporting 1,4,5,8-naphthalenetetracarboxilic dianhydride derivatives; estimation of the performance in bulk-heterojunction solar cells.

The main statements of the doctoral thesis:

- Star-shaped derivatives of 2,4,6-triphenyl-1,3,5-triazine and 1,3,5-triphenylbenzene may be applied to the solution-processable blue and white fluorescent OLEDs as emitting materials owing to good photoluminescent characteristics, appropriate energy levels, superior thermal behaviour and high charge mobility.

- Bicarbazolyl-substituted boomerang-shaped compounds are relevant for the application as the emitting layer in doped blue OLEDs and phosphorescent host matrix in green PhOLEDs, depending on the utilized core fragment.
- Multichromophore fluorenone-based compounds exhibit balanced ambipolar charge transport, superior thermal and electrochemical stability and aggregation induced emission enhancement phenomenon.
- Depending on the substitution pattern, bipolar carbazolyl and cyano-substituted 1,3,5-triphenylbenzene derivatives can be suggested as promising emitters for blue fluorescent and DF OLEDs and phosphorescent ambipolar hosts for blue TADF OLEDs and PhOLEDs.
- Owing to the remarkable electron mobility and conductivity 1,4,5,8-naphthalenetetracarboxilic dianhydride derivatives may be applied as electron transporting layer in bulk-heterojunction solar cells.

The scientific novelty of the work:

- Investigation of the influence of the linking topology on the characteristics of new star-shaped derivatives of 2,4,6-triphenyl-1,3,5-triazine and 1,3,5-triphenylbenzene was found to suggest the guidelines for the design of organic semiconductors with various target characteristics.

- New bicarbazolyl-substituted boomerang-shaped compounds were prepared and their properties were investigated. It was established, that the bicarbazolyl group is a stronger donor than a single carbazole fragment, providing lower ionization potential, superior thermal and electrochemical stability and strong phosphorescence.

- New multichromophore fluorenone-based compounds, displaying balanced ambipolar charge transport, superior thermal and electrochemical stability and aggregation induced emission enhancement phenomenon, were synthesized and characterized. A mechanism of emission in the investigated materials was suggested.

- New carbazolyl and cyano-substituted 1,3,5-triphenylbenzene derivatives were synthesized. The variation of the substitution manner was demonstrated to affect the characteristics of compounds, resulting in the delayed fluorescence phenomenon and ambipolar charge transport. High performance organic light emitting diodes were fabricated.

- New electron-transporting 1,4,5,8-naphthalenetetracarboxilic dianhydride derivatives were prepared and characterized. The influence of symmetrical and asymmetrical molecular structure on the properties was studied. High performance bulk heterojunction solar cells were fabricated.

The contribution of the author

The author has designed, synthesized and purified six different series of bipolar and electron transporting compounds. The author has performed and analyzed the results of the melting point, infrared spectroscopy, absorption, cyclic voltammetry and photophysical measurements. The ionization potential and charge mobility investigations were performed in collaboration with dr. Dmytro Volyniuk (Kaunas University of Technology), the results of which were further analyzed by the author. Organic light emitting diodes were prepared with the help of dr. Khrystyna Ivaniuk (Lviv Polytechnic University, Ukraine) (the results were analyzed and described by the author). The author performed the theoretical calculations and analysis for all the compounds. For the compounds, described in Chapter 4.4, the analysis of the theoretical calculations was carried out in cooperation with dr. Gjergji Sini (University of Cergy-Pontoise, France). Bulk heterojunction solar cells were obtained with the assistance of prof. Karl Leo and co-workers (Dresden University of Technology, Germany).

2. LITERATURE REVIEW

2.1. Introduction for the literature review

Nowadays, consumers are using a wide variety of organic electronic devices, such as smart phones, coloured light sources, portable solar cells and curved television screens, often without even being aware of the organic nature of the electronic technology on hand [16,17]. Due to the lower cost and higher throughput manufacture of organic-based electronic devices, compared to silicon-based devices, organic electronics also promises to expand the use of electronic technology in resource-limited areas of the world where supplies are limited or the necessary infrastructure is lacking [18]. Since the first demonstration of a low voltage and efficient thin film OLED by Tang and van Slyke almost thirty years ago [19], the research field of organic electronics has expanded enormously. Currently, a growing body of investigation in the fields of physics and chemistry focuses on three main types of existing applications: displays and lighting, transistors, and solar cells. Thus, OPVs offer the exciting prospect of large-area solar cells; organic lasers are potential compact sources of tunable, coherent light; plastic OFETs are being studied for low-cost, flexible electronic applications, such as radiofrequency identification (RFID) tags [20]. In turn, OLEDs hold great promise for energy-efficient light sources with unique properties, and, unlike the inorganic LEDs, have a large light-emitting area and can be produced by using flexible substrates [21]. To be able to address the market, organic electronic solutions must provide unique advantages such as cost, flexibility, functionality and appearance [22].

As the key to the design of high performance electronic organic devices implies the development of new materials, interdisciplinary scientists target understanding of the electronic structure, as well as optimization and simplification of the device architecture. To predict outstanding performance of a device, materials chemists should project semiconducting compounds having an appropriate trade-off between the charge transport and luminescence/absorption properties and the preservation of these characteristics in the bulk. Therefore, molecular control over the morphology of organic films in devices should be a priority, as well [23,24].

In general, organic materials used in electronic and optoelectronic devices can be classified into two groups: small molecules and polymers. Small molecular compounds possess a well-defined molecular weight and are typically deposited by vapour methods in low or high vacuum environments. On the contrary, high molecular weight polymers with non-unit molecular weight distribution must be processed from solution. In turn, dendrimers are a class of materials that in some ways fall between molecular and polymeric materials [23]. Dendrimers are highly branched molecules with moderately high and preserved well-defined molecular weight. Thus, the construction of dendrimers helps to control the properties of materials on the nanometre scale by combining the advantages of small molecules and polymers in organic electronics application.

Depending on the objective role in the electronic device, electron donating and accepting fragments can be employed for the construction of organic semiconductors. Combination of donor and acceptor units [1], i.e. the bipolar motif, is the state-of-the-art methodology to tune the energetic levels, overall stability,

optical, photophysical and photoelectrical characteristics. Design and synthesis of π-conjugated compounds with efficient photoinduced charge transfer and separation, as well as ambipolar charge transport with high mobility, are crucial for device production. These properties result from the ICT interaction within D-A molecules and depend on the efficiency of the π-electron delocalization along the conjugated systems and the electron donating/accepting capability of the involved chromophores [25,26,27].

Generally, such features, as excellent optical and photophysical properties, superior thermal and morphological stability, appropriate energy levels and balanced charge transport are required from the organic semiconductors to be used in highly efficient devices. By the combination of multichromophore molecular architecture with the donor-acceptor structure it is possible to achieve a wide range of desirable properties, which may lead to multifunctionality and a variety of applications.

In this review, recent advances in the design, synthesis and properties investigation of the organic compounds featuring bipolar molecular architecture for the optoelectronic applications will be discussed.

2.2 Methods of OLED efficiency enhancement

OLED has inspired the research of many scientists all over the world and has thus become an important component for the display and lighting technologies since its first commercialization in 1997 [28]. Generally, OLEDs are double charge injection devices, requiring simultaneous injection of both electrons and holes into the adjacent organic layers, which is followed by the emission of the EL material, sandwiched between two electrodes [29,30]. The basic structure of the device consists of three layers: the anode, the cathode and the thin layer of organic emissive semiconducting compound, placed between them [31]. However, for a successful OLED facile and steady charge transport as well as high conversion efficiency of excitons to light is necessary. Therefore, poor efficiency stemming from the unbalanced charge recombination of the OLED with a monolayer structure induced the development of the multilayer device configurations (**Fig. 2.1**). Such layers, as HTL, ETL and EML, and sometimes hole injection and electron injection layers, were introduced in order to improve the device efficiency [32,33].

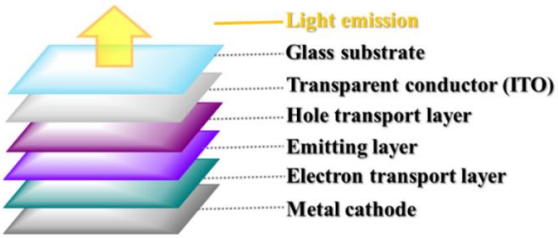

Fig. 2.1. Schematic representation of the multilayer OLED structure

The principal ways for the fabrication of OLED devices involve thermal evaporation and solution-process deposition of organic materials. Apparently, both approaches have advantages and disadvantages. Thus, thermal evaporation appears to be a successful way to achieve high efficiency with such advantages as the

immaculate deposition and precise layer thickness control, however, huge wastage of compounds in the chamber makes it extremely expensive. In comparison, solution processing with such methods like coating or printing, which are highly cost-effective and feasible for mass manufacturing, provides a promising alternative to vacuum deposition. Nevertheless, such problems as the solubility of some organic materials in various organic solvents and the undesired blending of two organic layers during subsequent coatings still remain the major challenges for the commercial application of solution-process deposition [28,34,35]. As a result, in order to be practically applicable in industry, it is desirable to simplify the OLED architecture and fabrication processes, at the same time maintaining or even upgrading the performance efficiency.

Efficiency plays a crucial role for the durability and the long life time of blue, green, red, and white OLEDs for displays and lighting. Numerous approaches towards the OLED efficiency improvement, involving the design of efficiency-effective device architectures and synthesis of new materials, have been proposed and elaborated upon [28]. The contribution of a materials scientist, in collaboration with physicists and engineers, can be defined as the careful design and synthesis of readily processable and thermally robust emissive and charge transporting materials with the improved multifunctional properties.

Currently, the most promising approaches towards the OLED efficiency enhancement include the development of multifunctional compounds exhibiting phosphorescence, delayed fluorescence, aggregation induced emission and mechanoluminescence phenomena.

2.2.1. Employment of multifunctional phosphorescent compounds

It is common knowledge, that, due to spin statistics, 25% of singlet and 75% of triplet excitons are formed in the OLED upon charge carrier recombination [36,37]. Therefore, only 25% IQE can be achieved by the conventional fluorescent emitters, whe 75% of the injected charge carriers are lost. Consequently, significant research efforts were dedicated to evolve phosphorescent emitters, which can emit efficiently from the triplet state and realize the maximum theoretical IQE of 100% [38]. The utilization of rare metal based phosphorescent emitters aided to improve the device efficiency and brightness greatly, owing to the effective conversion of both singlet and triplet excitons into light. Particular attention was paid to iridium (III) complexes, among which, the most well-known and widely investigated triplet emitters are blue **FIrpic** [39], green **Ir(ppy)$_3$** [40] and **[(ppy)$_2$Ir(acac)]** [41], and red **(piq)$_2$Ir(acac)** [42] (**Fig. 2.2**). The usage of an iridium complex as an emitter for PhOLED led to the maximum EQE of nearly 20% [38].

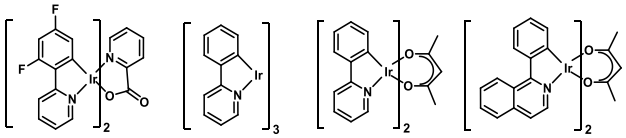

Fig. 2.2. Molecular structures of widely investigated triplet emitters

However, PhOLEDs with iridium emitters suffer from a serious efficiency roll-off at a high current density and the high application cost due to the scarcity of rare metals. Hence, the development of new phosphorescent materials remains a challenge for the scientists.

In order to attain high efficiency PhOLEDs, the advancement of suitable host materials is of equal importance to phosphorescent emitters. An appropriate host material should possess higher triplet energy level, than the guest emitter; balanced charge carrier mobility for the hole-electron recombination process and confinement of the exciton formation zone in the emissive layer; decent thermal, electrochemical and morphological characteristics; and matching with the adjacent layers HOMO/LUMO energy levels to reduce the hole and electron injection barrier [33,43]. The suppression of dopant aggregation should be achieved as well. According to the charge-transporting properties, host materials can be divided into hole, electron and ambipolar transport. The concept of bipolar (D–A) phosphorescent host opens up the opportunities to provide more balance in electron and hole fluxes thus simplifying the device structure [33]. Consequently, during the recent years much attention has been addressed towards the design and creation of multifunctional host materials.

2.2.2. Utilization of materials exhibiting delayed fluorescence

One of the recent ways to improve OLED efficiency and brightness, whilst avoiding the usage of expensive and scarce rare metals, is the employment of compounds exhibiting DF. The concept of DF is based on the achievement of total exciton utilization through efficient upconversion of nonradiative triplet states to radiative singlets by the usage of conventional organic emitters [44,45]. Generally, DF can be classified into two types: P-type, occurring by triplet fusion through the TTA mechanism; and E-type –TADF (**Fig. 2.3**). In the case of TTA, each S_1 excited state can be generated from the fusion of two T_1 states during the upconversion process. The production of this additional singlet exciton can significantly increase the efficiency up to 37.5%. By adding the prompt fluorescence emission, the total maximum IQE can reach 62.5%, depending on the upconversion ratio of the triplet excitons [28]. The main advantages of the TTA triplet upconversion technique for commercial applications include low excitation power, long lifetime and possibility of fabrication deep-blue OLEDs. TTA mechanism can take place both inter- and intramolecularly (in case of bipolar molecules) through Dexter energy transfer [33].

In turn, by utilizing TADF, it is possible to reach 100% IQE due to the total triplet harvesting, thus enormously raising the external device efficiency. Therefore, noble-metal-free TADF compounds have attracted great attention during the recent years. The E-type fluorescence mechanism takes place in several steps. Since the D-A molecular architecture is the key feature of TADF molecules, firstly the stabilization of singlet CT excited state $S_{1(CT)}$ should take place (after the electron transfer from the readily formed upon excitation singlet locally excited state $S_{1(LE)}$). If $S_{1(CT)}$ is energetically close to the locally excited triplet state $T_{1(LE)}$, reversible intersystem crossing occurs upon thermal activation, thus harvesting triplets to the isoenergetic singlet. The RISC process is followed by delayed emission from $S_{1(CT)}$

at the same location, as PF [44,46,47]. For the efficient triplet exciton upconversion by the TADF technique, a small difference between the singlet and triplet CT states energy ΔE_{ST} is required. This parameter can be tailored by the careful design of rigid angle-controlled donor-acceptor molecules with the well-pronounced ICT feature. The usage of building blocks with the balanced electron donating and accepting strength leads to the precise separation of HOMO/LUMO orbitals, which results in a small ΔE_{ST} and efficient CT emission simultaneously. However, a small overlap between HOMO and LUMO is of great importance as well, since it ensures good optical characteristics [48]. Nevertheless, due to the strong ICT requirement the development of deep blue TADF emitters still remains a challenge.

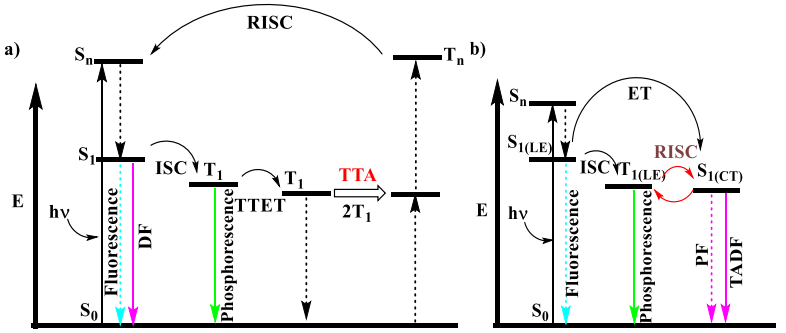

Fig. 2.3. Schematic representation of a) P-type DF; b) E-type DF mechanisms

The delayed fluorescence concept is currently the leading approach to the improvement of the efficiency in the case of fluorescent OLEDs due to the reduced cost of the materials along with much enhanced efficiency through triplet exciton harvesting. Therefore, materials scientists continue searching for new structures and cheaper synthesis of multifunctional TADF compounds.

2.2.3. Involvement of compounds possessing aggregation induced emission phenomenon

PLQY (external and internal) is a very important characteristic of an OLED. It mainly depends on the luminescent properties of the emitting material. However, most of the compounds employed for this role in the devices, suffer from severe weakening of fluorescence in the thin layers, despite showing high efficiency in dilute solutions. Since the main reason of emission quenching is associated with the formation of aggregates, which leads to π-π stacking and non-luminescent excimers, the concentration quenching is usually referred to as ACQ. Therefore, the ACQ effect is considered detrimental for many practical applications, including OLEDs [49,50,51]. The overall occurrence of the ACQ is induced by the usage of multiple planar benzene rings in conventional luminophores (e.g. perylene tetracarboxylic acid dianhydride, **Fig. 2.4**). Since the ACQ effect is an obstacle for the fabrication of an efficient device, numerous approaches, including chemical reactions, physical and engineering methods, have been developed by scientists in order to tackle the emission weakening problem. Thus, the attempts to introduce bulky substituents, longer alkyl chains and to break the conjugation between the chromophores have

been made; however, the problem of ACQ has been only partly solved and, meanwhile, new drawbacks, such as diminished charge transport, have appeared, still causing a drop in the OLED efficiency [52,53].

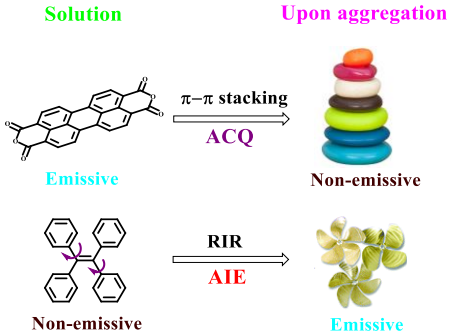

Fig. 2.4. Schematic representation of the AIE mechanism

In order to solve the aggregation quenching problem, it was suggested by Tang and co-workers in 2001 to make use of the aggregation effect. Thus, an uncommon luminogen system, in which aggregation worked constructively, was discovered. Though the dilute solutions of new luminogens were weakly fluorescent, upon the aggregation in solid state the emission was found to increase significantly. Consequently, the novel phenomenon was termed AIE [54,55]. It was discovered, that the AIE-activity of the compound strongly depends on its conformational flexibility and vibrational amplitude. In the solutions, the intramolecular rotations and vibrations of the rotor-carrying luminogens are active, accounting for the very fast radiationless decay of singlet excited states. To the contrary, in the aggregates the rotation is restricted due to the physical constraint, blocking the non-radiative and activating the radiative path. Hence, RIR and intramolecular motion in general was found to be the major mechanism in AIE-active systems (**Fig. 2.4**) [56,57]. The AIE phenomenon can partly overlap with other mechanisms, such as TICT, JAF, ESIPT, depending on the structural peculiarities of the molecules. However, in all the luminescence enhancement systems the RIR process is competing with other mechanisms, and, if it prevails, the system exhibits AIE activity [50]. The nature of the RIR process originates from the structural rigidification or conformational stiffening. Noteworthy, other variations of the AIE process, such as aggregation induced emission enhancement (AIEE), crystallization induced emission (CIE), crystallization induced phosphorescence (CIP) and aggregation induced phosphorescent emission (AIPE) have been discovered and found their applications as well [50,57,58].

As the development of highly emissive materials is of great interest nowadays, numerous AIE systems have already been designed and synthesized [57]. Plenty of structures, comprising purely hydrocarbon, heteroatom-containing, organometallic and macromolecular architecture, are known. The key issue for the construction of an AIE-gen is controlling non-planar twisted molecular skeleton upon aggregation. This can be achieved by employing sterically bulky substituents, ensuring propeller

conformation of the resulting molecule, or by attaching AIE-active groups to the conventional luminogens.

It is evident, that through the application of the RIR principle, many AIE active systems of various colours can be designed and constructed [59,60]. Apparently, due to the enhanced emission in the solid state, the AIE-gens are promising candidates materials for full-colour optical display applications.

2.2.4. Usage of the compounds with ambipolar charge transport behaviour

In recent years, tremendous efforts have been dedicated not only to the enhancement of the OLED brightness, but also to the reduction of the turn-on voltage and the increase of the lifetime of the device. As in most OLED structures HTL and ETL were employed, the stability and turn-on voltage suffered significantly from the unbalanced charge transport [61]. Consequently, the compounds, capable of balanced hole and electron charge transport simultaneously, i.e. ambipolar, have recently attracted much attention [62,63]. Nowadays, there are two major directions for the utilization of ambipolar materials: multifunctional emitters for OLEDs and multifunctional host compounds for PhOLEDs. The development of blue-emitting molecules combining high triplet level and fair balanced ambipolar charge transport still remains a challenge [64,65]. However, the elaboration of the smart ambipolar compounds may lead to the construction of cost-efficient single-layer devices [65].

The direct approach to achieve ambipolar charge transport in an organic molecule is to combine both electron-donating and electron-accepting fragments within the same molecule. Such synthetic strategies, as the interruption of π-conjugation by means of coupling in *meta*- and *ortho*-positions, incorporating bulky groups and/or changing the linkage between the two moieties can be employed for the construction of ambipolar compounds. Interestingly, some materials without the donor-acceptor conjunction, exhibit excellent non-dispersive ambipolar charge transport properties, thus suggesting an alternative way to achieve balanced hole and electron mobility [64,66].

Recently, the increased research concern is dedicated to the investigation and analysis of the relationship between charge transporting characteristics, luminescent properties of the compounds and the molecular structure. Theoretical calculations are a powerful tool to predict and understand structure-property correlations. Thus, simulation of electron-density distribution of HOMO/LUMO orbitals, ionization potentials and electron affinities, reorganization energy, dipole moments in ground and excited states can give an insight on the possible ambipolar behaviour of the material [67].

Hence, since a condition for high-performance OLEDs is the utilization of compounds with high photoluminescence quantum yield and fair balanced electron and hole mobility, the employment of ambipolar materials can offer a possibility to achieve efficient and stable single-layer OLEDs, which is highly desirable for simplifying the manufacturing process and reducing the production cost [66].

2.3. Bipolar compounds for OLED efficiency enhancement

The utilization of bipolar molecular architecture is a state-of-the-art approach towards the construction of multifunctional well-defined π-conjugated systems [27]. The bipolar structure implies the incorporation of both electron-rich and electron-deficient subunits at the molecular level by means of chemical reactions. The involvement of donating and accepting moieties results in a combination of properties of the building fragments, on the one hand, and a wide range of tunable characteristics originating from ICT, on the other hand. Thus, ICT is responsible for the regulation of the HOMO/LUMO energies, ionization potential, electron affinity, enhancement of PLQY, affecting the band gap and causing efficient photoinduced charge transfer and separation, resulting in ambipolar charge transport. All these features are essential for the fabrication of efficient devices. Moreover, multifunctionality of bipolar compounds leads to the desirable simplification of device architecture.

There are two major approaches to the design of bipolar molecules. According to one of them electron-rich and electron-deficient fragments are connected directly (**Fig. 2.5 (a)**). By the control of the angle between the chromophores, as well as varying the donating and accepting ability of the fragments, it is possible to alter the characteristics. The other strategy implies the incorporation of the spacer, either prolonging or breaking conjugation, between the donor and acceptor, depending on the expected performance (**Fig. 2.5 (b)**). Since nowadays the search for efficient blue-emitting compounds is on the wave, the consideration of retaining blue photoluminescence in the bulk implies the preservation of one type of conformation in the solid layers. This can be achieved by the usage of rigid building blocks with bulky substituents, preventing π-π stacking.

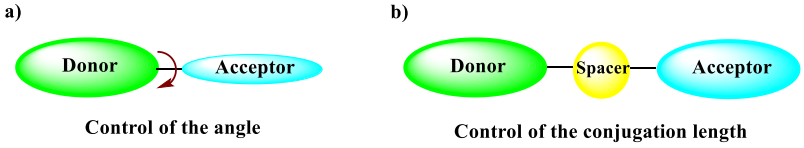

Fig. 2.5. Strategies of the molecular design of bipolar molecules

For the construction of D-A molecules, the formation of covalent C–C and N–C is necessary. The chemical methods for the preparation of bipolar compounds include mainly nucleophilic substitution and rare metal catalyzed cross-coupling reactions, such as Suzuki-Miyaura [68], Hagihara-Sonogashira [69], Stille [70], Heck [71], Ullmann [72], Buchwald-Hartwig [73] and other.

Bipolar compounds find a wide range of applications across various fields of organic electronics. Currently, there are two major research directions in OLED evolution: the development of multifunctional emitting materials for OLEDs and the design of multifunctional host compounds for PhOLEDs. The mployment of D-A materials provides opportunities to simplify the device structure, enhance the efficiency and greatly reduce cost of OLED production.

2.3.1. Bipolar compounds possessing phosphorescence

Evidently, the development of high performance host compounds for phosphorescent OLEDs is of great importance. In recent years, numerous hosts for red and green PhOLEDs were realized [74,75]. However, the elaboration of suitable high E_T hosts for blue devices still remains a challenge for scientists. Therefore, this review will focus on the recent advances in the development of host materials for blue PhOLEDs.

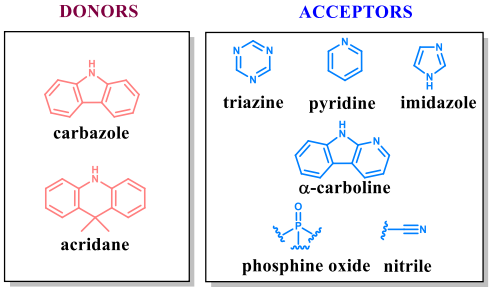

Fig. 2.6. Commonly used building blocks for the construction of bipolar host compounds for blue PhOLEDs

There are two most efficient approaches to design a bipolar material with high E_T: a careful combination of donor and acceptor moieties with the intrinsically high triplet level and control of the π-conjugation length either by shortening the linkage or by creating large hindrance between the adjacent groups. From materials chemist's point of view, the most commonly used donating fragments include carbazole, indole and acridane, while the variety of accepting units is more diverse: triazine, pyridine, imidazole, phosphine oxide, carbonline and arylnitriles (**Fig. 2.6**). Obviously, the choice of electron-donors with high E_T is very limited. The carbazole unit proved to be one of the most popular donors due to its structural rigidity, thermal stability, sufficiently high triplet level, good hole transporting ability and a variety of functionalization positions [76]. Hence, most of the efficient host materials include the carbazole backbone. Consequently, bipolar hosts can be classified by the acceptor unit involved.

1,3,5-Triazine derivatives have gathered considerable interest in recent years due to their strong electronegative nature, high electron mobility, superior thermal stability, high triplet energy and interesting photophysical properties [9,10]. Hence, a combination of TRZ and carbazole units in one molecule can prove to be an effective strategy for the design of host compounds. However, direct conjugation of the above mentioned moieties leads to lower E_T, suitable for green PhOLEDs, due to the ICT [77]. Obviously, the interruption of conjugation is required for the increase of the triplet energy value. Thus, Strohriegl and coworkers applied the strategy of conjugation interruption by synthesizing two bipolar host materials **BPTRZ** and **MBPTRZ** (**Fig. 2.7**), exploiting biphenyl and 2,2′-dimethylbiphenyl linkages, respectively, between the donor and acceptor [78], and comparing their properties. *IP* and *EA* values, deduced from CV measurements, were found to be similar for both molecules and appropriate for the efficient electron and hole injection (**Table**

2.1). In turn, geometry optimization shows, that the usage of different spacers greatly influences the torsion angle between donor and acceptor. Thus, the value of dihedral angle between PCz and the adjacent phenyl ring, attached to TRZ moiety, was found to be 35° for **BPTRZ**, while introduction of methyl-containing linkage in **MBPTRZ** enhances the twist up to 90°, what results in the conjugation interruption between the chromophores. Despite basic optical characteristics, such as absorption and fluorescence, are nearly identical for both derivatives, larger twist in molecular architecture of **MBPTRZ** is responsible for the restriction of intramolecular rotations and, hence, more blue-shifted phosphorescence, leading to higher E_T of 2.81 eV compared to 2.70 eV for **BPTRZ**. Moreover, due to the introduction of methyl substituents, higher thermal characteristics were detected for **MBPTRZ** (**Table 2.1**). Both triazine derivatives were tested as bipolar hosts in blue PhOLEDs using FIrpic as the emitter. While usage of **BPTRZ** as host material resulted in a maximum EQE of 6.2%, power efficiency of 4.6 lm/W and maximum brightness of 24400 cd/m^2 (at 15.7 V), the exploitation of its methylated analogue **MBPTRZ** increased these characteristics up to 7.0%, 6.3 lm/W and 30600 cd/m^2 (at 15.0 V), respectively, demonstrating the efficiency of the involved synthetic strategy.

A similar approach was attampted by Lee's group in the preparation of bipolar host **TrzmPCz** [79] (**Fig. 2.7**). The methyl substituent distorted the backbone structure of **TrzmPCz** and led to the increase of the torsion angle between PCz and TRZ fragments up to 55°, while the dihedral angle of the non-methylated analogue was found to be just 38°. The conjugation break resulted in the higher E_T of 2.79 eV, which is suitable for the application in blue PhOLEDs. The incorporation of robust carbazole and triazine units resulted in high T_g and T_{ID} of 109 and 376 °C, respectively, and appropriate *IP* and *EA* (**Table 2.1**). The blue PhOLED, using **TrzmPCz** host, achieved the EQE of 16.4%, current efficiency of 32 cd/A and a power efficiency of 21.5 lm/W upon the optimization of the device structure.

Another strategy to increase the triplet level was demonstrated by Zhang et al. The triazine skeleton was decorated by phenyl and phenoxy-substituents to give rise to the host compounds **DPTPCz** and **DPOTPCz** [80]. π-Conjugation between the phenyl ring and TRZ core is broken by the introduction of an oxygen atom, thus narrowing the π-electron delocalization zone of compound **DPOTPCz**. The utilization of the phenoxy group was proved to be responsible for the enhancement of E_T (2.78 and 2.86 eV for **DPTPCz** and **DPOTPCz**, respectively). However, the usage of oxygen linkage leads to the reduction of high T_g and T_{ID} due to the occurrence of more flexible molecular architecture (**Table 2.1**). While *IP* values of TRZ derivatives are quite similar (5.69 and 5.70 eV for **DPTPCz** and **DPOTPCz**, respectively), the *EA* of **DPTPCz** is slightly higher (2.74 eV) than that of **DPOTPCz** (2.64 eV), due to the more efficient electron delocalization through the phenyl-substituted triazine unit. Blue PhOLEDs, constructed to evaluate the performance of triazine hybrids **DPTPCz** and **DPOTPCz** as bipolar hosts, exhibit remarkably low turn-on voltages of 3.4 and 3.2 V, respectively, which can be attributed to the ambipolar charge carrier transport. However, irrespectively of the higher E_T and lower turn-on voltage, the device based on **DPTPCz** showed better

performance (EQE 14.4%), comparing to that based on **DPOTPCz** (EQE 11.2%). This result can be explained by the more balanced carrier mobility in **DPTPCz**.

On the whole, bipolar hosts comprising a triazine unit can be characterized by superior thermal characteristics, good hole/electron charge transport, and appropriate *IP/EA* values. However, the triplet energy and EQE values are moderate.

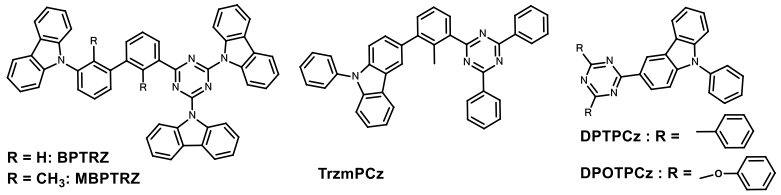

Fig. 2.7. Triazine-based bipolar host compounds for blue PhOLEDs

Compounds, bearing a phosphine oxide fragment, open another class of bipolar host materials. In recent times, aryl-substituted phosphine oxides have been found to perform the facile electron injection and transport properties [81,82]. While offering good electron transport behaviour, a phosphine oxide unit is interrupting conjugation as well, retaining the high triplet energy. By combining the structural features of carbazole and phosphine oxide promising host materials for blue PhOLEDs can be prepared. Thus, by the one-step reaction a novel tricarbazolyl-substituted phosphine oxide **POCz3** (**Fig. 2.8**) with high triplet energy was obtained and characterized by two research groups, those of Chang and Wong [83]. Since phosphine oxide is responsible for breaking the conjugation between the chromophores, the optical characteristics of **POCz3** remind of those of the parent PCz unit. Due to this fact, the triplet energy of **POCz3** reaches the remarkably high value of 3.03 eV. The utilization of three bulky and rigid PCz fragments ensures high thermal tolerance: T_g and T_{ID} of 163 and 395 °C, respectively. A shallow *IP* suitable for the injecting holes from the anode and appropriate *EA* (**Table 2.1**) are the result of careful combination of electron donating and accepting fragments. Balanced ambipolar charge transport was exhibited by **POCz3** as well. An efficient blue PhOLED with 14.5% EQE (at 31.3 lm/W) and maximum luminance reaching 60098 cd/m^2 was constructed utilizing **POCz3** as bipolar host material for FIrpic. Noteworthy, a single-layer PhOLED with EQE 9% and low efficiency roll-off was fabricated as well, indicating that **POCz3** is a promising bipolar host material.

The possibility of functionalization of phosphine oxide with bulky substituents unfurls the opportunities for the preparation of sterically hindered molecular structures, which may alleviate concentration quenching of the dopant and possess excellent morphological stability. Thus, a bipolar bulky host compound **PCF** (**Fig. 2.8**) was synthesized by Shu and coworkers [84]. The incorporation of the electron donating carbazole and accepting diphenylphosphine oxide moieties to the fluorene core provides to **PCF** such important characteristics as ambipolar charge transport behaviour and enhanced amorphous stability aas well as superior thermal properties (T_g and T_{ID} of 147 and 440 °C, respectively). Importantly, the triplet energy value remains as high as 2.75 eV, due to the connection of individual building blocks through a non-conjugated linkage – the sp^3-hybridized C-9 atom of fluorene. As it is

known, the device efficiency is often strongly dependent on the concentration of the triplet dopant [85]. Therefore, to examine the performance of amorphous host **PCF** in PhOLEDs, the devices with the concentration of FIrpic varying from 7 to 28 wt %, were constructed. Surprisingly, at the highest dopant concentration, 28 wt %, the device exhibited maximum EQE of 14.8% (30.8 cd/A and 26.2 lm/W), thus proving that **PCF**, owing to its hindered molecular structure, successfully suppresses the self-quenching of the Iridium complex at high doping levels.

In general, the main advantages of utilizing the phosphine oxide based bipolar materials is the sufficiently high triplet level, excellent thermal and morphological stability, alleviation of the emitter self-quenching and suitable *IP/EA* values. The external quantum efficiency remains only considerably high.

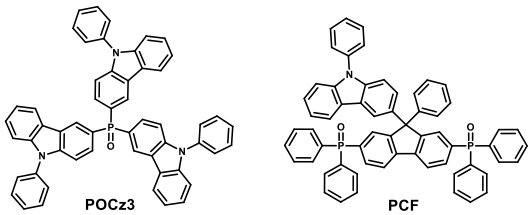

Fig. 2.8. Phosphine oxide based bipolar host compounds for blue PhOLEDs

The conjunction of pyridine and carbazole units provides an attractive approach for the cost-effective production, due to the commercial availability and inexpensiveness of the starting materials and simplicity of synthetic pathways. The weak accepting ability of pyridine leads to the reduction of ICT, accompanied by the sufficiently high E_T and retaining the ambipolar mobility behaviour [86]. Thus, a series of seven bipolar host compounds was prepared by the efficient high-yielding one-step catalyst free C–N coupling of di-, tri-, tetra-fluorosubstituted pyridines and the carbazole donor (**Fig. 2.9**) [87]. All the prepared pyridine derivatives exhibited excellent thermal characteristics with T_{ID} reaching 434 ^{o}C and T_g in the range of 70 to 150 ^{o}C (**Table 2.1**). Evidently, by increasing the number of carbazole units the thermal properties can be greatly improved. However, the increment of carbazolyl fragments leads to the bathochromic shifts in absorption and emission, as well as lowering the triplet energy. Although the T_1 states of the pyridine-carbazole hybrids are located only at the carbazole unit [88], the linking position of donor and acceptor controls the location of E_T peak. Thus, the triplet levels of **2,6-CzPy**, **3,5-CzPy**, **2,4,6-CzPy** and **2,3,4,6-CzPy** remain as high as 2.99-3.00 eV, while those of **2,4-CzPy** and **2,3-CzPy** are reduced to 2.95 eV. Noteworthy, the E_T of the tetra-substituted derivative **2,3,5,6-CzPy** was lowered to 2.81 eV. This may be attributed to the relatively strong D– A interactions between carbazole and pyridine in this molecule. All the multi-carbazole pyridine hybrids were tested as bipolar host matrixes for FIrpic in blue PhOLEDs. All the prepared devices can be characterized by remarkably low turn-on voltages reaching 3.4 eV, maximum current and external quantum efficiency in the range of 32.5–42.1 cd/A and 15.4–18.0%, respectively. Noteworthy, the compounds employing the 2,6-linking pattern, i.e. **2,6-CzPy** and **2,4,6-CzPy**, demonstrated the highest EQE of 18%, giving a hint for the further design optimization of efficient bipolar pyridine-based hosts.

Junji Kido and coworkers developed another approach for the design of bipolar pyridine hybrids (**Fig. 2.9**) by introducing a phenyl spacer between the donating and accepting fragments. Two compounds, **2,6-DCzPPy** and **3,5-DCzPPy**, were synthesized by substituting various positions of pyridine by PCz moiety [89]. Both synthesized compounds possess similar E_T of 2.71 eV, which is appropriate for the usage as the host matrix for FIrpic emitter. Since efficient exothermic energy transfer from the host triplets to those of guest, as well as excellent triplet energy confinement are necessary for the high efficiency of the device, the transient photoluminescence decay and PLQY of 3 wt % FIrpic doped into **2,6-DCzPPy** and **3,5-DCzPPy** were measured. The observation of the clear monoexponential decay curves with a relatively long lifetime of 1.59 and 1.73 μs for **3,5-DCzPPy**:FIrpic and **2,6-DCzPPy**:FIrpic films, respectively, in addition to the PLQY of ca. 0.88 proves excellent confinement of the triplet energy on the FIrpic molecules when doped into bipolar pyridine-based hosts. The constructed blue PhOLEDs exhibited outstanding efficiency of 19.1% (34.6 lm/W) and 24.3% (46.1 lm/W) for **3,5-DCzPPy**- and **2,6-DCzPPy**-based devices, respectively. Importantly, the significantly higher EQE of 2,6-substituted pyridine-based host is in agreement with the previously described results [87].

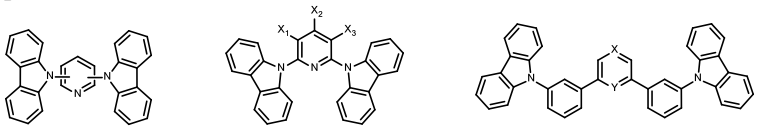

Fig. 2.9. Pyridine-based bipolar host compounds for blue PhOLEDs

To conclude, the involvement of pyridine moiety opens opportunities for the preparation of inexpensive bipolar hosts with high E_T, adequate *IP/EA* values and excellent performance in PhOLEDs.

Recently, compounds bearing α-carboline moiety have attracted great attention. α-Carboline, combining the features of carbazole and pyridine, possesses a rigid molecular skeleton and is known for the excellent electron transport properties in conjunction with high triplet level [90]. Promising structures, exploiting carbazole as donor and α-carboline as acceptor, were prepared by the group of Choi (**Fig. 2.10**) [91,92]. The researchers investigated the influence of the chromophore position on the device performance, aiming to preserve such important physical parametres as T_g, T_{ID} and E_T. All the prepared carboline derivatives can be characterized by superior thermal stability: T_g and T_{ID} reaching 146 and 491 ^oC, recpectively. Interestingly, *para*-substituted compounds, ***p*PCB2Cz** and ***p*BCb2Cz**, demonstrate better thermal behaviour, than *meta*-analogue ***m*PCB2Cz**. This may be explained by the reduced steric hindrance of more linear molecules with *para*-linkage in the solid state. DFT calculations reveal HOMO and LUMO located on carbazole and carboline units, respectively. However, in the case of ***p*PCB2Cz** and ***m*PCB2Cz** a slight overlap of the orbitals can be observed. This feature leads to the more facilitated ICT and, consequently, more pronounced low-energy absorption bands

and more red-shifted emission, in comparison to those of ***p*BCb2Cz**. Nevertheless, the triplet energy of the compounds remains significantly high and similar: ca. 2.92 eV. The investigated carboline hybrids displayed fair and balanced ambipolar charge transport behaviour. *IP* and *EA* values were found to be appropriate for hole and electron injection (**Table 2.1**). Noteworthy, compound exploiting *para*-linkage ***p*PCB2Cz** revealed the lowest *IP* of 5.60 eV. Estimation of the blue FIrpic-based PhOLEDs performance, using ***p*BCb2Cz**, ***m*PCB2Cz** and ***p*PCB2Cz** as bipolar host matrixes, resulted in extraordinary high EQE values of 22.6, 23.7, 23.0 %, respectively, and low efficiency roll-off. Importantly, the investigated hosts were tested in efficient (EQE up to 16.2 %) deep-blue PhOLEDs with FCNIrpic emitter as well.

Evidently, the bipolar hosts based on α-carboline unit, take the advantages of the high triplet level, excellent thermal characteristics, balanced charge transport, suitable *IP* and *EA* values, what makes them attractive candidates for the utilization in blue and deep-blue PhOLEDs.

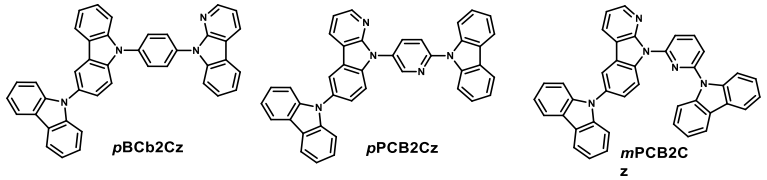

Fig. 2.10. α-Carboline-based bipolar host compounds for blue PhOLEDs

An attempt to enhance the triplet energy and the morphological stability may result in the deterioration of other important parameters, such as *IP* and *EA*, as well as charge transport. Therefore, engineering the appropriate host, balancing all the requirements, remains a challenging task. However, the utilization of various aromatic derivatives, substituted by the strongly electron-accepting nitrile (CN) group, provides opportunities for tuning thermal and charge transport characteristics to a large extent, while preserving the photophysical and photoelectrical properties. Thus, a group of bipolar host compounds, exploiting carbazole donor and cyano-decorated carbazole, dibenzofuran or dibenzothiophene as acceptors, linked through *meta*- or *ortho*-positions of the phenylene bridge, were designed and prepared in the laboratories of Li (**Fig. 2.11**) [93]. Single carrier devices confirmed balanced ambipolar charge transport behaviour of the hybrids. All the five compounds of the series demonstrate high decomposition temperatures in the range of 320-437 ^{o}C, except ***m*-CzCzCN** (T_{ID} = 186 ^{o}C), and T_g reaching 167 ^{o}C, thus implying good thermal stability (**Table 2.1**). High E_T values (2.78-2.89 eV) were observed for the CN-substituted compounds under consideration. Interestingly, the highest E_T of 2.89 eV was found for the ***m*-CzOCN**, while dibenzothiophene-based ***m*-CzSCN** displayed a significantly higher phosphorescence intensity relative to fluorescence, comparing to other studied molecules. Noteworthy, all the prepared compounds can be characterized by the adequate for high performance devices values of *IP* (5.62-5.66 eV) and *EA* (2.19-2.37 eV). High efficiency and slow efficiency roll-off were revealed by the blue PhOLEDs, utilizing these bipolar hosts, even with a simple

device architecture. The devices exploiting ***o*-CzCzCN** and ***m*-CzSCN**, exhibited remarkably high efficiency of 21.0% (43.9 cd/A) and 23.3% (46.1 cd/A), respectively. Even at high brightness of 10 000 cd/m^2, the ***o*-CzCzCN** hosted device preserved high efficiency of 28.5 cd/A.

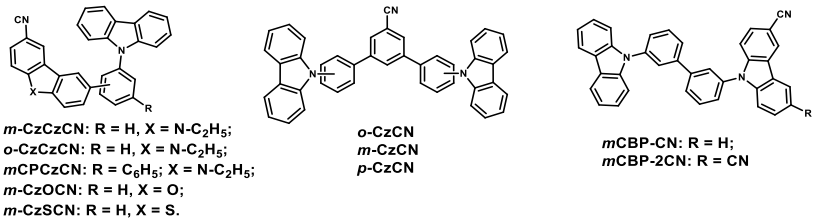

Fig. 2.11. Nitrile-based bipolar host compounds for blue PhOLEDs

In their further work, Li and coworkers applied the strategy of extending conjugation, by introducing a spacer between the carbazole donor and benzonitrile acceptor [13]. Thus, a series of three isomers, ***o*-CzCN**, ***m*-CzCN** and ***p*-CzCN**, was obtained by adjusting the *ortho*-, *meta*-, or *para*-linking pattern of the functional units (**Fig. 2.11**). Though the compounds exhibited analogous behaviour in absorption and emission spectra, the linking position was found to affect greatly the position of the triplet level. Thus, the E_T values were found to increase in the range of ***p*-CzCN**<***m*-CzCN**<***o*-CzCN** reaching a maximum of 3.01 eV. The same trend was observed for the *IP* values. Moreover, though all the three materials displayed satisfactory thermal stability with T_d well exceeding 350 °C, the values of glass transition temperature are evidently influenced by the linking topology (**Table 2.1**). Evidently, this variety in physical properties results from great difference in molecular geometries of *ortho*-, *meta*- and *para*-substituted compounds. Thus, owing to sterically hindered *ortho*-linkage in ***o*-CzCN**, a large torsional angle of 70.98° is formed between the carbazole and the adjacent phenylene bridge, as well as 77.14° between the two contiguous benzene rings, giving a hint about the interrupted conjugation between the chromophores. On the contrary, the dihedral angles in ***m*-CzCN** (54.31° and 38.34°) and ***p*-CzCN** (53.13° and 35.65°) are greatly reduced due to the weaker steric hindrance, indicating similar conjugation state in *para*- and *meta*-linked molecules. Consequently, the interrupted conjugation in ***o*-CzCN** results in higher E_T and *IP*. On the other hand, *ortho*- and *meta*-linkages are responsible for highly twisted molecular skeletons of the compounds, which led to lower T_g. Noteworthy, only ***o*-CzCN** and ***m*-CzCN** revealed good charge balance of holes and electrons, while ***p*-CzCN** was found to be capable only of hole transport. For the evaluation of the compounds under consideration as potential host matrices, blue PhOLEDs with FIrpic emitter were constructed. The ***m*-CzCN** based device exhibited the best performance, with a maximum luminance of 18340 cd/m^2, the peak current efficiency of 46.81cd/A, a peak power efficiency of 24.50 lm/W and EQE of 23.14%, along with a slow efficiency roll-off. Noteworthy, ***o*-CzCN** was utilized as bipolar host in the blue TADF device with prominently high EQE of 14.98%.

Another way to project efficient host compounds implies modification of already known molecules. Lee *et al*. developed the molecular design of host materials by upgrading the widely used *m*CBP [94]. By the incorporation of single or double cyano-moieties into the *m*CBP backbone the researchers gave rise to new hosts ***m*CBP-CN** and ***m*CBP-2CN**, aiming to facilitate electron injection and to reduce driving voltage, while retaining high triplet level. Indeed, the E_T values of new compounds were found to be 2.79 and 2.77 eV for ***m*CBP-CN** and ***m*CBP-2CN**, respectively, which is comparable with the triplet energy of parent *m*CBP (2.80 eV). Moreover, modification of carbazole with nitrile moieties resulted in improved electron accepting character and, hence, balanced ambipolar charge transport behaviour. The realization of ***m*CBP-CN** and ***m*CBP-2CN** as bipolar host matrices for $Ir(dbi)_3$ based PhOLED resulted in uncommonly high efficiencies of 24.2 and 21.3 %, respectively, along with the low driving voltage.

Table 2.1. Comparison of host characteristics in blue PhOLEDs with FIrpic emitter

Moiety	Name	E_T [a][eV]	T_g/T_{ID} [b][°C]	IP/EA [c][eV]	EQE_{max} [%]
Triazine	BPTRZ [78]	2.70	134/445	5.60/2.36	6.2
Triazine	MBPTRZ [78]	2.81	154/475	5.58/2.28	7.0
Triazine	TrzmPCz [79]	2.79	109/376	6.04/2.70	16.4
Triazine	DPTPCz [80]	2.78	86/373	5.69/2.76	14.4
Triazine	DPOTPCz [80]	2.86	79/357	5.70/2.64	11.2
Phosphine oxide	POCz3 [83]	3.03	163/395	5.5/1.8	14.5
Phosphine oxide	PCF [84]	2.75	147/440	5.86/2.76	14.8
Pyridine	2,6-CzPy [88]	3.00	75/329	5.63/2.08	18.0
Pyridine	3,5-CzPy [88]	3.00	74/310	5.72/2.16	16.7
Pyridine	2,4-CzPy [88]	2.95	70/337	5.69/2.08	15.4
Pyridine	2,3-CzPy [88]	2.95	78/286	5.66/2.07	15.5
Pyridine	2,4,6-CzPy [88]	2.99	124/412	5.67/2.21	18.0
Pyridine	2,3,5,6-CzPy [88]	2.81	150/434	5.67/2.48	15.8
Pyridine	2,3,4,6-CzPy [88]	2.99	-/419	5.67/2.43	15.8
Pyridine	2,6-DCzPPy [89]	2.71	n.p.	n.p.	24.3
Pyridine	3,5-DCzPPy [89]	2.71	n.p.	n.p.	19.1
Carboline	*p*PCB2Cz [92]	2.92	144/451	5.60/2.11	22.6
Carboline	*m*PCB2Cz [92]	2.92	128/418	5.73/2.21	23.7
Carboline	*p*BCb2Cz [91]	2.93	146/491	5.69/2.26	23.0
Nitrile	*m*-CzCzCN [93]	2.82	-/186	5.62/2.20	16.4
Nitrile	*o*-CzCzCN [93]	2.82	104/320	5.62/2.37	21.0
Nitrile	*m*CPCzCN [93]	2.78	167/437	5.66/2.23	9.2
Nitrile	*m*-CzOCN [93]	2.89	98/334	5.63/2.19	15.3
Nitrile	*m*-CzSCN [93]	2.78	111/330	5.63/2.20	23.3
Nitrile	*o*-CzCN [13]	3.01	94/426	5.74/2.16	19.1
Nitrile	*m*-CzCN [13]	2.81	121/440	5.62/2.14	23.1
Nitrile	*p*-CzCN [13]	2.77	140/350	5.59/2.16	7.03
Nitrile	*m*CBP-CN [94]	2.79	n.p.	6.06/2.95	24.2 (for $Ir(dbi)_3$)
Nitrile	*m*CBP-2CN [94]	2.77	n.p.	6.09/3.14	21.3 (for $Ir(dbi)_3$)

[a] Determined from phosphorescence spectra, recorded at 77K. [b] Measured by DSC/TGA. [c] Estimated from CV measurements. N. p. stands for "not presented".

These results suggest, that CN-substituted compounds can act as excellent hosts for triplet emitters owing to high triplet energy, balanced electron/hole

mobility, excellent thermal and morphological characteristics and appropriate *IP/EA* values.

To conclude, several classes of host materials for blue PhOLEDs, comprising various acceptor fragments, were analysed. Although each class is denoted by certain advantages and disadvantages, the best performance in devices was exhibited by pyridine-, carboline- and cyano-containing compounds, what gives a hint concerning the further design of efficient host materials. As a final benchmark, the simplicity of the synthetic pathway plays a great role in the commercialization of the materials. At this point, molecules containing pyridine and nitrile moieties, prove to be the promising candidates for the commercially applicable bipolar hosts.

2.3.2. Bipolar compounds exhibiting delayed fluorescence

For the sake of avoiding utilization of expensive noble metals in industrial applications, several approaches, including TTA [95], tuning spin–orbit coupling by side-stepping Kasha's rule [96], hybridized local and charge transfer [97] and TADF [14,44] were proposed for the device efficiency enhancement. Among these strategies, TADF proved to be the leading concept in the latest investigations. In recent years, red, green and blue TADF emitters have been developed. Nevertheless, elaboration of TADF deep-blue compounds still remains challenging; yet, efficiency increase by utilization of the TTA mechanism was reported [98]. However, since the utilization of TADF emitters made a breakthrough in OLED evolution during recent years, the current review is devoted to the advances of TADF-based devices.

For the realization of the TADF mechanism some important requirements should be considered: 1) small ΔE_{ST}; 2) stable $T_{1(LE)}$ state; 3) efficient RISC process; 4) spatially separated HOMO/LUMO with a slight overlap. For the design of efficient TADF emitters nitrogen-containing electron donors, such as carbazole, phenothiazine, phenoxazine, acridane and their derivatives found the widest application, due to strong electron donating ability and stable and high triplet states. In turn, various acceptor units, including triazine, nitrile, oxadiazole, sulfone adducts may be employed in bipolar molecules to tune the TADF emission strength, colour, and device performance (**Fig. 2.12**). As for the linking bridge, largely sterically hindered structures, such as spirojunction, bulky substituents, twisted patterns, should be utilized in order to ensure fair orbital separation with only slight overlap [99]. Since the selection of the accepting moieties is much more diverse than that of the donating units, the classification of TADF compounds will be carried out accorting to the electron deficient fragment involved.

Being efficiently used as the host materials in PhOLEDs, triazine derivatives have found wide application in the design of TADF emitters as well. Coupling with various donating substituents allows to tune the ICT character and emission properties of the bipolar compounds, promoting effective HOMO/LUMO separation and facilitating singlet-triplet up conversion and high PLQY. Thus, Kim and coworkers developed an efficient triazine-based TADF compound **DTPDDA** (**Fig. 2.13**), employing a novel azasiline donating fragment [100]. Azasiline, containing a six-membered ring with an introduced tetravalent silicon atom, offers good thermal and morphological stability, reduced conformation disorder and enlarged energy gap

between the HOMO and LUMO states for blue emission [101]. Indeed, **DTPDDA** exhibits high thermal stability (T_g and T_{ID} 325 and 404 ºC, recpectively) and good bipolar behaviour with estimated *IP* and *EA* values of 5.57 and 2.80 eV (**Table 2.2**). Taking into account, that DFT calculations predicted a small ΔE_{ST} value of 0.01 eV and well-separated HOMO/LUMO orbitals with a weak overlap, the authors decided to check TADF behaviour of new compound by examining the properties of **DTPDDA** film doped into mCP and TSPO1 cohost. Thus, slightly larger than theoretically calculated ΔE_{ST} of 0.14 eV, as well as PLQY of 0.74 were experimentally estimated for the film. The transient PL decay curves of the film showed larger delayed emission and faster decay rate at room temperature than at 35 K, giving a hint on the thermally activated nature of DF. In order to test the new compound as a TADF emitter, an OLED with mCP/TSPO1/16 wt % **DPTDDA** as the emitting layer was fabricated. The blue OLED exhibited a remarkably high EQE of 22.3 % (with the maximum power efficiency of 30.4 lm/W and turn-on voltage of 3 eV) (**Table 2.2**), proving the **DTPDDA** may be a promising candidate for TADF devices.

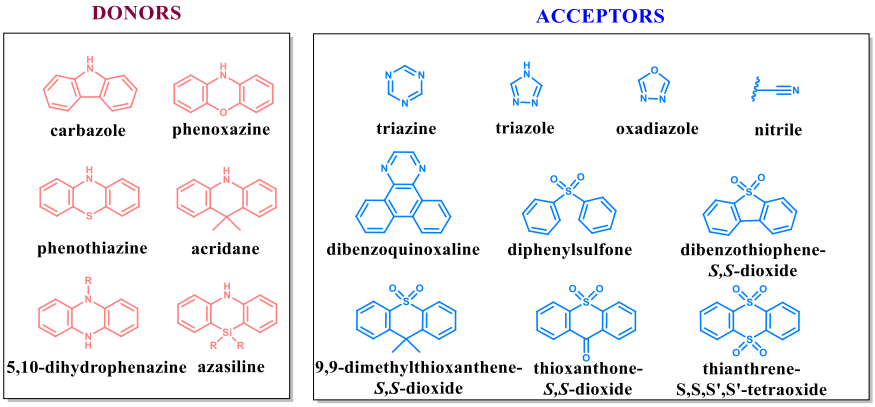

Fig. 2.12. Commonly used building blocks for the construction of TADF compounds

The compounds, preserving prominent TADF behaviour and high PLQY not only in solutions and doped films, but also in the neat layers, are particularly desirable for the achievement of high efficiency, device fabrication simplification and cost reduction. **DMAC-TRZ** (**Fig. 2.13**), achieving these goals, was designed and prepared by the groups of Wong and Wu [102]. Twisted configuration with the large dihedral angle of 88º between donating acridane and accepting triazine fragments proved to be beneficial for the conjugation diminution, HOMO/LUMO separation and reduction of ΔE_{ST} for the efficient RISC. Apparently, the experimentally estimated for the doped into mCPCN **DMAC-TRZ** ΔE_{ST} was found to be just 0.046 eV. Noteworthy, while the PL efficiency of the doped film reached 0.90, the PLQY of the neat layer remained as high as 0.83, revealing significantly suppressed concentration quenching due to the steric hindrance caused by methyl groups. TADF behaviour of doped and non-doped **DMAC-TRZ** films was proved by the temperature-dependent time-resolved measurements, revealing significant drop of delayed component with temperature reduction. Since efficient TADF was

observed for new materials both in the doped and neat films, **DMAC-TRZ** was tested as a TADF emitter in doped and non-doped OLEDs. While doped device exhibited outstanding EQE, current efficiency and power efficiency of 26.5%, 66.8 cd/A and 65.6 lm/W, respectively, the non-doped OLED demonstrated an astonishing EQE of 20%, being on par with the most efficient doped devices.

An interesting case of dual fluorescence caused by the presence of two stable conformers was reported for the phenothiazine-substituted triazine **PTZ-TRZ** (**Fig. 2.13**) by Adachi [103]. As **PTZ-TRZ** possesses the rotational dynamics of the phenothiazine unit through the N–C bond, the occurrence of two energetically profitable conformers, quasi-axial and quasi-equatorial, in the ground and excited states, becomes possible. Interestingly, both conformers were shown to emit from CT states, which is an unusual case for dual photoluminescence. Moreover, while ΔE_{ST} of quasi-axial conformer was found to be 1.14 eV, the energy difference for the quasi-equatorial was discovered to be only 0.18 eV, enabling triplet upconversion mechanism. The clear oxygen and temperature dependence of PL intensity of the quasi-equatorial **PTZ-TRZ** conformer proved the TADF nature of the long-lived PL component. An OLED exploiting **PTZ-TRZ** as a dual ICT fluorescent emitter, demonstrated the maximum EQE of 10.8%. Promising device characteristics suggest, that combination of the TADF properties with ΔE_{ST} control and conformational heterogeneity, stemming from the introduction of the phenothiazine unit, opens a new class of perspective TADF materials.

The efficient TADF phenomenon was observed in a derivative of triazine and phenoxazine, **PXZ-TRZ** [104], as well (**Fig. 2.13**). Inspired by the results of theoretical calculations, the authors achieved good HOMO/LUMO separation and small ΔE_{ST} (0.07 eV) by designing a molecule with a twisted D–A system and interfered π-conjugation. Indeed, exploitation of the phenoxazine moiety allowed a large dihedral angle between the chromophores (74.9°), thus enabling effective orbital separation and facilitated CT transition. The TADF behaviour of **PXZ-TRZ** was confirmed by the deoxygenation test (PLQY increased from 0.14 to 0.29 and the delayed component appeared in the decay transient upon deoxygenation) and PL temperature dependence. A green TADF OLED, fabricated by using **PXZ-TRZ** doped in CBP as the emitting layer, demonstrated a considerably high EQE of 12.5% with the maximum luminance reaching 10000 cd/m^2.

As organic compounds exhibiting highly efficient stable blue emission are desirable for the realization of the low-cost OLEDs, Adachi et al. conducted a systematic study in order to define the design rules for the enhancement of the electroluminescence efficiency of blue TADF emitters [105]. Thus, Adachi found out, that the utilization of spacious and bulky chromophores in a CT compound leads to good delocalization through HOMO and LUMO orbitals, while preserving the necessary charge separation. As a result, a large transition dipole moment, small ΔE_{ST} and high internal PLQY can be achieved. Several triazine derivatives were investigated with various sizes of donating and accepting fragments. Interestingly, the efficient delocalization through HOMO of the bulky tricarbazolyl donor of **3Cz-TRZ** compound resulted in the remarkably high PLQY of ca. 1 and negligible ΔE_{ST} of 0.09 eV. The blue OLED, utilizing **3Cz-TRZ** as TADF emitter, reached the

internal quantum efficiency of nearly 1, and EQE of 20.6% (**Fig. 2.13**, **Table 2.2**), which is comparable with the characteristics of blue Ir-based PhOLEDs. The PL on temperature dependence provides a proof, that blue electroluminescence with the high PLQY is a consequence of the efficient thermally activated RISC process.

The material design employing the distortion of conjugation was successfully realized by coupling substituted indolocarbazole with biphenyltriazine fragment yielding **PIC-TRZ** [106] (**Fig. 2.13**). Thus, considerable steric hindrance around the biphenyl triazine unit, induced by the bulky indolocarbazole unit, resulted in exclusive localization of HOMO and LUMO on D and A moieties. Broad, non-resolved emission of **PIC-TRZ**, molecularly dispersed in toluene and mCP host, gave a hint on the CT character of PL, critical for TADF. Strong oxygen sensitivity, expressed in drastic reduction of PLQY from 0.35 to 0.10 and disappearance of the delayed component in the transient curve in toluene solution upon oxygen saturation, provides evidence of the triplet excitons contribution. The produced green TADF OLED with the structure ITO/ NPD/ mCP/6 wt %-**PIC-TRZ**: mCP/BP4mPy/LiF/Al demonstrated the EQE of 5.3 % and the maximum luminance 10000 cd/m^2, well exceeding the theoretical limits. Moreover, the authors are confident, that the optimization of device parameters could increase the efficiency.

Being smartly designed, carbazole/triazine derivatives possess such essential for TADF features, as good orbital separation and reduced ΔE_{ST}. Thus, **CzT** (**Fig. 2.13**), firstly reported as a host material for PhOLEDs [107], was found to be an efficient TADF emitter as well [108], due to the suitable design. Noteworthy, **CzT** displayed TADF behaviour not only in a solution (hexane, toluene), but also in the solid state (dispersed in DPEPO host). In all the investigated media strong oxygen-sensitive behaviour of PL intensity and PLQY was observed. In turn, temperature dependent time-resolved measurements, conducted for the 3 wt% **CzT**:DPEPO film, demonstrated evident increase of the DF intensity and contribution to the PL transient at the temperatures $\geq$150K, being responsible for the overall PL enhancement. Such behaviour is a key feature of TADF as triplet excitons do not have sufficient energy for up-conversion at low temperatures, enabling RISC only with temperature increase. **CzT** was tested as a TADF emitter in an OLED. The green device demonstrated the EQE of 6 % at low current densities (>10^{-1} mA/cm^2).

Most of the reported blue TADF OLEDs suffer from the instability and short lifetime comparing to the Ir-based PhOLEDs. Therefore, the search for the stable and efficient blue and deep-blue TADF emitters remains a challenge for researchers. In order to obtain deep blue emitters of pure colour, a weaker donating component is desirable for the singlet energy stabilization. Therefore, Lee and coworkers [109] introduced a dicarbazolylphenyl unit in order to weaken the carbazole donating strength and tune the emission colour by preparing two mono- and disubstituted triazines **DCzTrz** and **DDCzTrz** (**Fig. 2.13**). Due to the strengthened donor character **DDCzTrz** displayed slightly red-shifted PL and phosphorescence (2.80 and 2.53 eV) in THF when compared to **DCzTrz** (2.89 and 2.64 eV). Nevertheless, both compounds can be characterized by similar and sufficiently small ΔE_{ST} of ca. 0.27 eV (**Table 2.2**). However, the enlarged chromophore system of **DDCzTrz** is responsible for its higher PLQY (0.43 and 0.66 for **DCzTrz** and **DDCzTrz**,

respectively). For the identification of DF behaviour, transient and time-resolved PL measurements were conducted. Thus, the delayed emission with the decay times of 3.1 and 2.8 μs was observed for **DCzTrz** and **DDCzTrz**, respectively, in addition to PF. Two blue efficient OLEDs were prepared by using **DCzTrz** and **DDCzTrz** as TADF emitters at 25% doping concentration. Interestingly, the disubstituted compound displayed a higher EQE value (18.9%) than its monosubstituted analogue (17.8%). It can be attributed to the higher PLQY of **DDCzTrz** achieved due to the larger chromophore system. The investigated lifetime of the **DDCzTrz** device was found to be three times as long as that of the $Ir(dbi)_3$ PhOLED, indicating the success of the employed molecular design.

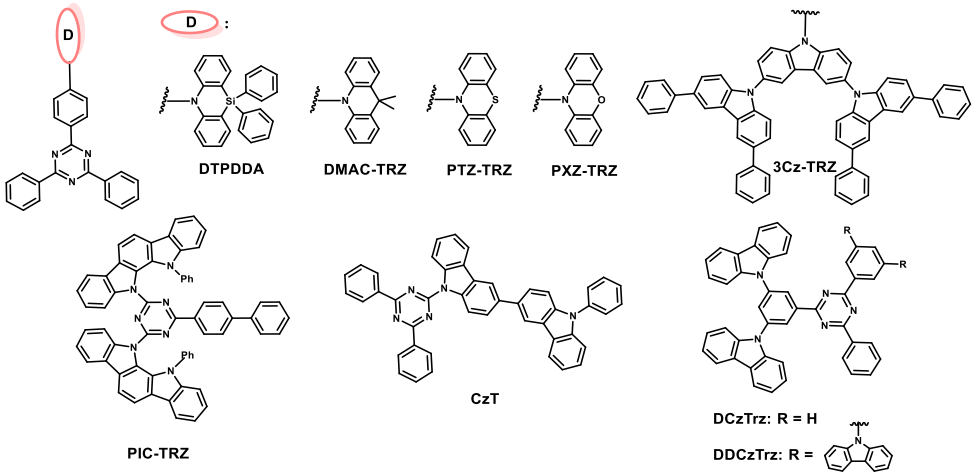

Fig. 2.13. Triazine-based TADF compounds

To conclude, the usage of the triazine unit gives an opportunity to obtain stable TADF emitters with small ΔE_{ST}, appropriate *IP/EA* values, sufficient PLQY and tunable from yellow to deep-blue emission. The EQE values of TADF devices vary from moderate (5.3 %) to remarkably high (26.5 %), giving a hint that by careful design rules and device structure optimization outstanding results can be achieved.

Lately, sulfone-containing compounds have been attracting increasing interest due to high electron-accepting ability of sulfone moiety and the possibility of realization of the high efficiency blue and deep blue TADF OLEDs [110]. Firstly, a 3,6-di-*tert*-butylcarbazolyl derivative **DTC-DPS** was prepared by Adachi and coworkers [48] (**Fig. 2.14**). Detailed photophysical investigation revealed a well-pronounced CT character of **DTC-DPS** emission in polar solvents due to the stabilization of the dipole moment, and the moderately small singlet-triplet energy splitting of 0.32 eV, which is in agreement with the theoretically calculated 0.34 eV. Moreover, the high PLQY value of 0.69 and a 270 μs delayed component in the PL transient (prompt 5.3 ns) weas observed upon the deoxygenation of the toluene solution, indicating a successful RISC process. As expected, slow decay component disappears in non-polar hexane solution, characterized by well-resolved PL, pointing out the key role of the CT state in the TADF phenomenon. The incorporation of **DTC-DPS** in the high triplet level DPEPO matrix resulted in a high PL quantum

efficiency of 0.80, which encouraged the authors to test a doped material in a multilayer TADF OLED. Consequently, an efficient pure blue device with the EQE of 10% was realized (**Table 2.2**).

However, a blue TADF OLED, employing **DTC-DPS**, suffered from remarkable efficiency roll-off under high current density due to the long DF lifetime. Therefore, an improved analogue of **DTC-DPS**, **DMOC-DPS**, was prepared by the group of Adachi [111]. The utilization of metoxy- substituents of the carbazole moiety resulted in stronger donating ability of 3,6-dimetoxycarbazole fragment, leading to the more pronounced CT character of **DMOC-DPS**, and, hence, a smaller ΔE_{ST} of 0.24 eV, although slightly red-shifted singlet emission was also observed. The better expressed CT feature of **DMOC-DPS** is responsible for the slightly smaller PLQY of 0.56 in oxygen-free toluene and significantly reduced DF decay lifetime of 93 μs. However, doping of the novel compound into DPEPO host resulted in the PLQY of 0.80, on par with **DTC-DPS**. The manufactured blue multilayer OLED, using DPEPO: 10 wt % **DMOC-DPS** exhibited the EQE of 14.5 %, turn on voltage of 4.0 V and maximum brightness of 2544 cd/m^2 at 12.5 V, confirming the role of substituents on the control of CT states, ΔE_{ST}, TADF component lifetime, and, consequently, the OLED performance.

The facilitated triplet exciton confinement and the negligible singlet-triplet energy gap can be achieved by the utilization of compounds with pretwisted conformation owing to the steric hindrance between D and A fragments [111,112]. This approach was successfully realized in the design of blue-emitting **DMAC-DPS** and green-emitting **PXZ-DPS** compounds [113] (**Fig. 2.14**). As it was mentioned in the discussion of triazine-based TADF materials, the employment of aromatic donors bearing a six-membered ring (acridane, phenoxazine, phenothiazine) is responsible for the twisted molecular structures with dihedral angles of 70-90^o. As expected, the donor strength is responsible for the emission colour control. Thus, the oxygen-free dilute toluene solutions of the studied compounds can be characterized by the maximum PL peak of 460 nm (**DMAC-DPS**) and 507 nm (**PXZ-DPS**), the PLQYs of around 0.80 and the negligible ΔE_{ST} of ca. 0.08 eV. Moreover, the delayed components of 0.9 and 2.5 μs for **DMAC-DPS** and **PXZ-DPS** in decay transients can be detected as well. The OLEDs, utilizing novel TADF emitters **DMAC-DPS** (doped in DPEPO) and **PXZ-DPS** (doped in CBP) demonstrated the outstanding device performance with EQE of 19.5 and 17.5%, respectively. Noteworthy, due to the bulky methyl substituents on the acridane units, **DMAC-DPS** was found to exhibit a remarkably high PLQY of 0.80 in the neat film, evidently avoiding the concentration quenching. Therefore, the material was tested in an undoped device, thus improving the charge transporting characteristics as well. The EQE of 14.4%, and, surprisingly, higher stability comparing to the doped device, were observed [114].

While most researchers are in search of materials with a small ΔE_{ST}, the work of Dias and Monkman shows that even compounds with relatively large $\Delta E_{ST} \geq 0.3$ eV are capable of exhibiting the TADF phenomenon [44]. Thus, detailed spectroscopic investigation of linearly and angularly substituted dibenzothiophene-*S*,*S*-dioxide derivatives was carried out. It was revealed that angularly substituted

compounds with the N–C bond between the donor and acceptor, exhibit a better pronounced ICT and strong phosphorescence. Moreover, angular disubstitution was found to shift the triplet states to higher energies, aiding consequently to the reduction of the ΔE_{ST} gap. All the compounds reported by Dias et al. displayed strong DF; still, the best results were obtained for carbazole and diphenylamine derivatives **DBTD-Cz** and **DBTD-DA** (ΔE_{ST} 0.35 and 0.48 eV, respectively) (**Fig. 2.14**). The evident proof of the TADF mechanism was produced by the linear dependence of the log-log plot of DF intensity with excitation dose. Complete DF quenching was observed under oxygen-saturated conditions as well. The intensity of delayed emission was found to increase with temperature for both materials, thus confirming a thermally activated step in RISC irrespectively of the ΔE_{ST} value. The authors concluded, that for the realization of pure TADF mechanism with 100% triplet harvesting the control of conjugation and CT states, as well as the presence of $^3n\pi*$ triplet state, play the crucial role in spite of relatively high ΔE_{ST}. As the final benchmark, highly efficient green TADF OLEDs with various dopant concentrations, using **DBTD-Cz** as the emitter, were fabricated, with the maximum EQE reaching 14.3 % [115].

Thioxanthone and its adducts are known to possess a high rate of intersystem crossing, high triplet yield and narrow ΔE_{ST} [116]. In turn, the oxidation of the sulfur atom of thioxanthone gives rise to a promising accepting unit for the design of new TADF emitters – thioxanthone-*S*,*S*-dioxide. Thus, Wang et al. developed two new TADF emitters, **TXO-TPA** and **TXO-PhCz**, by utilizing the thioxanthone-*S*,*S*-dioxide and TPA and PCz donors [117] (**Fig. 2.14**). The angular substitution of the acceptor ensured well-separated HOMO/LUMO orbitals with a slight overlap and well-expressed CT character. The strong CT feature results in green (**TXO-PhCz**) and yellow (**TXO-TPA**) PL in Me-THF, significant solvatochromism, unstructured phosphorescence and remarkably narrow singlet-triplet energy splitting (**Table 2.2**). Noteworthy, the neat films of new compounds demonstrated outstandingly high PLQYs of 0.93 (**TXO-PhCz**) and 0.36 (**TXO-TPA**) indicating the AIE feature. In order to confirm the TADF mechanism, solid films of new compounds, doped into the mCP host, were prepared. The delayed component decaying within 78 μs, was observed in the PL transients of both compounds. Sensitivity to oxygen, expressed in the disappearance of the long decay component and drastic reduction of PLQY, revealed for the **TXO-TPA** and **TXO-PhCz** doped films, is a clear sign of triplet states involvement. Consequently, the increasing trends of PLQY and DF efficiency of the films with temperature point out the thermally activated pathway. Promising characteristics of **TXO-TPA** and **TXO-PhCz** inspired the authors to test new compounds as emitters in TADF OLEDs. Thus, a multilayer device with 5 wt % of **TXO-TPA** in mCP exhibited intense yellow electroluminescence, the turn on voltage of 5.3 V, a power efficiency of 47.4 lm/W and a high EQE of 18.5% with a maximum luminance up to 16300 cd/cm^2. **TXO-PhCz**-based green OLED with similar architecture performed even better: turn on voltage of 4.7 V, maximum brightness of 21000 cd/cm^2 at 18.3 V, and the current efficiency and power efficiency up to 76.0 cd/A and 70.0 lm/W, and remarkably high EQE of 21.5%. Superior performance of the **TXO-PhCz**-based device can probably be attributed to

the higher PLQY of this material and better electronic levels confinement with the host. These results indicate, that bipolar compounds utilizing thioxanthone-*S*,*S*-dioxide moiety are promising candidates for the TADF emitter production.

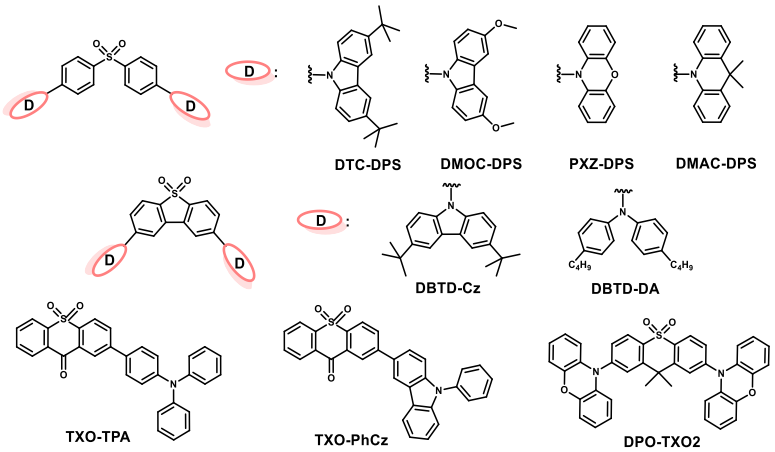

Fig. 2.14. Sulfone-based TADF compounds

It is common knowledge, that a narrow singlet-triplet gap plays an important role in the engineering of successful TADF emitters. By detailed photophysical investigation of a new compound **DPO-TXO2** (**Fig. 2.14**), bearing phenoxazine donor and 9,9-dimethylthioxanthene-*S*,*S*-dioxide acceptor, Santos and Monkman revealed strong dependence of ΔE_{ST} on the environment, thus making important contribution towards the understanding of the principles of the underlying mechanism of TADF emitters [46]. The usage of strong and rigid donating and accepting fragments resulted in a nearly orthogonal molecular architecture of **DPO-TXO2** (torsion angles of 89.9 and 73.2° were revealed by X-ray analysis), facilitating the CT. Investigation of photophysical characteristics in solvents of different polarity (MCH, toluene, *o*-DCB), as well as solid solutions in zeonex and CBP matrices, revealed strong solvatochromism with CT-originated PL even in non-polar media, small ΔE_{ST} (0.01–0.16 eV), as well as oxygen- and temperature sensitive PL intensity, lifetime and DF, thus confirming the TADF mechanism. The linear dependence of PL intensity on the laser excitation dose fully proves the thermally activated intramolecular process. The authors showed, that the ^{1}CT emission is better stabilized in the polar media, thus reducing ΔE_{ST} and leading to a more efficient DF. However, the realization of TADF is possible in non-polar media, close to the nature of host materials used in OLEDs, as well. Since a quenching of the donor ^{3}LE excitons by the CBP host was identified, the co-deposited film of **DPO-TXO2** and DPEPO was utilized for the fabrication of an efficient green TADF OLED with the EQE of 13.5%, high brightness of >10,000 cd/m^2 and excellent resistance to roll-off up to 11 mA/cm^2.

In general, the usage of sulfone-based TADF compounds opens the opportunities to develop highly efficient (EQE up to 21.5%) blue and deep blue OLEDs, while preserving the possibility of evolving green, yellow and red devices

as well, owing to the careful design of stable bipolar molecules with the narrow singlet-triplet splitting.

The employment of a stable electron-accepting nitrile group in the projection of the TADF emitters unfurls the amazing diversity of functionalization, leading to the variety of structures and properties. While providing sufficient CT character, good PLQY and electron mobility, a nitrile moiety barely affects the triplet level, which is especially attractive for the design of blue TADF emitters. Inspired by the versatility of properties, offered by the nitrile unit, Adachi et al. designed and prepared a series of multicarbazolyl-substituted dicyanobenzene derivatives [45]. By varying the amount of carbazolyl sunstituents and position of nitrile groups photophysical properties were tuned. The most efficient materials **2CzPN** and **4CzIPN** are presented in **Fig. 2.15**. Steric hindrance between the chromophores resulted in good HOMO/LUMO orbitals separation (confirmed by DFT calculations), suggesting narrow singlet-triplet energy splitting. Indeed, the small ΔE_{ST} of ca. 0.08 eV (**Table 2.2**) encouraged the authors to check for the TADF phenomenon in the newly obtained compounds. Under nitrogen-rich conditions the toluene solution of **2CzPN** demonstrated sky-blue emission with a PLQY of 0.47, while the solution of green-emitting **4CzIPN** exhibited impressive PL efficiency of 0.94. Bathochromic shift in PL, as well as the much higher PLQY of **4CzIPN** can be solely explained by the increased number of donating carbazole fragments. Both compounds displayed a delayed component (166 and 5.1 μs for **2CzPN** and **4CzIPN**, respectively) in the decay transients, disappearing upon oxygen saturation. The presence of a well-expressed long transient component and good overlap of PF and DF the authors attributed to TADF. In order to evaluate the performance of new compounds as TADF emitters, multilayer OLEDs were prepared, by using CBP as a host for **4CzIPN** and PPT as matrix in the sky-blue OLED with **2CzPN**, for better triplet levels confinement. While sky-blue OLED demonstrated the EQE of 8%, the remarkably high PLQY of **4CzIPN** is responsible for the outstanding performance of the green device (EQE 19.3 %).

Efficient minimization of the HOMO/LUMO wave functions overlap, leading to a narrow ΔE_{ST}, can be achieved by steric separation of the donor and acceptor through the spiro-junction [106]. Following these considerations, a bipolar compound **ACRFLCN** (**Fig. 2.15**), bearing the spiro-conjugated acridane donor and 2,7-dicyanofluorene acceptor, was projected and synthesized [118]. The DFT approach confirmed fairly separated HOMO/LUMO orbitals and a negligible ΔE_{ST} of 0.0083 eV. Even though yellow-emitting **ACRFLCN** showed a tendency for self-quenching in the neat film, upon doping (6 wt %) into the TPSi-F [119] host the intense green emission with 0.67 PLQY was observed in nitrogen-rich conditions. The delayed component in the decay transient (3.9 μs), vanishing after oxygen saturation, was revealed for the doped film as well. Complete overlap of prompt and delayed emissions, as well as the thermally activated enhancement of the delayed component, are clear signs of the triplet upconversion by the TADF mechanism. The experimental ΔE_{ST} of 0.1 eV, sufficiently high PLQY and discovered TADF properties were inspiring to test **ACRFLCN** as an emitting layer in OLED. The TADF device with the ITO (110 nm)/ TAPC (40 nm)/mCP (5 nm)/6 wt%

ACRFLCN:TPSi-F (20 nm)/ TmPyPB (35 nm)/LiF (1 nm)/Al (62 nm) stack demonstrated high performance (EQE 10.1 % at a low current density of $3.3 \cdot 10^{-4}$ mA/cm^2). However, the authors are confident that further optimization of the device may result in better performance.

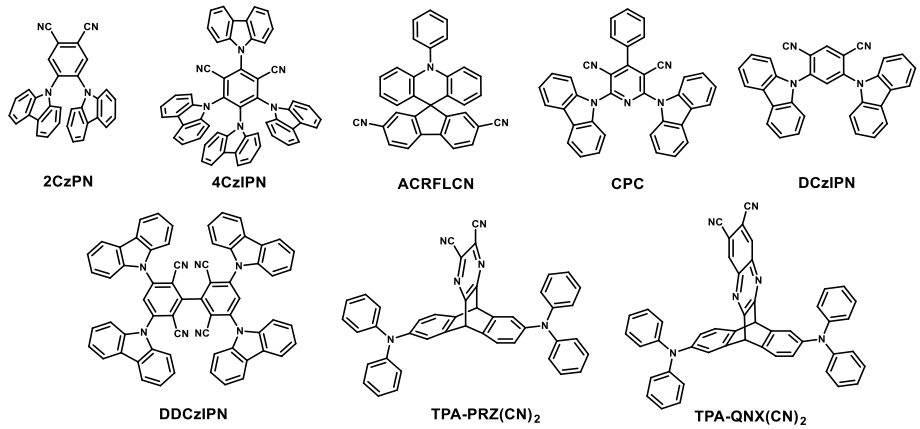

Fig. 2.15. Nitrile-based TADF compounds

Incorporation of nitrile moieties into the actual electron-deficient molecule results in the enhancement of electron-accepting abilities of the latter. Thus, the introduction of cyano- and carbazolyl- fragments to the 4-phenylpyridine core gave rise to the novel TADF emitter **CPC** [37] (**Fig. 2.15**). The enhanced electron-withdrawing ability of pyridine-3,5-dicarbonitrile core and prominent electron-donating strength of the carbazole groups resulted in pronounced CT band in absorption and well-expressed solvatochromism in the emission of **CPC**. Upon the incorporation into mCP host, **CPC** revealed intense blue photoluminescence with the PLQY of 0.50, a narrow ΔE_{ST} of 0.04 eV and a strong delayed component (46.6 μs) in the decay transient in oxygen-free conditions. Noteworthy, the delayed component became more significant with the temperature enhancement, which is typical for TADF emitters. Based on the attractive characteristics of the new compound, several TADF OLEDs with various doping **CPC** concentrations and device architecture of ITO/TAPC (40 nm)/TCTA (5 nm)/**CPC**: mCP (20 nm)/TmPyPB (40 nm)/LiF (0.8 nm)/Al were fabricated. As expected, at the highest concentration (13 wt %) the blue-emitting devices demonstrated the best performance (EQE 21.2%), probably, owing to the more efficient exciton utilization with higher emitter component.

Recently Cho et al. have shown, that a smartly designed single TADF molecule can be successfully used for various applications [120]. Thus, since a blue TADF emitter has a high triplet level, it can serve as an efficient host material in a yellow PhOLED as well; in turn, the combination of the blue TADF device and the yellow PhOLED gives rise to the high efficiency hybrid WOLED without any interlayer between the blue and yellow emitting layer. In order to fulfill the requirements for these multiple applications, a bipolar carbazolyl-substituted 1,3-dicyanobenzene derivative **DCzIPN** was prepared (**Fig. 2.15**).

Table 2.2. Comparison of the TADF emitters characteristics in OLEDs of various emission colour

Moiety	Compound	ΔE_{st}[a], eV	QY[b]	CIE[c] (x, y)	Emission colour[c]	IP/EA[d]	EQE_{max} [c], %
Triazine	DTPDDA [100]	0.14	n.p.	0.15, 0.19	Deep blue	5.57/2.80	22.3
Triazine	DMAC-TRZ [102]	0.048	0.90	n.p.	Green	5.30/2.78	26.5
Triazine	PIC-TRZ [106]	0.11	0.35	n.p.	Green	n.p.	5.3
Triazine	CzT [108]	0.008	0.45	0.23, 0.4	Green	5.49/2.77	6.0
Triazine	3Cz-TRZ [105]	0.09	1.00	n.p.	Blue	n.p.	20.6
Triazine	PTZ-TRZ [103]	0.18	n.p.	n.p.	Green	5.50/3.00	10.8
Triazine	PXZ-TRZ [104]	0.07	0.29	n.p.	Green	5.50/3.10	12.5
Triazine	DCz-Trz [109]	0.25	0.43	0.15, 0.14	Blue	5.88/2.86	17.8
Triazine	DDCz-Trz [109]	0.27	0.66	0.16, 0.22	Blue	6.01/2.90	18.9
Sulfone	DTC-DPS [48]	0.32	0.69	0.15, 0.07	Blue	5.81/2.52	10.0
Sulfone	DMOC-DPS [111]	0.21	0.56	0.16, 0.16	Blue	n.p.	14.5
Sulfone	PXZ-DPS [113]	0.08	0.80	n.p.	Green	5.59/2.79	17.5
Sulfone	DMAC-DPS [113]	0.09	0.80	0.16, 0.20	Deep blue	5.92/2.92	19.5
Sulfone	DBTD-Cz [44]	0.35	0.26	n.p.	Green	n.p.	14.3
Sulfone	DBTD-DA [44]	0.48	0.30	n.p.	Green	n.p.	n.p.
Sulfone	TXO-TPA [117]	0.04	0.36	0.45, 0.53	Yellow	5.37/3.49	18.5
Sulfone	TXO-PhCz [117]	0.09	0.93	0.31, 0.56	Green	5.78/3.48	21.5
Sulfone	DPO-TXO2 [46]	≤0.16 *	n.p.	n.p.	Green	5.37/2.61	13.5
Nitrile	TPA-QNX$(CN)_2$ [123]	0.11	0.44	0.45, 0.54	Green	5.22/2.57	9.4
Nitrile	TPA-PRZ$(CN)_2$ [123]	0.075	0.52	0.43, 0.55	Green	5.23/2.48	4.0
Nitrile	2CzPN [45]	n.p.	0.47	n.p.	Blue	n.p.	8.0
Nitrile	4CzIPN [45]	0.08	0.94	n.p.	Green	n.p.	19.3
Nitrile	DCzIPN [120]	0.05	0.67	0.17, 0.19	Blue	6.26/3.56	16.4
Nitrile	DDCzIPN [121]	0.13	0.91	0.22, 0.46	Green	6.40/3.88	18.9
Nitrile	CPC [37]	0.04	0.50	0.18, 0.26	Blue	6.25/3.47	21.2
Nitrile	ACRFLCN [118]	0.10	0.67	n.p.	Blue-green	6.07/2.53	10.1

[a]Deduced from the measurements in the medium, where TADF was observed; [b] Estimated from the measurements in oxygen-free conditions, where TADF was observed; [c]Device characteristics; [d] Determined by CV measurements; *investigated in various media. N. p. stands for "not presented".

Doped into mCP host **DCzIPN**, exhibiting a strong CT character in both absorption and emission, displayed the singlet emission at 2.77 eV, high PL quantum efficiency of 0.67 and small ΔE_{ST} (0.05 eV). The TADF emission pathway of **DCzIPN** was proved by transient and time resolved PL measurements, which revealed a long-living component (1.2 μs) in nitrogen-rich conditions and good overlap of PF and DF. These characteristics enabled Cho and coworkers to test **DCzIPN** as the blue TADF emitter. Thus, with the optimum doping concentration (15 wt % of **DCzIPN** in mCP) an efficient TADF OLED with the EQE of 16.4 % was obtained. In turn, the utilization of **DCzIPN** as the host material in the yellow-emitting PhOLED resulted in the remarkable EQE of 24.9 %. Furthermore, the high efficiency white-emitting hybrid OLEDs were prepared by stacking the blue TADF device and the yellow PhOLED without any interlayer. Consequently, the WOLEDs

of cool white colour (CIE 0.31, 0.33) and warm white colour (CIE 0.39, 0.43) were obtained with the eminent external efficiency values (21 and 22.9 %, respectively). To conclude, the usage of a single material as a blue TADF emitter and a phosphorescent host greatly simplifies the structure and cost of the device preparation and leads to the significant efficiency enhancement.

It is common knowledge, that the extended conjugation system leads to the enhancement of PLQY and improvement of thermal characteristics. Therefore, in order to increase the efficiency of already known TADF emitters, the concept of the dual core, based on the prolonged conjugation, can be adopted [121]. Thus, for the sake of upgrading the described previously blue TADF emitter **DCzIPN** [120], a novel compound **DDCzIPN** [121] with a dual emitting core was synthesized by the simple coupling of two TADF **DCzIPN** units (**Fig. 2.15**). Comparing to its smaller analogue **DCzIPN**, the newly synthesized **DDCzIPN** demonstrated a significant enhancement of the absorption intensity and PLQY (from 0.67 to 0.91) (data for films in PS matrix). However, the extended conjugation system of **DDCzIPN** resulted in the bathochromically shifted PL and phosphorescence as well, leading to green emission. Time-resolved measurements revealed the delayed emission (2.8 μs), well matching the prompt PL. The TADF OLED, employing **DDCzIPN** doped in the mixed host of mCP and BmPyPb as the emitting layer, was prepared. As expected, exhibiting green electroluminescence device demonstrated improved efficiency (18.9 %) due to the higher PLQY of **DDCzIPN**, thus revealing the success of the dual core strategy.

It has been emphasized many times, that fair HOMO/LUMO separation plays a crucial role in the minimization of ΔE_{ST} and observation of TADF. The conventional strategies of TADF compounds design involve twisted geometry, obtained through the usage of bulky D and A units or the spirojunction [99]. An alternative approach, by employing the through-space interaction of donating and accepting systems by homoconjugation [122] was successfully realized by Baldo, Swager and coworkers [123]. Thus, two novel bipolar triptycene-based compounds **TPA-QNX(CN)$_2$** and **TPA-PRZ(CN)$_2$**, bearing the diphenylamine donating unit and dicyanoquinoxaline or dicyanopyrazine, respectively, as the acceptor, were prepared (**Fig. 2.15**). As expected, DFT calculations revealed perfect wave function separation with a slight overlap and a negligible ΔE_{ST} (0.075–0.111 eV), thus encouraging the authors to check for the TADF phenomenon. Impressive PLQY enhancement was observed in the oxygen-free cyclohexane solutions of new compounds: from 0.22 to 0.44 for **TPA-QNX(CN)$_2$** and from 0.28 to 0.52 for **TPA-PRZ(CN)$_2$**, suggesting the involvement of the triplet states. The long-lived components of 2.4 and 6.5 μs for **TPA-QNX(CN)$_2$** and **TPA-PRZ(CN)$_2$**, respectively, were observed in the decay transients of the degassed solutions. The major proof of the TADF mechanism was provided by the linear dependence of the PL intensity on the excitation dose. Finally, new compounds were tested as TADF emitters in the green OLEDs. Thus, **TPA-QNX(CN)$_2$** displayed the EQE 9.4%, while the other triptycene derivative **TPA-PRZ(CN)$_2$** demonstrated only 4% EQE. Better performance of the **TPA-QNX(CN)$_2$** based OLED can be probably explained

by the larger conjugation system, better delocalization of electron density on LUMO, and the better confinement with the host.

Evidently, the nitrile-containing compounds impress with the diversity of structures and properties. The realization of high efficiency OLEDs with different emission colours is possible with the usage of cyano-decorated materials.

In conclusion, several classes of various emission colour TADF materials with different acceptor units have been analysed. Each class of compounds can be characterized by a sufficiently small ΔE_{ST} gap, high PLQY, good thermal and morphological stability and appropriate *IP/EA* values, thus opening the opportunities for the realization of highly efficient (EQE up to 26.5 %) devices. However, from the point of view of the synthesis pathway rationality, materials cost-efficiency and the possibility of various applications the nitrile-based compounds are advantageous to other described TADF molecules. This conclusion may serve as the indication towards the further design of perspective TADF compounds.

2.3.3. Bipolar compounds possessing aggregation induced emission phenomenon

Although in recent years many efficient emitters have been produced, most of them can perform successfully in OLEDs only in the doped layers due to the problem of severe concentration quenching [55].Therefore, compounds, exhibiting the AIE feature [50], can prove advantageous in the fabrication of cost-efficient non-doped devices. In turn, the AIE materials with bipolar molecular architecture can offer not only full colour range emission, but also ambipolar charge transport and superior thermal and electrochemical stability. Moreover, the combination of such beneficial features, like AIE, DF and ambipolar charge transport behaviour, can result in astonishing device efficiency enhancement.

The presence of a flexible rotor-carrying unit, responsible for the non-radiative pathways in solutions and radiative routes in the solid state due to the RIR process, is a necessary condition for the realization of the AIE mechanism [55]. Therefore, bipolar compounds possessing the AIE phenomenon can be classified mainly by the AIE active fragment employed. Thus, the most well-known AIE systems involve such units, as stilbene [124], TPE [125], 9-fluorenone [126,127] and silole [54] derivatives (**Fig. 2.16**). Interestingly, the AIE phenomenon can be traced as well just from the fixed angle in the rigid molecular structures, thus avoiding π-stacking in the condensed state [102]. Since the choice of donating and accepting fragments for the construction of the AIE compounds is very diverse, the classification will be carried out according to the involved AIE active moiety.

Although the actual stilbene moiety is prone to π-π stacking interactions in the solid state, leading to the excimer formation and weakened light emission [49], the additional substitution of the double bond results in a twisted non-planar conformation, activating the RIR process [50]. Consequently, by varying the amount and the nature of the double bond substituents, a great number of the stilbene-based AIE-active fragments can be prepared. The most well-known and efficient derivatives include TPE, 2,3-diphenylfumaronitrile, 2,3,3-triphenylacrylonitrile (**Fig. 2.16**). Moreover, the usage of electron donating or accepting substituents gives

rise to the new building blocks for the construction of bipolar compounds possessing the AIE property.

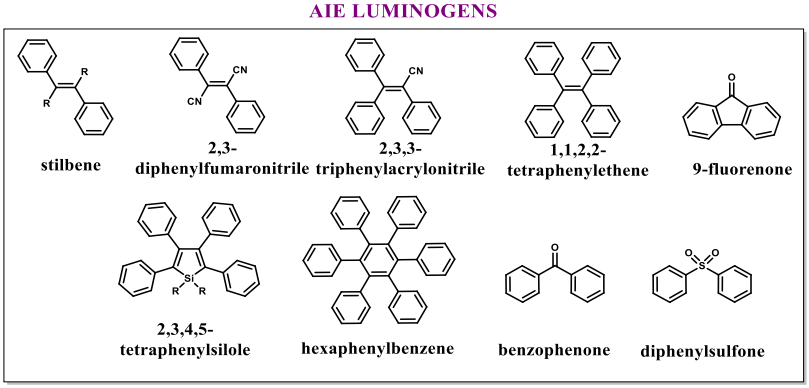

Fig. 2.16. Commonly used building blocks for the construction of AIE compounds

A successful approach towards the production of solid state emissive bipolar materials was undertaken by Tang and coworkers [128]. Keeping in mind, that the regulation of the D–A interaction is the clue to control the PL efficiency and ambipolar charge transport behaviour, the authors prepared two new green-emitting AIE luminogens **TPE-PNPB** and **TPE-PB** (**Fig. 2.17**), by employing diphenylamino- and dimesitylboryl fragments as electron donor and acceptor, and TPE as the spacing AIE-active bridge. By the variation of the conjugation length between donor and acceptor, the alteration of the emission profile and efficiency, affecting the target device performance, was expected. Indeed, owing to the readily formed CT state and free rotations around the single bonds, both compounds are only weakly emissive in the THF solutions (**Table 2.3**). On the contrary, upon the addition of water to the THF solutions, a boost in PL was detected for both compounds due to the aggregates formation, proving the AIE feature. Moreover, twisted conformations of the TPE and dimesitylboryl moieties were found to impede the molecular rotations, resulting in the intense solid-state emission (PLQY 0.64 and 0.94 for **TPE-PB** and **TPE-PNPB**, respectively). Interestingly, the PL efficiency of **TPE-PNPB** (0.94) neat film is much higher than that of **TPE-PB** (0.64). This result can be explained by the more pronounced D–A interactions in the case of **TPE-PB**, leading to partly quenched emission. Calculated by the DFT method ground (1.52 and 1.40 D) and excited (20.7 and 17.06 D for **TPE-PB** and **TPE-PNPB**, respectively) states dipole moments clearly demonstrate that that the D−A interaction is much weaker in **TPE-PNPB** with the extended conjugation than in **TPE-NB**. Complete HOMO/LUMO separation, detected for **TPE-PNPB**, confirms weak D–A interaction as well. On the other hand, good orbital separation led to the ambipolar charge behaviour of the compounds under consideration. High solid state PLQY values inspired the authors to test the materials as the emitting and hole transporting layer simultaneously in OLEDs. Noteworthy, **TPE-PNPB** performed better in the OLED (current efficiency 16.2 cd/A, power efficiency 14.4 lm/W and

EQE 5.35%) than **TPE-PB** (11.9 cd/1, 9.90 lm/W and 3.73%), due to the stronger D–A interaction.

The efficiency of the separation between the D and A units by an AIE-active component was demonstrated by Shi et al. [129] as well. Thus, since carbazolyl and dimesitylboryl moieties found wide application in optoelectronics, the authors have designed and prepared four novel carbazole-decorated TPE-based emitters, ***p*-DBPDECZ**, ***m*-DBPDECZ**, ***p*-DPDECZ** and ***m*-DPDECZ**, substituted by the arylboron groups in *meta*- and *para*-positions (**Fig. 2.17**). The impact of the conjugation length and D-A interactions on the photoluminescent and electroluminescent properties of the compounds has been investigated thoroughly. The absorption spectra in THF readily revealed the differences in D-A interplay among the compounds: firstly, due to the extra phenyl ring, ***p*-DBPDECZ** and ***m*-DBPDECZ** exhibited blue-shifted absorption bands when compared to their analogues with a shorter conjugation system, ***p*-DPDECZ** and ***m*-DPDECZ**; secondly, the interruption of conjugation by *meta*-substitution in ***m*-DBPDECZ** resulted in the vanishing ICT band, thus confirming very faint D–A interaction. As expected, all the investigated compounds displayed only weak emission in the THF solutions (**Table 2.3**). In order to test the AIE behaviour, a solvent-non-solvent test [126] was carried out: under gradual addition of water to the THF solutions of the compounds, a significant burst in PL (increase up to 250 times) was observed. While intense green emission was detected for the aggregates of ***p*-DPDECZ** and ***p*-DBPDECZ**, ***m*-DPDECZ** and ***m*-DBPDECZ** revealed sky-blue emission due to the interrupted conjugation by *meta*-linkage. The remarkably high solid state PLQYs (up to 0.99, **Table 3**) prove the well-expressed AIE feature of the molecules. The variety in the solid state PL efficiency was explained by the differences in the electronic structure of the compounds: while all the prepared molecules adopt twisted conformations owing to the TPE unit, only ***p*-DPDECZ** revealed the sufficient HOMO/LUMO overlap, resulting in radiative pathway and high PLQY. Weak D–A interactions of the other compounds led to the decrease in solid state emission. Non-doped OLEDs employing novel compounds as the emitting layers, were constructed. Noteworthy, green devices employing materials with stronger D–A impact and *para*-substitution, exhibited promising electroluminescence properties with the turn-on voltage of 4.80 V, a maximum brightness of 30210 cd/m^2 (at 15 V), maximum current efficiency of 9.96 cd/A (at 9.2 V) and EQE 2.73% for ***p*-DPDECZ** and 4.2 V, a higher maximum luminance of 65150 cd/m^2 (at 15 V), slightly lower maximum current efficiency of 8.60 cd/A (at 6 V) and EQE of 3.28% for ***p*-DBPDECZ**. In turn, sky-blue OLEDs displayed slightly lower EQEs of 1.26 and 2.16% for ***m*-DPDECZ** and ***m*-DBPDECZ**, respectively. It should be noted, that *para*-substituted compounds perform better than their *meta*-substituted analogues. In turn, prolonged conjugation results in better OLED efficiency as well. These results can be explained by the better ambipolar charge transport properties in the materials with efficient HOMO/LUMO separation.

The elaboration of effective solid state emitters with tunable charge mobility is a challenge for materials scientists. Therefore, the knowledge that the TPE fragment is remarkable not only for its AIE activity, but also for the excellent charge transport

characteristics [130], encouraged Zhu and coworkers to prepare a series of bipolar AIE luminogens with different ratios of TPE and diphenylphosphine oxide units – **TPEDPO**, **TPEPO**, **DTPEPO** and **TTPEPO** (**Fig. 2.17**) – and study the structure-property relationship [131]. All the investigated compounds were found to be non-emissive in THF. However, upon the addition of water to the THF solutions, up to 470-fold enhancement of PL was detected, clearly pointing at the AIE property. Noteworthy, the aggregates and solid films of the compounds emit light in the sky-blue region, which is particularly desirable for non-doped OLEDs. The differences in the molecular architecture were found to affect greatly the charge transporting properties of the compounds. Thus, while **TPEDPO**, bearing two acceptor fragments, is an electron-transporting material, the increase of the donating component leads to the ambipolar charge transport in **TPEPO** and clear hole transport in **DTPEPO** and **TTPEPO**. These results clearly indicate, that by simple modification of the TPE unit the compounds with tunable charge transport behaviour can be prepared. Blue-emitting OLEDs were fabricated using **TPEDPO**, **TPEPO**, **DTPEPO**, and **TTPEPO** as the emitting and transporting layer simultaneously. The devices turned on at a moderately low voltage (3.6-4.2 V) and exhibited maximum luminance values of 396, 1058, 952, and 834 cd/m^2 for **TPEDPO**, **TPEPO**, **DTPEPO**, and **TTPEPO**, respectively. As expected, the best result was displayed by **TPEPO**, owing to its balanced hole and electron charge mobility.

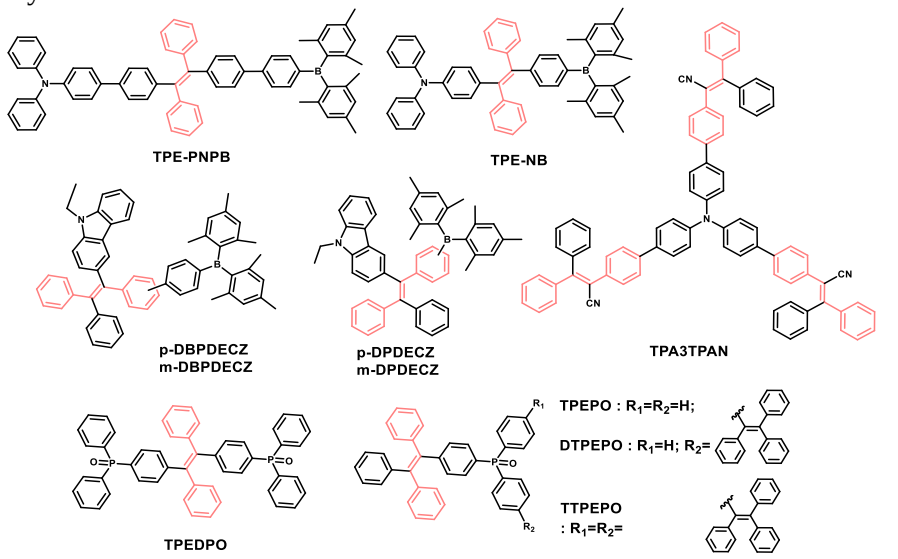

Fig. 2.17. Substituted stilbene-based bipolar AIE compounds

As the stilbene moiety can be easily constructed by means of chemical reactions, by variation of the nature of substituents it is possible to prepare donating and accepting building blocks. Thus, primarily synthesizing an electron-deficient 2,3,3-triphenylacrylonitrile fragment, Yuan et al. [132] then attached it to the donating triphenylamine core, giving rise to a novel starburst compound **TPA3TPAN** (**Fig. 2.17**). Due to the exploitation of the strong donor and acceptor,

TPA3TPAN exhibited ready CT even in non-polar solvents. Unlike most of D–A molecules, which are highly emissive in non-polar media, while basically non-emissive in polar media [133], **TPA3TPAN** revealed vanishing PLQY values in all organic solvents, owing to the highly twisted molecular structure (twisted propeller, confirmed by DFT calculations). On the contrary, aggregates formed in the THF/water mixtures emitted intense yellow light, giving a hint on the AIE mechanism. Moreover, a high PLQY of 0.38 was detected for the solid powder of **TPA3TPAN**. Since **TPA3TPAN** was found to show hole transporting abilities, a bilayer device without an additional hole transporting layer was fabricated. The OLED displayed the maximum luminance of 3101 cd/m^2, power efficiency of 6.16 cd/A and the EQE of 2.78%. Noteworthy, such multifunctional ability of **TPA3TPAN** to serve as an emitter and a hole transporting material greatly simplifies the device structure, thus reducing the production cost.

To conclude, the utilization of the substituted stilbene unit in the preparation of bipolar AIE-gens leads to the great diversity of structures, properties and emission colours. Not only efficient ambipolar solid state emitters can thus be obtained, but also the scarce blue-emitting component for the non-doped OLEDs can be achieved. Generally, stilbene-based materials prove to be promising candidates for efficient devices.

Owing to the bulky, sterically hindered structures hexaphenylsilole and hexaphenylbenzene derivatives open another class of efficient AIE-genes. Thus, such molecules, thoroughly investigated in the group of Tang [55], where found to form highly emissive nanoparticles (size up to 200 nm) upon the aggregation. Hence, the utilization of multisubstituted siloles and benzenes as spacing units in the design of bipolar molecules can result in a well-expressed AIE feature. Thus, Wang and Du [134] chose the silole moiety as a π-bridge to construct the D–A–π–A–D compounds **2-BTSi-T** and **2-BTSi-TPA** (**Fig. 2.18**). By selecting benzothiazole group as an acceptor, thiophene and triphenylamine as strong electron-donors and substituted silole as a conjugated spacer, the authors aimed to prepare stable red solid-state emitters for OLEDs, since most of D–A near-infrared compounds are very weakly emissive due to the ACQ [135]. Moreover, red emitters are also often prone to non-emissive TICT states in polar and aggregated media, therefore careful molecular design is particularly important. Indeed, the AIE property of the new compounds, probed by the solvent-non solvent test, revealed a great increase in the PL of **2-BTSi-T** and **2-BTSi-TPA** (up to 29 times) upon gradual addition of water to the THF solution, confirming the emissive aggregates formation. Moreover, both compounds exhibited enhanced PLQYs in the solid state. Noteworthy, the authors showed, that **2-BTSi-T** and **2-BTSi-TPA** can be used in the guest host systems as well, in order to obtain the efficient emission in the region of >750 nm. Though the novel silole-based compounds were not probed in the non-doped OLEDs, their remarkable PL properties suggest a promising performance in devices.

While Wang [134] aspired to obtain red emitters by using the silole moiety as spacer, Bhalla and Kumar directed their efforts towards the preparation of the efficient blue emitters **CzPP-SD** and **CzPP-BT** (**Fig. 2.18**), separating carbazole donors from various acceptors (dibenzothiophene-*S*,*S*-dioxide and benzothiazole) by

the branched hexaphenylbenzene bridge [136]. The substituted benzene fragment was used non only as an AIE-active unit, but also as the prevention of co-facial interaction of donor and acceptor in the aggregates, which was found to be detrimental for the solid state emission of bipolar compounds [137]. Indeed, the ground state geometry optimization (DFT) confirmed the highly twisted conformations of **CzPP-SD** and **CzPP-BT**. Such twisted conformations reduce the intramolecular TICT and impede the intermolecular π-π stacking interactions, thus opening the radiative pathways in the solid state. The aggregation studies, carried out in the THF/water mixtures, proved, that **CzPP-SD** and **CzPP-BT** are AIE active. Interestingly, the maximum emission was observed for **CzPP-SD** in the fraction with 60% of water, while **CzPP-BT** demonstrated steep PL enhancement with the addition of water. Tunnelling electron microscopy (TEM) investigations revealed crystalline nanoparticles for **CzPP-SD** at the 60% water fractions, followed by less emissive amorphous ones at 70-80% of water, while the analysis of **CzPP-BT** unfolded only emissive crystalline aggregates. Moreover, intense solid state emission was detected for **CzPP-SD** and **CzPP-BT** as well. Thus, according to all the studies the authors showed, that the restriction of TICT, reduced D–A interactions and conformational twisting play a major role in maintaining good solid state emission.

To conclude, utilization of multisubstituted siloles and benzenes as spacing units proves to be an efficient way to add the AIE property to the bipolar molecule.

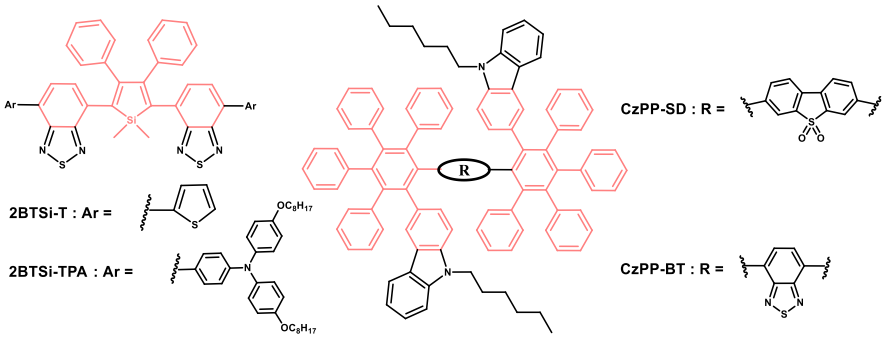

Fig. 2.18. Bipolar AIE-exhibiting derivatives of silole and hexaphenylbenzene

First observed as an undesired emission from keto-defects in fluorene-based blue emitters [12,138,139,140,141], the fluorenone emission in the yellow-red region became subsequently a desired target due to the excellent PLQY [8,126,142]. Unlike the above discussed rotating AIE-genes, the emission in the rigid fluorenone moiety was found to originate from excimer [8,126] and *J*-aggregates [143,144] formation, facilitated by the hydrogen-bonding with the C=O group of fluorenone. Hence, the incorporation of the fluorenone moiety can add the AIE feature to the bipolar molecule. Thus, in search for a new solution-processable AIE-active emitter for OLEDs, Ananthakrishnan et al. [145] prepared a fluorenone-fluorene oligomer **FF** (**Fig. 2.19**). Due to the bipolar molecular architecture, **FF** exhibited broad yellow emission in organic solvents. However, the remarkably high PLQY in the solid state (0.79) suggests that **FF** is an AIEE-active compound, i.e. aggregation was found to

enhance the emission of the material. The THF/water test confirmed the AIEE property as well. The red-shifted absorption and emission upon the gradual water addition gave a hint to the authors, that *J*-aggregates, caused by the planarization of the molecules, are responsible for the PL enhancement. A solution-processed OLED with a simple configuration ITO/PEDOT:PSS/**FF**/Al which displayed the bright yellow emission with the maximum brightness of 26551 cd/m^2 (at 14 V), current efficiency 12.3 cd/A and power efficiency 7.8 lm/W, proving, that fluorenone derivatives are appropriate candidates for the non-doped devices.

In turn, Liu and coworkers [126] proved, that AIE mechanism in fluorenone derivatives is totally different from that found in conventional AIE-genes. Upon synthesizing and thoroughly investigating the photophysical characteristics of bipolar yellow-emitting molecule **DSFO** (**Fig. 2.19**), the authors observed, that, while displaying the usual for AIE-genes PL enhancement in ethanol-water mixtures and intense solid state emission, the drop of **DSFO** solution on the TLC plate is totally non-emissive. Moreover, large Stokes shift, featureless PL and relatively long lifetime (ca. 7 ns) provided a hint on the excimers formation. The guess was confirmed by the careful investigation of the **DSFO** crystal structure. Thus, the molecules of the new compound were found to adopt a coplanar conformation, facilitating the dimer formation by means of hydrogen bonding. Every molecular pair is packed in a parallel staggered style. According to the proposed mechanism, upon the excitation, the dimer turns into an excimer without arrangement adjustment and repulsive interactions, thus avoiding common for excimers non-radiative pathways and inducing a strongly enhanced luminescence in the solid state.

Inspired by the interesting photophysical properties of **DSFO**, Liu et al. [8] prepared further two fluorenonearylamine derivatives **1DPAFO** and **2DPAFO** (**Fig. 2.19**). The optical and crystal structure investigation of orange (**1DPAFO**) and red (**2DPAFO**) emitters provided the final proof of the proposed mechanism of AIE in fluorenone adducts. Both new AIE luminogenes were tested as emissive compounds in the non-doped OLEDs with the following configuration: ITO/NPB (40 nm)/**1DPAFO** or **2DPAFO** (30 nm)/TPBI (40 nm)/LiF (1 nm)/Al (80 nm). The **1DPAFO** and **2DPAFO** based devices exhibited good performance with the maximum brightness approaching 14135 and 4813 cd/m^2 and luminance efficiency of 1.50 (1.40 lm/W) and 0.60 cd/A (0.35 lm/W), respectively.

As the final benchmark, fluorenone-based AIE compounds offer not only an unusual and efficient mechanism of emission enhancement, but also the remarkable performance in OLEDs. Facile synthesis, easy chemical modification and stability make fluorenone-based compounds particularly promising candidates for optoelectronic devices.

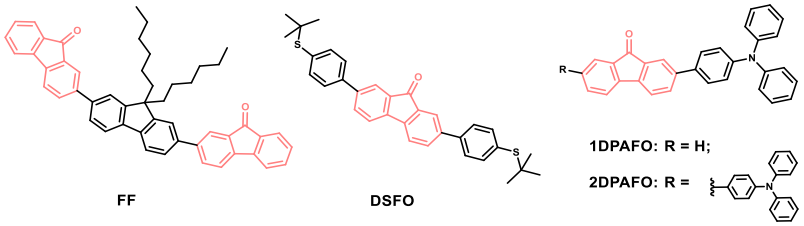

Fig. 2.19. Flurenone-based bipolar AIE compounds

In all the above discussed cases the emission enhancement in bipolar molecules can be attributed to the presence of an AIE-active unit with specific properties. Meanwhile, as nowadays the development of compounds with DF phenomenon is of top importance, materials scientists observed, that the efficient solid state PL enhancement can be achieved without using the conventional AIE-gene, just by modulation of the molecular structure. Thus, by introducing non-planar moieties (such as phenoxazine, phenothiazine) a fixed dihedral angle between the chromophores can be obtained, resulting in the loose molecular packing and overcoming fluorescence quenching at high concentration. In the meantime, successful DF can be observed as well. As most of the reported AIE-DF compounds comprise sulfone and benzophenone acceptor units, we will classify them in this manner. Zhao and Tang [146] successfully applied this strategy by synthesizing bipolar molecules **DPS-PXZ**, **DPS-PTZ**, **DBTO-PXZ** and **DBTO-PTZ** (**Fig. 2.20**), containing non-planar phenoxazine and phenothiazine units. All the compounds were found to be weakly emissive in THF, while displaying the remarkably enhanced PL in the solid state (**Table 2.3**). Noteworthy, higher PLQYs were observed for **DPS-PXZ** and **DPS-PTZ**, due to additional rotation of the diphenylsulfone moiety, on the one hand, and for phenothiazine-containing **DPS-PTZ** and **DBTO-PTZ**, on the other hand. THF/water test confirmed the AIE feature of the compounds as well. DFT calculations revealed highly twisted conformations for the compounds, preventing intermolecular π-π interactions and facilitating AIE. Moreover, well-separated HOMO/LUMO and small ΔE_{ST} (0.06-0.26 eV) suggested a hint on the possibility of DF. Indeed, the transient PL decay curves of the solid powders, measured in ambient condition, unfolded apparent delayed components in the excited state with the lifetimes of 0.8, 0.7, 52.3 and 2.3 μs, for **DPS-PXZ**, **DBTO-PXZ**, **DPS-PTZ** and **DBTO-PTZ**, respectively. Thus, these luminogenes, exhibiting efficient AIE and triplet harvesting simultaneously, may become promising candidates as light emitters for non-doped OLEDs.

In turn, Xu et al. [147] suggested a new approach toward an aggregation-enhanced DF with efficient triplet harvesting in the solid state. By designing a **DPS-CzPTZ** molecule with an asymmetric structure, comprising carbazole and phenothiazine donors, the authors aimed to improve the symmetric **DPS-PTZ** [146] by ensuring the efficient DF and enhancing the AIE property. The inspection of the single crystal of **DPS-CzPTZ** revealed a tightly packed and highly ordered alignment without any π–π interactions, only weak hydrogen bonds, resulting in a remarkably high solid state PLQY (0.66) of the non-emissive in solution **DPS-CzPTZ**. The PL intensity was significantly enhanced in the THF/water mixtures as well. As the calculated (DFT) ΔE_{ST} of 0.2 eV gives a clue of DF, the PL decay transient of the **DPS-CzPTZ** powder was obtained. Unlike usual DF systems, the solid sample of **DPS-CzPTZ** showed a strong delayed component with $\tau = 1.23$ μs even in air. Moreover, the PLQY enhancement up to 0.93 was observed for the **DPS-CzPTZ** powder upon argon treatment, confirming the contribution from triplet states. Such high PLQY can evidently be ascribed to the combination of AIE and DF features. In addition to these properties, **DPS-CzPTZ** exhibited

mechanoluminescence – luminescence induced by mechanical stimuli such as grinding, rubbing, cutting, cleaving, shaking, scratching, compressing, or crushing [148]. Obviously, such advantageous properties, as DF, AIE and mechanoluminescence, make **DPS-CzPTZ** an appropriate candidate for the high efficiency OLED.

Recently, Zhang and Chi [149] have employed the successful approach of asymmetric AIE-DF compounds to prepare a benzophenone derivative with carbazole and phenothiazine donors **OPC** (**Fig. 2.20**). Bearing the advantages of blue-emitting carbazole-decorated wing and yellow-emitting phenothiazine-substituted part, the unique butterfly-shaped molecule **OPC** is capable of emitting white light due to the dual PL in blue and yellow regions. Furthermore, the phenothiazine wing introduced the AIE yellow PL, while the carbazole-decorated part exhibited a TICT-AIE attribute in the blue-emission region. These characteristics make **OPC** a unique AIE-active white emitter with the CIE coordinates of 0.35, 0.35. Moreover, a vanishing ΔE_{ST} of 0.01 eV suggested efficient upconversion of triplet excitons. Indeed, the TADF mechanism was proved by degassing experiment and temperature-dependent time-resolved measurements. As the final benchmark, **OPC** also exhibited unique mechanofluorochromic nature. Thus, by careful design the authors proposed a good strategy for the facile preparation of efficient AIE-DF white emitters.

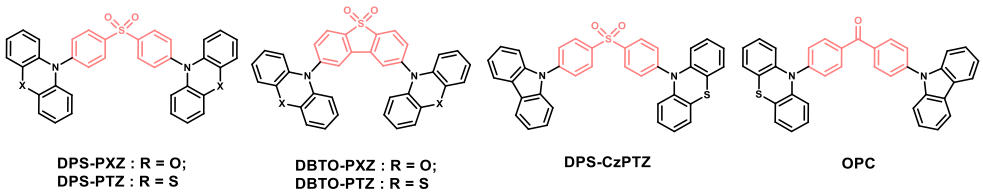

Fig. 2.20. Sulfone- and benzophenone-based bipolar AIE compounds

To conclude, bipolar compounds with the fixed dihedral angle and modulated molecular interaction unfurl the highly innovative approach towards the preparation of efficient AIE-featured luminogenes with well-expressed DF phenomenon in the solid state. Such compounds may find extensive application in the non-doped TADF OLEDs.

As the final benchmark, several classes of bipolar materials demonstrating the AIE phenomenon, were described and analysed. As a general rule, the incorporation of any AIE-active unit to a molecule can induce the aggregation effect. By varying such units, bipolar emitters with different emission colours, PLQY and other characteristics can be obtained. From the data discussed in the present chapter and displayed in **Table 2.3** it can be seen, that not many bipolar AIE-genes were probed in the OLED application. However, eben though simple fluorescent non-doped OLEDs with AIE emitters demonstrate only moderate efficiency, when combined with such advantageous properties, as DF and ambipolar mobility, devices with the outstandingly high EQE can be expected. Hence, the approaches of AIE-DF compounds with the modulated molecular interaction and excimer-induced AIE of

fluorenone derivatives represent the most successful strategies for the fabrication of efficient OLEDs.

Table 2.3. Comparison of various colour bipolar AIE emitters

AIE luminogen	Compound	Emission colour[a]	QY_s [b]	QY_f [c]	IP/EA [d] [eV]	EQE [%]
Stilbene	TPE-PNPB [128]	Green	0.005	0.94	5.18/2.26	5.12
Stilbene	TPE-NB [128]	Green	0.002	0.64	5.14/2.34	3.24
Stilbene	TPEDPO [131]	Blue	n.p.	n.p.	6.11/2.84	n.p.
Stilbene	TPEPO [131]	Blue	n.p.	n.p.	6.08/2.71	n.p.
Stilbene	DTPEPO [131]	Blue	n.p.	n.p.	6.12/2.79	n.p.
Stilbene	TTPEPO [131]	Blue	n.p.	n.p.	6.12/2.79	n.p.
Stilbene	p-DPDECZ [129]	Green	0.004	0.99	5.05/1.75	2.73
Stilbene	m-DPDECZ [129]	Blue	0.004	0.34	5.00/1.72	1.26
Stilbene	p-DBPDECZ [129]	Green	0.004	0.48	5.01/1.53	3.28
Stilbene	m-DBPDECZ [129]	Blue	0.003	0.65	5.10/1.74	2.16
Stilbene	TPA3TPAN [132]	Yellow	0.002	0.33	5.20/2.60	2.78
Silole	2BTSi-T [134]	Red	0.001	0.037	n.p.	n.p.
Silole	2BTSi-TPA [134]	Red	0.006	0.091	n.p.	n.p.
Hexaphenyl-benzene	CzPP-SD [136]	Blue	0.0004	n.p.	5.51/2.26	n.p.
Hexaphenyl-benzene	CzPP-BT [136]	Blue	0.0001	n.p.	5.51/2.62	n.p.
Fluorenone	FF [145]	Yellow	0.003	0.79	5.71/3.60	n.p.
Fluorenone	1DPAFO [8]	Orange	Weakly emissive	n.p.	n.p.	n.p.
Fluorenone	2DPAFO [8]	Red	Weakly emissive	n.p.	n.p.	n.p.
Fluorenone	DSFO [126]	Yellow	Weakly emissive	n.p.	n.p.	n.p.
Diphenylsulphone	DPS-CzPTZ [147]	Green	Weakly emissive	0.93 (in Ar)	n.p.	n.p.
Diphenylsulphone	DPS-PXZ [146]	Green	0.031	0.16	6.31/1.01*	n.p.
Diphenylsulphone	DPS-PTZ [146]	Green	0.01	0.203	6.37/1.39*	n.p.
Dibenzothiophene-S,S-dioxide	DBTO-PXZ [146]	Yellow	0.016	0.067	6.53/1.00*	n.p.
Dibenzothiophene-S,S-dioxide	DBTO-PTZ [146]	Yellow	0.012	0.107	6.59/1.39*	n.p.
Benzophenone	OPC [149]	White	n.p.	0.23	n.p.	n.p.

[a] Determined for the aggregate. [b] PLQY in solution. [c] PLQY in solid state. [d] Determined by CV measurements. *Calculated by TD-DFT/M062X/6-31G (d,p) method. N.p. stans for "not presented".

2.4. Summary of literature review

In this work, in terms of the comparison of the device and employed materials characteristics, several methods of OLED efficiency enhancement were analyzed. Thus, the application of the phosphorescent bipolar hosts in PhOLEDs provides an opportunity to increase EQE significantly while reducing efficiency roll-off and device turn on voltage, owing to ambipolar charge transport behaviour, efficient triplet exciton and *IP/EA* confinement, ACQ prevention and superior thermal and electrochemical stability. Noteworthy, phosphorescent bipolar hosts can be applied

to TADF OLEDs, as well. However, it still remains challenging to prepare a high triplet energy multifunctional bipolar host for deep blue emitters. In turn, the involvement of TADF emitters leads to the production of noble-metal-free highly efficient devices due to the singlet-triplet upconversion mechanism. However, frequently applied twisted molecular conformation often results in poor charge mobility and partially quenched emission. Bipolar motif with CT makes the obtaining of deep blue emitters complicated as well. Furthermore, most of the reported TADF OLEDs suffer from insufficiently short lifetime and ACQ. Successively, the ACQ issue can be treated by the molecular design of appropriate emitters with high solid state PLQY employing the AIE mechanism. Efficient purely organic yellow, orange and red emitters, which are generally hard to obtain, may still be prepared by the AIE approach as well. Nevertheless, due to the usage of strong donors and acceptors and prolonged conjugation, yellow-red AIE emitters frequently demonstrate only exclusively hole or electron mobility.

Table 2.4. Comparison of the efficiency enhancement methods for the preparation of promising cost-effective compounds for the large scale OLED production

Efficiency enhancement method	Compound	Design strategy	EQE / [%]
Bipolar host	**2,6-DCzPPy** [89]	Usage of spacer and *meta*-conjugation	24.3
Bipolar host	***m*-CzSCN** [93]	Usage of spacer and *meta*-conjugation	23.3
Bipolar host	***m*-CzCN** [13]	Usage of spacer and *meta*-conjugation	23.1
Bipolar host	***m*-CBP-CN** [94]	Usage of spacer and *meta*-conjugation	24.2
TADF	**DMAC-TRZ** [102]	Control of dihedral angle	26.5
TADF	**DMAC-DPS** [113]	Control of dihedral angle	21.2
TADF	**CPC** [37]	Control of dihedral angle	21.2
AIE	**TPE-PNPB** [128]	Usage of AIE units and prolonged conjugation	5.12
AIE-DF	**DPS-PTZ** [146]	Control of dihedral angle	Not presented
AIE-DF	**OPC** [149]	Control of dihedral angle	Not presented

Table 2.4 summarizes the involved strategy and characteristics of the most promising reported compounds and fabricated OLEDs, which can be suggested for the large scale applications. For the preparation of the listed below materials relatively inexpensive starting compounds and rational synthetic pathways were used. From the point of view of the applied design strategy, it can be concluded, that efficient bipolar host compounds can be prepared by the utilization of spacer units and interrupted conjugation. In turn, successful TADF emitters may be achieved via the approach of controlling the dihedral angle between the chromophores. At last, for the preparation of AIE-active materials, the involvement of an AIE unit and the fixed torsional angle between the donating and accepting fragments giving rise to the new phenomenon of AIE-DF, should be ensured. The AIE-DF strategy may result in fabrication of non-doped TADF OLEDs with high EQE values. However, efficient bipolar blue AIE emitters, in line with the red ones, still require further development. Even though several cases of highly efficient OLEDs were reported [37,93,113], the challenge of design and preparation of stable blue emitters and blue

phosphorescent hosts still remains. Furthermore, new TADF emitters require the involvement of new suitable host compounds. Evidently, it remains arguable, which approach to the device fabrication – solution-processing and vacuum deposition – can be considered more efficient. Eventually, the optimization of device architecture, which can be reached by the utilization of multifunctional compounds, would lead to the reduction of production cost, regardless of the fabrication method.

The preparation of multifunctional compounds, exhibiting such phenomena as phosphorescence, high PLQY, ambipolar charge transport, AIE and DF, while preserving superior thermal and photoelectrical characteristics, offers an opportunity to improve the materials performance in devices. Thus, dendritic molecular architecture may greatly improve the optical, photophysical and thermal characteristics of the compound, making it suitable for the emissive layer. In turn, the usage of appropriate units, linked in a suitable manner, may lead to the efficient ambipolar host and solely charge transporting materials. Furthermore, by combining the advantages of blue DF emitters (either on their own or doped in high triplet energy bipolar hosts) with yellow-red ambipolar AIE compounds, it is possible to achieve organic noble-metal-free white OLEDs. Hence, for the preparation of efficient multifunctional compounds, profound understanding of the structure-property relationship is required. Consequently, the choice of suitable donating, accepting and linking units proves to be the crucial challenge for the achievement of multifunctional compounds, combining all the discussed in the literature review phenomena. This work focuses on the discussion of the structure-property relationship of multifunctional compounds.

3. EXPERIMENTAL

3.1. Analytical techniques and methods

3.1.1. Analytical techniques

^{1}H and ^{13}C NMR spectra were recorded by using Bruker Avance III 400 spectrometer (400 MHz (^{1}H), 100 MHz (^{13}C)), Bruker DRX-500 P (500 MHz (^{1}H), 125 MHz (^{13}C)) and Bruker Avance III (700 MHz (^{1}H), 176 MHz (^{13}C)) spectrometers. Chemical shifts (δ) are reported in ppm referenced to tetramethylsilane or the internal solvent signal.

IR spectra were recorded in KBr pellets on Perkin Elmer Spectrum GX II FT-IR System. ATR-FT-IR spectra were recorded on Bruker Vertex 70.

Mass spectra were obtained by employing the MALDI-TOF method on Shimazu Biotech Axima mass spectrometer.

Elemental analysis data were obtained on EuroEA Elemental Analyser.

UV/Vis absorption spectra of 10^{-4} M solutions and thin films of the compounds were recorded in quartz cells using Perkin Elmer Lambda 35 spectrometer.

PL spectra of 10^{-5} M solutions and thin films of the compounds were recorded by using Edinburgh Instruments' FLS980 Fluorescence Spectrometer.

CV measurements were performed by using AUTOLAB potentiostat "PGSTAT20" (produced by the Eco Chemie Company) in the dry solvent solution containing 0.1 M tetrabutylammonium hexafluorophosphate ($TBAPF_6$) as the electrolyte at room temperature under nitrogen atmosphere.

Electron photoemission spectra in air were recorded by using UV deuterium light source ASBN-D130-CM and CM110 1/8m monochromator for the illumination of the samples and 6517B Keithley electrometer for the photocurrent measurement.

Charge mobility measurements by employing TOF and CELIV techniques were conducted using digital storage oscilloscope Tektronix.

TGA was performed on Metter TGA/SDTA851e/LF/1100 apparatus at a heating rate of 20 ^oC/min under nitrogen atmosphere.

DSC measurements were conducted on DSC Q 100 TA Instrument at a heating rate of 10^oC/min under nitrogen atmosphere.

Melting points of the prepared compounds were estimated by using Electrothermal Melt-Temp apparatus.

3.1.2. Methods

3.1.2.1. Optical and photophysical measurements

Thin solid films for the recording of UV/Vis and PL spectra were prepared by drop casting 2 mg/ml solutions of the compounds in toluene on pre-cleaned quartz substrates. Solid solutions of molecularly dispersed compounds in PS and Zeonex polymer matrices were obtained with the concentrations of 0.25 wt% and 1 wt%, respectively, by mixing the dissolved compounds and polymer in toluene solutions at the appropriate ratio and casting the solutions on quartz substrates in ambient air. Fluorescence quantum yields (η) of the solutions and of the solid films were estimated using the integrated sphere (calibrated with two standards: quinine sulphate in 0.1 H_2SO_4 and rhodamine 6G in ethanol) method [150].

The phosphorescence spectra were recorded at 77K for the solid solutions of the materials in zeonex matrix by using nanosecond-gated luminescence measurements (from 400 ps to 1 s) using a high energy pulsed Nd:YAG laser emitting at 355 nm (EKSPLA). Emission was focused onto a spectrograph and detected on a sensitive gated iCCD camera (Stanford Computer Optics) having sub-nanosecond resolution. A model liquid nitrogen cryostat (Janis Research) was used for the experiment.

3.1.2.2. Electrochemical and photoelectrical measurements

CV measurements were carried out at 50 mV/s potential rate with a glassy carbon working electrode in a three electrode cell. The results were collected by using GPES (General Purpose Electrochemical System) software. The electrochemical cell comprised platinum wire with 1 mm diameter of working area as the working electrode, Ag wire calibrated versus ferrocene/ferrocinium redox couple as the quasi-reference electrode and platinum coil as the auxiliary electrode.

IP of the layers of the synthesized compounds were measured by the electron photoemission method in air [151]. For the recording of the electron photoemission

spectra the layers were prepared by drop casting of the THF solutions on the pre-cleaned ITO-coated glass substrates. The negative voltage of 300 V was applied to the sample substrate. The deep UV deuterium light source ASBN-D130-CM and CM110 1/8m monochromator were used for the illumination of the samples with monochromatic light. 6517B Keithley electrometer was connected to the counter-electrode for the photocurrent measurement, which was flowing in the circuit under illumination. Energy scan of the incident photons was performed while increasing the photon energy.

3.1.2.3. Charge mobility measurements

The samples for TOF measurements were prepared by spin-coating the solutions of the synthesized compounds in toluene on pre-cleaned ITO coated glass plates [152]. The samples were heated at 70 °C for 20 min in a hot air oven. Next, 60 nm of aluminum was deposited by using a mask by thermal evaporation under vacuum below $5 \cdot 10^{-5}$ mbar. The light pulse was used to photo generate the charge carriers by exciting layers of compounds through the ITO. For hole/electron mobility measurements, the positive/negative voltage was applied to the ITO electrode. Delay generator Tektronix AFG 3011 was used to generate square pulse voltage with pulsed third-harmonic Nd:YAG laser EKSPLA PL2140 working at a pulse duration of 25 ps and the wavelength of 355 nm. Digital storage oscilloscope Tektronix DPO4032 was used to record TOF transients of the layers of the synthesized materials. Transit time t_{tr} for the samples with the charge transporting material was determined by the kink on the curve of the transient in log–log scale. The drift mobility was calculated by using the formula $\mu = d^2/Ut_{tr}$, where d is the layer thickness, and U is the surface potential at the moment of illumination.

For CELIV measurements sandwich-like structures ITO/Compound/Al were prepared. The thickness of the layers was measured by CELIV technique [153]. The layers from the 10 mg/ml THF solution of the compounds were formed by applying the casting method onto clean ITO coated glass substrate within a glove box. Al was evaporated at 15 Å/s at a pressure below $5 \cdot 10^{-5}$ mbar. The experimental setup consisted of delay generator Tektronix AFG 3011 and digital storage oscilloscope Tektronix DPO 4032. The mobility measurements were conducted in a dark box by applying a triangular voltage pulse to the samples. The charge carrier mobility was calculated by formula $\mu = 2d^2/At_{max}^2$, where $A = U(t)/t$ is the voltage rise rate, t_{max} is the time for the current to reach its extraction maximum peak, d is the sample thickness.

The electron mobility in electron-only devices is determined by means of "potential mapping" (POEM) by thickness variation in n-i-n electron-only single carrier devices [154]. The measurement characterizes electron transport in vertical direction perpendicular to the substrate [155]. The devices are manufactured by thin film deposition, the stack is designed as follows: Electron injection into the material under investigation is facilitated by an n-doped electron transport layer (ETL) consisting of the matrix electron transport material Bis-HFl-NTCDI (density assumed for layer thickness control: ρ = 1.25 g/cm³; [156]) n-doped with 3 weight-% $Cr_2(hpp)_4$ (tetrakis(1,3,4,6,7,8-hexahydro-2*H*-pyrimido[1,2-a]pyrimidinato) dichromium (II); Novaled; [157,158]). This kind of molecularly doped layer is

known to form a low-resistive selective contact for the respective kind of charge carriers [159]. To avoid the influence of a built-in field, the devices are made symmetrical, sandwiching the material under investigation between two nominally identical ETLs of 20 nm thickness each. A series of samples to determine the mobility of one material consists of 18 samples with constant metal and ETL thicknesses and varying thickness of the material under investigation (using an estimated density of ρ = 1.3 g/cm³). All the samples of a series are manufactured on one glass wafer in one processing run. The thickness variation for the material is realized by temporarily covering variable parts of the wafer by a metal shield. For each thickness, three different device areas (0.88 mm², 1.68 mm², and 3.27 mm²) are used to check that edge-effects do not affect the measurement. Space-charge limited current is typically reached above a threshold between 0.1 mA/cm² (low μ) and 10 mA/cm² (high μ). Ohmic self-heating [160] starts to dominate above 100 mA/cm². Consequently, the range in between these boundaries is used for the POEM evaluation. The evaluation yields a series of μ values at varying though well-defined electric field strength F and charge carrier density n values. Depending on the size of the covered parameter range, either only the absolute μ value at given F and n can be well resolved, or the field dependence at a given n (most materials), or both field and density dependence can be separately resolved [160]. The absolute accuracy of μ is estimated to be better than half an order of magnitude in all cases.

3.1.2.4. Thin film deposition

Single thin films, electron-only devices, and solar cells are manufactured by vacuum processing on pre-cleaned glass substrates (Thin Film Devices). For solar cells, the substrate is pre-coated with structured indium tin oxide (ITO; Thin Film Devices; 90 nm; 30 Ω/□) as the bottom electrode. The top electrode – and for electron-only-devices also the bottom electrode – is made of 100 nm aluminum (density used for layer thickness control: ρ = 2.73 g/cm³) thermally evaporated from a metal crucible through a shadow mask for structuring. The top and bottom electrodes are structured in a way that they form perpendicular stripes, defining the 6.44 mm² active device area by the approximately square-shaped spatial overlap of bottom and top contact. All organic materials except for the dopants and DCV5T-Me are purified by vacuum temperature gradient sublimation prior to processing. The dopants are used as received, and DCV5T-Me is heated out in vacuum prior to processing. All organic materials are deposited by thermal sublimation of the materials from electrically heated inert ceramic crucibles onto the substrate in vacuum. The base pressure for all deposition processes is below 10^{-6} mbar. The layer thickness is controlled with the help of pre-calibrated quartz crystal microbalance (QCM) near the substrate. For the deposition of doped and blend layers, both materials are controlled independently by separate QCMs, allowing for precise adjustment of the mixing ratio. After fabrication, the devices are encapsulated under nitrogen atmosphere with a glass cavity glued onto the substrate with the solvent-free UV hardening resin XNR5590 (Nagase ChemteX). A moisture getter (Dynic) is placed inside the encapsulation to increase device stability.

3.1.2.5. Conductivity measurement

The conductivity of doped layers is measured laterally, in a thin film in bottom-contact geometry. Under vacuum, two interlocked comb-shaped metal contacts are deposited, consisting of 1 nm chromium and (40 … 45) nm gold. The distance between the stripes represents the channel length of ℓ = 0.5 mm, the effective channel width is w = 111 mm. Subsequently, the material under investigation is co-deposited with the dopant $Cr_2(hpp)_4$ or $W_2(hpp)_4$ (tetrakis(1,3,4,6,7,8-hexahydro-2H-pyrimido[1,2-a]pyrimidinato)ditungsten (II); Novaled) where doping concentration c is given in molar weight-percent (wt-%). During the deposition a voltage of V = 10 V is applied between the electrodes and the current I is monitored simultaneously with the layer thickness d. Conductivity σ is then obtained from the $I(d)$ slope in the linear part of this dependence (i.e. above an initial d threshold with very low I and non-constant slope indicating the formation of the first closed layer) as $\sigma = (\partial I/\partial d) \cdot \ell / (V \cdot w)$.

3.1.2.6. Solar cells fabrication

The solar cells contain C_{60} (ρ = 1.63 g/cm³; CreaPhys) as the acceptor and DCV5T-Me (ρ = 1.3 g/cm³ assumed; Synthon Chemicals; [161]) as the donor material, as well as BPAPF (ρ = 1.2 g/cm³; Lumtec) as the hole transport material and the commercial p-dopant NDP9 (ρ = 1.2 g/cm³ assumed; Novaled). The layer stack is as follows: glass substrate / ITO / ETL / C_{60} (15 nm) / blend layer DCV5T-Me:C_{60} 2:1 deposited onto a substrate at either room temperature or 80 °C substrate temperature with the total deposition rate of 0.15 Å/s (20 nm in unheated samples, 40 nm in heated samples) / BPAPF (5 nm) / BPAPF p-doped with 10 wt-% NDP9 (40 nm) / NDP9 (1 nm) / Al (100 nm). The solar cell performance is measured under simulated sun light (SolarLight 16S-003-300-AM1.5) with mismatch corrected intensity of 1 sun (100 mW/cm²) by using a source measure unit (Keithley 2400).

3.1.2.7. Organic light emitting diodes fabrication

The electroluminescent devices with the architecture ITO / CuI (8 nm) / TPD (10 nm) / host:guest (20%) (60 nm) /PBD (10 nm) /Ca (50 nm) / Al (200 nm) were fabricated by means of vacuum deposition of organic semiconductor layers and metal electrodes onto the pre-cleaned ITO coated glass substrate under vacuum of 10^{-6} Torr. PBD was used as an ETL, whereas TPD was employed as the HTL. The active area of the obtained devices was 3 x 6 mm^2. The density-voltage and luminance-voltage characteristics were measured by using a Keithley 6517 Binair without passivation immediately after the preparation of the device. The brightness measurements were carried out by using a calibrated photodiode. The electroluminescence spectra were recorded with Avaspec-2048L spectrometer.

3.2. Computational details

The theoretical calculations were carried out by using the Gaussian 09 quantum chemical package [162]. Full geometry optimizations of the compounds in their electronic ground state were performed with DFT by using the B3LYP functional consisting of Becke's three parameter hybrid exchange functional combined with the Lee-Yang-Parr correlation functional with the 6-31G(d) basis set

in vacuum. The energies of the highest occupied (HOMO) and the lowest unoccupied (LUMO) molecular orbitals were obtained from single point calculations in the framework of DFT B3LYP/6-311G(d,p) and BMK/6-31G approaches for the CH_2Cl_2 solution and gas phase, respectively. Absorption spectra were simulated from the oscillator strengths of singlet transitions calculated by the TD-DFT B3LYP/6-31G(d) and BMK/6-31G methods in vacuum. The vertical ionization potentials were calculated by the DFT B3LYP/6-311G(d,p) method.

3.3. Materials and structures

The starting compounds i.e. 4-iodobenzonitrile, 4-(bromomethyl)benzonitrile, 4-(4,4,5,5-tetramethyl-1,3,2-dioxaborolan-2-yl)benzonitrile, 9*H*-fluorene-2-carbaldehyde, 2-bromo-9*H*-fluorene, 9*H*-carbazole, fluorenone, triphenylamine, 1-(4-iodophenyl)ethanone, 1,4-diiodobenzene, 1-bromo-4-iodobenzene, 1,3,5-tribromobenzene, 1,4,5,8-naphthalenetetracarboxylic acid dianhydride, 1,3,4-thiadiazol-2-amine, pyridine-2-amine, pyridine-3-amine, pyridine-4-amine, pyridine-3,4-diamine, pyrimidine-4,5-diamine and the required chemicals, i.e. trifluoromethanesulphonic acid (CF_3SO_3H), 1-bromo-2-ethylhexane, 1-bromohexane, 2-chloro-2-methylpropane, potassium *tert*-butoxide (*t*-BuOK), triphenylphosphine (PPh_3), Aliquat 336, *tetrakis*-triphenylphosphine palladium ($Pd(PPh_3)_4$), *bis*-triphenylphosphine palladium dichloride ($Pd(PPh_3)_2Cl_2$), copper iodide (CuI), ethynyltrimethylsilane, tetrabutylammonium fluoride (*n*-Bu_4NF) solution in THF, copper (Cu), 18-crown-6, potassium iodide (KI), potassium iodate (KIO_3), sodium hydroxide (NaOH), sodium hydrosulfate ($NaHSO_4$), potassium carbonate (K_2CO_3), anhydrous sodium sulfate (Na_2SO_4), potassium hydroxide (KOH), 65% phosphoric acid (H_3PO_4), anhydrous acetic acid (CH_3COOH), anhydrous acetic acid anhydride ($(CH_3CO)_2O$), polystyrene were purchased from Sigma-Aldrich and used as received. Zeonex cyclo-olefin polymer was purchased from ZEON Corporation.

The solvents, i.e. toluene, chloroform, ethyl acetate, *n*-hexane, diethyl ether, methanol, acetone, acetonitrile, tetrahydrofuran (Penta), dichloromethane (Poch), *o*-dichlorobenzene, diisopropylamine (*i*-PrA), pyridine and *N*,*N*-dimethylformamide (DMF) (Sigma-Aldrich) were dried and distilled according to the conventional procedures [163].

The structure of newly synthesized intermediate compounds was proven by ^1H and ^{13}C NMR (exception: if a compound is unstable, it was used in further synthetic steps without characterization). The structure of newly synthesized target compounds was confirmed by ^1H and ^{13}C NMR, IR spectroscopy, mass spectrometry and elemental analysis methods.

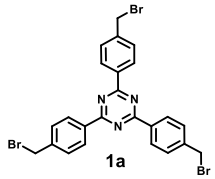

1a

Chemical folmula: $C_{24}H_{18}Br_3N_3$

2,4,6-Tris[4-(bromomethyl)phenyl]-1,3,5-triazine (**1a**, FW = 588.14 g/mol, m.p.: 190-192 °C, lit. m.p.: 191-193 °C [164]) was prepared by acid-catalyzed electrophilic cyclization according to the procedure reported in literature [165]. Off-white powder (2.00 g, 3.40 mmol, 96% yield).

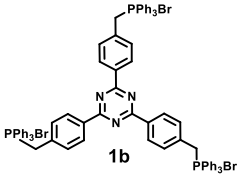

Chemical formula: $C_{72}H_{60}N_3P_3Br_3$

({4-[Bis{4-[(triphenylphosphoniumyl)methyl] phenyl}-1,3,5-triazin-2-yl]phenyl}methyl) triphenylphosphoniumtribromide (**1b**, FW = 1374.99 g/mol, m.p.: 279-281 °C) was obtained by similar procedure as **1a** [165]. Off-white powder (2.6 g, 1.89 mmol, 87% yield).

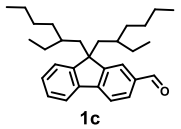

Chemical formula: $C_{29}H_{40}O$

9,9-Bis(2-ethylhexyl)-9*H*-fluorene-2-carbaldehyde (**1c**, FW = 404.64 g/mol) was prepared by the alkylation reaction of commercially available 9*H*-fluorene-2-carbaldehyde by the reported procedure [166]. Viscose yellow liquid (2.52 g, 6.22 mmol, 56% yield).

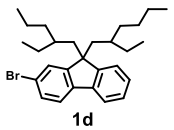

Chemical formula: $C_{28}H_{39}O$

2-Bromo-9,9-bis(2-ethylhexyl)-9*H*-fluorene (**1d**, FW = 455.53 g/mol) was prepared by the alkylation reaction of commercially available 2-bromo-9*H*-fluorene by the reported procedure [167]. Viscose pale yellow liquid (3.50 g, 7.68 mmol, 82% yield).

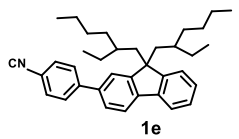

Chemical formula: $C_{36}H_{45}N$

4-[9,9-Bis(2-ethylhexyl)-9H-fluoren-2-yl]benzonitrile (**1e**, FW = 491.77 g/mol) was obtained by the standard Suzuki coupling reaction. An aqueous 2M K_2CO_3 solution (4.36 mL) containing toluene (10 mL) was added to the mixture of **1d** (2.35 g, 5.01 mmol), 4-cyanophenylboronic acid pinacol ester (1.0 g, 4.36 mmol), Aliquot 336 (0.1 g, 0.25 mmol) and ($Pd(PPh_3)_4$) (0.05 g, 0.04 mmol) under argon atmosphere. The resulting solution was kept at reflux temperature for 48 hours and then cooled down to room temperature. The reaction mixture was treated with water, extracted with ethyl acetate and washed with brine twice. The organic phase was dried over anhydrous Na_2SO_4. After evaporation of the solvents under reduced pressure the residue was purified by column chromatography on silica gel using the eluent mixture of hexane and ethyl acetate in volume ratio of 30:1 and recrystallized from ethanol to afford white crystals (2.20 g, 4.47 mmol, yield 42%, m.p.: 79-80 °C). ^{1}H NMR (400 MHz, $CDCl_3$, δ): 7.72-7.81 (m, 6H), 7.55-7.61 (m, 2H), 7.39-7.44 (m, 1H), 7.34-7.39 (m, 1H), 7.29-7.34 (m, 1H), 1.98-2.11 (m, 4H), 0.57-0.96 (m, 22H), 0.48-0.57 (m, 8H). ^{13}C NMR (100 MHz, $CDCl_3$, δ): 151.47, 150.66, 146.33, 142.08, 140.42, 137.17, 132.63, 127.60, 126.96, 126.15, 124.17, 122.77, 119.97, 110.45, 55.05, 44.45, 44.41, 34.62, 34.58, 33.78, 33.68, 28.15, 28.09, 27.12, 26.91, 26.88, 22.70, 22.66, 14.00, 13.96, 10.37, 10.27, 10.24.

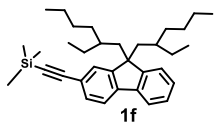

Chemical formula: $C_{34}H_{50}Si$

{2-[9,9-Bis(2-ethylhexyl)-9H-fluoren-2-yl]ethynyl} trimethylsilane (**1f**, FW = 486.86 g/mol) was obtained by Sonogashira coupling reaction described in literature [168]. Ethynyltrimethylsilane (1.45 g, 14.90 mmol) was added to the mixture of **1d** (3.50 g, 7.45 mmol), $Pd(PPh_3)_2Cl_2$ (0.10 g, 0.14 mmol), CuI (0.017 g, 0.08 mmol) and PPh_3 (0.19 g, 0.74 mmol) in dry diisopropylamine (iPrA) (20 mL) under argon atmosphere. After stirring for 24 h at 90 ˚C the reaction mixture was treated with water, extracted with ethyl acetate and washed with brine twice. The organic phase was dried over

anhydrous Na_2SO_4. After evaporation of the solvent under reduced pressure the residue was purified by silica gel chromatography using hexane as eluent to afford the pale yellow liquid (1.85 g, 3.79 mmol, yield 51%). ^{1}H NMR (400 MHz, $CDCl_3$, δ): 7.67-7.72 (m, 1H), 7.62-7.67 (m, 1H), 7.45-7.52 (m, 2H), 7.43-7.31 (m, 3H), 2.00 (dd, 4H, *J* = 5.41 Hz, *J* = 3.4 Hz), 0.71-0.95 (m, 22H), 0.53-0.55 (m, 8H), 0.31 (t, 6H, *J* = 2.42 Hz), 0.23 (s, 3H). ^{13}C NMR (100 MHz, $CDCl_3$, δ): 151.04, 150.69, 141.92, 140.75, 131.30, 131.16, 131.03, 127.80, 127.66, 127.51, 127.15, 127.08, 124.33, 121.18, 121.11, 121.05, 120.17, 119.59, 106.52, 93.71, 55.06, 44.97, 44.90, 44.58, 44.49, 34.81, 33.81, 33.78, 33.65, 28.29, 28.23, 28.20, 27.28, 27.23, 27.20, 27.17, 23.01, 22.93, 14.36, 14.25, 10.65, 10.62, 10.47, 0.33.

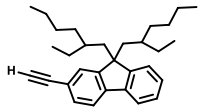

1g

Chemical formula: $C_{31}H_{42}$

9,9-Bis(2-ethylhexyl)-2-ethynyl-9H-fluorene (**1g**, FW = 414.68 g/mol) was obtained by the procedure described in literature [169]. The 2.5M solution of *n*-Bu_4NF in THF (4.62 mL) was added drop-wise to the vigorously stirred solution of **1f** (1.50 g, 3.00 mmol) in anhydrous THF (15 mL) under argon atmosphere. After stirring for 2 hours at room temperature the reaction mixture was treated with water, extracted with dichloromethane and washed with brine twice. The organic layer was dried over anhydrous Na_2SO_4. After evaporation of the solvent under reduced pressure the residue was purified by silica gel chromatography using hexane as an eluent to afford the yellow liquid (1.14 g, 2.75 mmol, yield 92%). The material was used for the further step without characterization.

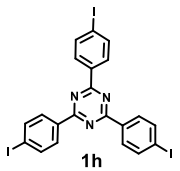

1h

Chemical formula: $C_{21}H_{12}I_3N_3$

2,4,6-Tris(4-iodophenyl)-1,3,5-triazine (**1h**, FW = 687.06 g/mol, m.p.: 377-379 °C, lit. m.p.: 378 °C [170]) was obtained by similar procedure as **1a** [165].

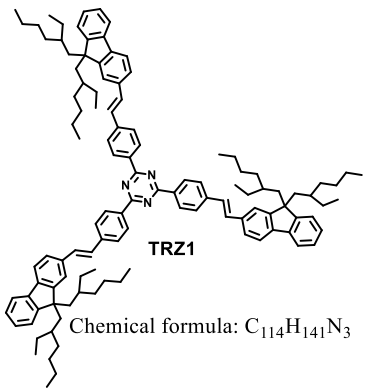

TRZ1

Chemical formula: $C_{114}H_{141}N_3$

2,4,6-Tris({4-[(E)-2-[9,9-bis(2-ethylhexyl)-9H-fluoren-2-yl]ethenyl]phenyl})-1,3,5-triazine (**TRZ1**, FW = 1553.36 g/mol). Potassium *t*-BuOK (0.58 g, 5.21 mmol) was added to the solution of **1c** (1.30 g, 3.04 mmol) and **1b** (1.20 g, 0.86 mmol) in dry THF (10 mL) under argon atmosphere. After stirring for 2 hours at room temperature the reaction mixture was treated with water, extracted with ethylacetate and washed with brine. The organic phase was dried over anhydrous Na_2SO_4. After evaporation of solvents under reduced pressure the residue was purified by multiple column chromatography on silica gel using the eluent mixture of hexane and dichloromethane at volume ratio of 10:1 and by multiple reprecipitations to methanol to afford the yellow solid (0.23 g, 0.14 mmol, yield 17%). ^{1}H NMR (500 MHz, $CDCl_3$, δ): 8.78 (d, 6H, *J* = 8.2 Hz), 8.69 (d, 3H, *J* = 8.0 Hz), 7.74 (d, 6H, *J* = 8.4 Hz), 7.70 (d, 6H, *J* = 7.4 Hz), 7.58-7-63 (m, 3H), 7.53-7.57 (m, 3H), 7.37-7.40

(m, 3H), 7.36-7.39 (m, 3H), 7.31-7.33 (m, 3H), 7.24-7.28 (m, 3H), 1.97-2.09 (m, 12H), 0.65-0.96 (m, 66H), 0.49-0.59 (m, 24H). ^{13}C NMR (125 MHz, $CDCl_3$, δ): 171.49, 171.10, 151.07, 150.79, 150.75, 150.71, 143.03, 141.67, 140.87, 135.38, 135.33, 135.23, 133.68, 131.43, 129.36, 128.96, 127.02, 126.80, 126.55, 126.06, 124.08, 122.05, 119.82, 119.70, 54.80, 44.68, 44.63, 44.48, 44.42, 34.59, 33.66, 28.12, 28.09, 27.05, 26.94, 22.74, 22.69, 14.12, 14.01, 10.36, 10.26. FT-IR (KBr, cm^{-1}): ν = 3064, 3023, 2956, 2923, 2870, 1575, 1512, 1453, 1369, 955, 821. MALDI-TOF MS (m/z): calculated for $C_{114}H_{141}N_3$ 1553.36 (M^++H), found 1553.55. Anal. calc. (%): C 88.15, H 9.15, N 2.71; found (%): C 87.98, H 9.11, N 2.70.

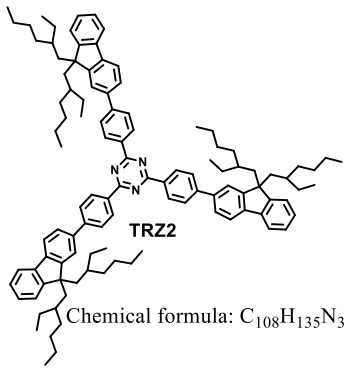

Chemical formula: $C_{108}H_{135}N_3$

2,4,6-Tris(4-[9,9-bis(2-ethylhexyl)-9H-fluoren-2-yl]phenyl)-1,3,5-triazine (**TRZ2**, FW = 1475.30 g/mol) 0.1M Solution of **1e** (0.50 g, 1.00 mmol) in dichloromethane was drop-wise added over the period of 1 hour to a vigorously stirred solution of CF_3SO_3H (1.53 g, 0.90 mL, 10.10 mmol) in dry dichloromethane (10 mL) at 0 °C under argon atmosphere. After being stirred for 72 hours at ambient temperature the reaction mixture was treated with a saturated aqueous $NaHCO_3$ solution, extracted with chloroform and washed with brine twice. The organic phase was dried over anhydrous Na_2SO_4. After evaporation of the solvents under reduced pressure the residue was purified by multiple column chromatography on silica gel by using the eluent mixture of hexane, ethyl acetate and dichloromethane in volume ratio of 40:1:1 and by reprecipitation to methanol to afford the white solid (0.33 g, 0.22 mmol, yield 35%). ^{1}H NMR (500 MHz, $CDCl_3$, δ): 8.91 (dd, 6H, *J* = 8.4 Hz, *J*=1.6 Hz), 7.87 (d, 6H, *J* = 8.2 Hz), 7.81 (d, 3H, *J* = 7.8 Hz), 7.75 (d, 3H, *J* = 7.5 Hz), 7.71 (t, 3H, *J*=4.2 Hz), 7.69 (d, 3H, *J* = 7.8 Hz), 7.39-7.43 (m, 3H), 7.32-7.37 (m, 3H), 7.29 (t, 3H, *J* = 7.3Hz), 1.99-2.14 (m, 12H), 0.60-0.96 (m, 66H), 0.50-0.60 (m, 24H). ^{13}C NMR (125 MHz, $CDCl_3$, δ): 171.42, 151.19, 150.74, 150.69, 150.64, 145.91, 141.39, 140.81, 140.78, 140.75, 138.61, 138.56, 138.50, 134.99, 129.47, 127.27, 126.83, 126.68, 126.16, 124.12, 122.97, 122.87, 122.77, 119.95, 119.80, 55.02, 44.50, 34.63, 33.84, 33.74, 33.71, 28.15, 28.12, 28.08, 27.12, 27.11, 26.93, 26.90, 22.72, 22.67, 13.99, 10.37, 10.34, 10.27, 10.24. FT-IR (KBr, cm^{-1}): ν = 3065, 3018, 2957, 2923, 2871, 1568, 1512, 1454, 1372, 813. MALDI-TOF MS (m/z): calculated for $C_{108}H_{135}N_3$ 1475.30, found 1475.6. Anal. calc. (%): C 87.93, H 9.22, N 2.85; found (%): C 87.75, H 9.20, N 2.84.

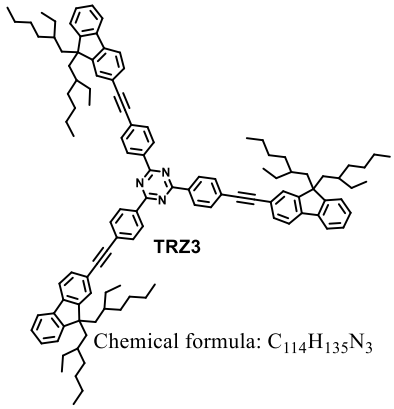

Chemical formula: $C_{114}H_{135}N_3$

2,4,6-Tris(4-{2-[9,9-bis(2-ethylhexyl)-9H-fluoren-2-yl]ethynyl}phenyl)-1,3,5-triazine (**TRZ3**, FW = 1547.37 g/mol). The mixture of **1g** (1.00 g, 2.40 mmol), **1h** (0.40 g, 0.58 mmol), $Pd(PPh_3)_2Cl_2$ (0.03 g, 0.04 mmol), CuI (0.004 g, 0.02 mmol), PPh_3 (0.05 g, 0.17 mmol) in dry *i*-PrA (20 mL) was stirred at 90 ˚C under argon atmosphere. After stirring for 24 hours the

reaction mixture was treated with water, extracted with chloroform and washed with brine twice. The organic layer was dried over anhydrous Na_2SO_4. After evaporation of the solvents under reduced pressure the residue was purified by multiple silica gel chromatography using hexane as eluent and by reprecipitation to methanol to afford the yellow solid (0.20 g, 0.13 mmol, yield 24%). ^{1}H NMR (500 MHz, $CDCl_3$, δ): 8.79 (d, 6H, *J* = 8.2 Hz), 7.74-7.79 (m, 6H), 7.70 (d, 6H, *J* = 7.8 Hz), 7.55-7.62 (m, 6H), 7.36-7.41 (m, 3H), 7.33 (t, 3H, *J*=6.8Hz), 7.29 (t, 3H, *J* = 7.3Hz), 1.96-2.05 (m, 12H), 0.66-0.98 (m, 66H), 0.49-0.58 (m, 24H). ^{13}C NMR (125 MHz, $CDCl_3$, δ): 171.12, 150.89, 150.82, 150.75, 150.69, 141.99, 140.50, 140.47, 140.45, 135.43, 131.81, 130.83, 130.73, 130.63, 128.91, 127.99, 127.35, 127.24, 127.14, 127.04, 126.90, 124.12, 120.59, 120.53, 120.47, 119.99, 119.60, 93.64, 89.00, 54.90, 44.71, 44.66, 44.44, 44.37, 34.58, 33.63, 33.59, 33.48, 28.04, 26.95, 22.73, 22.67, 14.09, 13.99, 10.38, 10.37, 10.26, 10.25. FT-IR (KBr, cm^{-1}): ν = 3063, 2955, 2921, 2855, 2201, 1569, 1506, 1451, 1369, 815. MALDI-TOF MS (m/z): calculated for $C_{114}H_{135}N_3$ 1547.37, found 1547.9. Anal. calc. (%): C 88.49, H 8.79, N 2.72; found (%): C 88.64, H 8.80, N 2.72.

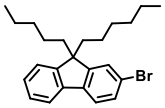

2a
Chemical formula: $C_{24}H_{31}O$

2-Bromo-9,9-dihexyl-9*H*-fluorene (**2a**, FW = 398.16 g/mol) was prepared by the alkylation reaction of commercially available 2-bromo-9*H*-fluorene by the reported procedure [167]. Viscose pale yellow liquid (3.43 g, 8.61 mmol, 82% yield).

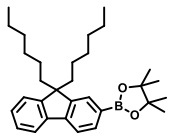

2b
Chemical formula: $C_{31}H_{45}BO_2$

2-(9,9-Dihexyl-9*H*-fluoren-2-yl)-4,4,5,5-tetramethyl-1,3,2-dioxaborolane (**2b**, FW = 460.35 g/mol) was synthesized as described in the literature source [171].Viscose colorless liquid (2.31 g, 5.02 mmol, yield 76%)

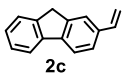
2c
Chemical formula: $C_{15}H_{12}$

2-Vinyl-9*H*-fluorene (**2c**, FW = 192.26 g/mol) was prepared according to the known procedure [172]. White solid (2.76 g, 14.35 mmol, yield 68%).

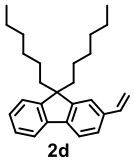
2d
Chemical formula: $C_{27}H_{36}$

9,9-Dihexyl-2-vinyl-9*H*-fluorene (**2d**, FW = 360.28 g/mol) was obtained by the reported procedure [167]. Viscose colorless liquid (3.41 g, 9.46 mmol, yield 78%).

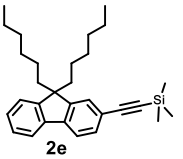

2e
Chemical formula: $C_{30}H_{42}Si$

((9,9-Dihexyl-9*H*-fluoren-2-yl)ethynyl)trimethylsilane (**2e**, FW = 430.31 g/mol) was synthesized by the Sonogashira coupling reaction as described earlier [168]. Pale yellow liquid (2.11 g, 4.90 mmol, yield 85%).

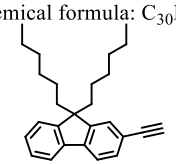
2f
Chemical formula: $C_{27}H_{34}$

2-Ethynyl-9,9-dihexyl-9*H*-fluorene (**2f**, FW = 358.27 g/mol) was prepared as described in the literature [169]. Pale brown liquid (1.78 g, 4.97 mmol, yield 92%).

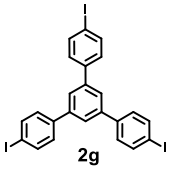

Chemical formula: $C_{27}H_{34}$

1,3,5-Tris(4-iodophenyl)benzene (**2g**, FW = 683.83 g/mol, m.p. = 261-263 °C, lit. 262-263 °C [173]) was obtained by the reported method [174]. White solid (2.73 g, 3.99 mmol, yield 86%).

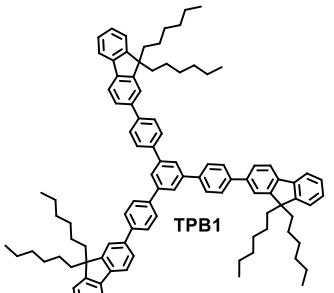

Chemical formula: $C_{99}H_{114}$

2-({3,5-Bis[4-(9,9-dihexyl-9H-fluoren-2-yl) phenyl]phenyl}phenyl)-9,9-dihexyl-9H-fluorene (**TPB1**, FW = 1304.01 g/mol) was obtained by Suzuki coupling reaction, similarly to compound **1e**. White powder (0.20 g, 0.15 mmol, yield 21%).^{1}H NMR (400 MHz, $CDCl_3$, δ_H, Me_4Si): 7.97 (s, 3H, Ar), 7.88 (q, 12H, *J* = 8.57 Hz, Ar), 7.83 (d, 3H, *J* = 7.8 Hz, Ar), 7.78 (d, 3H, *J* = 7.5 Hz, Ar), 7.70 (d, 3H, *J* = 7.8 Hz, Ar), 7.67 (s, 3H), 7.34-7.42 (m, 9H, Ar), 2.05-2.09 (m, 12H, C−CH_2), 1.10-1.18 (m , 36H, CH_2), 0.80 (t, 18H, *J* = 6.8 Hz, CH_3), 0.66-0.77 (m, 12H, CH_2). ^{13}C NMR (100 MHz, $CDCl_3$, δ_C): 151.51, 151.02, 142.15, 141.07, 140.73, 140.65, 139.91, 139.39, 127.80, 127.71, 127.25, 126.83, 126.91, 125.06, 122.92, 121.43, 120.03, 119.80, 55.20 ($(CH_2)_2C$) , 40.48 (CH_2), 31.53 (CH_2), 29.76 (CH_2), 23.80 (CH_2), 22.62 (CH_3), 14.05 (CH_3). FT-IR (KBr, ν_{max}/cm^{-1}): 3054 (=C−H), 3030, 2954 (C−H), 2927, 2855, 1594, 1465 (C=C Ar), 1392, 1377, 1253, 1014, 820 (C−H Ar). ESI-MS (m/z): calc. for $C_{99}H_{114}$ 1304.01 [M^++H], found 1304.30. Elemental analysis calc. for $C_{99}H_{114}$ (%): C, 91.19; H, 8.81. Found (%): C, 91.24; H, 8.76.

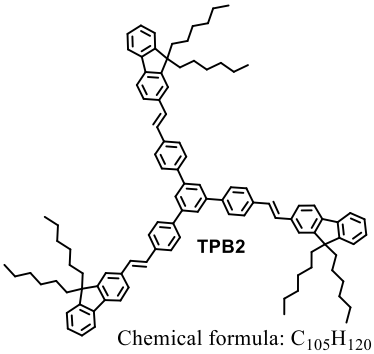

Chemical formula: $C_{105}H_{120}$

2-[(E)-2-{4-[3,5-Bis({4-[(E)-2-(9,9-dihexyl-9H-fluoren-2-yl)ethenyl]phenyl})phenyl]phenyl} ethenyl]-9,9-dihexyl-9H-fluorene (**TPB2**, FW = 1382.13). The mixture of compounds **2g** (0.48 g, 0.70 mmol), **2d** (1.51 g, 4.20 mmol), $Pd(OAc)_2$ (0.03 g, 0.15 mmol), *n*-Bu_4Br (0.87g, 2.72 mmol), anhydrous K_2CO_3 (0.37 g, 2.67 mmol) in dry DMF (20 mL) was stirred at 110˚C in argon atmosphere. After stirring for 24 h the reaction mixture was treated with water, extracted with ethyl acetate, washed with brine twice and dried over anhydrous Na_2SO_4. After the evaporation of solvents under reduced pressure the residue was purified by silica gel chromatography (eluent hexane/toluene 10/1) and reprecipitation into methanol to afford a white powder (0.23 g, 0.17 mmol, yield 24%). ^{1}H NMR (400 MHz, $CDCl_3$, δ_H, Me_4Si): 7.90 (s, 3H), 7.79 (d, 6H, *J*= 8.4 Hz, Ar), 7.71-7.74 (m, 12H, Ar), 7.57 (d, 3H, *J* = 7.9 Hz, Ar), 7.55 (s, 3H, Ar), 7.33-7.39 (m, 9H, Ar), 7.30 (d, 6H, *J* = 8.72 Hz, Ar), 2.04 (t, 12H, *J* = 8.2 Hz, C−CH_2), 1.06-1.17 (m, 36H, CH_2), 0.80 (t, 18H, *J* = 6.8 Hz, CH_3), 0.64-0.73 (m, 12H, CH_2). ^{13}C NMR (100 MHz, $CDCl_3$, δ_C) δ:151.31, 151.02, 141.96, 141.10, 140.80, 140.04,

137.00, 136.19, 129.65, 127.63, 127.31, 127.10, 126.98, 126.81, 125.67, 124.72, 122.88, 120.81, 119.93, 119.72, 55.04 ($(CH_2)_2C$), 40.52 (CH_2), 31.54 (CH_2), 29.77 (CH_2), 23.77 (CH_2), 22.63 (CH_3), 14.05 (CH_3). FT-IR (KBr, ν_{max}/cm^{-1}): 3051 (=C−H), 3025, 2952 (C−H), 2926, 2853, 1940 (C=C), 1592, 1509, 1451 (C=C Ar), 1376, 1248, 1015, 961 (trans C=C), 944 (trans C=C), 828 (C−H Ar). ESI-MS (m/z): calc. for $C_{105}H_{120}$ 1382.13 [M^++H], found 1383.00. Elemental analysis calc. for $C_{105}H_{120}$ (%): C, 91.25; H, 8.75. Found (%): C, 91.22; H, 8.78.

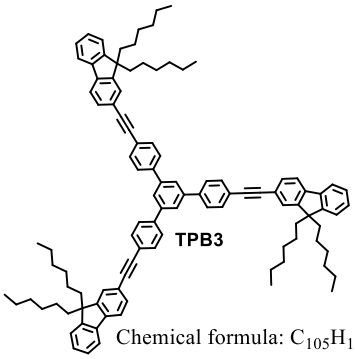

Chemical formula: $C_{105}H_{114}$

2-(2-{4-[3,5-Bis({4-[2-(9,9-dihexyl-9H-fluoren-2-yl)ethynyl]phenyl})phenyl] phenyl}ethynyl)-9,9-dihexyl-9H-fluorene (**TPB3**, FW = 1376.08 g/mol) was prepared by the Sonogashira coupling reaction similarly to compound **TRZ3**. White powder (0.50 g, 0.36 mmol, yield 50%). ^{1}H NMR (400 MHz, $CDCl_3$, δ_H, Me_4Si): 7.88 (s, 3H, Ar), 7.75-7.78 (m, 6H, Ar), 7.72-7.74 (m, 9H, Ar), 7.72 (d, 3H, *J* = 2.3 Hz, Ar), 7.587 (d, 6H, *J* = 8.5 Hz, Ar), 7.33-7.39 (m, 9H, Ar), 2.01 (t, 12H, *J* = 8.2 Hz, C−CH_2), 1.01-1.19 (m, 36H, CH_2), 0.80 (t, 18H, *J* = 6.9 Hz, CH_3), 0.58-0.75 (m, 12H, CH_2). ^{13}C NMR (100 MHz, $CDCl_3$, δ_C) δ: 151.05, 150.82, 141.79, 141.57, 140.48, 140.41, 132.14, 130.68, 127.56, 127.29, 126.90, 125.97, 125.15, 122.91, 122.88, 121.31, 120.03, 119.69, 91.59 (C≡C), 89.20 (C≡C), 55.17 ($(CH_2)_2CH$), 40.45 (CH_2), 31.56 (CH_2), 29.75 (CH_2), 23.74 (CH_2), 22.64 (CH_3), 14.04 (CH_3). FT-IR (KBr, ν_{max}/cm^{-1}): 3062 (=C−H), 3034, 2953 (C−H), 2927, 2855, 2210 (C≡C), 1595, 1510, 1465 (C=C Ar), 1377, 1255, 1017, 888, 829 (C−H Ar). ESI-MS (m/z): calc. for $C_{105}H_{114}$ 1376.08 [M^++H], found 1376.20. Elemental analysis calc. for $C_{105}H_{114}$: C, 91.65; H, 8.35. Found (%): C, 91.62; H, 8.38.

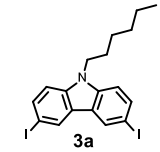

Chemical formula: $C_{18}H_{19}I_2N$

9-Hexyl-3,6-diiodo-9H-carbazole (**3a**, FW = 502.96 g/mol, m.p. = 141-143 °C) was obtained by the reported procedures [175,176]. Off-white solid (5.02 g, 10.00 mmol, yield 83%).

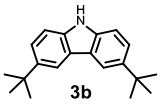

Chemical formula: $C_{20}H_{25}N$

3,6-Di-tert-butyl-9*H*-carbazole (**3b**, FW = 279.43 g/mol, m.p. = 226-228 °C, lit. 228-230 °C [177]) was synthesized as described in the literature source [177]. Off-white solid (6.32 g, 22.6 mmol, yield 67%).

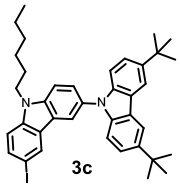

Chemical formula: $C_{38}H_{42}IN_2$

3',6'-Di-tert-butyl-9-hexyl-6-iodo-9H-3,9'-bicarbazole (**3c**, FW = 654.68 g/mol). Was obtained by Ullmann reaction [72]. White solid (2.73 g, 4.17 mmol, yield 70%). ^{1}H NMR (400 MHz, $CDCl_3$, δ): 8.38 (d, 1H, *J* = 1.59 Hz, Ar), 8.21 (d, 2H, *J* = 1.66 Hz, Ar), 8.18 (d, 1H, *J* = 1.81 Hz, Ar), 7.77 (dd, 1H, J_1 = 8.62 Hz, J_2 = 1.67 Hz, Ar), 7.62-7.65 (m, 1H, Ar), 7.58 (d, 1H, *J* = 8.61 Hz, Ar), 7.48 (dd, 2H, *J* = 8.64 Hz, *J* = 1.91 Hz, Ar), 7.34 (d, 1H, *J* = 8.61 Hz, Ar), 7.28(d, 2H, *J* =

8.63 Hz, Ar), 4.37 (t, 2H, J = 7.31 Hz, N−CH_2), 1.95 (quintet, 2H, J = 7.36 Hz, CH_2), 1.51 (s, 18H, CH_3), 1.31-1.47 (m, 6H, CH_2), 0.92 (t, 3H, J = 7.03 Hz, CH_3). ^{13}C NMR (100 MHz, $CDCl_3$, δ): 142.4, 140.1, 139.1, 134.2, 129.8, 129.4, 125.6, 124.8, 123.5, 123.0, 122.3, 119.2, 116.2, 111.0, 109.7, 81.5 (C−I), 43.4 (N−C), 34.7, 32.0, 31.5, 29.0, 26.9, 22.5, 14.0.

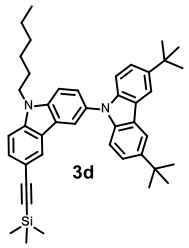

Chemical formula: $C_{43}H_{52}N_2Si$

3',6'-Di-tert-butyl-9-hexyl-6-((trimethylsilyl)ethynyl)-9H-3,9'-bicarbazole (**3d**, FW = 624.99 g/mol) was obtained by Sonogashira coupling reaction as described in literature [167]. Off-white solid (2.10 g, 3.36 mmol, yield 70%). ^{1}H NMR (400 MHz, $CDCl_3$, δ): 8.23 (d, 1H, J = 1.11 Hz, Ar), 8.20 (d, 3H, J = 1.74 Hz, Ar), 7.64-7.66 (m, 1H, Ar), 7.62-7.63 (m, 1H, Ar), 7.58 (d, 1H, J = 8.61 Hz, Ar), 7.48 (dd, 2H, J = 8.64 Hz, J = 1.85 Hz, Ar), 7.40 (d, 1H, J = 8.56 Hz, Ar), 7.34 (d, 1H, J = 8.61 Hz, Ar), 7.33 (d, 1H, J = 8.64 Hz, Ar), 4.50 (t, 2H, J = 7.32 Hz, N−CH_2), 2.08 (quintet, 2H, J = 7.56 Hz, CH_2), 1.51 (s, 18H, CH_3), 1.41-1.49 (m, 6H, CH_2), 0.98 (t, 3H, J = 7.20 Hz, CH_3), 0.29 (s, 9H, Si−CH_3).^{13}C NMR (100 MHz, $CDCl_3$, δ): 142.1, 140.6, 140.2, 139.7, 129.8, 124.9, 124.7, 123.5, 123.0, 122.1, 119.0, 116.2, 113.4, 109.8, 109.1, 106.6 (C≡C), 91.9 (C≡C), 43.5 (N−C), 34.5, 31.9, 31.5, 28.9, 27.0, 22.3, 14.1, 0.16 (C−Si).

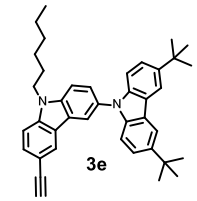

Chemical formula: $C_{40}H_{44}N_2$

3',6'-Di-tert-butyl-6-ethynyl-9-hexyl-9H-3,9'-bicarbazole (**3e**, FW = 552.81 g/mol) was obtained by the procedure described in literature [169]. Off-white solid (1.65 g, 2.98 mmol, yield 93%). ^{1}H NMR (400 MHz, $CDCl_3$, δ): 8.26 (d, 1H, J = 1.11 Hz, Ar), 8.25 (d, 1H, J = 1.90 Hz, Ar), 8.23 (d, 2H, J = 1.71 Hz, Ar), 7.67 (dd, 1H, J_1 = 8.51 Hz, J_2 = 1.49 Hz, Ar), 7.65 (dd, J_1 = 8.48 Hz, J_2 = 2.01 Hz, Ar), 7.60 (d, 1H, J = 8.81 Hz, Ar), 7.51 (d, 1H, J = 1.89 Hz, Ar), 7.50 (d, 1H, J = 1.87 Hz, Ar), 7.43 (d, 1H, J = 8.55 Hz, Ar), 7.35 (d, 2H, J = 8.58 Hz, Ar), 4.39 (t, 2H, J = 7.37 Hz, N−CH_2), 3.10 (s, 1H, −C≡C−H), 1.98 (quintet, 2H, J = 7.47 Hz, CH_2), 1.53 (s, 18H, CH_3), 1.34-1.49 (m, 6H, CH_2), 0.94 (t, 3H, J = 7.12 Hz, CH_3).^{13}C NMR (100 MHz, $CDCl_3$, δ): 141.4, 139.8, 139.2, 138.6, 129.1, 124.5, 123.8, 122.4, 122.0, 121.4, 118.2, 115.1, 111.4, 108.8, 108.1, 87.7 (C≡C), 74.3 (≡C−H), 42.4 (N−C), 33.6, 31.0, 30.5, 28.0, 25.9, 21.5, 12.9.

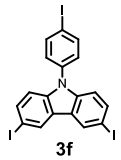

Chemical formula: $C_{18}H_{44}I_3N$

3,6-Diiodo-9-(4-iodophenyl)-9*H*-carbazole (**3f**, FW = 621.00 g/mol, m.p. = 203-205 °C) was obtained by the reported procedures [72,175]. White solid (3,02 g, 4.86 mmol, yield 83%).

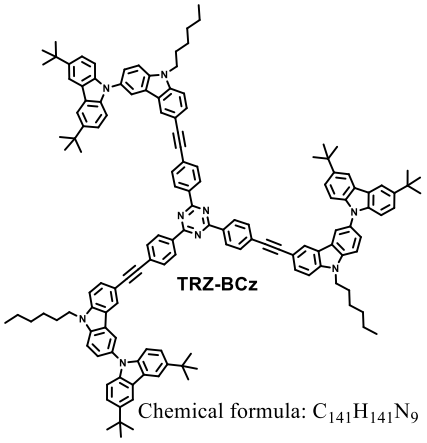

Chemical formula: $C_{141}H_{141}N_9$

2,4,6-Tris(4-((3',6'-di-tert-butyl-9-hexyl-9H-3,9'-bicarbazol-6-yl)ethynyl)phenyl)-1,3,5-triazine (**TRZ-BCz**, FW = 1961.76 g/mol) was obtained by Sonogashira coupling reaction similarly to compound **TRZ3**. Yellow solid (0.70 g, 0.36 mmol, yield 65%). ^{1}H NMR (400 MHz, $CDCl_3$, δ): 8.77 (d, 6H, *J* = 8.41 Hz, Ar), 8.34 (s, 3H, Ar), 8.28 (d, 3H, *J* = 1.72 Hz, Ar), 8.23 (d, 6H, *J* = 1.60 Hz, Ar), 7.76 (d, 9H, *J* = 8.30 Hz, Ar), 7.66 (dd, 3H, *J* = 8.59 Hz, *J* = 1.86 Hz, Ar), 7.60 (d, 3H, *J* = 8.65 Hz, Ar), 7.51 (dd, 6H, J_1 = 8.68 Hz, J_2 = 1.83 Hz, Ar), 7.46 (d, 3H, *J* = 8.60 Hz, Ar), 7.38 (d, 6H, *J* = 8.62 Hz, Ar), 4.39 (t, 6H, *J* = 7.16 Hz, N−CH_2), 1.98 (quintet, 6H, *J* = 7.29 Hz, CH_2), 1.52 (s, 54H, CH_3), 1.30-1.44 (m, 18H, CH_2), 0.86-1.01 (m, 9H, CH_3). ^{13}C NMR (100 MHz, $CDCl_3$, δ): 171.0, 142.5, 140.9, 140.1, 139.6, 137.2, 135.1, 131.5, 130.0, 129.9, 128.9, 128.1, 125.4, 124.5, 123.5, 123.3, 123.0, 122.6, 119.2, 116.2, 113.3, 109.8, 109.1, 93.8 (C≡C), 87.9 (C≡C), 43.5 (N−C), 34.7, 32.0, 31.6, 29.0, 26.9, 22.6, 14.0. FT-IR (KBr, cm^{-1}): ν = 3046 (=C−H), 2952 (C−H), 2927, 2859, 2204 (C≡C), 1862, 1731, 1569, 1505, 1489 (C=C Ar), 1362, 1285, 813(C−H Ar). MALDI-TOF MS (m/z): calculated for $C_{141}H_{141}N_9$ 1961.76 (M^++H), found 1961.10. Anal. calc. for $C_{141}H_{141}N_9$: C 86.33; H 7.24; N 6.43; found: C 86.28; H 7.27; N 6.45.

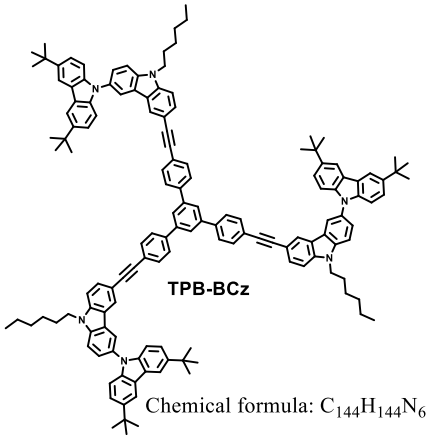

Chemical formula: $C_{144}H_{144}N_6$

Tris(4-((3',6'-di-tert-butyl-9-hexyl-9H-3,9'-bicarbazol-6-yl)ethynyl)phenyl)-1,3,5-benzene (**TPB-BCz**, FW = 1958.79 g/mol) was obtained by Sonogashira coupling reaction similarly to compound **TRZ3**. Slightly brownish solid (0.53 g, 0.27 mmol, yield 60%). ^{1}H NMR (400 MHz, $CDCl_3$, δ): 8.32 (d, 3H, *J* = 1.11 Hz, Ar), 8.27 (d, 3H, *J* = 1.72 Hz, Ar), 8.22 (d, 6H, *J* = 1.63 Hz, Ar), 7.85 (s, 3H, Ar), 7.69-7.76 (m, 15H), 7.66 (dd, 3H, *J* = 8.59 Hz, *J* = 1.88 Hz, Ar), 7.60 (d, 3H, *J* = 8.63 Hz, Ar), 7.47-7.51 (m, 9H, Ar), 7.37 (d, 6H, *J* = 8.61 Hz, Ar), 4.41(t, 6H, *J* = 7.18 Hz, N−CH), 1.99 (quintet, 6H, *J* = 7.31 Hz, CH_2), 1.52 (s, 54H, CH_3), 1.29-1.43 (m, 18H, CH_2), 0.94 (t, 9H, *J* = 7.02 Hz, CH_3). ^{13}C NMR (100 MHz, $CDCl_3$, δ): 142.5, 141.8, 140.7, 140.1, 139.6, 132.0, 129.8, 129.7, 127.2, 125.4, 124.3, 123.5, 123.3, 123.0, 122.5, 119.2, 116.2, 113.6, 109.8, 109.1, 91.5 (C≡C), 87.7 (C≡C), 43.4 (N−C), 34.7, 32.0, 31.6, 29.0, 27.0, 22.6, 14.0. FT-IR (KBr, cm^{-1}): ν = 3044 (=C−H), 2952 (C−H), 2927, 2859, 2206 (C≡C), 1864, 1739, 1573, 1510, 1489 (C=C Ar), 1362, 1285, 806 (C−H Ar). MALDI-TOF MS (m/z): calculated for $C_{144}H_{144}N_6$ 1958.79 (M^++H), found 1958.97. Anal. calc. for $C_{144}H_{144}N_6$: C 88.30; H 7.41; N 4.29; found: C 88.25; H 7.44; N 4.31.

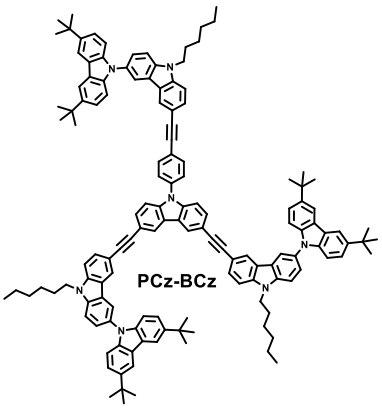

Chemical formula: $C_{139}H_{143}N_7$

6,6'-(9-(4-((3',6'-Di-tert-butyl-9-hexyl-9H-3,9'-bicarbazol-6-yl)ethynyl)phenyl)-9H-carbazole-3,6-diyl)bis(ethyne-2,1-diyl)bis(3',6'-di-tert-butyl-9-hexyl-9H-3,9'-bicarbazole) (**PCz-BCz**, FW = 1895.69 g/mol) was obtained by the similar procedure as **TRZ-BCz** and **TPB-BCz**. Slightly yellowish solid (0.52 g, 0.27 mmol, yield 58%). ^{1}H NMR (400 MHz, $CDCl_3$, δ): 8.38 (d, 2H, J = 0.89 Hz, Ar), 8.34 (d, 3H, J = 1.00 Hz, Ar), 8.27-8.29 (m, 3H, Ar), 8.21-8.23 (m, 6H, Ar), 7.82 (d, 2H, J = 8.44 Hz, Ar), 7.75-7.78 (m, 3H, Ar), 7.66 (dd, 4H, J_1 = 8.33 Hz, J_2 = 1.38 Hz, Ar), 7.57-7.64 (m, 6H, Ar), 7.47-7.51 (m, 9H, Ar), 7.43 (d, 2H, J = 8.53 Hz, Ar), 7.37 (d, 6H, J = 8.63 Hz, Ar), 4.42 (t, 6H, J = 7.18 Hz, N−CH), 2.00 (quintet, 6H, J = 7.16 Hz, CH_2), 1.51 (s, 54H, CH_3), 1.29-1.44 (m, 18H, CH_2), 0.94 (t, 9H, J = 6.99 Hz, CH_3). ^{13}C NMR (100 MHz, $CDCl_3$, δ): 142.4, 140.5, 140.4, 140.2, 139.6, 130.0, 129.8, 124.0, 123.5, 123.3, 123.0, 116.1, 115.7, 114.1, 109.8, 109.1, 89.1 (C≡C), 83.3 (C≡C), 43.4 (N−C), 34.7, 32.0, 31.6, 29.0, 26.9, 22.6, 14.3. FT-IR (KBr, cm^{-1}): ν = 3044 (=C−H), 2952 (C−H), 2928, 2860, 2206 (C≡C), 1867, 1744, 1573, 1514, 1490 (C=C Ar), 1362, 1284, 807 (C−H Ar). MALDI-TOF MS (m/z): calculated for $C_{138}H_{139}N_7$ 1895.69 (M^++H), found 1895.67. Anal. calc. for $C_{138}H_{139}N_7$: C 87.44; H 7.39; N 5.17; found: C 87.39; H 7.42; N 5.19.

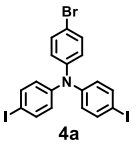

Chemical formula: $C_{18}H_{12}BrI_2N$

4-Bromo-*N*,*N*-bis(4-iodophenyl)aniline (**4a**, FW = 574.82 g/mol, m.p. = 147-149 °C, lit. 148 °C [178]) was prepared by the reported procedures [72,179,180]. Off-white solid (4.21 g, 7.32 mmol, yield 67%).

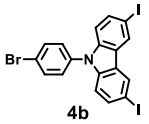

Chemical formula: $C_{18}H_{10}BrI_2N$

9-(4-Bromophenyl)-3,6-diiodo-9*H*-carbazole (**4b**, FW = 574.00 g/mol, m.p. = 237-239 °C, lit. 239-341 °C [181]) was obtained by the reported procedures [72,175]. Off-white solid (3.56 g, 6.20 mmol, yield 89%).

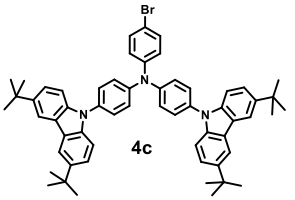

Chemical formula: $C_{58}H_{60}BrN_3$

4-Bromo-N,N-bis(4-(3,6-di-tert-butyl-9H-carbazol-9-yl)phenyl)aniline (**4c**, FW = 879.04 g/mol) was prepared by Ullmann reaction [72]. Off-white solid (2.00 g, 2.27 mmol, yield 86%). ^{1}H NMR (400 MHz, $CDCl_3$, δ): 8.17 (d, 4H, J = 1.62 Hz), 7.50-7.53 (m, 10H), 7.43 (d, 4H, J = 8.58 Hz), 7.38 (d, 4H, J = 8.50 Hz), 7.21 (d, 2H, J = 8.68 Hz), 1.50 (s, 36H, CH_3-).^{13}C NMR (100 MHz, $CDCl_3$, δ): 145.8, 142.8, 139.3, 133.2, 132.7, 127.7, 126.1, 125.1, 123.6, 123.3, 116.3, 109.2, 34.8 (C−CH_3), 32.0 (CH_3-).

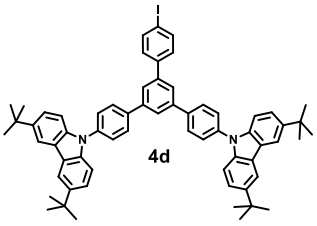

Chemical formula: $C_{64}H_{63}IN_2$

9,9'-(5'-(4-Iodophenyl)-[1,1':3',1''-terphenyl]-4,4''-diyl)bis(3,6-di-tert-butyl-9H-carbazole) (**4d**, FW = 987.13 g/mol) was prepared by Ullmann reaction [72]. Off-white solid (1.57g, 1.59 mmol, yield 63%). ^{1}H NMR (400 MHz, $CDCl_3$, δ): 8.09 (d, 4H, *J* = 1.69 Hz), 7.91 (t, 1H, *J* = 1.66 Hz), 7.86 (d, 4H, *J* = 8.32 Hz), 7.80 (d, 2H, *J* = 1.51 Hz), 7.78 (d, 2H, *J* = 8.38 Hz), 7.62 (d, 4H, *J* = 8.33 Hz), 7.45 (d, 2H, *J* = 8.41 Hz), 7.42 (dd, 4H, *J* = 8.57 Hz, *J* = 1.81 Hz), 7.37 (d, 4H, *J* = 8.58 Hz), 1.38 (s, 36H, CH_3-).^{13}C NMR (100 MHz, $CDCl_3$, δ): 143.1, 142.0, 141.5, 140.5, 139.3, 139.1, 138.1, 137.9, 129.2, 128.7, 127.1, 125.5, 125.0, 123.7, 123.5, 116.3, 109.3, 93.6 (C−I), 34.8 (C−CH_3), 32.0 (CH_3-).

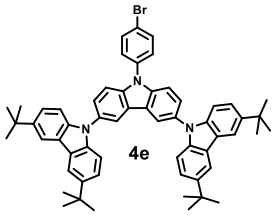

Chemical formula: $C_{58}H_{58}BrN_3$

9'-(4-Bromophenyl)-3,3'',6,6''-tetra-tert-butyl-9'H-9,3':6',9''-tercarbazole (**3a**, FW = 877.03 g/mol) was prepared by Ullmann reaction [72]. Off-white solid (1.80g, 2.05 mmol, yield 78%). ^{1}H NMR (400 MHz, $CDCl_3$, δ): 8.16 (t, 2H, *J* = 1.29 Hz), 8.08 (d, 4H, *J* = 1.61 Hz), 7.76 (d, 2H, *J*=8.63 Hz), 7.55 (d, 2H, *J* = 8.63 Hz), 7.53 (d, 4H, *J* = 1.76 Hz), 7.38 (dd, 4H, *J* =8.67 Hz, *J* = 1.82 Hz), 7.24 (d, 4H, *J* = 8.63 Hz), 1.39 (s, 36H, CH_3-).^{13}C NMR (100 MHz, $CDCl_3$, δ): 142.6, 140.1, 133.6, 128.8, 124.1, 123.6, 123.2, 119.4, 116.2, 109.1, 34.7 (C−CH_3), 32.0 (CH_3-).

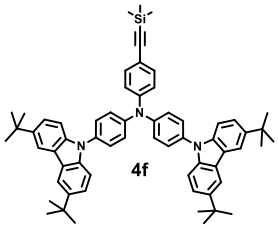

Chemical formula: $C_{63}H_{69}N_3Si$

4-(3,6-Di-tert-butyl-9H-carbazol-9-yl)-N-(4-(3,6-di-tert-butyl-9H-carbazol-9-yl)phenyl)-N-(4-((trimethylsilyl)ethynyl)phenyl)aniline (**4f**, FW = 896.35 g/mol) was obtained by Sonogashira coupling reaction as described in literature [168]. White solid (1.87 g, 2.08 mmol, yield 92%).^{1}H NMR (400 MHz, $CDCl_3$, δ): 8.19 (d, 4H, *J* = 1.62 Hz), 7.49-7.52 (m, 10H), 7.43 (d, 4H, *J* = 8.58 Hz), 7.37 (d, 4H, *J* = 8.50 Hz), 7.20 (d, 2H, *J* = 8.68 Hz), 1.50 (s, 36H, CH_3-), 0.32 (s, 9H, Si−CH_3).^{13}C NMR (100 MHz, $CDCl_3$, δ): 145.8, 142.8, 139.3, 133.2, 132.7, 127.7, 126.1, 125.1, 123.6, 123.3, 116.3, 110.2, 104.0 (C≡C), 96.2 (C≡C), 34.7 (C−CH_3), 32.0 (CH_3-), 0 (Si−CH_3).

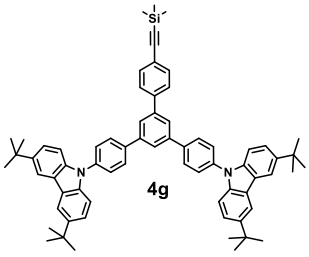

Chemical formula: $C_{69}H_{72}N_2Si$

9,9'-(5'-(4-((Trimethylsilyl)ethynyl)phenyl)-[1,1':3',1''-terphenyl]-4,4''-diyl)bis(3,6-di-tert-butyl-9H-carbazole) (**4g**, FW = 957.43 g/mol) was obtained by Sonogashira coupling reaction as described in literature [168]. White solid (1.38 g, yield 90 %).^{1}H NMR (400 MHz, $CDCl_3$, δ): 8.19 (d, 4H, *J* = 1.41 Hz), 8.01 (t, 1H, *J* = 1.54 Hz), 7.97 (d, 4H, *J* = 8.50 Hz), 7.94 (d, 2H, *J* = 1.62 Hz), 7.77 (d, 2H, *J* = 8.49 Hz), 7.73 (d, 4H, *J* = 8.50 Hz), 7.65 (d, 2H, *J* = 8.50 Hz), 7.52 (dd, 4H, *J* = 8.68 Hz, *J* = 1.87 Hz), 7.47 (d, 4H, *J* = 8.54 Hz), 1.51 (s, 36H, CH_3-), 0.32 (s, 9H, Si−CH_3).^{13}C NMR (100 MHz, $CDCl_3$, δ):143.0, 141.8, 140.8, 139.4, 139.1,

137.8, 132.6, 128.7, 127.1, 127.0, 125.2, 123.7, 123.5, 122.6, 116.3, 109.2, 104.8 (C≡C), 95.3 (C≡C), 34.7 (C−CH_3), 32.0 (CH_3-), 0 (Si−CH_3).

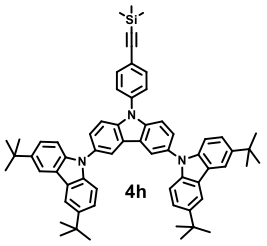

Chemical formula: $C_{63}H_{67}N_3Si$

3,3'',6,6''-Tetra-tert-butyl-9'-(4-((trimethylsilyl) ethynyl)phenyl)-9'H-9,3':6',9''-tercarbazole (**4h**, FW = 894.34 g/mol) was obtained by Sonogashira coupling reaction as described in literature [168]. White solid (1.52 g, 1.69 mmol, yield 87 %).^{1}H NMR (400 MHz, $CDCl_3$, δ): 8.06-8.09 (m, 2H), 8.00 (d, 4H, *J* = 1.45 Hz), 7.64 (d, 2H, *J* = 8.28 Hz), 7.53 (d, 2H, *J* = 8.39 Hz), 7.47 (d, 2H, *J* = 8.61), 7.45 (dd, 2H, *J* = 8.66 Hz, *J*= 1.85 Hz), 7.30 (d, 4H, *J* = 8.58 Hz), 7.18 (d, 4H, *J* = 8.61 Hz), 1.30 (s, 36H, CH_3-), 0.16 (s, 9H, Si−CH_3). ^{13}C NMR (100 MHz, $CDCl_3$, δ): 142.6, 140.1, 137.2, 133.8, 131.2, 126.9, 126.1, 124.1, 123.6, 123.1, 119.3, 116.3, 111.2, 109.1, 104.0 (C≡C), 96.0 (C≡C), 34.9 (C−CH_3), 32.1 (CH_3-), 0 (Si−CH_3).

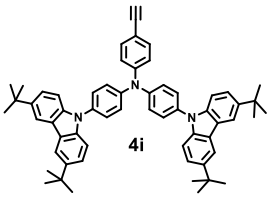

Chemical formula: $C_{60}H_{61}N_3$

4-(3,6-Di-tert-butyl-9H-carbazol-9-yl)-N-(4-(3,6-di-tert-butyl-9H-carbazol-9-yl)phenyl)-N-(4-ethynyl phenyl)aniline (**4i**, FW = 824.17 g/mol) was prepared as described in literature [169]. White solid (1.65 g, 2.00 mmol, yield 96 %).^{1}H NMR (400 MHz, $CDCl_3$, δ): 8.17 (d, 4H, *J* = 1.57 Hz), 7.48-7.54 (m, 10H), 7.44 (d, 4H, *J* = 8.72 Hz), 7.41 (d, 4H, *J* = 8.76 Hz), 7.23 (d, 2H, *J* = 8.70 Hz), 3.77 (s, 1H, C≡C−H), 1.50 (s, 36H, CH_3-).^{13}C NMR (100 MHz, $CDCl_3$, δ): 145.6, 142.9, 139.3, 127.6, 125.6, 123.6, 123.4, 123.1, 116.2, 109.2, 84.3 (C≡C), 68.0 (C≡C), 34.8 (C−CH_3), 32.0 (CH_3-).

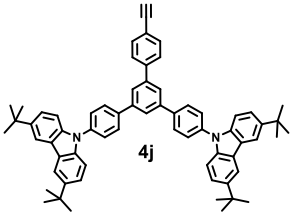

Chemical formula: $C_{66}H_{64}N_2$

9,9'-(5'-(4-Ethynylphenyl)-[1,1':3',1''-terphenyl]-4,4''-diyl)bis(3,6-di-tert-butyl-9H-carbazole) (**4j**, FW = 885.25 g/mol) was prepared as described in literature [169]. Off-white solid (1.13 g, 1.27 mmol, yield 89 %).^{1}H NMR (400 MHz, $CDCl_3$, δ): 8.10 (d, 4H, *J* = 1.34 Hz), 7.92-7.96 (m, 4H), 7.87 (d, 2H, *J* = 8.50 Hz), 7.84 (d, 1H, *J* = 1.52 Hz), 7.69 (d, 2H, *J* = 8.45 Hz), 7.61 (d, 4H, *J* = 8.48 Hz), 7.56 (d, 2H, *J* = 8.26 Hz), 7.40 (dd, 4H, *J* = 8.72 Hz, *J* = 1.84 Hz), 7.38 (d, 4H, *J* = 8.67 Hz), 3.72 (s, 1H, C≡C−H), 1.62 (s, 36H, CH_3-). ^{13}C NMR (100 MHz, $CDCl_3$, δ): 142.6, 141.3, 141.2, 140.8, 138.6, 137.4, 132.3, 128.2, 126.8, 126.4, 124.9, 124.6, 123.4, 122.9, 115.9, 108.9, 82.9 (C≡C), 68.4 (C≡C), 34.3 (C−CH_3), 31.6 (CH_3-).

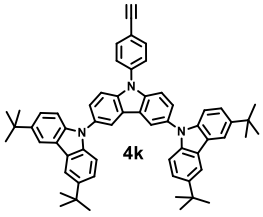

Chemical formula: $C_{60}H_{59}N_3$

3,3'',6,6''-Tetra-tert-butyl-9'-(4-ethynylphenyl)-9'H-9,3':6',9''-tercarbazole (**4k**, FW = 822.15 g/mol) was prepared as described in literature [169]. Off-white solid (1.34 g, 1.63 mmol, yield 92 %).^{1}H NMR (400 MHz, $CDCl_3$, δ): 8.16 (d, 2H, *J* = 1.78 Hz), 8.08 (d, 4H, *J* = 1.67 Hz), 7.75 (d, 2H, *J* = 8.45 Hz), 7.65 (d, 2H, *J* = 8.47 Hz), 7.57 (d, 2H, *J* = 8.61 Hz), 7.53 (dd, 2H, *J* = 8.65 Hz, *J* = 1.98 Hz), 7.38 (dd, 4H, *J* = 8.43 Hz, *J* = 1.91 Hz), 7.25 (d, 4H, *J* = 8.72 Hz), 3.16 (s, 1H, C≡C−H), 1.39 (36H, , CH_3-).^{13}C

NMR (100 MHz, $CDCl_3$, δ): 142.6, 140.1, 139.9, 137.6, 134.0, 131.2, 126.9, 126.1, 124.2, 123.6, 123.1, 121.8, 119.3, 116.2, 111.1, 109.1, 82.7 (C≡C), 78.6 (C≡C), 34.7 (C−CH_3), 32.1 (CH_3-).

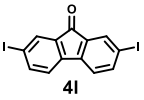

Chemical formula: $C_{136}I_2O$

Diiodo-9*H*-fluoren-9-one (**4l**, FW = 432.00 g/mol, m.p. = 209-211 °C, lit. 209 °C [182]) was synthesized by the reported method [183]. Yellow crystals (5.32 g, 12.3 mmol, yield 67%).

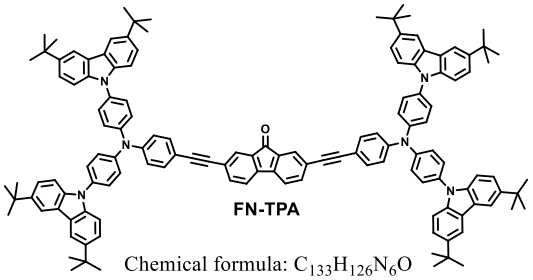

Chemical formula: $C_{133}H_{126}N_6O$

2,7-Bis((4-(bis(4-(3,6-di-tert-butyl-9H-carbazol-9-yl)phenyl)amino) phenyl)ethynyl)-9H-fluoren-9-one (**FN-TPA**, FW = 1824.46 g/mol) was obtained by the similar procedure as compounds **TRZ-BCz**, **TPB-BCz**, **PCz-BCz**. Orange solid (1.16 g, 0.63 mmol, yield 83 %). ^{1}H NMR (700 MHz, $CDCl_3$, δ): 8.07 (d, 8H, *J* = 1.60 Hz), 7.75 (d, 2H, *J* = 0.87 Hz), 7.58 (dd, 2H, *J* = 7.74 Hz, *J* = 1.22 Hz), 7.74-7.76 (m, 12H), 7.42 (dd, 8H, *J* = 8.62 Hz, *J* = 1.78 Hz), 7.35 (d, 8H, *J* = 8.62 Hz), 7.33 (d, 8H, *J* = 8.67 Hz), 7.18 (d, 6H, *J* = 8.59 Hz), 1.40 (s, 72H, CH_3-). ^{13}C NMR (176 MHz, $CDCl_3$, δ): 192.4 (C=O), 147.8, 145.5, 143.1, 142.9, 139.3, 137.7, 134.5, 133.7, 133.0, 127.8, 127.4, 125.7, 124.7, 123.7, 123.3, 123.1, 120.5, 116.6, 116.3, 109.2, 91.7 (C≡C), 88.4 (C≡C), 34.7 (C−CH_3), 32.0 (CH_3-). ATR-FTIR (ν_{max}/cm^{-1}): 3022 (=C−H), 2962 (C−H), 2862, 2240 (C≡C), 1748 (C=O), 1603, 1498 (C=C Ar), 1366, 1302, 1267 (=C−N), 810 (C−H Ar). MALDI-TOF MS (m/z): calculated for $C_{133}H_{126}N_6O$ 1824.46 (M^++H), found 1824.76. Anal. calc. for $C_{133}H_{126}N_6O$: C 87.56; H 6.96; N 4.61; O 0.88; found: C; 87.55; H 6.93; N 4.63; O 0.89.

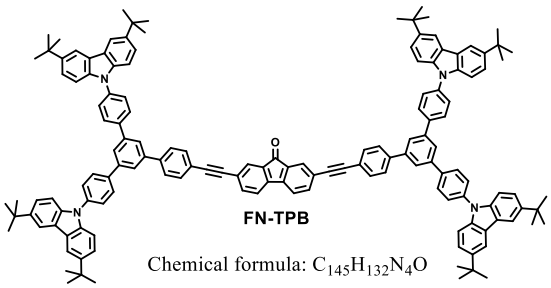

Chemical formula: $C_{145}H_{132}N_4O$

2,7-Bis((4''-(3,6-di-tert-butyl-9H-carbazol-9-yl)-5'-(4-(3,6-di-tert-butyl-9H-carbazol-9-yl) phenyl)-[1,1':3',1''-terphenyl]-4-yl) ethynyl)-9H-fluoren-9-one (**FN-TPB**, FW = 1946.63 g/mol) was obtained by the similar procedure as compounds **TRZ-BCz**, **TPB-BCz**, **PCz-BCz**. Yellow solid (0.73 g, 0.37 mmol, yield 74 %). ^{1}H NMR (700 MHz, $CDCl_3$, δ): 8.09 (d, 8H, *J*= 1.62 Hz), 7.92 (t, 2H, *J* = 1.34 Hz), 7.88 (d, 12H, *J* = 8.26 Hz), 7.79 (d, 2H, *J* = 0.78 Hz), 7.73 (d, 4H, *J* = 8.23 Hz), 7.62-7.65 (m, 14H), 7.47 (d, 2H, *J* = 7.75 Hz), 7.42 (dd, 8H, *J* = 8.62 Hz, *J* = 1.84 Hz), 7.37 (d, 8H, *J* = 8.58 Hz), 1.41 (s, 72H, CH_3-). ^{13}C NMR (176 MHz, $CDCl_3$, δ): 192.2 (C=O), 143.3, 143.0, 141.9, 141.7, 141.1, 139.4, 139.2, 137.9, 137.8, 134.5, 132.3, 128.7, 127.5, 127.4, 127.1, 125.5, 125.2, 124.5, 123.7, 123.5, 122.2, 120.7, 116.3, 109.2, 91.4 (C≡C), 89.6 (C≡C), 34.7 (C−CH_3), 32.0 (CH_3-). ATR-FTIR (ν_{max}/cm^{-1}): 3026 (=C−H), 2967 (C−H), 2862, 2215 (C≡C), 1741 (C=O), 1599, 1465

(C−H Ar), 1366, 1302, 1218 (=C−N), 789 (C−H Ar). MALDI-TOF MS (m/z): calculated for $C_{145}H_{132}N_4O$ 1946.63 (M^++H), found 1945.19. Anal. calc. for $C_{145}H_{132}N_4O$: C 89.46; H 6.84; N 2.88; O 0.82; found: C; 89.45; H 6.87; N 2.87; O 0.81.

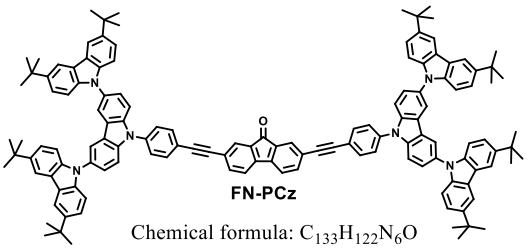

Chemical formula: $C_{133}H_{122}N_6O$

2,7-Bis((4-(3,3'',6,6''-tetra-tert-butyl-9'H-[9,3':6',9''-tercarbazol]-9'-yl)phenyl) ethynyl)-9H-fluoren-9-one (**FN-PCz**, FW = 1819.97 g/mol) was obtained by the similar procedure as compounds **TRZ-BCz**, **TPB-BCz**, **PCz-BCz**. Yellow solid (0.94 g, 0.51 mmol, yield 79 %). ^{1}H NMR (700 MHz, $CDCl_3$, δ): 8.17 (d, 4H, *J* = 1.83 Hz), 8.09 (d, 8H, *J* = 1.64 Hz), 7.84 (d, 2H, *J* = 0.82 Hz), 7.79 (d, 4H, *J* = 8.27 Hz), 7.69 (d, 4H, *J* = 8.49 Hz), 7.67 (d, 2H, *J* = 1.24 Hz), 7.61 (d, 4H, *J* = 8.63 Hz), 7.55 (dd, 4H, *J* = 8.50 Hz, *J* = 1.95 Hz), 7.52 (d, 2H, *J* = 7.61 Hz), 7.38 (dd, 8H, *J* = 8.61 Hz, *J* = 1.83 Hz), 7.27 (d, 8H, *J* = 8.59 Hz), 1.39 (s, 72H, CH_3-). ^{13}C NMR (176 MHz, $CDCl_3$, δ): 192.2 (C=O), 143.5, 142.6, 140.1, 138.0, 137.5, 134.6, 133.5, 131.3, 129.1, 128.2, 127.6, 127.0, 126.1, 124.2, 123.6, 123.2, 122.4, 120.8, 119.4, 116.2, 111.1, 109.1, 90.6 (C≡C), 89.9 (C≡C), 34.7 (C−CH_3), 32.0 (CH_3-). ATR-FTIR (ν_{max}/cm^{-1}): 3021 (=C−H), 2966 (C−H), 2871, 2211 (C≡C), 1742 (C=O), 1549, 1494 (C−H Ar), 1368, 1303, 1218 (=C−N), 808 (C−H Ar). MALDI-TOF MS (m/z): calculated for $C_{133}H_{122}N_6O$ 1819.97 (M^++H), found 1819.02. Anal. calc. for $C_{133}H_{122}N_6O$: C 87.75; H 6.76; N 4.62; O 0.88; found: C; 88.03; H 6.78; N 4.29; O 0.90.

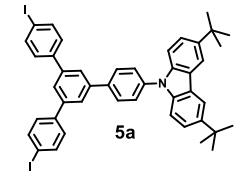

Chemical formula: $C_{44}H_{39}I_2N$

3,6-Di-tert-butyl-9-(4''-iodo-5'-(4-iodophenyl)-[1,1':3',1''-terphenyl]-4-yl)-9H-carbazole (**5a**, FW = 835.61 g/mol) was obtained by Ullmann reaction [72]. Off-white solid (1.03 g, 1.23 mmol, yield 55%). ^{1}H NMR (400 MHz, $CDCl_3$, δ): 8.19 (d, 2H, *J* = 1.42 Hz, Ar), 7.89 (d, 2H, *J* = 8.52 Hz, Ar), 7.87 (d, 3H, *J* = 3.98 Hz, Ar), 7.86 (d, 3H, *J* = 6.25 Hz, Ar), 7.75 (t, 1H, *J* = 1.64 Hz, Ar), 7.69 (d, 2H, *J* = 8.51 Hz, Ar), 7.52 (dd, 2H, *J* = 8.68 Hz, *J* = 1.90 Hz, Ar), 7.49 (d, 4H, *J* = 8.52 Hz, Ar), 7.46 (d, 2H, *J* = 8.58 Hz, Ar), 1.51 (s, 18H, CH_3-).^{13}C NMR (100 MHz, $CDCl_3$, δ): 143.0, 141.9, 141.6, 140.3, 139.2, 139.1, 138.0, 137.9, 129.2, 128.6, 127.0, 125.2, 124.8, 123.7, 123.5, 116.3, 109.2, 93.6 (C–I), 34.8 (C−CH_3), 32.0 (CH_3-).

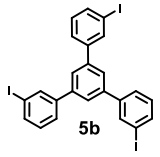

Chemical formula: $C_{24}H_{15}I_3$

1,3,5-Tris(3-iodophenyl)benzene (**5b**, FW = 684.10 g/mol, m.p. = 164-166 °C, lit. 164 °C [184]) were prepared by the electrophilic cyclization according to the known procedure [185]. Off-white crystals (2.00 g, 2.92 mmol, yield 78%).

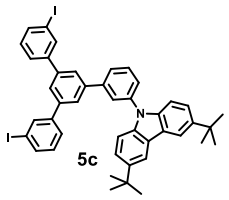

Chemical formula: $C_{44}H_{39}I_2N$

3,6-Di-tert-butyl-9-(3''-iodo-5'-(3-iodophenyl)-[1,1':3',1''-terphenyl]-3-yl)-9H-carbazole (**5c**, FW = 835.61 g/mol) was obtained by Ulmann condensation [72]. Off-white solid (0.46 g, 0.55 mmol, yield 41%). ^{1}H NMR (400 MHz, $CDCl_3$, δ): 8.18 (d, 2H, *J* = 1.65 Hz, Ar), 8.05 (t, 2H, *J* = 1.67 Hz, Ar), 7.89 (t, 1H, *J* = 1.63 Hz, Ar), 7.79 (dd, 2H, *J* = 5.26 Hz, *J* = 1.67 Hz, Ar), 7.75 (d, 3H, *J* = 6.35 Hz, Ar), 7.73 (d, 1H, *J* = 6.24 Hz, Ar), 7.71 (t, 1H, *J* = 1.80 Hz, Ar), 7.66 (dt, 2H, *J* = 7.79 Hz, *J* = 0.98 Hz, Ar), 7.62 (dt, 1H, *J* = 7.69 Hz, *J* = 1.73 Hz, Ar), 7.50 (dd, 2H, *J* = 8.65 Hz, *J* = 1.90 Hz, Ar), 7.44 (d, 2H, *J* = 8.66 Hz, Ar), 7.23 (t, 2H, *J* = 7.86 Hz, Ar), 1.49 (s, 18H, CH_3-).^{13}C NMR (100 MHz, $CDCl_3$, δ): 143.0, 142.9, 142.5, 141.7, 141.1, 139.2, 138.9, 136.7, 136.3, 130.5, 130.3, 126.6, 126.1, 125.9, 125.6, 125.4, 123.7, 123.4, 122.9, 116.3, 109.2, 94.9 (C–I), 34.7 (C−CH_3), 32.0 (CH_3-).

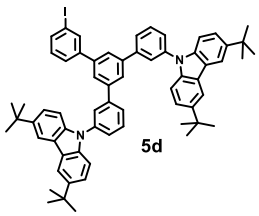

Chemical formula: $C_{64}H_{63}IN_2$

9,9'-(5'-(3-Iodophenyl)-[1,1':3',1''-terphenyl]-3,3''-diyl)bis(3,6-di-tert-butyl-9H-carbazole) (**5d**, FW =987.13 g/mol) was obtained by Ulmann condensation [72]. Off-white solid (0.78 g, 0.79 mmol, yield 68%). ^{1}H NMR (400 MHz, $CDCl_3$, δ): 8.18 (d, 4H, *J* = 1.47 Hz, Ar), 8.06 (t, 1H, *J* = 1.71 Hz, Ar), 7.89-7.91 (m, 2H, Ar), 7.81 (d, 2H, *J* = 1.61 Hz, Ar), 7.78 (dt, 2H, *J* = 7.84 Hz, *J* = 1.35 Hz, Ar), 7.74 (dt, 1H, *J* = 7.84 Hz, *J* = 0.88 Hz, Ar), 7.72 (t, 3H, *J* = 7.72 Hz, Ar)7.66 (dt, 1H, *J* = 7.81 Hz, *J* = 1.00 Hz, Ar), 7.62 (dt, 2H, *J* = 7.75 Hz, *J* = 1.78 Hz, Ar), 7.49 (dd, 4H, *J* = 8.67 Hz, *J* = 1.87 Hz, Ar), 7.44 (d, 4H, *J* = 7.81 Hz, Ar), 7.22 (t, 1H, *J* = 7.81 Hz, Ar), 1.49 (s, 36H, CH_3-).^{13}C NMR (100 MHz, $CDCl_3$, δ): 142.9, 142.6, 141.8, 141.2, 139.3, 138.9, 136.7, 136.2, 130.5, 130.3, 126.6, 126.1, 126.0, 125.6, 125.5, 123.7, 123.4, 116.3, 109.2, 94.9 (C–I), 34.7 (C−CH_3), 32.0 (CH_3-).

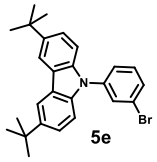

Chemical formula: $C_{26}H_{28}BrN$

9-(3-Bromophenyl)-3,6-di-tert-butyl-carbazole (**5e**, FW = 434.42 g/mol) was prepared as described in literature [186]. Off-white solid (1,56 g, 3.59 mmol, yield 82%).

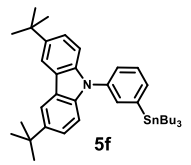

Chemical formula: $C_{38}H_{55}NSn$

3,6-Di-tert-butyl-9-(3-(tributylstannyl)phenyl)-9H-carbazole (**5f**, FW = 645.34 g/mol). To a three-neck round-bottom flask compound **5e** (1.00 g, 2.30 mmol), bis(tri-*n*-butyltin) (1.10 mL, 2.17 mmol) and dry toluene (10 mL) were added, and deoxygenated for 30 min. $Pd(PPh_3)_4$ (0.13 g, 0.11 mmol) was added, and the reaction mixture was heated at 110 °C for 24h. After being cooled down to room temperature, the reaction mixture was neutralized (stirring for 2h) by the addition of the solution of KF (1.50 g) in water (10 mL) to remove the residual tin byproducts. After neutralization, the reaction mixture was extracted with chloroform. After the organic phase was washed with brine three times, dried over anhydrous Na_2SO_4 and

concentrated under reduced pressure, the crude product was purified by the column chromatography on silica gel using hexane as eluent. Colorless oil (0.70 g, 1.08 mmol, yield 41%). ^{1}H NMR (400 MHz, $CDCl_3$, δ): 8.16 (d, 2H, *J* = 1.77 Hz, Ar), 7.64 (dd, 1H, *J* = 9.10 Hz, *J* = 1.79 Hz, Ar), 7.60-7.62 (m, 1H, Ar), 7.56-7.59 (m, 1H, Ar), 7.53 (t, 1H, *J* = 6.03 Hz, Ar), 7.47 (dt, 2H, *J* = 8.70 Hz, *J* = 1.94 Hz, Ar), 7.35-7.39 (m, 2H, Ar), 1.59-1.69 (m, 6H, Sn–CH_2-), 1.49 (s, 18H, CH_3-), 1.28-1.41 (m, 12H, CH_2-), 0.90-0.97 (m, 9H, CH_3-).^{13}C NMR (100 MHz, $CDCl_3$, δ): 144.0, 142.7, 142.6, 139.3, 135.4, 134.9, 134.5, 129.7, 129.0, 128.7, 128.1, 127.1, 126.8, 126.3, 123.5, 123.2, 116.1, 109.2, 34.7, 32.0, 29.1, 17.5, 13.7, 9.7.

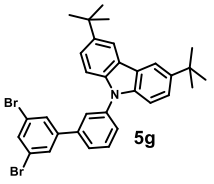

Chemical formula: $C_{32}H_{31}Br_2N$

3,6-Di-tert-butyl-9-(3',5'-dibromo-[1,1'-biphenyl]-3-yl) -9H-carbazole (**5g**, FW = 587.08 g/mol) was obtained by Stille coupling. To a three-neck round-bottom flask 1,3,5-tribromobenzene (0.20 g, 0.63 mmol), compound **5f** (0.42 g, 0.65 mmol) and dry DMF (10 mL) were added, and deoxygenated for 30 min. CuI (0.012 g, 0.06 mmol), KF (0.075 g, 1.29 mmol) and $Pd(PPh_3)_4$ (0.037 g, 0.03 mmol) were added, and the reaction mixture was heated at 80 °C for 24h. After being cooled down to room temperature, the reaction mixture was neutralized (stirring for 2h) by the addition of the solution of KF (1.50 g) in water (10 mL) to remove the residual tin byproducts. After neutralization, the reaction mixture was extracted with chloroform. After the organic phase was washed with brine three times, dried over anhydrous Na_2SO_4 and concentrated under reduced pressure, the crude product was purified by the column chromatography on silica gel using hexane: toluene 10:1 as eluent and precipitation to methanol. White solid (0.25 g, 0.42 mmol, yield 39%). ^{1}H NMR (400 MHz, $CDCl_3$, δ): 8.18 (d, 2H, *J* = 1.47 Hz, Ar), 7.63-7.64 (m, 4H, Ar), 7.59-7.62 (m, 3H, Ar), 7.49 (dd, 2H, *J* = 8.66 Hz, *J* = 1.91 Hz, Ar), 7.38 (d, 2H, *J* = 8.64 Hz, Ar), 1.50 (s, 18H, CH_3-).^{13}C NMR (100 MHz, $CDCl_3$, δ): 142.8, 139.3, 138.2, 133.0, 129.7, 128.9, 126.9, 126.8, 123.6, 123.4, 123.3, 116.2, 109.2, 34.7 (C−CH_3), 32.0 (CH_3-).

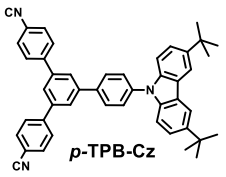

Chemical formula: $C_{46}H_{39}N_3$

5'-(4-(3,6-Di-tert-butyl-9H-carbazol-9-yl)phenyl)-[1,1': 3',1''-terphenyl]-4,4''-dicarbonitrile (***p*-TPB-Cz**, FW = 633.31 g/mol) was obtained by Rosenmund-von Braun reaction (cyanation of arylhalides). In the two-neck round-bottom compound **5a** (0.74 g, 0.89 mmol) was dissolved in DMF (15 mL) under argon atmosphere. After the reaction mixture was heated up to 150 °C, CuCN (0.12 g, 1.33 mmol) was added. The reaction mixture was stirred for 24 h at 150 °C. After being cooled down to room temperature, the reaction mixture was extracted with chloroform. After the organic phase was washed with brine three times, dried over anhydrous Na_2SO_4 and concentrated under reduced pressure, the crude product was purified by the column chromatography on silica gel using hexane: toluene 3:1 as eluent and recrystallization from isopropanol. White crystals (0.42 g, 0.66 mmol, yield 74 %, m.p. = 327-329 °C). ^{1}H NMR (400 MHz, $CDCl_3$, δ): 8.19 (d, 2H, *J* = 1.48 Hz, Ar), 7.96 (d, 2H, *J* = 1.67 Hz, Ar), 7.91 (d, 2H, *J* = 8.52 Hz, Ar), 7.81-7.88 (m, 9H, Ar), 7.73 (d, 2H, *J* = 8.51 Hz, Ar), 7.52 (dd, 2H, *J* = 8.68 Hz, *J* = 1.89 Hz,

Ar), 7.45 (d, 2H, *J* = 8.83 Hz, Ar), 1.51 (s, 18H, CH_3-). ^{13}C NMR (100 MHz, $CDCl_3$, δ):145.0, 143.2, 142.4, 141.0, 139.1, 138.5, 138.1, 132.8, 128.6, 128.0, 127.1, 126.3, 125.3, 123.7, 123.5, 118.7, 116.4, 111.7, 109.1, 34.8 (C−CH_3), 32.0 (CH_3-). ATR-FTIR (ν_{max}/cm^{-1}): 3029 (=C–H), 2958 (C–H), 2862, 2228 (C≡N), 1605, 1522, 1462 (C=C Ar), 1366, 1294, 1258 (=C–N), 816 (C–H Ar). ESI-MS (m/z): calculated for $C_{46}H_{39}N_3$ 633.31 (M^++H), found 633.42. Anal. calc. for $C_{46}H_{39}N_3$: C 87.17; H 6.20; N 6.63; found: C 87.18; H 6.22; N 6.60.

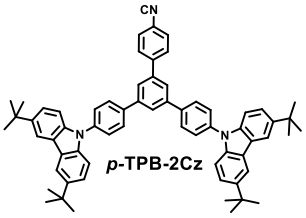

Chemical formula: $C_{65}H_{63}N_3$

4''-(3,6-Di-tert-butyl-9H-carbazol-9-yl)-5'-(4-(3,6-di-tert-butyl-9H-carbazol-9-yl)phenyl)-[1,1':3',1''-terphenyl]-4-carbonitrile (***p*-TPB-2Cz**, FW = 885.50 g/mol) was obtained by Rosenmund-von Braun reaction. White crystals (0.56 g, 0.63 mmol, yield 81 %, m.p. = 368-372 °C). ^{1}H NMR (400 MHz, $CDCl_3$, δ):8.20 (d, 4H, *J* = 1.41 Hz, Ar), 8.08 (t, 1H, *J* = 1.62 Hz, Ar), 7.97 (d, 4H, *J* = 8.52 Hz, Ar), 7.94 (d, 2H, *J* = 1.62 Hz, Ar), 7.92 (d, 2H, *J* = 8.58 Hz, Ar), 7.85 (d, 2H, *J* = 8.56 Hz, Ar), 7.74 (d, 4H, *J* = 8.52 Hz, Ar), 7.53 (dd, 4H, *J* = 8.68 Hz, *J* = 1.88 Hz, Ar), 7.47 (d, 4H, *J* = 8.72 Hz, Ar), 1.51 (s, 36H, CH_3-). ^{13}C NMR (100 MHz, $CDCl_3$, δ): 145.4, 143.1, 142.2, 140.7, 139.1, 139.0, 138.1, 132.8, 128.6, 128.0, 127.1, 126.3, 125.3, 123.7, 123.6, 116.3, 109.2, 34.7 (C−CH_3), 32.0 (CH_3-). ATR-FTIR (ν_{max}/cm^{-1}): 3049 (=C–H), 2954 (C–H), 2859, 2224 (C≡N), 1615, 1528, 1465 (C=C Ar), 1367, 1258 (=C–N), 812 (C–H Ar). ESI-MS (m/z): calculated for $C_{65}H_{63}N_3$ 885.50 (M^++H), found 885.67. Anal. calc. for $C_{65}H_{63}N_3$: C 88.09; H 7.17; N 4.74; found: C 88.06; H 7.19; N 4.75.

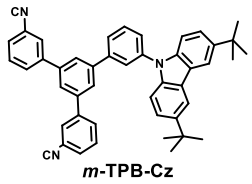

Chemical formula: $C_{46}H_{38}N_3$

5'-(3-(3,6-Di-tert-butyl-9H-carbazol-9-yl)phenyl)-[1,1':3',1''-terphenyl]-3,3''-dicarbonitrile (***m*-TPB-Cz**, WF = 633.31 g/mol) was obtained by Rosenmund-von Braun reaction. White crystals (0.61 g, 0.96 mmol, yield 72 %, m.p. = 245-247 °C). ^{1}H NMR (400 MHz, $CDCl_3$, δ):8.20 (d, 2H, *J* = 1.54 Hz, Ar), 8.00 (t, 2H, *J* = 1.51 Hz, Ar), 7.94 (dt, 2H, *J* = 7.84 Hz, *J* = 1.52 Hz, Ar), 7.90 (t, 1H, *J* = 1.66 Hz, Ar), 7.86 (d, 2H, *J* = 1.67 Hz, Ar), 7.77-7.78 (m, 1H, Ar), 7.76 (t, 1H, *J* = 1.51 Hz, Ar), 7.73 (dt, 2H, *J* = 7.87, *J* = 1.31 Hz, Ar), 7.63 (t, 2H, *J* = 7.62 Hz, Ar), 7.51 (dd, 2H, *J* = 8.65 Hz, *J* = 1.91 Hz, Ar), 7.43 (d, 2H, *J* = 8.68 Hz, Ar), 7.27-7.30 (m, 1H, Ar), 7.19-7.21 (m, 1H, Ar), 1.50 (s, 18H, CH_3-). ^{13}C NMR (100 MHz, $CDCl_3$, δ):143.1, 142.4, 141.9, 141.7, 140.7, 139.2, 139.0, 137.9, 131.7, 131.3, 130.9, 130.5, 129.9, 129.0, 128.2, 126.4, 126.1, 125.9, 125.6, 125.3, 123.7, 123.5, 118.6, 116.4, 113.3, 109.1, 34.8 (C−CH_3), 32.0 (CH_3-). ATR-FTIR (ν_{max}/cm^{-1}): 3053 (=C–H), 2952 (C–H), 2867, 2234(C≡N), 1592, 1583, 1482 (C=C Ar), 1364, 1288, 1262 (=C–N), 807 (C–H Ar). ESI-MS (m/z): calculated for $C_{46}H_{39}N_3$ 633.31 (M^++H), found 633.40. Anal. calc. for $C_{46}H_{39}N_3$: C 87.17; H 6.20; N 6.63; found: C 87.19; H 6.23; N 6.58.

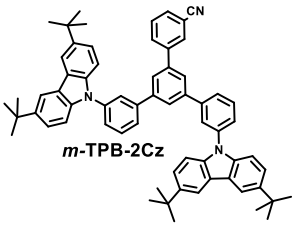

Chemical formula: $C_{65}H_{63}N_3$

3''-(3,6-Di-tert-butyl-9H-carbazol-9-yl)-5'-(3-(3,6-di-tert-butyl-9H-carbazol-9-yl)phenyl)-[1,1':3',1''-terphenyl]-3-carbonitrile (***m*-TPB-2Cz**, FW = 885.50 g/mol) was obtained by Rosenmund-von Braun reaction. White solid (0.62 g, 0.70 mmol, yield 88 %). ^{1}H NMR (400 MHz, $CDCl_3$, δ): 8.19 (d, 4H, *J* = 1.47 Hz, Ar), 8.00 (t, 1H, *J* = 1.46 Hz, Ar), 7.94-7.95 (m, 1H, Ar), 7.91 (t, 2H, *J* = 1.75 Hz, Ar), 7.82 (d, 2H, *J* = 1.61 Hz, Ar), 7.80 (t, 1H, *J* = 1.35 Hz, Ar), 7.78 (t, 1H, *J* = 1.49 Hz, Ar), 7.73 (t, 2H, *J* = 7.74 Hz, Ar), 7.69 (dt, 1H, *J* = 7.79 Hz, *J* = 1.30 Hz, Ar), 7.63 (dt, 2H, *J* = 8.21 Hz, *J* = 1.36 Hz, Ar), 7.60 (t, 1H, *J* = 7.91 Hz, Ar), 7.49 (dd, 4H, *J* = 8.66 Hz, *J* = 1.90 Hz, Ar), 7.43 (d, 4H, *J* = 8.42 Hz, Ar), 1.50 (s, 36H, CH_3-). ^{13}C NMR (100 MHz, $CDCl_3$, δ): 143.1, 142.3, 142.0, 141.7, 140.7, 139.2, 139.0, 137.9, 131.7, 131.3, 130.9, 130.5, 129.9, 129.0, 128.2, 126.5, 126.1, 125.9, 125.6, 125.3, 123.7, 123.5, 118.6, 116.4, 113.3, 109.1, 34.8 (C−CH_3), 32.0 (CH_3-). ATR-FTIR (ν_{max}/cm^{-1}): 3058 (=C–H), 2957 (C–H), 2869, 2239 (C≡N), 1596, 1470 (C=C Ar), 1370, 1256 (=C–N), 803 (C–H Ar). ESI-MS (m/z): calculated for $C_{65}H_{63}N_3$ 885.5 (M^++H), found 886.66. Anal. calc. for $C_{65}H_{63}N_3$: C 88.09; H 7.17; N 4.74; found: C 88.11; H 7.16; N 4.73.

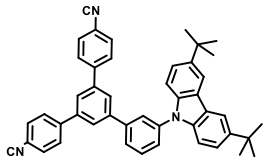

Chemical formula: $C_{46}H_{38}N_3$

5'-(3-(3,6-Di-tert-butyl-9H-carbazol-9-yl)phenyl)-[1,1':3',1''-terphenyl]-4,4''-dicarbonitrile (***p*-TPB-*m*-Cz**, FW = 633.31 g/mol) was obtained by Suzuki coupling similarly to the compound **TPB1**. White crystals (0.32 g, 0.50 mmol, yield 57 %, m.p. = 282-284 °C). ^{1}H NMR (400 MHz, $CDCl_3$, δ): 8.18 (d, 2H, *J* = 1.77 Hz, Ar), 7.88 (d, 1H, *J* = 0.98 Hz, Ar), 7.87 (d, 2H, *J* = 1.66 Hz, Ar), 7.80-7.81 (m, 1H, Ar), 7.79 (d, 6H, *J* = 1.19 Hz, Ar), 7.78 (q, 2H, *J* = 1.76 Hz, Ar), 7.76 (dt, 1H, *J* = 7.76 Hz, *J* = 1.38 Hz, Ar), 7.73 (t, 1H, *J* = 7.54 Hz, Ar), 7.64 (dt, 1H, *J* = 7.51 Hz, *J* = 1.48 Hz, Ar), 7.48 (dd, 2H, *J* = 8.60 Hz, *J* = 1.88 Hz, Ar), 7.41 (d, 2H, *J* = 8.59 Hz, Ar), 1.49 (s, 18H, CH_3-). ^{13}C NMR (100 MHz, $CDCl_3$, δ):144.9, 143.1, 142.3, 141.9, 141.0, 139.2, 139.1, 132.8, 130.5, 128.0, 126.5, 126.4, 125.9, 125.6, 124.4, 123.7, 123.5, 118.7, 116.4, 111.7, 109.1, 34.8 (C−CH_3), 32.0 (CH_3-). ATR-FTIR (ν_{max}/cm^{-1}): 3051 (=C–H), 2950 (C–H), 2868, 2228 (C≡N), 1596, 1495 (C=C Ar), 1367, 1294, 1258 (=C–N), 825 (C–H Ar). ESI-MS (m/z): calculated for $C_{46}H_{39}N_3$ 633.31 (M^++H), found 633.42. Anal. calc. for $C_{46}H_{39}N_3$: C 87.17; H 6.20; N 6.63; found: C 87.19; H 6.19; N 6.62.

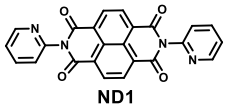

Chemical formula: $C_{24}H_{12}N_4O_4$

2,7-Di(pyridin-2-yl)benzo[lmn][3,8]phenanthroline-1,3,6,8(2H,7H)-tetraone (**ND1**, FW = 420.38 g/mol) [187]. To the suspension of 1,4,5,8-naphthalenetetracarboxylic dianhydride (4.00 g, 15 mmol) in anhydrous pyridine (90 mL) the solution of pyridin-2-amine (3.23 g, 25 mmol) in pyridine (40 mL) was added drop wise. After being stirred at 130 °C for 20 h in nitrogen atmosphere, the reaction mixture was cooled down to room temperature. The off-white precipitate was filtered and washed with distilled water (300 mL), methanol (100 mL) and chloroform (50mL). After drying under reduced pressure the off-white solid was obtained (5.98 g, 14.22 mmol,

yield 96%, m.p. = 474-476 °C). The material was further purified by the two-step vacuum temperature gradient sublimation before the usage. ^{1}H NMR (500 MHz, DMSO-d_6, δ): 8.75 (s, 2H; Ar), 8.68 (d, *J* = 5.61 Hz, 4H; Ar), 8.10 (td, *J* = 7.73 Hz, *J* = 1.70 Hz, 2H; Ar), 7.66 (d, *J*=7.78 Hz, 2H; Ar), 7.61 (d, *J* = 4.96 Hz, 1H; Ar), 7.59 (d, *J* = 4.95 Hz, 1H; Ar). ^{13}C NMR (125 MHz, DMSO-d_6, δ): 162.7, 149.5, 149.1, 138.9, 130.6, 126.8, 124.5, 124.3. ATR-FTIR (ν_{max}/cm^{-1}): 3068 (=C−H), 2970, 2338 (C=N), 1712, 1671 (C=O), 1585, 1430 (C=C Ar), 1368, 1349 (C=N), 1257, 991, 866 (C−H Ar), 782. ESI-MS (m/z): calculated for $C_{24}H_{12}N_4O_4$ 420.38 (M^++H), found 421.20 (M^+). Anal. calc. for $C_{24}H_{12}N_4O_4$: C 68.57; H 2.88; N 13.33; O 15.22; found: C 68.58; H 2.87; N 13.28; O 15.27.

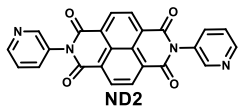
ND2
Chemical formula: $C_{24}H_{12}N_4O_4$

2,7-Di(pyridin-3-yl)benzo[lmn][3,8]phenanthroline-1,3,6,8(2H,7H)-tetraone (**ND2**, FW = 420.38 g/mol) [188] was prepared and purified according to the same procedure as **ND1** starting with (3.52 g, 13 mmol) of 1,4,5,8-naphthalenetetracarboxylic dianhydride. Yellowish solid (5.34 g, 12.77 mmol, yield 97%, m.p. = 441-443 °C). The material was further purified by the two-step vacuum temperature gradient sublimation before the usage. ^{1}H NMR (500 MHz, $CDCl_3$, δ): 8.87 (s, 4H; Ar H), 8.76 (dd, *J* = 4.83 Hz, *J* = 1.48 Hz, 2H; Ar H), 8.64 (d, *J* =2.39 Hz, 2H; Ar H), 7.73 (dd, *J* = 8.06 Hz, *J* = 4.04 Hz, 2H; Ar H), 7.55 (dd, *J* = 8.06 Hz, *J* = 4.85 Hz, 2H; Ar H). ^{13}C NMR (125 MHz, DMSO-d_6, δ): 162.6, 149.8, 149.6, 142.0, 138.4, 130.5, 126.9, 124.0, 113.2, 111.3. ATR-FTIR (ν_{max}/cm^{-1}): 3077 (=C−H), 2968, 2339 (C=N), 1711, 1668 (C=O), 1585, 1427 (C=C Ar), 1371, 1348 (C=N), 1248, 982, 861 (C−H Ar), 783. ESI-MS (m/z): calculated for $C_{24}H_{12}N_4O_4$ 420.38 (M^++H), found 421.20 (M^+). Anal. calc. for $C_{24}H_{12}N_4O_4$: C 68.57; H 2.88; N 13.33; O 15.22; found: C 68.59; H 2.88; N 13.30; O 15.23

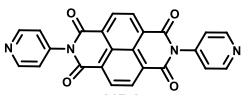
ND3
Chemical formula: $C_{24}H_{12}N_4O_4$

2,7-Di(pyridin-4-yl)benzo[lmn][3,8]phenanthroline-1,3,6,8(2H,7H)-tetraone (**ND3**, FW = 420.38 g/mol) [188] was prepared and purified according to the same procedure as **ND1** starting with (3.51 g, 13.09 mmol) of 1,4,5,8-naphthalenetetracarboxylic dianhydride. Off-white solid (4.35 g, 10.34 mmol, yield 79%, m.p. = 455-457 °C). The material was further purified by the two-step vacuum temperature gradient sublimation before the usage. ^{1}H NMR (500 MHz, DMSO-d_6, δ): 8.80 (d, *J* = 5.77 Hz, 4H; Ar H), 8.74 (s, 4H; Ar H), 7.57 (d, *J* = 5.97 Hz, 4H; Ar H). ^{13}C NMR (125 MHz, DMSO-d_6, δ): 161.7, 157.3, 156.7, 143.4, 136.6, 105.4. ATR-FTIR (ν_{max}/cm^{-1}): 3079 (=C−H), 3044, 2343 (C=N), 1714, 1674 (C=O), 1578, 1451 (C=C Ar), 1346, 1308 (C=N), 1248, 987, 828 (C−H Ar), 782. ESI-MS (m/z): calculated for $C_{24}H_{12}N_4O_4$ 420.38 (M^++H), found 421.20. Anal. calc. for $C_{24}H_{12}N_4O_4$: C 68.57; H 2.88; N 13.33; O 15.22; found: C 68.55; H 2.89; N 13.31; O 15.25.

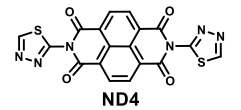
ND4
Chemical formula: $C_{24}H_{12}N_4O_4$

2,7-Di(1,3,4-thiadiazol-2-yl)benzo[lmn][3,8] phenanthroline-1,3,6,8(2H,7H)-tetraone (**ND4**, FW = 433.99 g/mol) was prepared and purified according to the same procedure as **ND1** starting with (3.49 g, 13.02 mmol) of 1,4,5,8-naphthalenetetracarboxylic dianhydride.

Off-white solid (4.75 g, 10.94 mmol, yield 84%). The material was further purified by the two-step vacuum temperature gradient sublimation before the usage. ^{1}H NMR (500 MHz, DMSO-d_6, δ): 9.86 (s, 2H; Ar H), 8.74 (s, 4H; Ar H). ^{13}C NMR (125 MHz, DMSO-d_6, δ): 168.3, 162.7, 162.3, 159.7, 131.7, 131.4, 127.5, 126.8. ATR-FTIR (ν_{max}/cm^{-1}): 3088 (=C−H), 2972, 2923, 2340 (C=N), 1746, 1722, 1686 (C=O), 1589, 1444 (C=C Ar), 1367, 1335 (C=N), 1249, 1143 (=N−N=), 986 (C−H Ar), 782, 760 (=C−S). ESI-MS (m/z): calculated for $C_{18}H_6N_6O_4S_2$ 433.99 (M^++H), found 434.00. Anal. calc. for $C_{18}H_6N_6O_4S_2$: C 49.77; H 1.39; N 19.35; O 14.73; S 14.76; found: C 49.69; H 1.40; N 19.42; O 14.78; S 14.71.

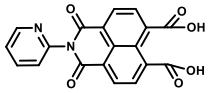

6a
Chemical formula: $C_{24}H_{12}N_4O_4$

1,3-Dioxo-2-(pyridin-2-yl)-2,3-dihydro-1H-benzo[de] isoquinoline-6,7-dicarboxylic acid (**6a**, FW = 362.05 g/mol). To the suspension of 1,4,5,8-naphthalenetetracarboxylic dianhydride (3.50 g, 13.00 mmol) in distilled water (150 mL) 1M KOH solution (3.44 g, 61.33 mL) was added and the reaction mixture was stirred at room temperature until complete dissolution of starting material. The pH was set to 6.3 with a 1M phosphoric acid solution. Pyridine-2-amine (1.23 g, 13.00 mmol) was added and the pH was reset to 6.3 using the 1M phosphoric acid solution. The reaction mixture was stirred at 110 °C overnight. The homogeneous solution was then allowed to come back to room temperature and was then acidified to pH 1–2 with 2M HCl. The off-white precipitate was filtered and washed with distilled water (300 mL), methanol (100 mL). After drying under reduced pressure the off-white solid was obtained (4.00 g, 11.05 mmol, yield 85%). The material was used for further steps without characterization.

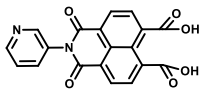

6c
Chemical formula: $C_{24}H_{12}N_4O_4$

1,3-Dioxo-2-(pyridin-3-yl)-2,3-dihydro-1H-benzo [de]isoquinoline-6,7-dicarboxylic acid (**6c**, FW = 362.05 g/mol) was prepared and purified by the same procedure as **6a** starting with (3.51 g, 13.09 mmol) of 1,4,5,8-naphthalenetetracarboxylic dianhydride and used for further steps without characterization. Off-white solid (3.98 g, 11.00 mmol, yield 84%).

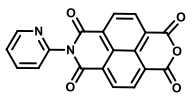

6b
Chemical formula: $C_{19}H_8N_2O_5$

7-(Pyridin-2-yl)-1H-isochromeno[6,5,4-def] isoquinoline-1,3,6,8(7H)-tetraone (**6b**, FW = 344.04 g/mol). The suspension of **6a** (4.00 g, 11.00 mmol) in acetic acid anhydride (100 mL) was stirred at 110 °C for 20 h under nitrogen atmosphere. After being cooled to room temperature, the precipitate was filtered and the crude product was washed with water (300 mL), methanol (100 mL) and chloroform (50 mL). After drying under reduced pressure **6b** was obtained as a the off-white solid (3.30 g, 9.59 mmol, yield 87%). ^{1}H NMR (500 MHz, DMSO-d_6, δ): 8.69-8.71 (m, 4H; Ar H), 8.66 (dd, *J* = 4.87 Hz, *J* = 1.08 Hz, 1H; Ar H), 8.09 (td, *J* = 8.12 Hz, *J* = 1.63 Hz, 1H; Ar H), 7.62 (d, *J* = 8.13 Hz, 1H; Ar H), 7.58 (dd, *J* = 7.37 Hz, *J* = 4.91 Hz, 1H; Ar H). ^{13}C NMR (125 MHz, DMSO-d_6, δ): 160.1, 149.5, 138.9, 131.8, 129.0, 128.6, 127.1, 126.6, 125.6, 124.6, 124.2, 121.8.

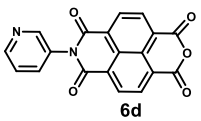

6d

Chemical formula: $C_{19}H_8N_2O_5$

7-(Pyridin-3-yl)-1H-isochromeno[6,5,4-def] isoquinoline-1,3,6,8(7H)-tetraone (**6d**, FW = 344.04 g/mol) was prepared and purified by the same procedure as **6b** starting with (3.98 g, 11.00 mmol) of **6c**. Off-white solid (3.48 g, 10.12 mmol, yield 92%).^{1}H NMR (500 MHz, $CDCl_3$, δ): 8.87 (d, *J* = 1.70 Hz, 4H; Ar H), 8.77 (dd, *J* = 4.87 Hz, *J* = 1.41 Hz, 1H; Ar H), 8.62 (d, *J* = 2.29 Hz, 1H; Ar H), 7.71-7.72 (m, 1H; Ar H), 7.54-7.71 (m, 1H; Ar H). ^{13}C NMR (125 MHz, DMSO-d_6, δ): 158.6, 141.9, 138.8, 137.5, 134.2, 133.4, 131.7, 129.3, 125.2, 124.7, 122.8, 121.4.

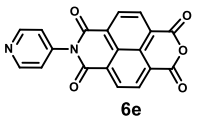

6e

Chemical formula: $C_{19}H_8N_2O_5$

7-(Pyridin-4-yl)-1H-isochromeno[6,5,4-def] isoquinoline-1,3,6,8(7H)-tetraone (**6e**, FW = 344.04 g/mol) was prepared according to the similar procedure as **ND3** with the usage of 1 eq. of pyridine-4-amine. Off-white powder (2.00 g, 5.81 mmol, yield 39%). ^{1}H NMR (500 MHz, DMSO-d_6, δ): 8.81 (d, *J* = 4.88 Hz, 2H; Ar H), 8.71 (d, *J* = 8.12 Hz, 4H; Ar H), 7.55 (d, *J* =5.86 Hz, 2H; Ar H). ^{13}C NMR (125 MHz, DMSO-d_6, δ): 162.6, 159.7, 150.7, 143.6, 143.5, 131.7, 131.6, 130.4, 130.1, 129.1, 127.4, 124.7.

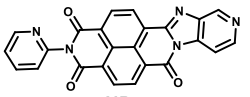

ND5

Chemical formula: $C_{24}H_{11}N_5O_3$

2-(Pyridin-2-yl)benzo[lmn]pyrido[3',4':4,5]imidazo [2,1-b][3,8]phenanthroline-1,3,6(2H)-trione (**ND5**, FW = 417.35 g/mol). Compound **6b** (3.20 g, 9.29 mmol) and pyridin-3,4-diamine (1.30 g, 11.91 mmol) were suspended in anhydrous acetic acid (100 mL) under nitrogen atmosphere and stirred at 120 °C for 20 h. After being cooled down to room temperature, orange particles were filtered and washed with water (300 mL), methanol (100 mL), chloroform (100 mL). The crude product was recrystallized from chloroform and methanol (1:1) mixture, filtered and dried under reduced pressure to afford to orange powder (3.00 g, 7.18 mmol, yield 77%, m.p. = 488-490 °C). The material was further purified by the two-step vacuum temperature gradient sublimation before the usage. ^{1}H NMR (500 MHz, TFA/DMSO-d_6, δ): 9.56-9.60 (m, 1H; Ar H), 9.21 (t, *J* = 2.98 Hz, 2H; Ar H), 9.12-9.16 (m, 2H; Ar H), 8.97-8.99 (m, 2H; Ar H), 8.82-8.86 (m, 2H; Ar H), 8.19-8.23 (m, 1H; Ar H), 8.05-8.08 (m, 1H; Ar H). ^{13}C NMR (125 MHz, TFA/DMSO-d_6, δ): 181.0, 161.5, 161.1, 148.7, 142.3, 137.8, 134.1, 133.6, 133.2, 132.3, 130.4, 128.5, 127.2, 121.9, 121.8, 114.7, 110.1. ATR-FTIR (ν_{max}/cm^{-1}): 3103, 3062 (=C−H), 3021, 2329 (C=N), 1707, 1673 (C=O), 1601, 1578 (C=N), 1548, 1500 (C=C Ar), 1397, 1351, 1328 (C=N), 1282, 1133 (C−N), 989, 889 (C−H Ar), 783. ESI-MS (m/z): calculated for $C_{24}H_{12}N_5O_3$ 417.35 (M^++H), found 417.30. Anal. calc. for $C_{24}H_{11}N_5O_3$: C 69.06; H 2.66; N 16.78; O 11.50; found: C 69.04; H 2.67; N 16.83; O 11.46.

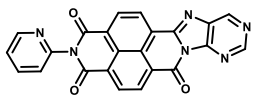

ND6

Chemical formula: $C_{23}H_{10}N_6O_3$

2-(Pyridin-2-yl)benzo[lmn]purino[8,9-b][3,8] phenanthroline-1,3,6(2H)-trione (**ND6**, FW = 418.37 g/mol) was prepared and purified by the same procedure as **ND5** starting with (3.47 g, 10.10 mmol) of **6b**. Yellow powder (3.00 g, 7.17 mmol, yield 71%, m.p. = 441-443 °C). The material was further purified by the two-step vacuum temperature gradient sublimation before the usage. ^{1}H NMR (500 MHz, DMSO-d_6, δ): 9.72 (s, 1H; Ar H),

9.28 (s, 1H; Ar H), 8.71 (d, *J* = 2.38 Hz, 3H; Ar H), 8.45 (d, *J* = 1.08 Hz, 1H; Ar H), 8.21 (d, *J* = 8.78 Hz, 1H; Ar H), 8.10 (td, *J* = 7.72 Hz, *J* = 1.82 Hz, 1H; Ar H), 7.66 (d, *J* = 7.93 Hz, 1H; Ar H), 7.59-7.61 (m, 1H; Ar H). ^{13}C NMR (125 MHz, DMSO-d_6, δ): 181.1, 162.8, 160.3, 159.0, 155.1, 149.5, 138.9, 131.6, 130.7, 130.1, 127.2, 127.0, 126.9, 124.6, 124.5, 114.2. ATR-FTIR (ν_{max}/cm^{-1}): 3057, 3028 (=C−H), 2967, 2337 (C=N), 1713, 1678 (C=O), 1617, 1585 (C=N), 1545 (C=C Ar), 1382, 1348 (C=N), 1282, 1225 (C−N), 990, 887 (C−H Ar), 782. ESI-MS (m/z): calculated for $C_{23}H_{11}N_6O_3$ 418.37 (M^++H), found 418.30. Anal. calc. for $C_{23}H_{10}N_6O_3$: C 66.03; H 2.41; N 20.09; O 11.47; found: C 65.99; H 2.42; N 20.16; O 11.43.

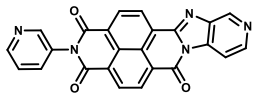

ND7

Chemical formula: $C_{24}H_{11}N_5O_3$

2-(Pyridin-3-yl)benzo[lmn]pyrido[3',4':4,5]imidazo [2,1-b][3,8]phenanthroline-1,3,6(2H)-trione (**ND7**, FW = 417.35 g/mol) was prepared and purified by the same procedure as **ND5** starting with (3.50 g, 10.18 mmol) of **6d**. Orange powder (3.70 g, 8.86 mmol, yield 87%, m.p. = 493-495 °C). The material was further purified by the two-step vacuum temperature gradient sublimation before the usage. ^{1}H NMR (500 MHz, TFA/DMSO-d_6, δ): 9.58 (dd, *J* = 7.70 Hz, *J* = 0.78 Hz, 1H; Ar H), 9.14 (dd, *J* = 6.69 Hz, *J* = 1.68 Hz, 3H; Ar H), 8.99 (dd, *J* = 6.72 Hz, *J* = 1.80 Hz, 2H; Ar H), 8.92 (d, *J* = 5.96 Hz, 1H; Ar H), 8.84 (d, *J* = 5.91 Hz, 1H; Ar H), 8.76 (d, *J* = 7.02 Hz, 1H; Ar H), 8.25 (dd, *J* = 5.87 Hz, *J* = 1.78 Hz, 1H; Ar H), 8.07 (dd, *J* = 6.03 Hz, *J* = 1.92 Hz, 1H; Ar H). ^{13}C NMR (125 MHz, TFA/DMSO-d_6, δ): 181.0, 162.2, 157, 3, 154.9, 147.2, 142.6, 140.8, 137.7, 133.3, 132.2, 130.3, 128.9, 127.1, 125.6, 121.7, 114.7, 110.2. ATR-FTIR (ν_{max}/cm^{-1}): 3059, 3022 (=C−H), 2971, 2336 (C=N), 1705, 1676 (C=O), 1604, 1576 (C=N), 1545, 1500 (C=C Ar), 1395, 1350, 1324 (C=N), 1284, 1229, 1131 (C−N), 988, 882 (C−H Ar), 782. ESI-MS (m/z): calculated for $C_{24}H_{12}N_5O_3$ 417.35 (M^++H), found 417.80. Anal. calc. for $C_{24}H_{11}N_5O_3$: C 69.06; H 2.66; N 16.78; O 11.50; found: C 69.03; H 2.68; N 16.81; O 11.48.

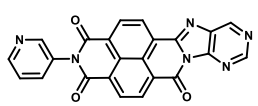

ND8

Chemical formula: $C_{23}H_{10}N_6O_3$

2-(Pyridin-3-yl)benzo[lmn]purino[8,9-b][3,8] phenanthroline-1,3,6(2H)-trione (**ND8**, FW = 418.37 g/mol) was prepared and purified by the same procedure as **ND5** starting with (3.47 g, 10.09 mmol) of **6d**. Yellow powder (3.00 g, 7.17 mmol, yield 71%, m.p. = 458-460 °C). The material was further purified by the two-step vacuum temperature gradient sublimation before the usage. ^{1}H NMR (500 MHz, TFA/DMSO-d_6, δ): 10.10 (d, *J* = 0.97 Hz, 1H; Ar H), 9.63 (d, *J* = 0.88 Hz, 1H; Ar H), 9.40 (d, *J* = 7.69 Hz, 1H; Ar H), 9.18-9.20 (m, 2H; Ar H), 9.03 (t, *J* = 7.69 Hz, 2H; Ar H), 8.94 (d, *J* = 5.91 Hz, 1H; Ar H), 8.76 (d, *J*= 8.97 Hz, 1H; Ar H), 8.27 (dd, *J* = 6.02 Hz, *J* = 1.92 Hz, 1H; Ar H). ^{13}C NMR (125 MHz, TFA/DMSO-d_6, δ): 180.7, 162.0, 160.8, 156.74, 149.1, 143.6, 136.8, 133.9, 132.1, 127.4, 127.0, 125,0, 123.0, 121.7, 114.2, 109.7. ATR-FTIR (ν_{max}/cm^{-1}): 3102, 3061, 3025 (=C−H), 2970, 2331 (C=N), 1711, 1670 (C=O), 1621, 1582 (C=N), 1544 (C=C Ar), 1409, 1386, 1355 (C=N), 1241, 1184 (C−N), 990, 887 (C−H Ar), 765. ESI-MS (m/z): calculated for $C_{23}H_{11}N_6O_3$ 418.37 (M^++H), found 418.00. Anal. calc. for $C_{23}H_{10}N_6O_3$: C 66.03; H 2.41; N 20.09; O 11.47; found: C 65.95; H 2.43; N 20.14; O 11.48.

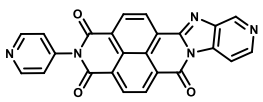

ND9

Chemical formula: $C_{24}H_{11}N_5O_3$

2-(Pyridin-4-yl)benzo[lmn]pyrido[3',4':4,5]imidazo [2,1-b][3,8]phenanthroline-1,3,6(2H)-trione (**ND9**, FW = 417.35 g/mol) was prepared and purified by the same procedure as **ND5** starting with (3.50 g, 10.18 mmol) of **6e**. Orange powder (3.70 g, 8.86 mmol, yield 87%, m.p. = 501-503 °C). The material was further purified by the two-step vacuum temperature gradient sublimation before the usage. ^{1}H NMR (500 MHz, TFA/DMSO-d_6, δ): 9.59 (dd, *J* = 8.22 Hz, *J*=0.81 Hz, 1H; Ar H), 9.22 (t, *J* = 6.00 Hz, 1H; Ar H), 9.15 (dd, *J* = 7.69 Hz, *J* = 1.72 Hz, 2H; Ar H), 9.00 (dd, *J* = 7.66 Hz, *J* = 1.76 Hz, 3H; Ar H), 8.85 (dd, *J*= 5.96 Hz, *J* = 0.81 Hz, 1H; Ar H), 8.26 (d, *J*= 6.92 Hz, 2H; Ar H), 8.07 (dd, *J* = 6 .07 Hz, *J* = 2.08 Hz, 1H; Ar H). ^{13}C NMR (125 MHz, TFA/DMSO-d_6, δ): 180.7, 161.9, 157.3, 151.9, 147.2, 142.2, 137.0, 133.3, 132.1, 128.8, 128.5, 127.1, 125.9, 125.6, 122.2, 116.9, 110.1. ATR-FTIR (ν_{max}/cm^{-1}): 3067, 3030 (=C−H), 2339 (C=N), 1700, 1672 (C=O), 1614, 1595, 1579 (C=N), 1544 (C=C Ar), 1390, 1351, 1311 (C=N), 1280, 1237, 1127 (C−N), 986, 889 (C−H Ar), 766. ESI-MS (m/z): calculated for $C_{24}H_{12}N_5O_3$ 417.35 (M^++H), found 418.20. Anal. calc. for $C_{24}H_{11}N_5O_3$: C 69.06; H 2.66; N 16.78; O 11.50; found: C 69.00; H 2.69; N 16.79; O 11.52.

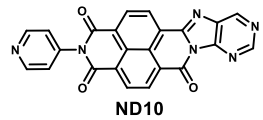

ND10

Chemical formula: $C_{23}H_{10}N_6O_3$

2-(Pyridin-4-yl)benzo[lmn]purino[8,9-b][3,8] phenanthroline-1,3,6(2H)-trione (**ND10**, FW = 418.37 mmol) was prepared and purified by the same procedure as **ND5** starting with (3.22 g, 9.37 mmol) of **6e**. Yellow powder (2.94 g, 7.03 mmol, yield 75%, m.p. = 400-402 °C). The material was further purified by the two-step vacuum temperature gradient sublimation before the usage. ^{1}H NMR (500 MHz, TFA/DMSO-d_6, δ): 10.04 (s, 1H; Ar H), 9.55 (d, *J* = 6.64 Hz, 1H; Ar H), 9.34 (d, *J* = 7.70 Hz, 1H; Ar H), 9.13 (d, *J* = 7.69 Hz, 1H; Ar H), 8.99 (d, *J* = 7.41 Hz, 2H; Ar H), 8.96-9.98 (m , 2H; Ar H), 8.22 (d, *J* = 6.90 Hz, 2H; Ar H). ^{13}C NMR (125 MHz, TFA/DMSO-d_6, δ): 180.6, 161.45, 156.7, 148.4, 142.2, 136.2, 133.9, 132.4, 128.2, 127.2, 127.0, 126.2, 123.1, 121.7, 116.9, 110.1. ATR-FTIR (ν_{max}/cm^{-1}): 3101, 3058, 3027 (=C−H), 2332 (C=N), 1705, 1683 (C=O), 1615, 1586 (C=N), 1543 (C=C Ar), 1406, 1384, 1348 (C=N), 1243, 1124 (C−N), 991, 891 (C−H Ar), 764. ESI-MS (m/z): calculated for $C_{23}H_{11}N_6O_3$ 418.37 (M^++H), found 418.30. Anal. calc. for $C_{23}H_{10}N_6O_3$: C 66.03; H 2.41; N 20.09; O 11.47; found: C 65.99; H 2.39; N 20.11; O 11.51.

4. RESULTS AND DISCUSSION

4.1. Star-shaped fluorenyl-substituted triazine derivatives

In recent years WOLEDs have been attracting much interest [189]. Generation of white electroluminescence in WOLEDs involves simultaneous emission of light of the three primary colours (red, green and blue) or two complementary colours (e.g. orange and blue) [190]. Solution-processable blue-emitting organic glass-forming materials thin films of which can be obtained by spin coating or casting are particularly attractive. Both polymers and low-molar-mass molecular materials, such as dendrimers and star-burst molecules can be used for the solution processing

[191]. In contrast to polymers, molecular glasses including dendritic ones possess well-defined and monodisperse molecular structures as well as superior chemical purity, which makes them more advantageous in comparison to polymers. Molecules having 1,3,5-triazine as a core have been gathering considerable interest because of their high thermal stability, interesting optical and electrochemical properties [9,192,193,194]. Incorporation of a donor moiety, such as fluorene, into molecules with the electron-deficient triazine core gives an opportunity to obtain materials with interesting photophysical and photoelectrical properties and to decrease the optical band gaps. The influence of linking topologies on the properties of organic semiconductors is of great interest. It is known, that the emission colour and charge transport can be controlled via the degree of conjugation [195]. Twisting of the molecular skeleton, as well as relative planarity of the molecule tailor the band gap and affect the charge mobility [196]. Therefore, in this work, the synthesis and comparative study of the properties of the series of star-shaped derivatives of 2,4,6-triphenyl-1,3,5-triazine and dialkyl fluorene, in which the chromophores are linked via different bridges containing single, double, and triple bonds, are presented, and the influence of the linking topologies on the characteristics of the compounds is discussed.

4.1.1. Synthesis

The synthetic routes to star-shaped derivatives of triazine and fluorene with various linking topologies **TRZ1, TRZ2, TRZ3** are shown in **Scheme 4.1**. Compound **TRZ1** in the ethenyl linkage was utilized, was prepared by the Wittig reaction of ylide **1b** and 9,9-bis(2-ethylhexyl)-9*H*-fluorene-2-carbaldehyde (**1c**). **TRZ2**, in which the chromophores are linked via the single C–C bond, was obtained by the electrophilic cyclization reaction of the aromatic precursor (**1e**). In turn, **TRZ3** in which TRZ and dialkyl fluorene are linked via the ethynyl-containing linkage was obtained by Sonogashira cross-coupling reaction between the iodo-derivative **1h** and 9,9-bis(2-ethylhexyl)-2-ethynyl-9*H*-fluorene (**1g**).

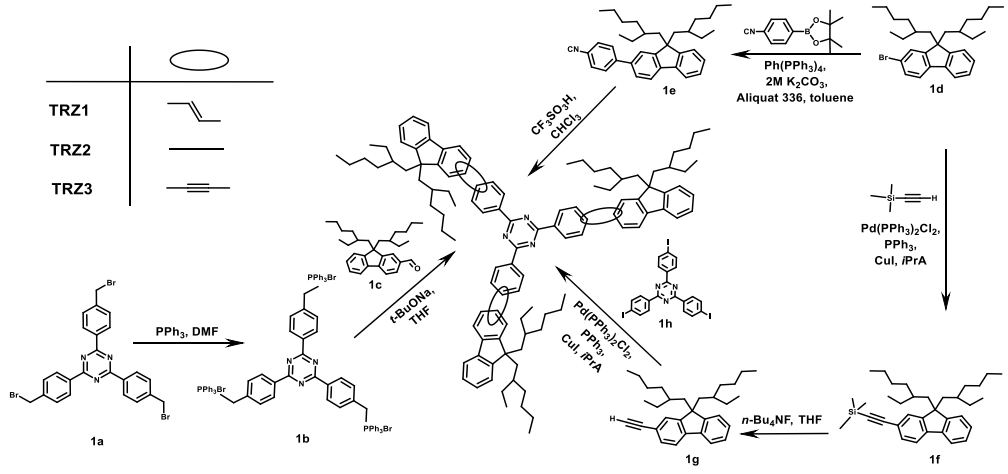

Scheme 4.1. Synthetic routes towards the star-shaped TRZ derivatives

It is known, that the signals of the protons of the *trans*- vinylene groups for TRZ derivatives can be observed around 7.19 ppm in the ^{1}H NMR spectra [7]. In the case of **TRZ1** the signals of protons of the ethenyl groups can probably appear in the interval of 7.24-7.40 ppm, however they overlap with the signals of the protons of the fluorene moiety. The presence of the *E*-isomer can be proven by the evident *trans*-vinylene C−H vibrational peak located at 955 cm^{-1} in the IR spectrum [197].The values of 93.64 and 89.00 ppm in the ^{13}C NMR spectrum of **TRZ3** correspond to the carbon atoms of triple −C≡C− bonds linking the chromophores of this compound. All the synthesized TRZ derivatives exhibit the characteristic signals of carbon atoms of the triazine unit (−C=N−) at ~171 ppm in their ^{13}C NMR spectra.

4.1.2. Theoretical investigation

Due to the electron deficient nature of the TRZ moiety the phenyl rings of the core fragment are efficiently involved into the conjugated system. This ensures planar molecular architecture. Thus, the ground state geometry optimization (**Fig. 4.1 (a)**) shows, that all the synthesized triazine adducts possess a planar central part, whereas the geometry of entire molecules is affected by the usage of various linkages, connecting the core and the side arms. Thus, the compounds with the unsaturated π-bridges, **TRZ1** and **TRZ3**, have planar structure of π-electron systems; meanwhile in **TRZ2** fluorene moieties are twisted with respect of TRZ which results in the reduced conjugation.

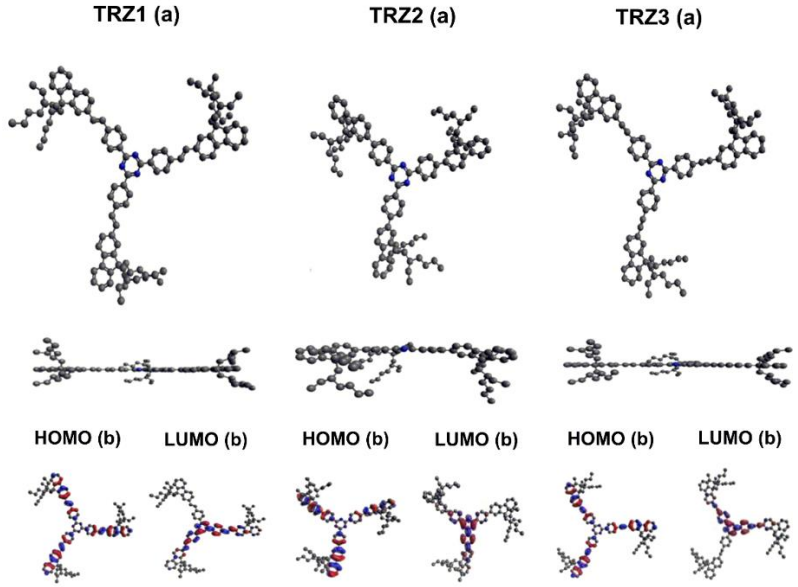

Fig. 4.1. (a) The view on the DFT B3LYP/6-31G(d) optimal structures; (b) TD-DFT B3LYP/6-31+G(d) frontier orbitals of **TRZ1-3**

The different frontier molecular orbitals were studied in order to understand the electronic transitions and charge delocalizations within the synthesized star-shaped derivatives (**Fig. 4.1 (b)**). Comparison of the distribution of electron density in HOMO and LUMO orbitals shows that HOMO→LUMO transition in these

molecules has a typical CT nature from the donor moieties to the acceptor ones. It can also be noted that in this transition the phenyl rings and double or triple bonds are involved. The LUMO has a high distribution density on the electron-accepting TRZ, whereas the HOMOs are dominated by the electron-rich fluorene moieties and by unsaturated conjunctions. Such D–A architecture may ensure separated electron density distribution between the HOMO and LUMO. This separation can provide the efficient hole- and electron-transporting properties [198].

A comparison of the theoretically calculated vertical ionization potentials IP_{vert}, electron affinities EA_{calc} and HOMO/LUMO energies E_{HOMO}, E_{LUMO} (for the molecules in CH_2Cl_2 solutions) was performed (**Table 4.1**) for the better understanding of the electronic energy levels of the triazine derivatives. Evidently, E_{HOMO} and IP_{vert} depend on the nature of the linking topology: the energy of HOMO increases, and, respectively, the IP_{vert} energy decreases in the range **TRZ2**<**TRZ3**<**TRZ1**, indicative of the more efficient conjugation in the molecules with unsaturated bridges, which is more pronounced in the case of **TRZ1** with ethenyl linkage. Similar trends can be observed for E_{LUMO} and EA^{calc}.

Table 4.1. The calculated data for **TRZ1-3**.

Compound	E_{HOMO}[a] [eV]	E_{LUMO}[a] [eV]	E^{calc}_g[b] [eV]	IP_{vert}[c] [eV]	EA_{calc}[c] [eV]
TRZ1	-5.62	-2.55	3.07	6.06	-2.99
TRZ2	-5.93	-2.38	3.55	6.38	-2.83
TRZ3	-5.83	-2.63	3.20	6.23	-3.03

[a] Obtained from the single point calculations by DFT B3LYP/6-311G (d,p) approach for the CH_2Cl_2 solution. [b] Calculated by using equation $E^{calc}_g = \left| E_{HOMO} - E_{LUMO} \right|$. [c] Calculated by the DFT B3LYP/6-311G(d,p) approach for the CH_2Cl_2 solution.

4.1.3. Thermal properties

The thermal properties of compounds **TRZ1**-**TRZ3** were investigated by DSC and TGA (**Table 4.2**). The T_{ID} of the compounds is rather high and comparable (399 to 402 ºC), indicating a minor effect of the linking topology on the thermal stability of the synthesized derivatives of TRZ and fluorene.

Table 4.2. Optical and thermal characteristics of **TRZ-3.**

Compound	T_g[a] [ºC]	T_{ID}[b] [ºC]	Stokes shift[c] [nm]	Stokes Shift[d] [nm]	η_{PL}[e]	τ_1[f] [ns]
TRZ1	61	402	87	52	0.70	0.97
TRZ2	56	399	75	45	0.50	1.02
TRZ3	57	401	71	59	0.53	0.91

[a] Determined by DSC. [b] Determined by TGA.[c] Dilute (10^{-4} M) solutions in THF. [d] Thin solid layers. [e] PLQY determined in 10^{-5}M toluene solutions with a 0.5M NaOH solution of fluoresceine (10^{-5}M, η_{PL}=0.92) as reference. [f] PL decay lifetimes are determined in 10^{-5} M toluene solutions.

All the three derivatives of triazine and fluorene were isolated after the synthesis and purification as amorphous solids. In the first and the following DSC heating scans they showed only glass transitions in the range of 56-61 ºC. The highest T_g of 61 ºC was observed for **TRZ1** utilizing the ethenyl linking bridge. The lowest T_g (56 ºC) was recorded for **TRZ2** in which TRZ and fluorene are linked via single C–C bonds. The slight difference in glass transition temperatures of the

derivatives can be attributed to the difference in self-organization of molecules, which stems from the variety in geometry. Thus, aromatic triazine and fluorene moieties of **TRZ1** and **TRZ3** are conjugated through unsaturated groups, which results in the planar molecular skeleton (**Fig. 4.1**). Due to the usage of single bond, in **TRZ2** fluorene and triazine moieties are twisted by the dihedral angle of 38° and conformationally are more labile than in conjugated molecules **TRZ1** and **TRZ3**. This apparently makes the intramolecular interaction weaker [196,199].

4.1.4. Optical and photophysical properties

UV/Vis and PL spectra of **TRZ1**-**TRZ3** are shown in **Fig. 4.2 (a)**. Two absorption bands around 250-290 and 350-380 nm were observed both for the solutions and the films of all the synthesized derivatives. These bands can be associated with π–π* transitions in triphenyltriazine and fluorene chromophores.

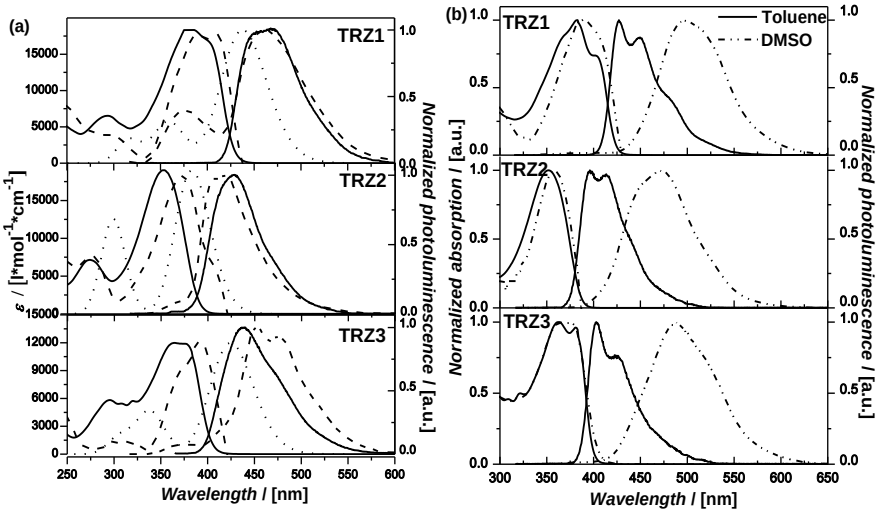

Fig. 4.2. (a) UV/Vis and PL (λ_{ex}=310 nm) spectra of 10^{-5} M solutions in THF (solid lines), thin layer films (dashed lines) and calculated by TD-DFT B3LYP/6-31G(d) method (dot lines); (b) UV/Vis and PL spectra of 10^{-5} M toluene and DMSO solutions of **TRZ1**-**3**

The absorption and emission spectra of **TRZ1** and **TRZ3** are red-shifted with respect to those of **TRZ2**. These observations are in agreement with the results of geometry optimization: **TRZ1** and **TRZ3** have a planar structure of π-electron systems, while in **TRZ2** fluorene moieties are twisted with respect to TRZ (**Fig. 4.1**) which results in the reduced conjugation. Absorption spectra of the neat films of the investigated compounds are broader and red-shifted by 22-27 nm comparing to those of the solutions. This may be attributed to the enhanced intermolecular interactions in the solid state. It should be noted that the long-wave absorption bands of solutions and thin solid films consist of two components. They are expressed more clearly in the spectra of **TRZ1** and **TRZ3**.

Theoretically calculated absorption spectra of **TRZ1**, **TRZ2** and **TRZ3** are bathochromically shifted comparing to the experimental ones (**Fig. 4.2**). The difference between the experimental and the calculated data could probably stem

from the solvation effects for the experimental measurements of UV/Vis spectra and gas-phase for the theoretical calculations [200].

PL spectra of the dilute THF solutions and thin films of the star-shaped compounds do not depend on the excitation wavelength. This observation allows to suggest that the excitation energy can efficiently be transferred from the electron-donating fluorene moieties to the electron-accepting triazine core. The Stokes shifts (**Table 4.2**) deduced for the dilute THF solutions of **TRZ1**, **TRZ2** and **TRZ3** range from 71 nm to 87 nm, while those observed for the thin films are in the range of 45-59 nm. The relatively large Stokes shifts of triazine-based star-shaped molecules in polar solvent (THF) indicates the stabilization of the ICT excited state.

In order to investigate the effect of solvatochromism on the excited state properties of the triazine derivatives UV/Vis and PL spectra of 10^{-5} M toluene, THF and DMSO solutions were compared (**Fig. 4.2 (a, b)**). Solvatochromism is caused by differential solvatation of the ground state and the first excited state of the light-absorbing molecule [201]. **TRZ1**-**TRZ3** exhibit positive solvatochromism, characterized by the bathochromic shift of the emission spectra with the increase of solvent polarity. Thus, the fluorescence spectra of the solutions of the investigated compounds in polar DMSO ($\varepsilon = 46.7$) are red-shifted by 30-48 nm comparing to the spectra of the solutions in less polar THF ($\varepsilon = 7.6$), which are, in turn, red-shifted by 29-42 nm relatively to the spectra of the solutions in non-polar toluene ($\varepsilon = 2.3$). This observation can be explained by the stabilization of the first excited state, compared to the ground state with the increase of the solvent polarity. In turn, the absorption spectra exhibit negligible solvent dependence. These phenomena can be explained by the remarkable changes of the dipole moments of the molecules upon photonic excitation relatively to the dipole moments of ground states, as it was previously shown in the work of J.-W. Wang [202], indicating the CT character of the lowest excited states. The fluorescence spectra of the solutions of all the three triazine derivatives in nonpolar toluene exhibit several low-energy (0.11-0.14 eV) sequence vibronic bands, indicating that emission originates from locally excited states.

The synthesized compounds exhibited moderate PLQYs in the range of 0.50−0.70 (**Table 4.2**). The highest value of 0.70 was observed for **TRZ1**, in which the chromophores are linked via a double bond. This result can be attributed to the fact that **TRZ1** has a completely flat aromatic part (**Fig. 4.1**). The lowest value of PLQY was observed for **TRZ2** ($\eta_{PL} = 0.50$) exploiting the C–C linkage. Thus, fluorescence efficiency of **TRZ1** is higher than that of **TRZ2** due to the presence of extended conjugation via the double bonds of the bridge. In turn, **TRZ3**, in which donor and acceptor units are linked through the ethynyl bridge, displayed the PLQY of 0.53.

Fluorescence decay curves of the dilute solutions of **TRZ1**, **TRZ2** and **TRZ3** can be adequately described by the single exponential functions with χ^2 not exceeding 1.26. Fluorescence lifetime values (**Table 4.2**) were found to be rather short and range from 0.91 to 1.02 ns.

4.1.5. Electrochemical properties

In order to investigate the redox properties of the compounds synthesized CV measurements were performed (**Fig. 4.3**, **Table 4.3**).

All the compounds under consideration undergo irreversible oxidation. The solid state ionization potential energy was estimated from the onset oxidation potential by using the relationship $IP_{SS} = |e|(4.8 + E_{ox}^{onset})$ [203], where the potential is related to that of ferrocenium/ferrocene. The IP_{SS} values are relatively high and range from 5.54 to 6.10 eV. The optical band gap E^{opt}_g values were determined from the onset of $S_0 \rightarrow S_1$ absorption band. The electron affinity EA_{SS} values were obtained by subtraction of the optical band gap from the IP_{SS} using the crude approximation $EA_{SS} = IP_{SS} - E^{opt}_g$ [203]. They were found to be 2.68, 2.35 and 3.00 eV for **TRZ1**, **TRZ2** and **TRZ3,** respectively. The optical band gaps of **TRZ1** and **TRZ3** are smaller, than that of **TRZ2**. These observations are consistent with the geometry optimization data.

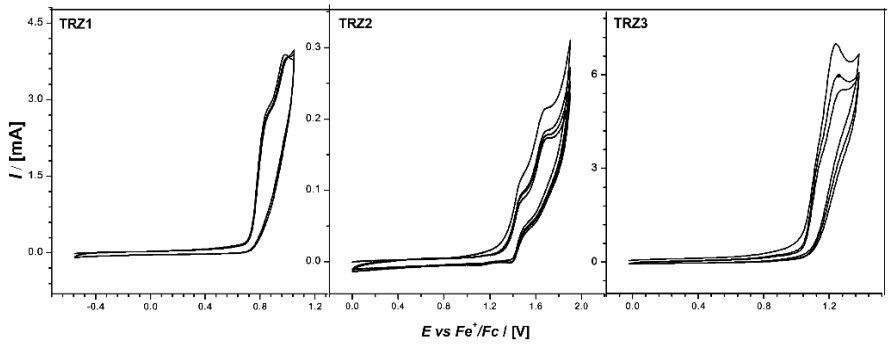

Fig. 4.3. CV curves of **TRZ1-3** measured in dilute CH_2Cl_2 solutions

The values of E_{HOMO}, E_{LUMO}, $E^{calc}_g = |E_{HOMO} - E_{LUMO}|$, vertical electron affinities (EA^{calc}) and ionization potentials (IP^{calc}), calculated by the DFT B3LYP/6-311G(d,p) approach for the CH_2Cl_2 solution (**Table 4.1**), correlate with the experimentally determined values of IP_{SS} and EA_{SS} (**Table 4.3**).

Table 4.3. Electrochemical characteristics of **TRZ1-3.**

Compound	$E_{ox\text{-}Fc+/Fc}^{onset\ a}$ [eV]	IP_{SS} [b][eV]	E^{opt}_g [c][eV]	EA_{SS} [d][eV]
TRZ1	0.74	5.54	2.86	2.68
TRZ2	1.30	6.10	3.75	2.35
TRZ3	1.23	6.03	3.03	3.00

[a] Determined by CV in dilute CH_2Cl_2 solutions. [b] Estimated from the onset oxidation potential by using the relationship $IP_{SS} = |e|(4.8 + E_{ox\ Fc+/Fc}^{onset})$. [c] Determined from the onset of λ_{abs}. [d] Estimated using the approximation $EA_{SS} = IP_{SS} - E^{opt}_g$.

4.1.6. Charge-transporting properties

Charge-transporting properties of the derivatives of TRZ and fluorene were estimated by XTOF and CELIV techniques. XTOF is a non-destructive technique characterized by the absence of the top contact influence and allowing to obtain charge carrier mobility at ethe lectric fields as high as $5 \cdot 10^5$ V/cm [204]. Since the

synthesized materials are promising for the two-electrode device application, we used the CELIV technique for additional investigation of the materials based on the diode structure. In air only the ability to transport holes was detected for the layers of **TRZ1-TRZ3.** The layers of the compounds **TRZ1-TRZ3** are characterized by dispersive hole transport (**Fig. 4.4**). The functional dependence of hole mobility on electric field is defined as $\mu=\mu_0 \cdot exp(\alpha \cdot E^{1/2})$, where μ_0 is zero field mobility, α is the field dependence parameter, and E is the electric field. The zero field hole mobilities for the layers of **TRZ1, TRZ2** and **TRZ3** are $8.8\pm2.3\cdot10^{-6}$, $2.3\pm0.2\cdot10^{-4}$, and $1.2\pm0.4\cdot10^{-8}$ cm^2/V respectively, and the field dependence parameters obtained are $4.9\pm0.3\cdot10^{-3}$, $2\pm0.2\cdot10^{-3}$ and $9.2\pm0.3\cdot10^{-3}$ cm/V, respectively. Hole drift mobilities in the layers of **TRZ1** and **TRZ2** well exceed 10^{-4} $cm^2/V\cdot s$ and approach 10^{-3} $cm^2/V\cdot s$ at high electric fields ($>1\cdot10^6$ V/cm).

From the data of the dark CELIV signals the charge carrier mobilities were calculated by formula $\mu=2d^2/At_{max}^2$, where $A=U(t)/t$ is the voltage rise rate, d is the sample thickness. The values of charge carrier mobility, derived from the dark CELIV experiments, were obtained at electric field $E^{1/2}=(U\cdot t_{max}/t\cdot d)^{1/2}$ (**Fig. 4.4**). The hole mobility values obtained by the dark CELIV technique are in good agreement with the results deduced from XTOF.

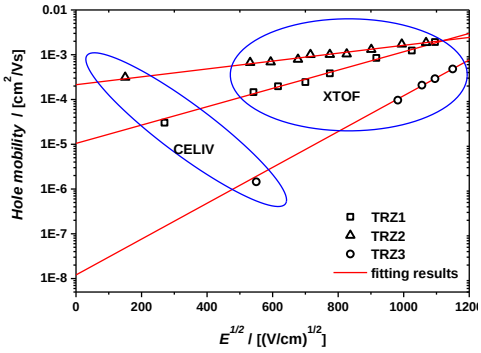

Fig. 4.4. Electric field dependencies of the XTOF and CELIV hole mobility for the layers of **TRZ1-3**

Despite the similarities of the structures of **TRZ1-TRZ3**, the hole mobility values and the field dependencies exhibited differences in the accessible electric field range. The hole mobility values are lower and the field dependence is stronger for **TRZ3** (**Fig. 4.4**). At high electric fields the hole mobility values of **TRZ3** approach those of **TRZ1** and **TRZ2**. The hole mobilities of **TRZ1-TRZ3** are strongly field-dependent. Many recent studies of charge-transporting properties of organic disordered materials were described by a formalism based on disorder, due to the theory of Borsenberger [205]. The formalism is premised on the argument that charge transport occurs by hopping through a manifold of localized states that are distributed in energy. From the point of view of this formalism the field dependence of charge mobility is caused by the difference between the energetic disorder σ and the positional disorder Σ dependent terms. The presence of different linking bridges in **TRZ1, TRZ2** and **TRZ3** containing single, double, and triple bonds apparently

affects energetic disorder σ and leads to the differences in hole mobility values and the field dependences. Free volume effects due to the different bridges containing single, double, and triple bonds in **TRZ1**-**TRZ3** might also be a possible a reason of the difference in charge-transporting properties.

To conclude, three star-shaped triazine-based molecules with fluorene side arms, linked through the linkages containing double, single, and triple bonds, were designed and synthesized. The obtained compounds show high thermal stability with values of T_{ID} reaching 402 °C. The nature of linking topology exerts minor influence on the thermal stability of the triazine derivatives. PL spectra of D–A compounds significantly depend on the solvent polarity, indicating the CT character of the lowest excited states, with the more pronounced character for the molecules with extended conjugation. The dilute solutions of the synthesized compounds are characterized by the single-exponential fluorescence decay transients, short fluorescence lifetimes (0.91-1.02 ns) and relatively high PLQY values (0.50-0.70). The highest PL efficiency was exhibited by the material with ethenyl linkage. Deduced from the CV IP_{SS} values are rather high due to the strong electron accepting nature of the triazine moiety. DFT calculations revealed flat geometry for the molecules with double and triple bond bridges, and twisted geometry for the compound with the C–C linkage. Charge-transporting properties of the triazine derivatives were estimated by the XTOF and CELIV techniques. They are characterized by dispersive hole transport with the values of hole mobility 1.9×10^{-3}, 1.6×10^{-3} and 4.4×10^{-4} $cm^2/V\cdot s$, respectively, at the electric field of 1.15×10^6 V/cm. The data obtained by XTOF method are in good agreement with those recorded by CELIV method. As they possessing such characteristics, the compounds may find application as emitters in the solution-processable fluorescent blue and white OLEDs.

4.2. Star-shaped fluorenyl-substituted triphenylbenzene derivatives

In recent years, the development of blue emitters with high colour purity, high efficiency and a long lifetime has been an extremely challenging research topic [206,207]. Molecules having 1,3,5-triphenylbenzene as a core have been gathering considerable interest because of their high thermal stability, interesting optical and electrochemical properties [208,209]. TPB unit possesses structural C_3 symmetry, as well as a twisted molecular skeleton [210], which makes it an excellent building block for the preparation of dendritic molecules with a wide energy gap and a high triplet energy level [11]. The above mentioned parameters are necessary for the achievement of the efficient blue emission. Apparently, the incorporation of the fluorene moiety also facilitates blue emission [3], since it is known that fluorene-based conjugated oligomers can emit deep blue light with high efficiencies of both solutions and films [4,211].

In this work the synthesis of three star-shaped TPB–based molecules end-capped with alkylated fluorene moieties is presented. The fluorophores in each molecule are connected via various linkages containing single, double and triple bonds. The results of optical, photophysical, electrochemical and computational

studies, which were carried out for the sake of superior understanding of the structure−property relationship of the synthesized compounds, are discussed.

4.2.1. Synthesis

The chemical structures of the synthesized dendritic molecules are presented in **Scheme 4.2**. All the synthesized compounds possess C_3 symmetry achieved by the usage of the TPB core linked to dialkyl fluorene moieties through various linkages.

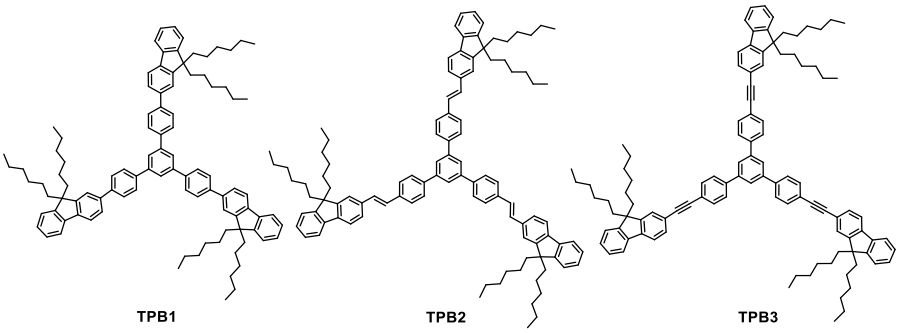

Scheme 4.2. Chemical structures of the star-shaped TPB derivatives

The synthetic approaches to the star-shaped conjugated compounds can comprise convergent and divergent strategies, protecting group techniques and orthogonal techniques [212,213,214]. In our case the divergent strategy for the construction of the dendritic molecules was used (**Scheme 4.3**).

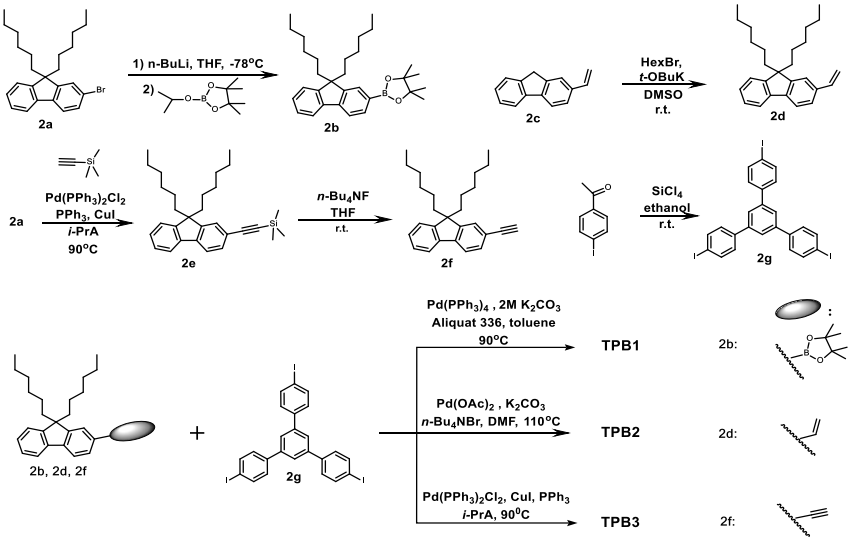

Scheme 4.3. Synthetic routes towards the star-shaped TPB derivatives

The core **2g** was prepared by the acid catalyzed cyclization of the commercially available 1-(4-iodophenyl)ethanone. The functional groups such as 4,4,5,5-tetramethyl-1,3,2-dioxaborolanyl, vinyl and ethynyl present in the

intermediates **2b**, **2d** and **2f** allow the further conversion. Thus, Suzuki-Miyaura reaction of **2b** and **2g** resulted in the formation of star-shaped molecule **TPB1**. Heck cross coupling of the vinyl derivative **2d** and 1,3,5-tris(4-iodophenyl)benzene afforded the desirable compound **TPB2**. Sonogashira reaction of the terminal alkyne **2f** with the iodinated star-shaped core produced the compound **TPB3**.

All the dendritic molecules exhibit the characteristic singlet signal at 7.88 – 7.97 ppm, corresponding to the protons at C-2, C-4 and C-6 positions of TPB core. It is known, that the signals of the protons of the *trans*- vinylene groups for the TPB derivatives can be observed in the region of 7.12 – 7.35 ppm in the ^{1}H NMR spectra [215,216]. In the case of **TPB2** the signals of protons of the ethenyl groups can probably appear in the interval of 7.29-7.39 ppm, however they are overlapped with the signals of the protons of the fluorene moiety. The presence of *E*-isomer can be proven by the evident *trans*-vinylene C−H vibrational peak located at 961 cm^{-1} in the IR spectrum [217]. The values of 91.59 and 89.20 ppm in the ^{13}C NMR spectrum of **TPB3** correspond to the carbon atoms of ethynyl groups linking the chromophores of this compound.

4.2.2. Theoretical investigation

In order to get insight into the structural differences of the TPB derivatives, ground-state geometries of the molecular structures were optimized at the DFT B3LYP/6-31G (d) level of theory (**Fig. 4.5**).

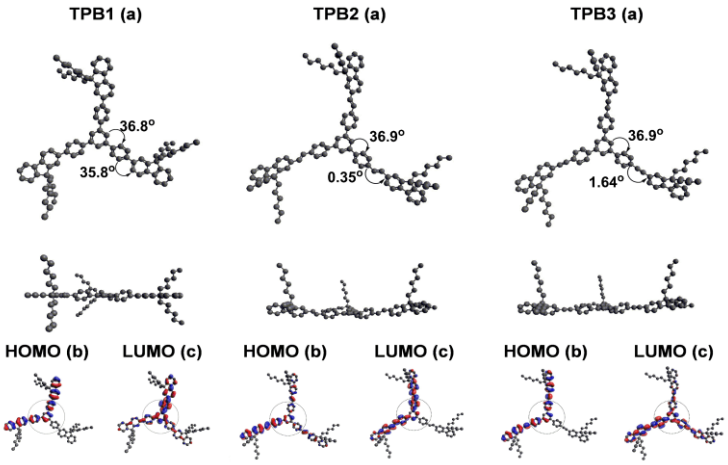

Fig. 4.5. (a) The view on the DFT B3LYP/6-31G(d) optimal structures; (b and c) DFT B3LYP/6-31G(d) frontier orbitals of **TPB1-3**

The molecular structure of the dendritic TPB derivatives is determined by the steric interaction between the *ortho*- hydrogen atoms of the peripheral ring and the hydrogen atoms of the central benzene ring. Therefore, these molecules are found to be propeller-shaped, with dihedral angles between 7 and 49°, depending on the substitution and the packing in the crystal structure [210,218]. All the three synthesized star-shaped molecules possess a propeller-like molecular skeleton with the dihedral angle between benzene rings of the core moiety having the values in the

range of 36.80−36.95° (**Fig. 4.5**). Apparently, DFT calculations revealed that the compounds under consideration exhibit different degree of conjugation, which can be characterized by the dihedral angle between the fluorene and TPB. Thus, it was found out, that the values of dihedral angles are 35.80°, 0.35° and 1.64° for **TPB1**, **TPB2** and **TPB3**, respectively, pointing at the most efficient conjugation in the dendritic molecule with the ethenyl bridge.

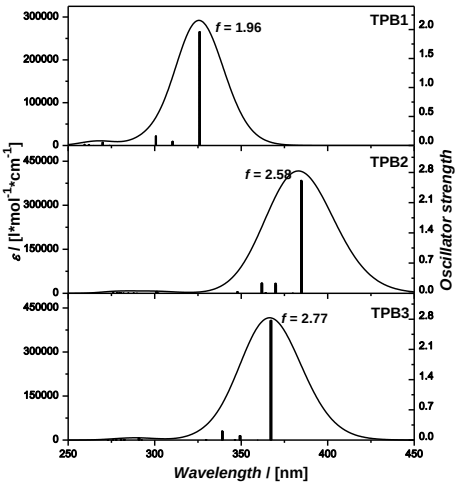

Fig. 4.6. Theoretical UV/Vis spectra of **TPB1-3** with the corresponding oscillator strengths

The frontier molecular orbitals were studied in order to understand the electronic transitions and charge delocalizations within the synthesized star-shaped derivatives (**Fig. 4.5 (b,c)**). The HOMOs and LUMOs of all the compounds are delocalized over TPB and fluorene moieties due to the nonorthogonal orientation of the subunits, indicating the efficient charge transport through the molecules. Delocalization of electrons from the electron-rich fluorene moieties to the core can occur due to the weak accepting strength of TPB and due to the presence of unsaturated bridges, enhancing conjugation. More pronounced electron density separation was observed for the electron-accepting TRZ core [198], where the HOMOs were dominated by the electron-rich fluorene moieties and the LUMOs were located mainly on the central triazine moiety.

Table 4.4. Theoretically calculated, electrochemical and photoelectrical characteristics **TPB1-3**

Compound	E_{HOMO} [a] [eV]	E_{LUMO} [a] [eV]	IP_{vert} [b] [eV]	$E_{ox\ vs\ Fc^+/Fc}$ [c] [eV]	IP_{SS} [d] [eV]	E_g^{opt} [e] [eV]	IP_{EP} [f] [eV]
TPB1	-5.46	-1.26	6.38	0.85	5.65	3.08	5.89
TPB2	-5.17	-1.63	6.05	0.68	5.48	2.50	5.78
TPB3	-5.34	-1.59	6.22	0.87	5.67	2.99	5.83

[a] Calculated by the DFT B3LYP/6-311G(d,p) approach for the CH_2Cl_2 solution. [b] Calculated by the DFT B3LYP/6-311G(d,p) approach in vacuum. [c] Determined by CV in dilute CH_2Cl_2 solutions. [d] Estimated from the onset oxidation potential by using the relationship $IP_{SS} = |e|(4.8 + E_{ox\ vs\ Fc+/Fc}^{onset})$. [e] Determined from the onset of λ_{abs} . [f] Determined by the EP method in air.

Theoretical UV/Vis spectra for compounds **TPB1**-**TPB3** (**Fig. 4.6**) indicate that the absorption maxima at 325, 385 and 367 nm, respectively, are dominated by $S_0 \rightarrow S_1$ electronic transitions. Apparently, the influence of higher excited states on the λ_{max} values is negligible. Evidently, the absorption spectra of **TPB2** and **TPB3** are bathochromically shifted comparing to that of **TPB1**. This observation along with higher oscillator strength values of **TPB2** and **TPB3** indicate the facilitated absorption in the compounds with unsaturated bridges.

For the deeper insight into the energy of electronic levels of the 1,3,5-triphenylbenzene derivatives, the HOMO/LUMO energies were calculated (**Table 4.4**). At the Hartree-Fock (HF) level, Koopmans' theorem suggests that the energy of the HOMO is a good approximation to the negative experimental *IP* [219]. The trends of E_{HOMO} are in good agreement with the geometry optimization results: the value of HOMO energy increases in the range of **TPB1**<**TPB3**<**TPB2**. The calculated E_{LUMO} values are expected to be much more sensitive to the basis set than the corresponding E_{HOMO} values [220]. However, we found that the calculated E_{LUMO} values depend on the nature of the linkage between the chromophores of **TPB1**, **TPB2** and **TPB3** decreasing with the increase of the conjugation length.

The IP_{vert} were found to depend on the structural differences between the molecules, as well. The lowest value was observed for **TPB2** with the most efficient conjugation, while the molecules with single and triple bonds in the linking bridges (**TPB1** and **TPB3**) exhibit higher values of IP_{vert}, indicative of the more difficult hole injection process in these compounds.

4.2.3. Thermal properties

The T_{ID}s of the compounds are rather high and fairly comparable (422–434 °C) (**Table 4.5**). Compounds **TPB2** and **TPB3**, in which TPB core and fluorene side arms are linked through either a double bond or a triple bond, exhibit higher T_{ID} as compared to that of **TPB1**. This observation can apparently be explained by the restriction of the intermolecular rotations in the star-shaped compounds with ethenyl and ethynyl-containing linkages, which leads to better π-π stacking of the molecules and, hence, to the increase of the thermal decomposition temperature.

Table 4.5. Thermal, optical and photophysical characteristics of **TPB1-3**

Compound	T_g [a] [°C]	T_{ID} [b] [°C]	*Stokes shift* [c] [nm]	*Stokes shift* [d] [nm]	η_{PL} [e]	τ_1 [f] [ns]	χ^2 [g]
TPB1	55	422	57	61	0.40	0.67	1.12
TPB2	74	434	36	30	0.54	0.72	1.08
TPB3	75	424	53	61	0.46	0.54	1.13

[a] Determined by DSC. [b] Determined by TGA. [c] Dilute (10^{-5} M) solutions in THF. [d] Thin layers. [e] PLQY determined for 10^{-5}M toluene solutions with a 0.5M NaOH solution of fluorescein (10^{-5}M, η_{PL}=0.92) as reference. [f] PL decay lifetimes determined for 10^{-5} M toluene solutions. [g] Chi-square values.

All the samples were isolated after the synthesis as amorphous powders and showed T_g in the range of 55 and 75 °C. The dependence of T_g on the nature of the bridge, linking the chromophores of the molecules, shows a similar tendency as the temperature of the onset of thermal degradation: more efficient π-π stacking tends to

hinder translational, rotational, and vibrational motions of the molecules and results in the enhancement of T_g [221].

4.2.4. Optical and photophysical properties

All the prepared TPB derivatives show transparency in across wide range of the visible region and intense absorption in the near UV range (**Fig. 4.7 (a)**).

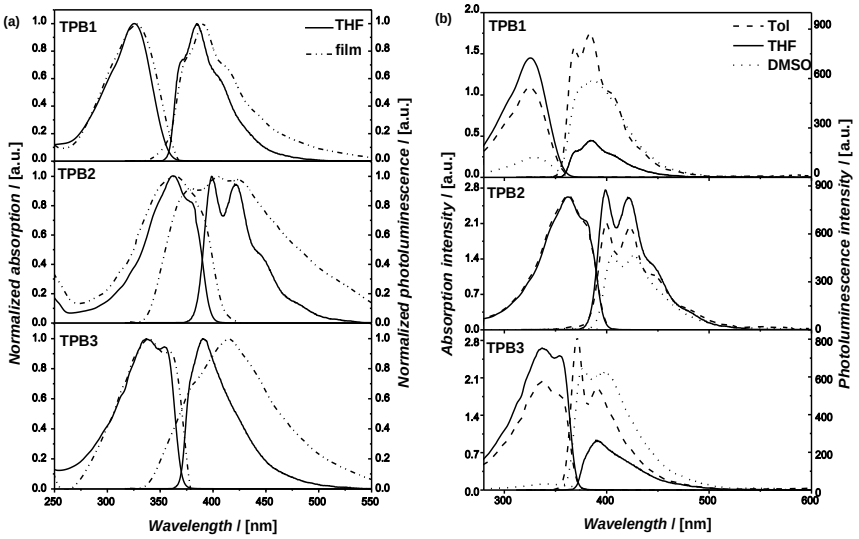

Fig. 4.7. (a) UV/Vis and PL (λ_{ex} = 310 nm) spectra recorded for 10^{-5} M THF solutions and thin films; (b) UV/Vis and PL spectra recorded for 10^{-5} M toluene, THF and DMSO solutions of **TPB1**-**3**

The UV region (<300 nm) of the absorption spectra does not contain any bands that can be attributed to the local excitation of fluorene [222] and TPB [223] units. New unstructured bands present on the longer wavelength side (>300 nm) can be associated with the excited states delocalized over two molecular fragments. The absorption maxima depend mainly on the length of the conjugated arms. As expected, a red shift of the absorption band is observed with the incorporation of the π-conjugated bridges in **TPB2** and **TPB3** [214]. Thus, absorption spectra of the above mentioned molecules are by 36 and 11 nm (for 10^{-5} M THF solutions) and by 48 and 11 nm (for thin films), respectively, red-shifted when compared to **TPB1**. Moreover, the absorption maxima of the spectra of **TPB2** exhibit bathochromic shifts compared to those of **TPB3** (by 25 and 37 nm for the THF solutions and thin films, respectively) indicative of more efficient conjugation in the dendritic molecule with the ethenyl-containing linking bridge. UV/Vis spectra of the solid films are broader and only slightly red-shifted (by 0-12 nm) if compared to the corresponding spectra of the THF solutions suggesting that there is only a little change in molecular conformation in the solid state. Comparing to the experimentally obtained absorption spectra, theoretically calculated ones are slightly red-shifted and lack the vibronic structure. These differences could probably result

from the solvation effects for the experimental measurements of UV/Vis spectra and gas-phase for the theoretical calculations [200].

TPB1, **TPB2** and **TPB3** emit light in the deep blue region with the intensity maxima at 385, 400, 392 nm (for THF solutions) and 389, 406, 412 nm (for the thin films), respectively. The dependence of the PL maxima on the nature of the linking bridge shows a similar tendency as that of the absorption maxima: more efficient conjugation leads to the bathochromic shift of the emission spectra. Interestingly, the PL spectrum of **TPB2** THF solution exhibits a clear vibrational structure with the maxima at 400 nm and 421 nm and a shoulder at 443 nm in contrast to the broad spectra of the solutions of **TPB1** (shoulders at 369 nm and 404 nm) and **TPB3**. This difference in the vibrational structure may arise from the difference in conjugation between the moieties of the star-shaped molecules. **TPB1** and **TPB3**, which possess less efficient conjugation comparing to **TPB2** may have a larger number of possible conformations. In contrast, the arrangement of the 2-styryl-9-dihexylfluorenyl units around the central core means that to the first approximation 2-styryl-9-dihexylfluorenyl units act as three individual chromophores, thus reducing the potential for conformational disorder [171]. In comparison to the spectra of dilute solutions, the PL spectra of the solid films are broader and have a large tail at longer wavelengths, which can apparently be attributed to the emission from excimers that arise from aggregation of chromophores.

All the TPB derivatives under consideration exhibit relatively small values of Stokes shifts both in THF solutions (36 – 57 nm) and thin films (30 – 61 nm) (**Table 4.5**). Interestingly, **TPB2** is characterized by the smallest Stokes shift (36 and 30 nm for the THF solution and thin film, respectively), probably, due to the more rigid skeleton, resulting in the suppressed non-radiative decay process from the excited state and more dominant radiative process [224].

The solvent dependency of the UV/Vis and PL spectra of the synthesized star-shaped compounds was also accessed (**Fig. 4.7 (b)**). Evidently, the absorption intensity of all the three TPB derivatives is the highest in THF (dielectric constant ε_r = 7.6), indicating that the ground state is more stabilized in this solvent [225]. The lowest absorption intensity was observed for the solution in polar DMSO (ε_r = 46.7), due to the large difference in dipole moments of the ground states of **TPB1**, **TPB2** and **TPB3** and the above mentioned solvent. The positions of the absorption bands do not depend on the solvent polarity. Interestingly, the emission shows a drastically different response to the solvent polarity, e.g. the emission intensity of **TPB1** and **TPB3** was found to be the highest in non-polar toluene (ε_r = 2.3) remaining high enough in polar DMSO, as well, indicating the stabilization of the first excited state in these solvents. Apparently, the emission of the compounds with single and triple bonds is quenched in THF. In turn, for **TPB2** only moderate changes of the PL intensity depending on the nature of the solvent were observed, which can be attributed to the CT feature [226]. The PL band shape remains the same. The PL spectra of the solutions of all the three TPB derivatives in nonpolar toluene exhibit several low-energy (0.13-0.17 eV) sequence vibronic bands due to the locally excited states origin of emission. The position of the PL maxima is only slightly affected by the solvent polarity ($\Delta\lambda$ in the range of 1 – 16 nm). This can be

explained by the small lifetimes of the excited molecules (**Table 4.5**), which are responsible for the obstructed reorientation of the solvent molecules preventing the formation of the relaxed excited state with a solvent shell in equilibrium [227].

The star-shaped derivatives showed moderately high PLQYs (0.40, 0.54, 0.46 for **TPB1**, **TPB2**, **TPB3**, respectively) in dilute toluene solutions (**Table 4.5**). The highest value of η_{PL} was observed for **TPB2**, while the lowest value of PLQY (0.40) was observed for **TPB1**, utilizing C–C linkage. Obviously, the increase of the PL efficiency in the range of **TPB1**<**TPB3**<**TPB2** can be attributed to the enhancement of conjugation between the fluorene and TPB moieties.

In order to get an insight into the excited state relaxation processes of the fluorene-end-capped compounds with the TPB core and to determine the governing relaxation pathway, fluorescence decay transients of **TPB1**, **TPB2** and **TPB3** were investigated. Excited state relaxation of the compounds in 10^{-5} M toluene solutions was found to follow the single exponential decay profile with the estimated τ of 0.54−0.72 ns with the values of χ^2 not exceeding 1.13 (**Table 4.5**). The estimated lifetimes are 2 orders of magnitude shorter than that of the unsubstituted TPB [209], indicating the permission of the lowest $S_1 \rightarrow S_0$ transition.

4.2.5. Electrochemical and photoelectrical properties

The redox behaviour of the synthesized TPB based dendritic molecules was examined in 10^{-3}M CH_2Cl_2 solutions by using the CV method (**Fig. 4.8**, **Table 4.4**).

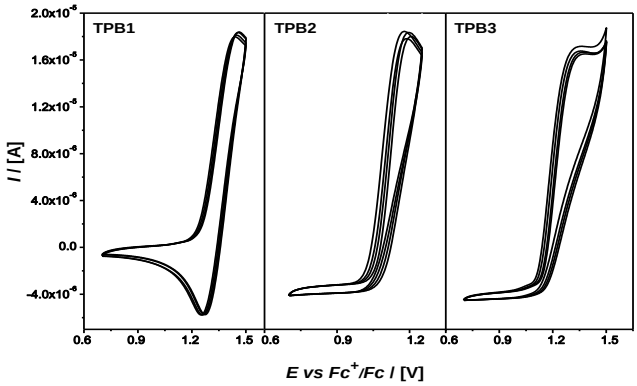

Fig. 4.8. CV curves of **TPB1**, **TPB2** and **TPB3** measured in 10^{-3} M CH_2Cl_2 solutions

TPB1 exhibits quasi-reversible first oxidation potential, while compounds with the prolonged conjugation (**TPB2** and **TPB3**) can be characterized by the irreversible oxidation processes. All the first oxidation potential values fall into the range of 0.68 – 0.87 eV. Evidently, all the synthesized fluorene-end-capped derivatives have a tendency for electropolymerization due to the presence of the unsubstituted C-7 position of the fluorene moieties [228]. The difference in the electrochemical behaviour of the TPB derivatives with various linkages can possibly be attributed to the presence of inclined to oxidation ethenyl and ethynyl bridges [229] in **TPB2** and **TPB3**. The above mentioned linkages can be characterized by

the tense electronic clouds in the bonding orbitals upon oxidation (See section 4.2.2), which, consequently, is responsible for the destabilization of the molecule.

The IP_{SS} (**Table 4.6**) values, estimated by using the relationship $IP_{SS} = |e|(4.8 + E_{ox}^{onset})$ [203], are relatively high and fall in the range of 5.48 – 5.67 eV. As expected, the lowest value of 5.48 eV was found for **TPB2**, utilizing ethenyl π-bridge, due to more efficient conjugation between the fragments of this molecule. In the first and the following CV scans of the TPB derivatives no reduction was observed, which rendered impossible the determination of the *EA* [230]. The optical gap E^{opt}_g values of **TPB2** and **TPB3** (2.50 and 2.99 eV, respectively) were found to be smaller than that of **TPB1** (3.08 eV), indicating the facilitated 0-0 electronic transition between the energy levels of the compounds having the linkages with expanded π-conjugation [231].

Ionization potentials (IP_{EP}) of the solid layers of the synthesized compounds were also estimated by the EP method (**Table 4.4**). IP^{EP} values were found to be rather close and ranged from 5.78 eV to 5.89 eV. Similarly to the results, deduced from CV, the lowest IP^{EP} was observed for **TPB2**, in which the chromophores are linked through the linkages containing double bonds. A small difference observed in the values of ionization potentials obtained by EP and electrochemical studies can be attributed to the difference in molecular interactions and molecular arrangements in thin solid layers and in dilute solutions of these derivatives [232].

The comparison of experimental and theoretical results revealed, that the absolute values of the estimated from CV IP_{SS} and E_{HOMO} are close and comparable. In turn, the ionization potentials IP_{EP} of the solid layers were compared with vertical ionization potentials, theoretically calculated in the framework of the DFT B3LYP/6-311G (d, p) approach. Evidently, the trends of the vertical ionization potentials are similar to those estimated by EP, as well as to the solid state ionization potentials estimated by CV.

4.2.6. Charge-transporting properties

The layers of **TPB1**, **TPB2** and **TPB3** demonstrate low dispersion hole transport and possess the expected scaling of the transit time. The most dispersive hole transport was observed for **TPB3** having utilizing ethynyl linkage. **TPB1-3** showed high hole mobilities as for the low-molar-mass organic semiconductors. **Fig. 4.9** shows the hole mobility plotted versus the square root of the electric field ($E^{1/2}$) at room temperature for the layers of **TPB1**, **TPB2** and **TPB3**. The functional dependence of hole mobility on the electric field is defined as $\mu=\mu_0 \cdot exp(\alpha \cdot E^{1/2})$ (1), where μ_0 is the zero field mobility, α is the field dependence parameter, and E is the electric field. The values of μ_0 and α values are presented in the insert of **Fig. 4.9**. The field dependencies of the hole mobility for **TPB1**, **TPB2** and **TPB3** can be adequately described by Eq (1). For the layers of the compounds clear Poole–Frenkel-type electric field dependent hole mobility was observed. The field dependence parameter was in the range of 0.0037 – 0.0043 $(cm/V)^{1/2}$. For the layers of compounds **TPB1**, **TPB2** and **TPB3** the values of hole mobility were found to be $2.3 \cdot 10^{-3}$, $2.4 \cdot 10^{-3}$ and $4.9 \cdot 10^{-4}$ $cm^2/V \cdot s$ at an electric field of $1 \cdot 10^5$ V/cm, respectively, with the lowest hole mobility values observed for **TPB3**. Such differencies in the

hole mobility values and in the dispersivity of charge transport can be caused by the different intermolecular interactions, such as the π-orbital overlap and/or variation of the relative orientation of the molecules. The hole mobility values were found to be comparable for the layers of **TPB1** and **TPB2** (of the order of 10^{-3} $cm^2/V{\cdot}s$) containing the linking bridges with single and double bonds. The samples of these compounds also displayed similar electric field dependencies, suggesting that the hole transport environment was similar for both materials.

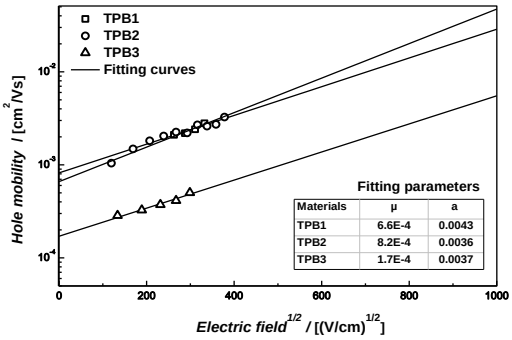

Fig. 4.9. The electric field dependencies of the TOF hole mobilities for the layers of **TPB1**, **TPB2** and **TPB3**. The inserted table shows zero field mobility (μ_0 [$cm^2/V{\cdot}s$]) and the field dependence parameter (α [$cm^{1/2}/V^{1/2}$])

To conclude, three star-shaped TPB-based compounds with fluorene side arms were synthesized and investigated. All the three derivatives are characterized by high values of T_{ID} (422−434°C) and moderately high T_g (55−75°C). The difference in the thermal characteristics of the synthesized compounds is explained by the restriction of the intermolecular rotations in the star-shaped compounds with ethenyl and ethynyl linkages, which leads to the enhancement of the intermolecular interaction, being in agreement with the results of geometry optimization. The star-shaped compounds emit light in the deep blue region and exhibit moderately high PLQYs (0.40 to 0.54). The synthesized molecules undergo irreversible oxidation and are characterized by relatively wide optical gaps (2.50-3.08 eV). The IP_{EP} values (5.8-5.98 eV) are in good agreement with those estimated by CV. All the three dendritic derivatives demonstrate low-dispersion hole transport and high hole mobilities reaching 2.4×10^{-3} $cm^2/V{\cdot}s$ at the electric field of 1×10^5 V/cm. DFT calculations revealed the differences in geometry of the synthesized compounds. The analysis of UV/Vis spectra and oscillation strengths proved that the absorption maxima are dominated by $S_0\rightarrow S_1$ electronic transitions. The comparison of the experimentally estimated *IP* with the calculated values and HOMO/LUMO energies revealed small differences and confirmed the similar dependencies of these parameters on the nature of the linkage between chromophores. Owing to the emission in the deep-blue region, appropriate energy levels, superior thermal characteristics and good charge mobility, the investigated TPB derivatives may be applied to the solution-processable blue fluorescent OLEDs as emitting materials.

4.3. Boomerang-shaped compounds containing bicarbazolyl moieties

It is known, that for the fabrication of efficient optoelectronic devices either fluorescent emitters with high PLQY or phosphorescent noble metal based emitters are desirable. However, in the conventional fluorescent OLEDs light emission originates from the radiative decay of only singlet excitons [86]. According to the spin statistics rule, the maximum IQE of such OLEDs is limited by ca. 25%. Therefore, PhOLEDs, which can efficiently utilize both singlets and triplets, giving an opportunity to realize IQEs up to 100%, have received considerable attention since the pioneering work of Forrest et al. [233,234]. For the sake of higher device efficiency, phosphorescent emitters are generally doped into an organic host matrix. Suitable host materials should possess thermal and electrochemical stability, balanced electron and hole (or ambipolar) charge mobility, high triplet energy relative to emissive phosphors for exciton confinement within the emissive layer and appropriate energy levels matching to cathode/anode for easy charge injection [83]. The requirements of stability, morphology and suitable energy levels should be fulfilled in the development of fluorescent emitters as well. Since homogeneity of the films is of great importance, the choice of compounds with suitable thermal and morphological properties is a challenge for material scientists. Thus, layers based on the small molecules are prone for crystallization, while many conjugated polymers lack a well-defined and monodisperse molecular structure [235]. On the contrary, the properties of dendritic compounds may be controlled through the selection of the core and attached arms. The type of core, in conjunction with the nature and amount of arms, determines the possible symmetry of the resultant compound and, consequently, the resulting characteristics. Thus, by simple variation of the core unit either a fluorescent emitter with high PLQY, or a stable host compound can be obtained.

In the present work the design, synthesis and a wide range of properties of the dendritic boomerang-shaped compounds with bicarbazolyl side arms is discussed. The usage of the novel bicarbazolyl fragment is the reason for the superior thermal and electrochemical stability of the materials, as well as lowering of the ionization potential. The variation of the central nucleus is responsible for the differences in optical and photophysical characteristics. Theoretical computations were carried out in order to gain better understanding of the structure−property relationship of the synthesized compounds.

4.3.1. Synthesis

The chemical structures of the synthesized boomerang-shaped compounds are presented in **Scheme 4.4**. Compounds **TRZ-BCz** and **TPB-BCz**, comprising TRZ and TPB fragments as core, respectively, possess C_3 symmetry, while C_2 symmetry of **PCz-BCz** was achieved by the usage of the PCz moiety.

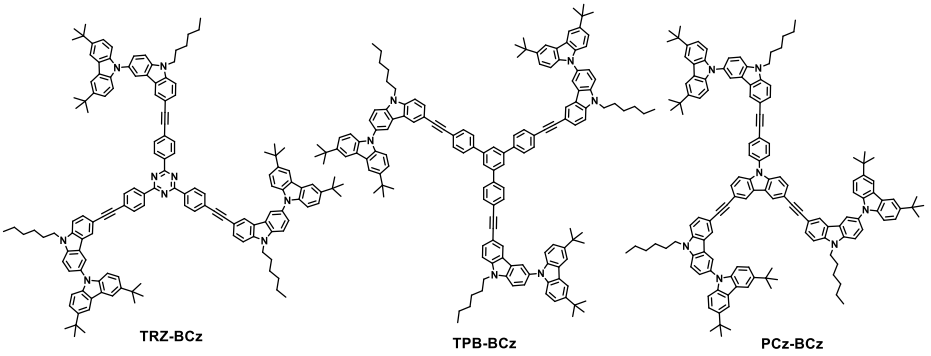

Scheme 4.4. Chemical structures of the boomerang-shaped bicarbazolyl derivatives

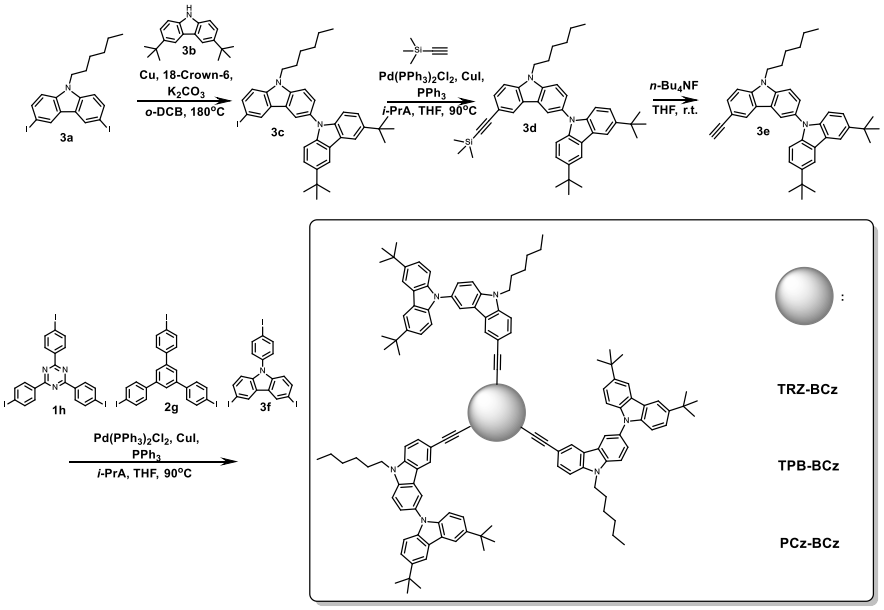

Scheme 4.5. Synthetic routes towards the boomerang-shaped bicarbazolyl derivatives

The divergent strategy was employed for the construction of the boomerang-shaped molecules [212] (**Scheme 4.5**). Firstly, the bicarbazolyl moiety **3c** was constructed from the alkylated carbazole derivatives **3a** and **3b** by using the copper-catalyzed Ullmann reaction conditions [72]. The trimethylsilylethynyl group of precursor **3d**, deprotected in the basic conditions to afford the ethynyl functional group (**3e**), allows the further conversion. The core fragments **1h** and **2g** were obtained by the electrophilic cyclization of the corresponding nitrile and phenylethanone, while the usage of Ullmann reaction followed by the iodination reaction resulted in the central unit **3f**. Hagihara-Sonogashira reaction of the terminal alkyne **3e** with the appropriate iodinated branched core units produced the desirable compounds **TRZ-BCz**, **TPB-BCz** and **PCz-BCz**.

All the boomerang-shaped molecules exhibit the characteristic triplet signal at 4.39-4.42 ppm, corresponding to the protons of the $N-CH_2$ group of the carbazole

moiety. The values in the range of 89.1−93.8 and 83.3−87.9 ppm in the ^{13}C NMR spectra correspond to the carbon atoms of ethynyl groups linking the chromophores of the compounds. The presence of the triple bond can be proved by the evident C≡C vibrational peaks located at 2204−2206 cm^{-1} in the IR spectra.^{13}C NMR spectrum of **TRZ-BCz** contains a characteristic signal at 171.1 ppm indicating the carbons of the triazine core. A singlet peak at 7.85 ppm, corresponding to the protons at C-2, C-4 and C-6 positions of TPB core, can be observed in the ^{1}H NMR spectrum of **TPB-BCz**.

4.3.2. Theoretical investigation

Fig. 4.10 depicts the DFT B3LYP/6-31G(d) optimized geometries of the synthesized target molecules, along with some geometrical parameters.

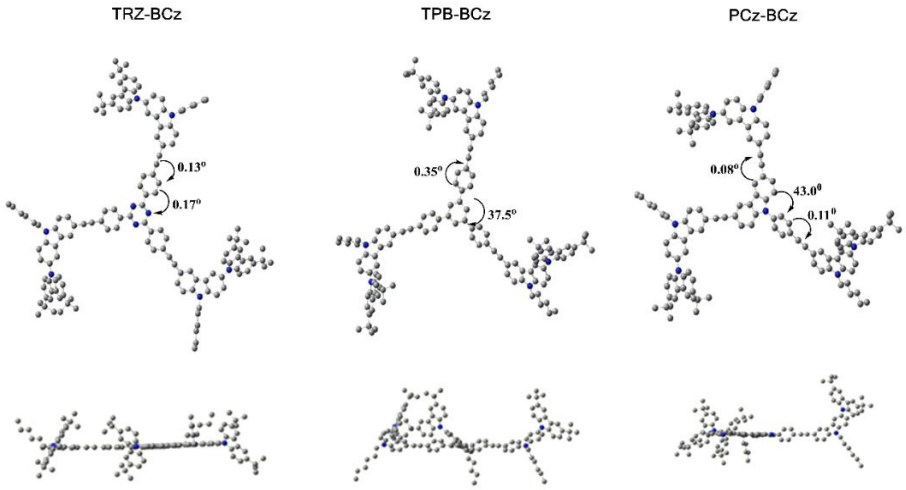

Fig. 4.10. The view on the DFT B3LYP/6-31G(d) optimal structures of **TRZ-BCz**, **TPB-BCz** and **PCz-BCz**

The molecular architectures of the bicarbazolyl derivatives differ considerably due to the usage of various central subunits. Thus, owing to the strong electron accepting nature of the TRZ moiety [236], the central part of **TRZ-BCz** is planar and can be characterized by the small dihedral angle of 0.17° between phenyl rings and the triazine nucleus. In turn, the molecular structure of the dendritic TPB derivatives is controlled by the steric interaction between the *ortho*- hydrogen atoms of the peripheral ring and the hydrogen atoms of the central benzene ring, ensuring the propeller shape [210,237]. In the case of **TPB-BCz** the value of the torsion angle between the benzene rings of the core moiety reaches 37.5°. As for **PCz-BCz**, its molecular skeleton is divided into two parts due to the twisting by 43.0° of the phenyl ring linked to the 9th position of the central carbazole unit. However, because of the additional substituents, causing sterical hindrance, this value of the torsion angle is smaller than that reported for the "naked" PCz (ca 60°) [238]. DFT calculations revealed very small dihedral angles (0.08−0.35°) between the

bicarbazolyl side arms and central cores, reached by the usage of ethynyl moieties, indicating the efficient conjugation between the chromophores.

The differences in the molecular architecture and the nature of the core unit are responsible for the diversity of the electron wave function overlap within the molecule, which can be visualized by the calculation of molecular orbitals. In the case of **TRZ-BCz** HOMO is mainly localized on the bicarbazolyl side arm, while LUMO is located on the electron deficient triazine center (**Fig. 4.11**). A slight overlap of the orbitals can be attributed to the efficient conjugation between the chromophores, achieved due to the usage of the ethynyl spacer. For **TPB-BCz**, containing a weaker electron acceptor, the HOMO orbital is still mainly localized on the side arms, though including ethynyl π-bridge, while LUMO is delocalized through the core and inner carbazole units due to the nonorthogonal orientation of the chromophores. HOMO of **PCz-BCz**, containing the electron-rich PCz moiety, is delocalized through the bicarbazolyl arms and central carbazole moiety, linked by the triple bond, while the electron clouds of LUMO cover the other part of the molecule, twisted by 43°.

A comparison of the theoretically calculated IP_{vert} and HOMO/LUMO energies was performed (**Fig. 4.12 (a)**) for the better understanding of the electronic energy levels of the bicarbazolyl derivatives.

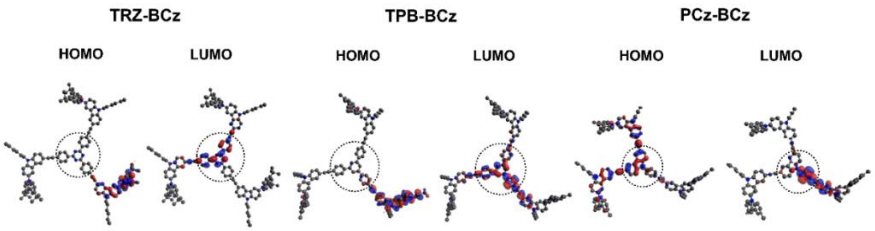

Fig. 4.11. DFT B3LYP/6-31G(d) frontier orbitals of **TRZ-BCz**, **TPB-BCz** and **PCz-BCz**

The absolute values of HOMO energies E_{HOMO} of the compounds were found to be comparable, clearly depending on the nature of the central unit. Thus, **TRZ-BCz** can be characterized by the low laying HOMO at -5.82 eV due to the presence of the electron-withdrawing triazine moiety. However, the usage of the bicarbazolyl fragment raises E_{HOMO} comparing to the fluorenyl-substituted analogue of **TRZ-BCz** [198] owing to the enhancement of the electron-donating ability implying higher electronic delocalization [239]. The values of E_{HOMO} grow with the increase of the donating strength of the core unit in the range **TRZ-BCz**<**TPB-BCz**<**PCz-BCz**, consistently with the analysis of frontier orbitals. The calculated LUMO energy values show a similar trend to those of HOMO. However, the calculation of the E_{LUMO} requires much more complex computational resources (the basis set) than the corresponding E_{HOMO} values [220], therefore some discrepancy with the experimentally estimated electron affinity can be expected. The E_{HOMO} proves to be a good approximation to the negative experimental ionization potential (-*IP*) on the basis of the Koopmans' theorem (HF level) [219]. The values of the calculated vertical ionization potentials IP_{vert} are in good agreement with those of HOMO energy. The lower IP_{vert} values were observed for compounds **TPB-BCz** and **PCz-**

BCz exploiting stronger electron donors than triazine indicative of the more facilitated hole injection process in these compounds.

The theoretical UV/Vis spectra of the compounds **TRZ-BCz**, **TPB-BCz** and **PCz-BCz** (**Fig. 4.12 (b)**) indicate that the absorption region contains bands, typical for molecular fragments forming the multichromophore molecules.

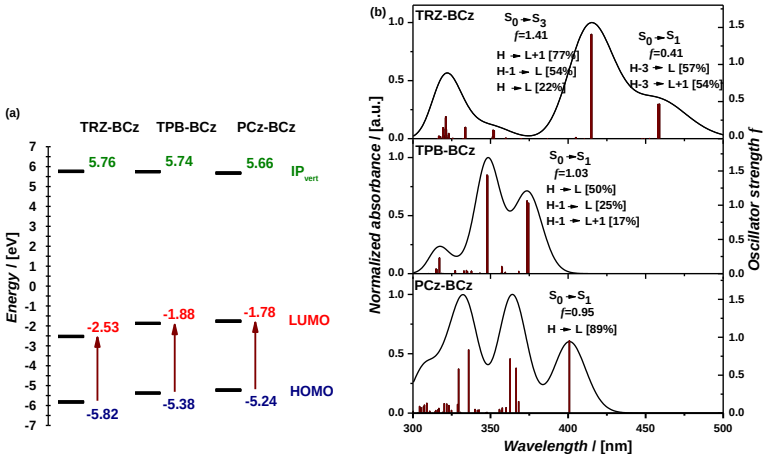

Fig. 4.12. (a) Energy diagram (DFT B3LYP/6-311G(d,p) method); (b) theoretical UV/Vis spectra of **TRZ-BCz**, **TPB-BCz** and **PCz-BCz** with the corresponding oscillator strengths calculated by the TD-DFT B3LYP/6-31G(d) method in vacuum

Higher energy bands (in the range of 309–330 nm) in the spectra of all the compounds under consideration with the moderate values of oscillator strength can be attributed to the local excitation of the carbazole moiety [222,240]. Strongly optically allowed transitions at 347 and 364 nm for **TPB-BCz** and **PCz-BCz**, respectively, can occur, probably, due to the excited states delocalized over the bicarbazolyl moiety. Apparently, this transition is pronounced only as a shoulder at 352 nm in the UV spectrum of **TRZ-BCz**. However, the probability of the low energy transitions varies significantly among the boomerang-shaped compounds with different cores. Transitions from HOMO to LUMO with the high value of oscillator strength (0.95-1.03) contribute mainly to the $S_0 \rightarrow S_1$ excitation of **TPB-BCz** and **PCz-BCz**. In turn, the absorption spectrum of **TRZ-BCz** contains two unstructured bands at 458 and 415 nm, attributed to $S_0 \rightarrow S_1$ and $S_0 \rightarrow S_3$ transitions, respectively. The first broad low-intensity band with the oscillator strength of 0.47 can occur due to the CT states, originating from the electron transfer between the carbazole and triazine moiety [241]. However, mainly HOMO→LUMO+1 and HOMO-1→LUMO processes are involved in this transition, whereas HOMO→LUMO provides only minor contribution of 22%. This observation can probably be explained by the degenerate nature [242] of HOMO, HOMO-1, HOMO-2, on the one hand, and LUMO, LUMO+1, LUMO+2 orbitals, on the other hand, of **TRZ-BCz**. The transition involves outer 3,6-di-*tert*-butyl-carbazole and TRZ fragments, being facilitated by the conjugated 6-ethynyl-9-hexyl-carbazole bridge. Strongly allowed (f = 1.41) transition at 415 nm is contributed by the HOMO-

3→LUMO and HOMO-3→LUMO+1 excitation proving the role of the extended π-delocalization through the inner carbazole moiety and triple bond in the charge transfer process [243].

The influence of the central fragment on the optical properties of the studied compounds can be observed from the location of spectral bands. Thus, the UV spectrum of **TRZ-BCz** is remarkably red-shifted due to the charge transfer when compared to **TPB-BCz**, containing weak acceptor TPB, and donating **PCz-BCz**. In turn, red shift can be observed when comparing the spectra of **TPB-BCz** and **PCz-BCz**, owing to the facilitated n−π^* transition in carbazole-based **PCz-BCz** [244].

4.3.3. Thermal properties

All the three synthesized compounds of the series can be characterized by high T_{ID} ranging from 461 to 475° (**Table 4.6**) demonstrating superior thermal stability, which is common in carbazole-based materials [245]. A slight difference in the values of the T_{ID} can be attributed to the variety in the geometry and molecular architecture (see **Fig. 4.10**). Thus, the restriction of the intermolecular rotations in **TRZ-BCz** leads to better π-π stacking of the molecules and, hence, to the increase of the thermal decomposition temperature [246].

Table 4.6. Thermal, electrochemical and photoelectrical characteristics of **TRZ-BCz**, **TPB-BCz** and **PCZ-BCz**

Compound	T_g [a] [°C]	T_{ID} [b] [°C]	$E^{1/2}_{ox\ vs\ Fc^+/Fc}$ [c] [V]	IP_{SS} [d] [eV]	E_g^{opt} [e] [eV]	IP_{EP} [g] [eV]
TRZ-BCz	96	472	0.55	5.35	2.74	5.48
TPB-BCz	92	461	0.57	5.36	3.18	5.50
PCz-BCz	95	465	0.65	5.45	3.15	5.45

[a]Determined by DSC. [b]Determined by TGA. [c]Determined by CV in dilute CH_2Cl_2 solutions. [d]Estimated from the halfwave oxidation potential by using the relationship $IP_{SS} = |e|(4.8 + E_{ox}^{1/2})$. [e]Determined from the onset of λ_{abs}. [g]Determined from EP spectra.

The DSC analysis revealed only glass transition (92−96 °C) in the first and the following heating scans of the isolated as amorphous solids samples of the bicarbazolyl derivatives (**Table 4.6**). The variation of the central core was found to affect T_g in the similar way as it was observed for T_{ID}: the enhancement of T_g is caused by more efficient π-π stacking hindering translational, rotational, and vibrational motions of the molecules [237].

4.3.4. Optical and photophysical properties

The shape and peak positions of the UV spectra of liquid and solid solutions and of the neat films of **TRZ-BCz**, **TPB-BCz** and **PCz-BCz** are similar (**Fig. 4.13 (a)**). The high energy region contains strongly optically allowed bands assigned to π−π^* excitations within the molecules. In turn, well-expressed shoulder-like peaks at 298 nm can be attributed to the local excitation of carbazole moiety [247]. New unstructured lower energy bands occur due to the excited state delocalization over the whole molecule. Thus, pronounced as shoulder peaks at 332–336 nm for **TPB-BCz** and **PCz-BCz**, and 349–354 nm for **TRZ-BCz**, respectively, can be assigned to the transitions within the bicarbazolyl fragment. The influence of the core nature on

the absorption of the target materials can be observed in the most red-shifted part of the spectra. In the case of **TPB-BCz** and **PCz-BCz**, the absorption bands at 403 nm (hexane solution) can be attributed to the HOMO→LUMO transition contributing mainly to the $S_0 \rightarrow S_1$ excitation, which is consistent with the DFT calculation results (**Fig. 4.15**). **TRZ-BCz** can be characterized by a very broad low intensity band peaked at 429 nm (hexane solution). Due to the electron donating nature of the bicarbazolyl fragment, and, in turn, electron deficient character of triazine, we attribute the long-wavelength band to the CT [241]. The slight red shift of the absorption bands of the neat films can be assigned to the intermolecular interactions [248], which are weaker for **TPB-BCz** and **PCz-BCz** due to the non-planar conformations of the bicarbazolyl fragments preventing close packing of the molecules in films, and stronger for **TRZ-BCz** owing to the incorporation of the TRZ core.

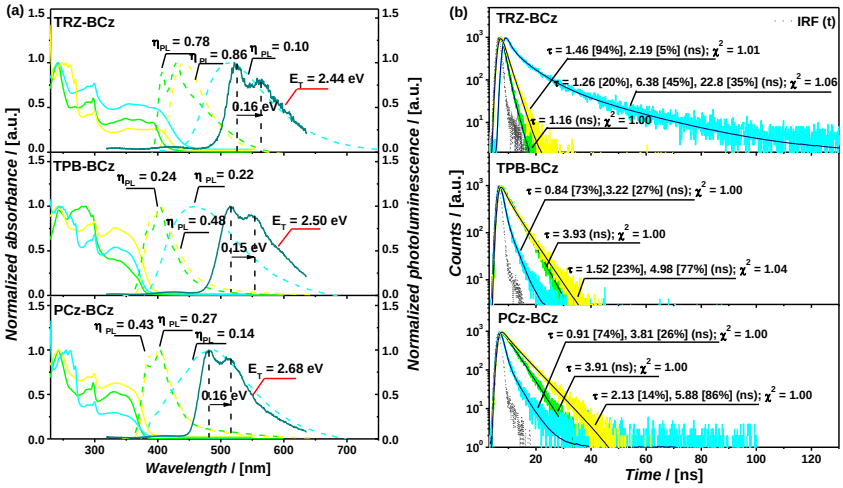

Fig. 4.13. (a) UV/Vis (solid lines) and PL (dashed lines) (λ_{ex} = 330 nm) spectra; (b) PL decay curves of **TRZ-BCz**, **TPB-BCz** and **PCz-BCz** and the instrument response function (IRF(t)), recorded for 10^{-5} M hexane solutions (green), neat films (cyan) and solid solutions in polystyrene (0.25 wt.% of compound) (yellow) and phosphorescence recorded for solid solution in Zeonex (1 wt. % of compound) at 77K (dark cyan solid lines), respectively

In order to eliminate the influence of intermolecular interactions and conformation changes the behaviour of the studied materials upon excitation was investigated in the rigid polymer matrix. However, it was observed that the shape and position of the absorption spectra of the solid PS solutions are similar to those of the liquid ones. Theoretical absorption spectra of **TRZ-BCz**, **TPB-BCz** and **PCz-BCz** are bathochromically shifted comparing to the experimental ones. The difference between the experimental and calculated data probably stems from the solvation effects for the experimental measurements of UV/Vis spectra and the gas-phase for the theoretical calculations [200].

Excitation at 330 nm of the 10^{-5} hexane solutions of the target derivatives resulted in intense blue PL with the intensity maxima peaked at 403−429 nm (**Fig.**

4.13 (a)). Clearly resolved vibronic mode of the PL proves that emission in non-polar hexane originates from locally excited states. Since carbazole and TPB emit in the region below 360 nm [223,249] and TRZ without a D–A structure is not photoluminescent [192], the observed PL bands at 406 and 429 nm for **TRZ-BCz**, 384 and 403 nm for **TPB-BCz** and **PCz-BCz**, respectively, can be attributed to the excitation delocalization over the entire molecules. The PL spectra of compounds **TPB-BCz** and **PCz-BCz**, molecularly dispersed in liquid hexane and solid in PS solutions, are nearly identical. Interestingly, the PL spectrum of **TRZ-BCz** in PS is represented only by a broad unstructured band with no vibronic structure, and is red-shifted comparing to the spectrum of the liquid solution. This observation can probably be explained by the stabilization in the PS medium of the **TRZ-BCz** conformation, facilitating CT from the outer 3,6-di-*tert*-butyl-carbazolyl fragments through the conjugated 6-ethynyl-9-hexyl-carbazolyl bridge to the electron deficient triazine. This phenomenon was not noticed for **TPB-BCz** and **PCz-BCz** due to the stronger donating ability of core moieties in these compounds, which induces more efficient charge delocalization through the molecule. PL spectra of the neat films are remarkably red-shifted and broadened, when compared to those of dilute liquid and solid solutions. A large tail at lower energies can be assigned to the emission from excimers arising from the aggregation of chromophores.

Evaluation of the PLQY revealed the differences between the bicarbazolyl derivatives (**Fig. 4.13 (a)**). Thus, **TRZ-BCz** exhibited the highest PL efficiency of 0.78 in 10^{-5}M hexane solution due to the facilitated by the ethynyl π-bridge CT from carbazole to triazine. In turn, **TPB-BCz** and **PCz-BCz**, showed three-fold lower η_{PL} values (0.24 and 0.27) than triazine-based compound. The quenching of fluorescence of **TPB-BCz** and **PCz-BCz** in the non-polar hexane solution can be attributed to the fast change of conformations due to the twists of the molecular skeleton. Incorporation of the molecules into the rigid PS matrix efficiently suppresses intramolecular rotations in the excited state, hence, providing the possibility of radiative pathways. PLQY for the solid solutions of **TRZ-BCz**, **TPB-BCz** and **PCz-BCz** in PS were found to be enhanced until 0.86, 0.48 and 0.43, respectively. PL efficiency appeared to be remarkably decreased in the neat films of the dendritic compounds, suggesting that non-radiative sites are significantly contributed by the exciton migration and migration-assisted exciton quenching [222]. The strongest PL quenching was observed for **TRZ-BCz** ($\eta = 0.10$) with the planar central aromatic part inclined to intermolecular interactions and aggregations through π–π stacking, while the weakest PL quenching effect was exhibited by the propeller-shaped **TPB-BCz** ($\eta = 0.22$).

The excited state relaxation of 10^{-5} M solutions of bicarbazolyl-armed compounds in hexane was found to follow single exponential decay profiles with the estimated PL lifetimes of 1.16, 3.93 and 3.91 ns for **TRZ-BCz**, **TPB-BCz** and **PCz-BCz**, respectively (**Fig. 4.13 (b)**). A threefold shorter τ of the **TRZ-BCz** solution, as well as the prominently higher PLQY (**Fig. 4.13 (a)**), relative to those of **TPB-BCz** and **PCz-BCz**, indicates the efficient CT and shows that $S_1 \rightarrow S_0$ transition is dominant for **TRZ-BCz**. Radiative and non-radiative decay rate constants [250], Γ and k_{NR} [251], respectively, were evaluated in order to determine the contribution of

radiative and non-radiative processes. Thus, **TRZ-BCz** features the longest Γ of 0.67 ns^{-1}, which is 9.5 times larger than those estimated for **TPB-BCz** and **PCz-BCz**. However, the non-radiative decay rate constants k_{NR} were found to be relatively close for all the studied materials. These observations are consistent with the obtained PL quantum yields for the hexane solutions. The PL transients of the neat films exhibit non-exponential behaviour, pointing out several various origins of the radiative transitions. The decay curves were fairly well described by the triple exponential model in the case of **TRZ-BCz** and double exponential fits for **TPB-BCz** and **PCz-BCz**. This observation, accompanied by the strong bathochromic shift of the PL bands and the reduction of the PL quantum yields, is a clear sign of energy transfer taking place via exciton hopping through the localized states in disordered media such as neat films [252,253]. The neat films of all the investigated compounds feature fast initial excited state decay, which is mainly determined by the migration of the excitation energy in the solid phase facilitating quenching at non-radiative decay sites [254]. Interestingly, the compounds bearing the molecularly twisted weak acceptor and strong donor, i.e. **TPB-BCz** and **PCz-BCz**, respectively, can be characterized by the sub-nanosecond τ_1, the intensity of which well exceeds 70%. On the contrary, the fast decay component of **TRZ-BCz** compiles only 20%. The PL decays of the solid solutions of bicarbazolyl derivatives in PS are best described by the biexponential fits (**Fig. 4.13 (b)**). **TRZ-BCz** features a dominant (95%) fast decay component which has τ by 26% longer than that of the dilute hexane solution. This fact, combined with the high PLQY (0.86) in PS, provides the evidence of the more planar and favourable for emission conformation in the excited state. In turn, **TPB-BCz** and **PCz-BCz**, doped in PS, exhibit a small short-lived component (14-23%) and strong contribution from the longer-lived component, what is consistent with the twofold increase of PLQYs of the solid solutions in PS of the above mentioned compounds.

The investigation of solvatochromic behaviour in the solvents of various polarity, i.e. hexane (ε = 1.88), toluene (ε = 2.3), chloroform (ε = 4.81), tetrahydrofuran (ε = 7.6), dichloromethane (ε = 8.93) and acetone (ε = 20.7), showed, that all the three bicarbazolyl derivatives exhibit only minor changes in their UV spectra, while the emitting behaviour differs for the molecules with various cores. Thus, well-expressed positive solvatochromism was observed for the D-A **TRZ-BCz** due to the strong ICT character, while only slight bathochromic shifts were observed in the PL spectra of **TPB-BCz** and **PCz-BCz**. Solvent polarity dependent CT properties of **TRZ-BCz** can be more precisely described by the Lippert-Mataga equation [255,256]. As it is expected for the compound with D-A architecture, Stokes shift linearly increases with the enhancement of the solvent orientation polarizability Δf (**Fig. 4.14 (a)**), noting the strong solute−solvent interactions. On the contrary, PLQY of the solutions of **TRZ-BCz** did not show the linear trend with the increase of the solvent orientation polarizability. **TRZ-BCz** displayed very high QY values (0.78−0.93) in non-polar solvents, and drastic drop of PL efficiency with the rise of the solvent polarity. We can attribute these observations to the existence of the more planar emissive ICT state of the molecule in the solvents with smaller Δf and the appearance of twisted ICT in more polar

solvents, leading to the radiationless decay [227]. The dependencies of Γ and k_{NR} constants on solvent orientation polarizability Δ*f* (**Fig. 4.14 (b)**) can be described by the corresponding decreasing and increasing exponential trends, which is in agreement with the enhancement of non-radiative processes and sharp regression of PLQY in polar solvents.

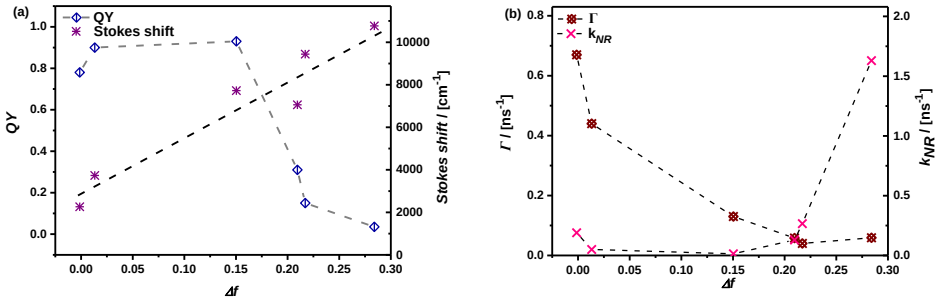

Fig. 4.14. Dependencies (a) of PLQY and of Stokes shift and (b) of radiative and nonradiative decay rate on the solvent orientation polarizability Δ*f* of **TRZ-BCz**

All the three compounds exhibited broad well-resolved phosphorescence spectra peaked at 523, 514 and 481 nm for **TRZ-BCz**, **TPB-BCz** and **PCz-BCz** (**Fig. 4.13 (a)**), respectively, consistently with the results reported for the other carbazole-based materials [257]. The values of E_T were estimated from the half blue-edge onset of the phosphorescence spectra and found to be 2.44, 2.50 and 2.68 eV for **TRZ-BCz**, **TPB-BCz** and **PCz-BCz**, respectively. Noteworthy, the triplet level of **PCz-BCz** is by ca. 0.18-0.24 eV higher, than those of triazine and triphenylbenzene derivatives, due to the multichromophore D–A molecular architecture in the latter. Interestingly, the comparison of the characteristics of the boomerang-shaped compounds confirms that the lowest T^1 state involves a $^3\pi\pi^*$ transition with the contribution from donor bicarbazolyl moiety. Two vibronic peaks with equal energy separation of 0.15-0.16 eV (Fig. 4.13 (a)), are clearly indentified in the phosphorescence spectra, confirming the carbazole involvement in the $^3\pi\pi^*$ triplet T^1 state of these molecules [44].

4.3.5. Electrochemical and photoelectrical properties

CV measurements revealed that **TRZ-BCz**, **TPB-BCz** and **PCz-BCz** undergo one-electron reversible oxidation processes which are principally related to the oxidation of the carbazolyl groups, which follows from the shape and localization of the HOMO orbitals. The reversibility of the process in the first and the following CV scans indicates the stability of the formed carbazole radical cation [203]. Evidently, protection of C-3 and C-6 positions of the outer carbazole moieties by the introduction of the *tert*-butyl groups prevents the C-C coupling at these positions, ensuring electrochemical stability of the compounds [257]. The first excited state oxidation potentials ($E^{1/2}_{ox\ vs\ Fc^+/Fc}$) were observed at 0.55, 0.57 and 0.65 V for **TRZ-BCz**, **TPB-BCz** and **PCz-BCz**, respectively (**Table 4.6**). The solid state ionization potentials IP_{SS} [203] were found to be relatively low and fall within the range of

5.35−5.45 eV. Similarity of the IP_{SS} values of **TRZ-BCz** and **TPB-BCz** is consistent with the mainly localized at the outer carbazole nature of HOMO, while in the case of **PCz-BCz** the HOMO orbital is delocalized over the side arm and part of the core, raising consequently the IP_{SS}. Interestingly, the best agreement between the experimentally obtained results from CV and E_{HOMO} calculation was demonstrated by **TPB-BCz** (5.36 and -5.38 eV, respectively). The exploitation of the stronger acceptor (**TRZ-BCz**) or donor (**PCz-BCz**) as a core is responsible for some discrepancy in the results. In the first and the following CV scans of the boomerang-shaped compounds no reduction was observed. This made impossible the determination of the electron affinity [230]. The optical gap $E^{opt}{}_g$ value of **TRZ-BCz** with the D-A molecular architecture (2.74 eV) was found to be smaller than those of **TPB-BCz** and **PCz-BCz** (3.18 and 3.15 eV), indicative of the facilitated 0-0 electronic transition between the energy levels of this compound owing to the CT (**Table 4.6**).

The IP_{EP} were found to be comparable, falling into the range of 5.45−5.50 eV. Analogically with the CV data, close values of IP_{EP} of **TRZ-BCz** and **TPB-BCz** (5.48 and 5.50 eV, respectively) are consistent with the similar space-distribution of the HOMO orbitals. A small difference observed between IP_{SS} and IP_{EP} can be attributed to the diversity of molecular interactions and arrangements in the neat films and dilute solutions. Noteworthy, the values of IP_{EP} show the same trend as those of the theoretically calculated IP_{vert} (**Fig. 4.12 (a)**).

4.3.6. Charge-transporting properties

In order to confirm the potential organic electronic device applications of **TRZ-BCz**, **TPB-BCz** and **PCz-BCz,** their charge-transporting properties were investigated by the TOF technique in a broad electric field range (**Fig. 4.18**).

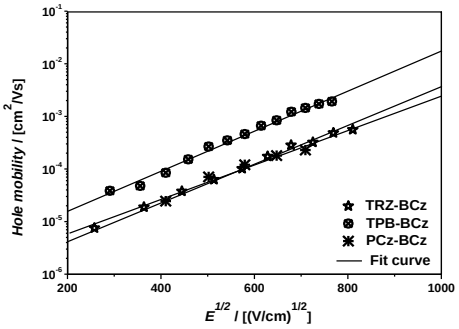

Fig. 4.15. Electric field dependencies of hole-drift mobility of **TRZ-BCz, TPB-BCz** and **PCz-BCz** measured by the TOF method at room temperature

The hole mobility values of the new boomerang-shaped compounds were found to fall within a range from 10^{-5} to 10^{-3} cm^2 V^{-1} s^{-1} at the electric field 5.8×10^5 Vcm^{-1}. The Poole–Frenkel field dependence parameters were estimated to be 6.62×10^{-3}, 7.35×10^{-3} and 5.78×10^{-3} $cm^{0.5}V^{-0.5}$ for **TRZ-BCz**, **TPB-BCz** and **PCz-BCz**, respectively. All the compounds under consideration demonstrate dispersive hole transport. Slightly higher hole mobility values of **TPB-BCz** comparing to those

of the other compounds of the series are apparently caused by the volume effects of the solid states layer. The hole mobility of **TPB-BCz** reaches a value of 2.1×10^{-3} $cm^2\ V^{-1}\ s^{-1}$ at the electric field 5.8×10^5 Vcm^{-1}.

To conclude, three boomerang-shaped molecules with various core moieties and bicarbazolyl side arms were designed and synthesized. Bicarbazolyl group proved to be a stronger donor than a single carbazole fragment, providing lower ionization potential and superior thermal and electrochemical stability. Photophysical properties were found to be dependent on the polarity and rigidity of the surrounding medium due to the conformational changes. The D–A architecture of the triazine-centered compound with the well-expressed ICT character is responsible for high PLQY (up to 0.93) in the non-polar media and non-monotonous variation of quantum efficiency with the increase in solvent polarity. The usage of the weaker acceptor and the stronger donor with a twisted molecular skeleton causes the enhancement of singlet and triplet energies, as well as changes in molecular packing, resulting in higher PLQY of the solid samples. All three compounds possess hole-transporting properties. As the final benchmark, high PLQY, appropriate *IP* and good hole mobility make the TRZ-based compound a promising candidate for the emitting layer in doped blue OLEDs, while the derivatives of TPB and PCz may be used as host compounds in green PhOLEDs.

4.4. Branched multichromophore fluorenone-based compounds

Development of new materials with advanced characteristics is evidently one of the vital goals in the constantly evolving field of organic optoelectronics. Conjugated compounds with advanced properties find their applications in efficient OLEDs [258], OSCc [259] and OFETs [260]. Recently, much attention has been addressed to the molecules exhibiting the TADF phenomenon [14,44,48,112], AIE behavior [50,55], non-linear optical (NLO) characteristics [261,262] and ambipolar charge transport [263,264]. The usage of multichromophore molecular architecture leads to great diversity in the optical, photophysical, charge-transporting characteristics of the compounds. Thus, exploitation of the strongly electron-accepting rigid fluorenone moiety results in efficient electron mobility [265]. Moreover, fluorenone containing systems have been found to exhibit enhanced emission due to intermolecular hydrogen bonding [12]. In turn, involving donating carbazole fragment provides high thermal stability, remarkable hole mobility and considerably high triplet level [5]. Triphenylamine unit not only exhibits excellent charge-transporting behaviour [6], but due to its propeller shape proves to be a good building block for AIE luminogenes [7,8]. Because of its twisted skeleton and C_3 symmetry 1,3,5-triphenylbenzene finds application in the preparation of wide energy gap materials [11].

The above-mentioned peculiarities encouraged us to design and prepare a series of fluorenone-centered multichromophore compounds, exhibiting superior thermal properties, balanced ambipolar charge transport, AIE features and unusual temperature-dependent emissive characteristics. The observed traits are supported by theoretical calculations.

4.4.1. Synthesis

Multichromophore compounds **FN-TPA**, **FN-TPB** and **FN-PCz** possess C_2 symmetry achieved by the usage of a symmetrical 2,7-functionalized fluorenone moiety (**Scheme 4.6**). The molecules comprise donating carbazolyl groups, linked to the accepting core by various branched spacer fragments – TPA, TPB and PCz. The ethynyl π-bridge is employed to achieve more efficient conjugation between the core and the side arms.

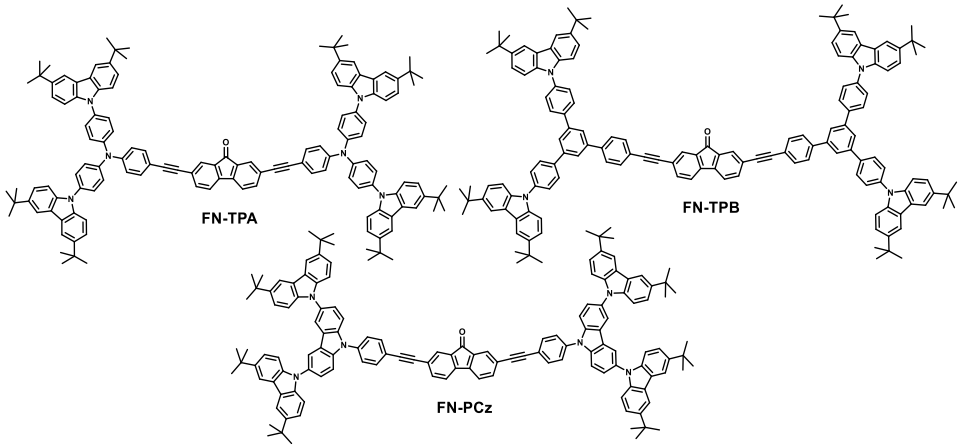

Scheme 4.6. Chemical structures of the branched multichromophore fluorenone-based compounds

Scheme 4.7 presents the synthetic routes, involving the divergent strategy [212], towards the multichromophore fluorenone adducts. On the first step, star-shaped spacer nuclei were obtained: halogenated derivatives **4a** and **4b** were prepared by Ullmann reaction [72] followed by the iodination reaction in Tucker's conditions [175], while **2g** was synthesized by the electrophilic cyclization catalyzed by $SiCl_4$ [174]. Further N–C coupling with **3b** in Ullmann conditions [72] yielded branched precursors **4c**, **4d**, **4e**. Introduction of the trimethylsilylethynyl group [168], producing the intermediates **4f**, **4g**, **4h**, followed by the deprotection reaction [169], resulted in the functionalized branched fragments **4i**, **4j**, **4k**. Hagihara-Sonogashira reaction [168] of the latter terminal alkynes with 2,7-diiodofluorenone **4l** gave rise to the target compounds **FN-TPA**, **FN-TPB** and **FN-PCz**.

^{13}C NMR spectra of all the target compounds contain characteristic signals at 192 ppm, corresponding to the carbon atom of C=O group, as well as attributed to the C≡C fragment peaks at 78-92 ppm. Moreover, the evidence of the keto and ethynyl groups can be proved by the presence of the appropriate bands in the IR spectra: 1741-1748 and 2211-2240 cm^{-1}, respectively. A characteristic singlet at ca. 1.40 ppm of the CH_3- group can be observed in the proton NMR spectra of the studied derivatives.

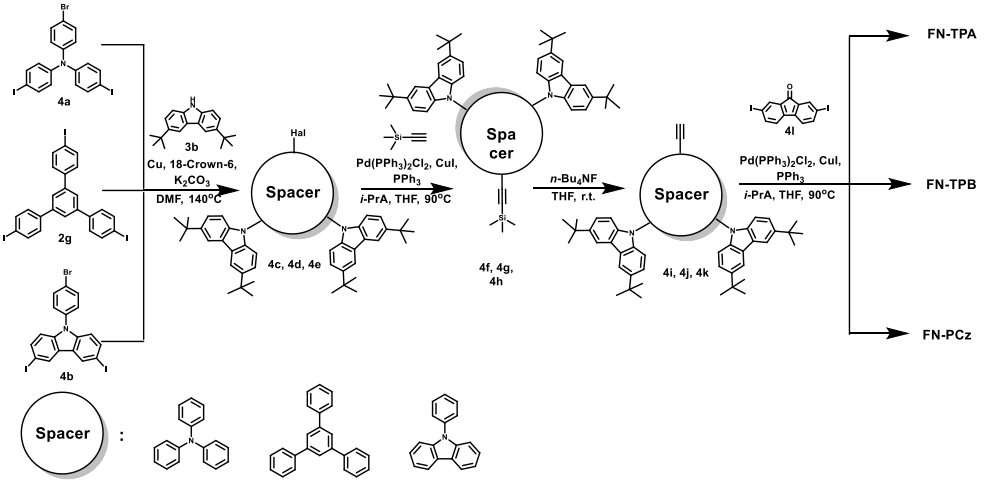

Scheme 4.7. Synthetic routes towards the branched multichromophore fluorenone-based compounds

4.4.2. Theoretical investigation

The coplanar conformation of the central part of the new compounds is sufficiently maintained by the usage of the 2,7-ethynyl substituted fluorenone core (**Fig. 4.16**) [262]. Small dihedral angles (0.5−2°) between the core and the branched arms indicate efficient conjugation between the chromophores. In the case of **FN-TPA,** the involvement of TPA moieties generates the propeller shape of the arms [266]. The dihedral angle between the phenyl units and the nitrogen atom is of 37°, in agreement with the previously reported calculations on the TPA derivatives [267,268]. The molecule of **FN-TPB** possesses propeller shape as well, [210,237], with the twisted by 38° outer phenyl groups. The PCz moiety, introduced to the branched part of **FN-PCz**, divides the molecular skeleton into two parts twisted by an angle of 53°, which is slightly smaller than the torsion angle reported for the "naked" PCz (ca 60°) [238]. In the molecules of all the target compounds the peripheral carbazole moieties are twisted by 51-56°.

The frontier orbitals of the three compounds are shown in **Fig. 4.16**. Similarly to previous calculations [269], the LUMOs of the three compounds are localized on the electron-deficient fluorenone fragment, involving additionally the ethynyl π-bridge, whereas the LUMO+1 is delocalized over the whole FN-di(CCPh) bridge. As expected, the HOMOs are localized on the donor part of each molecule. Thus, in case of **FN-TPA**, HOMO exhibits the contributions from TPA and ethynyl moieties, whereas the HOMO of **FN-TPB** is mainly localized at the peripheral carbazole units, slightly involving the phenyl rings of TPB. An intermediate situation is found in the case of **FN-PCz** exhibiting partial HOMO delocalization through the inner carbazoles spacer. These differences are consequently reflected in the HOMO energy trend, increasing in the order **FN-TPB**<**FN-PCz**<**FN-TPA** (**Fig. 4.16**).

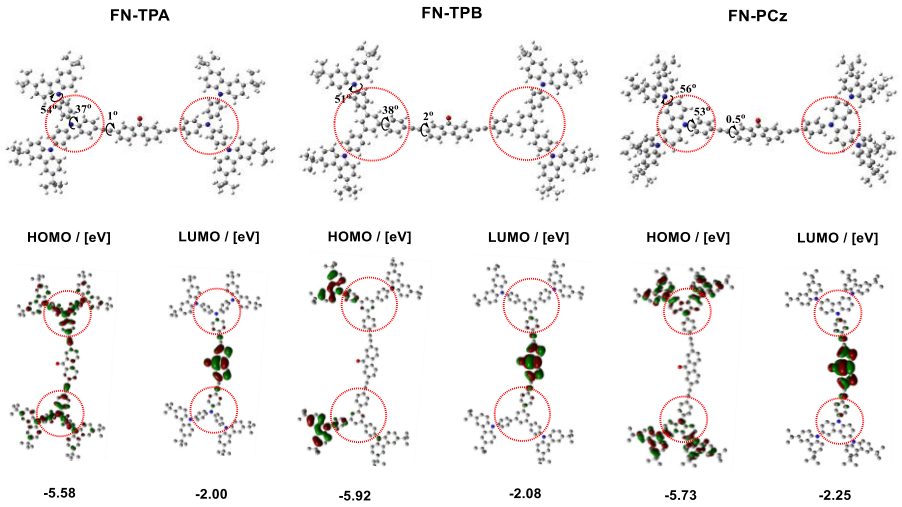

Fig. 4.16. Geometries and frontier orbitals of **FN-TPA**, **FN-TPB** and **FN-PCz** obtained at the B3LYP/6-31G level in gas phase. The HOMO and LUMO energy values were calculated at the BMK/6-31G level of theory (gas phase)

The origin of these different HOMO distributions and energies can be traced back to the energy ordering between local HOMOs of the central FN-di(CC) fragment, the spacer, and the peripheral di-carbazole fragment, in the order TPB (-6.85 eV) < FN-di(CC) (-6.28 eV) < Cz (-6.24 eV) < TPA (-5.67 eV) (calculated by TD-DFT BMK/6-31 G method in the gas phase). The bridging between the peripheral di-Cz fragment and the central FN-di(CC) one is consequently very poor in the case of **FN-TPB**, and the most efficient in the case of **FN-TPA**. Due to these particularities, **FN-TPB** and **FN-PCz** possess clear space separation between HOMO and LUMO, whereas less pronounced separation is found in the case of **FN-TPA** (**Fig. 4.16**).

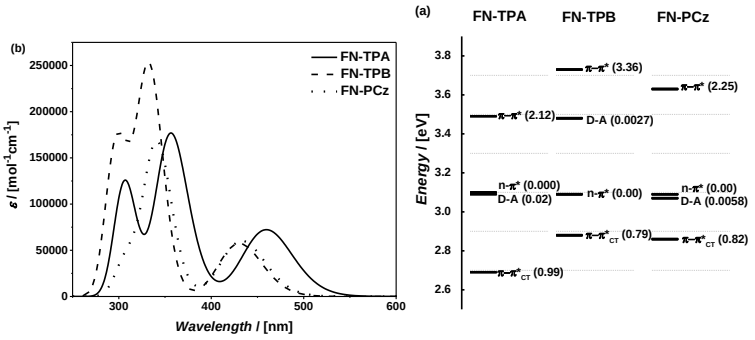

Fig. 4.17. (a) Theoretically calculated absorption spectra (BMK/6-31G level in gas phase); (b) energy diagram corresponding to the evolution of n-π*, π-π*$_{CT}$, π-π*, and D–A transitions (TD-BMK/6-31G level in gas phase) with the corresponding oscillator strengths of the isolated **FN-PCz, FN-TPA,** and **FN-TPB**

Theoretically calculated absorption spectra (**Fig. 4.17 (a)**) display the high intensity high-energy region (>400 nm), corresponding to the excitations within the branched side arms, and a weak and broad low energy band (LEB) of π-π^*_{CT} nature, involving the FN-di(CCPh) bridge. The energy diagram, corresponding to the evolution of various transitions, is presented in **Fig. 4.17 (b)**. Noteworthy, the low energy band of **FN-TPB** almost overlaps with that of **FN-PCz**, while the spectrum of **FN-TPA** shows a general red shift. This difference can be explained by the additional contributions to the HOMO-1 of **FN-TPA**, coming from the TPA moieties, resulting in the decreased gap with LUMO and the bathochromical shift of the high energy bands of **FN-TPA**.

4.4.3. Thermal properties

Due to the increased molecular weight (ca. 1900 g/mol) and the employment of thermally stable chromophores all the target materials exhibited outstanding thermal stability (**Table 4.7**). Thus, TGA experiments revealed T_{ID} exceeding 481 ^oC. Although three target fluorenone adducts demonstrated similar values of T_{ID} in the range 481 – 500 ^oC, the highest stability was displayed by **FN-TPB**, bearing the TPB spacer. Remarkable thermal stability was previously reported for the TPB derivatives [223,237], however, in our case the improvement of **FN-TPB** T_{ID} can be additionally explained by the smaller amount of prominent to degradation C–N bonds, comparing to **FN-TPA** and **FN-PCz**.

Table 4.7. Thermal, electrochemical and photoelectrical characteristics of **FN-TPA**, **FN-TPB** and **FN-PCz**

Compound	T_g [a] [°C]	T_{ID} [b] [°C]	$E^{1/2}_{ox\ vs\ Fc+/Fc}$ [c] [V]	$E^{1/2}_{red\ vs\ Fc+/Fc}$ [c] [V]	IP_{SS} [d] [eV]	EA_{SS} [e] [eV]	$E_{g(CV)}$ [f] [eV]	IP_{EP} [g] [eV]
FN-TPA	238	494	0.58	-1.40	5.38	3.40	1.98	5.45
FN-TPB	265	500	0.83	-1.36	5.63	3.44	2.19	5.53
FN-PCz	293	481	0.52	-1.53	5.32	3.27	2.06	5.46

[a]Determined by DSC. [b] Determined by TGA. [c] Determined by CV in dilute CH_2Cl_2 solutions. [d] Estimated from the halfwave oxidation potential by using the relationship $IP_{CV} = |e|(4.8 + E_{ox\ vs\ Fc+/Fc}^{1/2})$. [e] Estimated from the halfwave reduction potential by using the relationship $EA_{CV} = |e|(4.8 – E_{red\ vs\ Fc+/Fc}^{1/2})$. [f] Determined from the onset of λ_{abs}^{max}. [g] Determined from EP spectra.

Owing to the involvement of the branched side arms with the alkylated outer carbazole groups, the target fluorenones were obtained as amorphous powders. Therefore, as expected, only glass transitions were revealed by the DSC analysis. The variety of T_g values of fluorenone adducts can be assigned to different rigidity of the spacer units (**Table 4.7**). Thus, propeller-shaped labile TPA and TPB groups with twisted phenyls reduce T_g of **FN-TPA** and **FN-TPB** (238 and 265 ^oC, respectively). In turn, the condensed rigid carbazole unit [245] is responsible for the significant improvement of T_g (293 ^oC for **FN-PCz**) by inhibiting rotational and vibrational molecular motions.

4.4.4. Optical and photophysical properties

The UV/Vis spectra of the butterfly-shaped molecules extend to the lower energies beyond the absorption bands of single carbazole [270], fluorenone [271],

TPA [272] and TPB [223] fragments involved, indicating the enhanced conjugation within the molecules (**Fig. 4.18 (a)**). The profiles and peak positions of the UV/Vis spectra, recorded in different media, are similar. The strongly allowed high energy bands can be assigned to the $\pi-\pi^*$ excitations. The involvement of the carbazole unit is responsible for the appearance of sharp peaks at ca. 300 nm [247], while bands in the 310-400 nm region can be attributed to the excitations due to charge delocalization through the branched side arms and the central fluorenone fragment. The UV/Vis spectra of all the target compounds feature a broad, structureless, low-intensity $S_0 \rightarrow S_1$ bands peaked at 447-463 nm, occurring due to the intrabridge FN-di(CCPh) excitations of π-π^*_{CT} nature, according to the theoretically obtained results. Interestingly, the LEB bands of **FN-TPB** and **FN-PCz** have similar position and intensity, while that of **FN-TPA** is by ca. 13 nm red-shifted and more expressed due to the additional contributions of TPA units [238]. Noteworthy, the UV spectra of hexane solutions show a similar tendency to the theoretical ones. Incorporation of the molecularly dispersed compounds into Zeonex only negligibly affected the shape and position of the absorption spectra. The UV/Vis spectra of the neat films of **FN-TPA**, **FN-TPB** and **FN-PCz** are slightly red-shifted featuring more pronounced LEB comparing to solid and liquid solutions, which can be assigned to the intermolecular interactions [248]. Indeed, ground state aggregation was observed in the media of various polarity and viscosity for the fluorenone derivatives, due to the presence of C=O unit [273].

Upon the excitation at 350 nm all the fluorenone derivatives under consideration emit light in the yellow spectral region (**Fig. 4.18 (a)**). The PL spectra of **FN-TPB** and **FN-PCz** in hexane and zeonex solutions feature clearly resolved vibronic structure and are less broad as could be expected for a typical excimeric emission profile. This property clearly points to the intramolecular origin for the emission in non-polar solvents. The analysis of the intensity ratio between the 0-0 and 0-1 transitions, which is very sensitive to the *H*- or *J*-aggregation [143,144], comforts the above assignment.

The intramolecular origin of the yellow emission of the compounds also seems to be comforted by the governing relaxation pathway (**Table 4.8**). The PL decays of the hexane and solid zeonex solutions are found to be best fitted by a monoexponential mode exhibiting PL lifetimes ranging 5.71-9.53 ns. Evidently, monoexponential lifetimes along with a well resolved vibronic structure of the emission profiles confirm the single intramolecular origin and the absence of excimeric contribution in non-polar media.

The new fluorenone derivatives demonstrated a significant difference in PLQY. Thus, **FN-TPA** and **FN-PCz** exhibited much higher PLQY of 0.76 and 0.82 in dilute hexane when compared to **FN-TPB** (0.31). In turn, two-fold increase in PL efficiency of **FN-TPB** is observed in the rigid Zeonex matrix, while only insignificant enhancement of η_{PL} was observed for **FN-TPA** and **FN-PCz**. While the lowest excited state in the case of all compounds is the π-π^*_{CT} transition, which is totally localized on the central part of the FN-di(CCPh) bridge [274], similar PLQY in hexane should consequently be expected for the three compounds. While this assumption seems to be verified by the similar PLQY of 0.76 and 0.82 in the case of

FN-TPA and **FN-PCz,** respectively (**Table 4.8**), much smaller PLQY of 0.31 is deduced for **FN-TPB**. This particular behavior of **FN-TPB** seems to stem from the intra- and/or intermolecular PL quenching, which is expected to be larger as compared to **FN-TPA** and **FN-PCz** due to the enhanced disorder induced by the free rotations on the donor moieties.

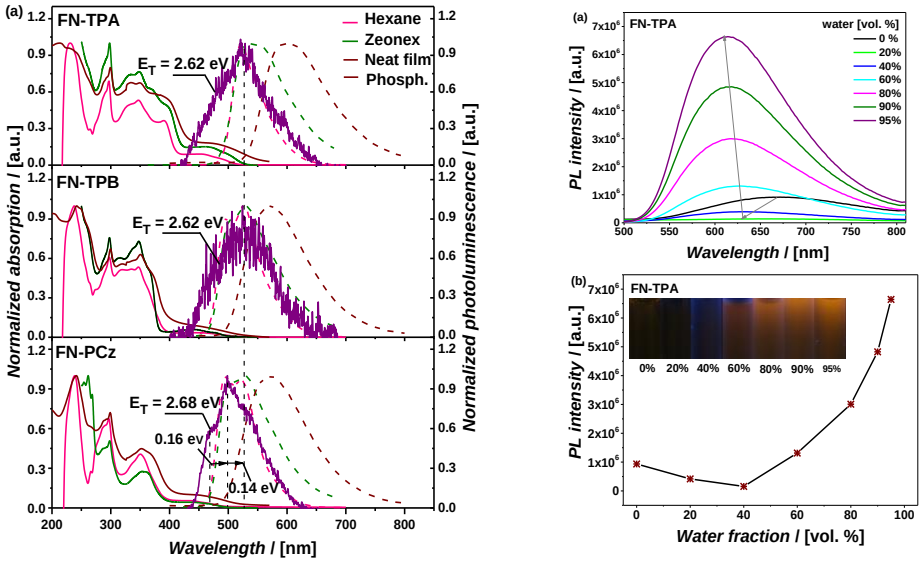

Fig. 4.18. (a) UV/Vis absorption (solid lines) and PL (dashed lines) (λ_{ex} = 350 nm) spectra of **FN-TPA**, **FN-TPB** and **FN-PCz** recorded for 10^{-5} M hexane solutions, solid solutions in Zeonex (1 wt.% of compound), neat films and phosphorescence spectra recorded for the solid solutions in Zeonex at 77K (delay 10 ms, integration time 10 ms); (b) PL spectra of **FN-TPA** in different THF/water (v/v) mixtures; (c) the dependence of PL intensity of **FN-TPA** on the fraction of water

In turn, the PL spectra of the neat films are bathochromically shifted comparing to the non-polar media, featuring the loss of the vibronic structure. Importantly, the PLQYs ranging from 0.14 to 0.22 are much smaller than in hexane or zeonex solutions. We hypothesize that the strongly radiative π-π^*_{CT} and the very weakly radiative D–A emissive states are close enough in energy in the neat films, that an equilibrium between different emissive species may exist, thus reducing the PLQY and de-structuring the PL profiles. This hypothesis seems to be supported by the PL decay measurements. Indeed, two exponential modes are necessary to fit the PL decay profiles in the case of **FN-TPA** and **FN-TPB**, with one fast component (2.55 ns and 2.65 ns, respectively), and one slower component (7.75 ns and 6.26 ns, respectively) (**Table 4.8**). The third exponential mode is necessary to fit the **FN-PCz** PL decay profile with an extremely long lifetime of 27.18 ns, most probably corresponding to the excimer formation or to energy transfer via exciton migration through the localized states in disordered media such as neat amorphous films [222,253]. However, this third component constitutes roughly 41% of the total radiation, the dominant radiation channel being again the intramolecular one.

Table 4.8. Photoluminescence quantum yields and decay lifetimes of **FN-TPA**, **FN-TPB** and **FN-PCz**

Compound	10^{-5} Hexane solution		10^{-5} THF solution		Zeonex film		Neat film	
	η [a]	τ [b] [ns]	η [a]	τ [b] [ns]	η [a]	τ [b] [ns]	η [a]	τ [b] [ns]
FN-TPA	0.76	5.71	0.01	2.78	0.85	7.13	0.14	2.55 [66.56%] 7.75 [33.44%]
FN-TPB	0.31	8.31	0.56	7.79	0.66	9.53	0.22	2.65 [37.58%] 6.26 [62.42%]
FN-PCz	0.82	8.24	0.01	1.68	0.90	9.20	0.16	1.47 [17.31%] 7.27 [41.82%] 26.18 [40.87%]

[a] PLQY estimated with the usage of the integrating sphere. [b] PL decay lifetimes (χ^2 = 1.00-1.13).

Interestingly, different PLQYs were observed in THF for the fluorenone derivatives. While the PLQYs of **FN-TPA** and **FN-PCz** drastically drop to 0.01, the PLQY of **FN-TPB** increases from 0.31 in hexane to 0.56 in THF. This intriguing difference can be explained by the assumption, that the D–A state in THF is more stabilized than π-π^*_{CT}, thus lowering in energy and becoming the emissive state [274]. Due to the involvement of strong TPA and PCz units, such switching of the D–A and π-π^*_{CT} can be valid for **FN-TPA** and **FN-PCz**. However, in the case of **FN-TPB** the solvent effect is not strong enough to produce switching of the energy order between D–A and π-π^*_{CT} states, assumedly resulting in the latter one being the emissive state responsible for the non-zero PLQY (0.56). Important support to this hypothesis comes from two additional measurements pointing to the role of the increasing polarity: (1) the PL intensity of the solution drops on the TLC plates is almost zero in the case of all the investigated compounds, which could be explained by the larger polarity of the TLC plate as compared to THF and the stabilization of the D–A state of **FN-TPB** below the π-π^*_{CT}. (2) The PL intensity of **FN-TPB** in THF/water mixtures [274] decreases by one order of magnitude, due to the strong increase in solvent polarity and additional stabilization of the D–A state. As for the increase of PLQY of **FN-TPB** from 0.31 (hexane) to 0.56 (THF), the decreased intermolecular interactions due to the charge stabilization in polar solvents can be supposed, resulting in turn in the decreased PL quenching. Such scenario is also supported by the analysis of the differences in the PL decay modes. Indeed, monoexponential decay modes were found for the three compounds in THF solutions, yet much smaller PL lifetimes of 1.68 ns and 2.78 ns were found for **FN-PCz** and **FN-TPA,** respectively, as compared to 7.79 ns for **FN-TPB**. While the PL lifetime of **FN-TPB** is similar to that in hexane (8.31 ns), thus suggesting similar nature of the emissive state (π-π^*_{CT}), the PL lifetimes of **FN-PCz** and **FN-TPA** are 2-4 times smaller as compared to the hexane ones (**Table 4.8**), suggesting a change in the nature of the emissive state, assumedly from π-π^*_{CT} to D–A.

While the intramolecular origin and the absence of excimer contribution of the **FN-TPB** PL can be safely deduced from the vibrational structure and monoexponental decay mode, in the case of **FN-PCz** and **FN-TPA** several observations seem to exclude efficient excimer contribution: (1) if π-stacking aggregation and excimeric emission were to be efficient, it would have been stronger

in hexane as compared to THF, due to the weaker electrostatic stabilization in hexane. The intramolecular origin of the PL in hexane thus suggests the absence of excimeric emission in hexane and in THF. (2) The intense intramolecular emission in hexane, disappearing in turn in THF, indicates that aggregation-induced quenching of the intramolecular emission (AIQ) instead of AIE could be observed in THF if excimers were involved. (3) While easy aggregation could happen in smaller size fluorenone-based compounds [8,126,275], the *H*- and *J*- aggregation is sterically hindered in **FN-TPA**, **FN-TPB** and **FN-PCz**. Based on these observations, it can be concluded that the PL in THF has the intramolecular origin for the three compounds.

In order to further support the above mechanism, a solvent/non-solvent PL test was conducted [276,277]. **Fig. 4.18 (b)** presents the PL spectra of the 10^{-5} M solutions of **FN-TPA** in THF/water mixtures with the different volume ratios. With the addition of first water fractions (up to 60% for **FN-TPA** and **FN-PCz**, and 40% for **FN-TPB**), extreme PL quenching was observed for all the compounds. Further addition of water led to the boost of PL intensities for 45 times for **FN-TPA**, 11 for **FN-TPB** (20 to 95 v.v. % of water) and 26 for **FN-PCz** (20 to 90 v.v. % of water) (**Fig. 4.18 (c)**). Since the butterfly-shaped molecules under consideration are insoluble in water, the observed enhancement of emission was apparently due to the aggregates formation [8]. As it was shown previously for the fluorenone luminogens [8,126], AIEE phenomena for these compounds seems to originate from the planarization of the molecules and the decreasing rotational degrees of freedom. Indeed, the decreasing AIEE efficiency in the order **FN-TPA** (45 times) > **FN-PCz** (26 times) > **FN-TPB** (11 times) is consistent with the decreasing contribution of the bridging moieties in the HOMO in the same order.

E_T of the butterfly-shaped molecules (**Fig. 4.18 (a)**) were found to be sensitive to the molecular structure [44]. From the profiles and position of the spectra it can be concluded, that triplet emission is manifested by the phosphorescence of the carbazole fragment [257]. While **FN-TPA** and **FN-TPB** exhibit at 77K only weak broad phosphorescence, peaked at 518-528 nm, **FN-PCz** with larger share of carbazole units, revealed well-resolved blue-shifted phosphorescence with the maximum at 498 nm. Three vibronic peaks with equal energy separation of 0.14-0.16 eV can be clearly indentified in the phosphorescence spectrum of **FN-PCz**, confirming the carbazole involvement in the $^3\pi\pi^*$ triplet T^1 state of this molecule [44]. The accessed E_T values were found to be close and comparable (2.62 eV for **FN-TPA** and **FN-TPB**, 2.68 eV for **FN-PCz**). The absence of the triplet emission originating from fluorenone moiety can be explained by “linear” 2,7-substitution of the ketone [269].

4.4.5. Electrochemical and photoelectrical properties

All the synthesized fluorenone adducts exhibit reversible oxidation and reduction in the CV traces proving the electrochemical stability of the compounds (**Fig. 4.19 (a)**). Similar values of the half-wave reduction potential ($E_{red}^{1/2}$) suggest the formation of fluorenone radical anion [278], in agreement with the exclusively fluorenone-localized LUMOs. In turn, the effect of the branched spacer on the

electrochemical behaviour is revealed in the positive scale (oxidation) of CV measurements. Thus, **FN-TPA** exhibits three oxidation peaks, **FN-PCz** – two, while **FN-TPB** shows only one. Apparently, the shape of HOMO orbitals can be involved for the explanation of the oxidation signal positions. Since **FN-TPB** HOMO is mainly located on the outer alkylated carbazole, $E^{1/2}_{ox}$ at 0.83 V can be attributed to the electron withdrawal from above mentioned fragment. The second oxidation potentials of **FN-TPA** and **FN-PCz** at a similar position as that of **FN-TPB** prove this assignment. Delocalized through the two types of carbazole nature of **FN-PCz** HOMO indicates the occurrence of an additional oxidation peak at a lower potential (0.52 V) involving inner carbazole [203], located closer to the electron-accepting core. Similarly, peak at 0.58 V of the TPA derivative can be ascribed to the oxidation of TPA unit [229]. Interestingly, **FN-TPA** shows third oxidation peak as well. As far as **FN-TPA** is the only material of the series, the HOMO of which is expanded to the phenylethynyl group, we can explain $E^{1/2}_{ox}$ at 1.38 V by electron withdrawal from this fragment [229].

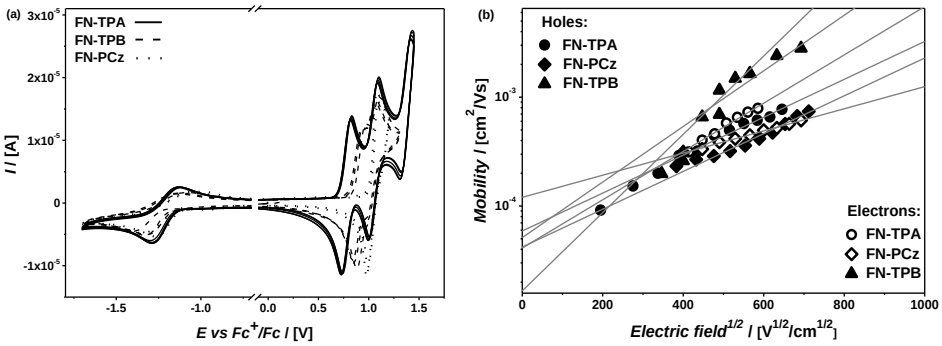

Fig. 4.19. (a) CV curves recorded for 10^{-3}M CH_2Cl_2 solutions and (b) electric field dependencies of hole and electron drift mobilities measured by the TOF method at room temperature of **FN-TPA, FN-TPB** and **FN-PCz**

As expected, since **FN-TPA** and **FN-PCz** exploit strongly donating spacer parts, TPA and PCz [238], the values of IP_{SS} are quite similar (5.38 and 5.32 eV) (**Table 4.7**). On the contrary, **FN-TPB** possesses a higher ionization potential (5.63 eV). It should be noted, that IP_{SS} values are slightly lower than the absolute E_{HOMO} values. High values of electron affinity, falling in the range 3.27-3.44 eV, indicate the strong electron accepting ability of fluorenone. According to the IP_{SS} and EA_{SS} values, the target multichromophore compounds are good candidates for both hole and electron injection and transport. Calculated electrochemical gaps ($E_{g(CV)}$) show similar trends as IP_{SS}. Small $E_{g(CV)}$ values (1.98-2.19 eV) point out the facilitated 0-0 electronic transition between the energy levels.

Electron photoemission was employed for the determination of solid layer ionization potentials (IP_{EP}) [239] (**Table 4.7**). Three fluorenone derivatives exhibited similar IP_{EP} values falling in the range 5.45-5.53 eV. Similarly to the data deduced from CV the highest value of 5.53 eV was displayed by **FN-TPB**, indicating that molecular packing forces do not alter the intramolecular electronic structure significantly.

4.4.6. Charge-transporting properties

Both hole and electron transport of **FN-TPA, FN-TPB** and **FN-PCz** molecules were estimated by using the TOF method. The current transients corresponded to the dispersive hole and electron transports. Electric field dependencies of hole and electron drift mobilities of spin-coated layers of **FN-TPA, FN-TPB** and **FN-PCz** are illustrated in **Fig. 4.19 (b)**. Practically, hole and electron mobilities of the compounds are proportional to 10^{-4} cm^2/Vs indicating good ambipolar transport, whereas the values of electron mobility are only slightly higher than those of hole mobility. Mobilities of **FN-TPB** with the TPB fragment reached values of 1.6×10^{-3} cm^2/Vs (for holes) and 2.8×10^{-3} cm^2/Vs (for electrons) at electric field higher than 3.5×10^5 V/cm. The hole and electron mobilities for **FN-TPB** were found to be higher than those of **FN-TPA** and **FN-PCz** with TPA and PCz fragments as spacers. Remarkably higher charge mobility of TPB derivatives was previously observed in our works [237] [250].

In conclusion, a series of three multichromophore fluorenone-based compounds was modelled and prepared. Theoretical investigation revealed differences in geometry and electronic levels of the molecules. **FN-TPA, FN-TPB** and **FN-PCz** exhibit superior thermal stability (T_{ID} up to 500 °C) and high T_g (up to 293 °C). Optical and photophysical properties were thoroughly investigated in the media of different polarity and rigidity. Compounds with a strongly donating spacer, **FN-TPA** and **FN-PCz**, show high PLQY (up to 0.9) in non-polar media. The yellow colour emission in these compounds in solution and neat films was found to originate from single molecule transitions, with only minor contribution from the excimer emissions. The emission behaviour and differences between the compounds are explained on the basis of the energy difference and the order of two excited states, the D–A state exhibiting a strong CT character, and the π-π* one exhibiting some degree of CT character. AIEE features were observed owing to the planarization of the molecules and the decreasing rotational degrees of freedom. Moderately low IP_{SS} were manifested by the CV method (5.32-5.63 eV), showing the same trends as those deduced from EP measurements (5.45-5.53 eV). All three multichromophore compounds demonstrate ambipolar charge transport behavior with balanced hole and electron mobility. Thus, the compounds under consideration may find application as emitters in non-doped and doped OLEDs with reduced amount of layers. Moreover, using studied fluorenone derivatives as yellow-emitting component, noble-metal-free white OLEDs can be achieved.

4.5. Differently carbazolyl and cyano-substituted 1,3,5-triphenylbenzene derivatives

The development of the highly efficient and stable deep-blue phosphorescent materials has proved to be a big challenge during the last decades [279]. Moreover, continuous efforts have been contributed to evolve blue-light emitters with good colour purity [234,280]. Noteworthy, deep-blue emitters can not only be a major constituent in full-colour displays, but also be used as the key element for generating white light in combination with its complementary colour [281]. A suitable blue emitter should comprise such features, as pure colour, high photoluminescence

quantum efficiency, long lifetime, remarkable thermal and electrochemical stability, as well as high triplet energy and ambipolar charge transport behaviour, which can make a promising candidate not only for blue OLEDs, but also serve as a desirable host for PhOLEDs. For the achievements of these goals a combination of donating and accepting building blocks can be used. Thus, efficient blue-emitting materials bearing anthracene [224], spyrofluorene [282], pyridine [87] were reported.

In the current work, the design and synthesis of new bipolar carbazole derivatives with 1,3,5-triphenylbenzene backbone is presented. The influence of the substituent orientation on the photophysical, thermal, charge-transporting properties of the compounds was investigated. Theoretical approach was employed for the clarification of the characteristics of the bipolar derivatives.

4.5.1. Synthesis

Various combinations of carbazolyl and cyano-substituents orientated in *para*- and *meta*- positions were involved for the preparation of target compounds (**Scheme 4.8**). These orientational differences were expected to affect significantly the properties of the materials.

The preparation of the bipolar adducts with exclusively *para*- or *meta*-substitution included a facile Ullmann reaction [72] of core fragments **2g** and **5b**, respectively, with 3,6-*tert*-butyl-carbazole **3b** yielding mono- and disubstituted products **5a**, **4d** and **5c**, **5d** in one pot. High-yielding cyanation of the above mentioned halogenated adducts in Rosenmund-von Braun [283] conditions resulted in the target compounds ***p*-TPB-Cz**, ***p*-TPB-2Cz**, ***m*-TPB-Cz** and ***m*-TPB-2Cz**. In turn, the synthetic pathway towards the molecule exploiting both *para*- and *meta*-substituents was more complex. Firstly, organotin derivative **5f** was prepared, which was used for the mono-substitution of 1,3,5-tribromobenzene in Stille conditions [284]. Suzuki-Miyaura palladium catalyzed coupling of thus obtained aromatic precursor **5g** with 4-(4,4,5,5-tetramethyl-1,3,2-dioxaborolan-2-yl)benzonitrile resulted in the target compound ***p*-TPB-*m*-Cz**.

^{1}H NMR spectra of the cyano-substituted TPB derivatives contain characteristic signals at ca. 8.20 ppm, assigned to hydrogens at the 4th and 5th positions of the carbazole moiety, as well as attributed to the protons at C-2, C-4, C-6 positions of 1,3,5-triphenylbenzene peaks at 7.80-7.96 ppm. A distinctive singlet at 1.50 ppm can be observed due to the protons of CH_3- group. Furthermore, characteristic signals at 34.8 and 32 ppm in the ^{13}C NMR of the compounds indicate the presence of a *tert*-butyl fragment. In addition, the evidence of C≡N group can be manifested by the peaks at 2224-2239 cm^{-1} of IR spectra.

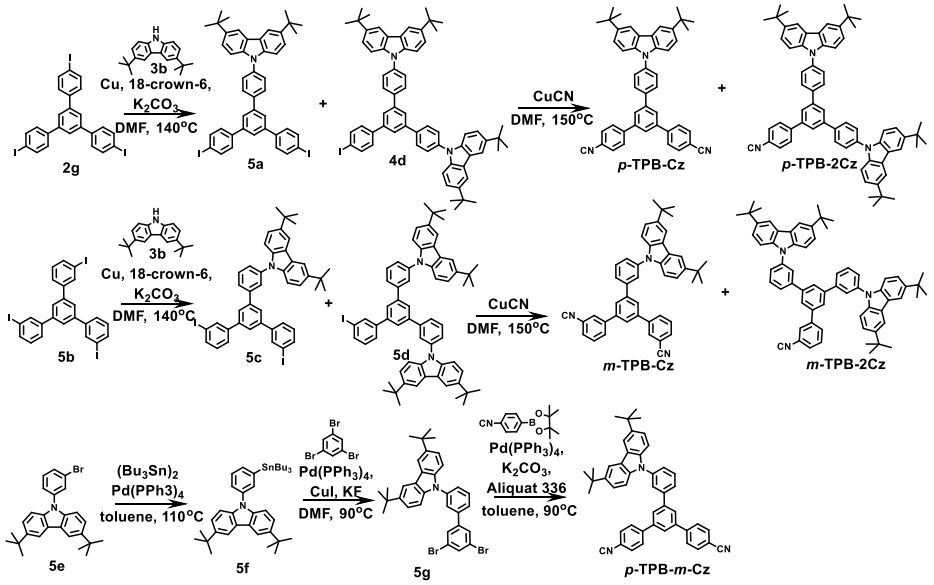

Scheme 4.8. Synthetic routes towards the carbazolyl and cyano-substituted TPB derivatives

4.5.2. Theoretical investigation

The geometry of the synthesized compounds is determined by the propeller shape of the TPB moiety and the orientation of the substituents. In case of the molecules under consideration the value of the torsion angle reaches 51-53º (**Fig. 4.20**). Evidently, the accepting nitrile moieties, compiling a triple bond between the carbon and nitrogen atoms, are located in the same plane with the adjacent phenyl ring. Despite the values of dihedral angles between the core and carbazolyl substituents are very similar for all the studied derivatives, the *meta*- and *para*-orientation of the substituents obviously affects the molecular profiles and, hence, may influence intermolecular packing. Thus, ***p*-TPB-Cz** and ***p*-TPB-2Cz**, due to more efficient conjugation, may form more planar structures, compared to ***m*-TPB-Cz**, ***m*-TPB-2Cz** and ***p*-TPB-*m*-Cz**.

The analysis of frontier orbitals (**Fig. 4.20**) shows that HOMOs of all differently carbazolyl and cyano-substituted TPB derivatives are located exclusively on the PCz fragments, while LUMOs are delocalized through accepting nitrile groups involving neighbouring phenyl rings. Noteworthy, HOMO and LUMO of ***p*-TPB-Cz** and ***p*-TPB-2Cz** possess a slight overlapping area, which is crucial for good optical characteristics. Evidently, all the synthesized molecules possess good charge separation between HOMO and LUMO, suggesting the significant ICT character. HOMO and LUMO energies of the D–A TPB derivatives were accessed in order to gain better understanding of the electronic energy levels (**Fig. 4.20**). The absolute E_{HOMO} values are very close (-5.28 – -5.33 eV) and are not affected by the differences in the amount and orientation of substituents. However, LUMO energies of the *para*-cyano-substituted compounds (***p*-TPB-Cz**, ***p*-TPB-2Cz** and ***p*-TPB-*m*-Cz**) are by ca. 0.3 eV lower than those of *meta*-analogues, giving a hint about the more pronounced accepting strength of the C≡N fragment in *para*-positions.

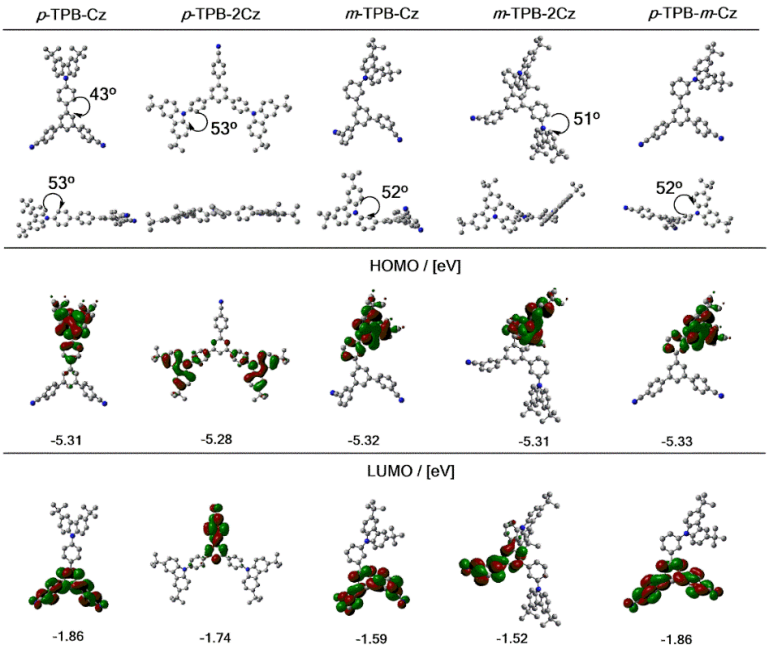

Fig. 4.20. DFT B3LYP/6-31G(d) optimal structures and profiles along with some geometrical parameters and the frontier orbitals along with the corresponding values (DFT rB3LYP/6-31G(d) for the THF solution) of the carbazolyl and cyano-substituted TPB derivatives

The view on theoretically calculated absorption spectra of the differently carbazolyl and cyano-substituted TPB derivatives (**Fig. 4.21 (a)**) indicates, that all the compounds under consideration absorb light in the UV and near UV region. Thus, the high energy region contains bands, which can be assigned to strongly allowed π–π* transitions within benzonitrile [285] and carbazole units. In turn, bands at ca. 277 and 315 nm occur due to the local excitation of the carbazole fragment [222] and can be attributed to $S_0 \rightarrow S_{4\text{-}15}$ transitions. Apparently, the low energy spectral region displays the differences, caused by the variety in substituents orientation. The compounds exploiting *meta*-substitution, i.e. ***m*-TPB-Cz**, ***m*-TPB-2Cz**, ***p*-TPB-*m*-Cz**, show very low intensity $S_0 \rightarrow S_1$ excitation manifested by HOMO→LUMO transition at 380-410 nm, which can occur due to ICT. On the contrary, theoretical UV/Vis spectra of ***p*-TPB-Cz** and ***p*-TPB-2Cz** exhibit broad low energy bands assigned to $S_0 \rightarrow S_{2\text{-}4}$ transitions, maintaining weak $S_0 \rightarrow S_1$ excitations (HOMO→LUMO) as well. However, mainly HOMO→LUMO+1 and HOMO-1→LUMO+1 processes are involved in $S_0 \rightarrow S_{2\text{-}4}$ transition. But due to the fact of HOMO, HOMO-1 and LUMO, LUMO+1, respectively, being of degenerate nature [242] , the above mentioned transitions, involving the donating 3,6-di-*tert*-butyl-carbazolyl and accepting benzonitrile fragments, can be attributed to ICT as well. The absorption of *para*-substituted compounds is obviously more bathochromically shifted than that of *meta*-compounds, owing to the efficient conjugation between the chromophores.

4.5.3. Thermal properties

All the bipolar derivatives exhibit remarkably high T_{ID} (401-480 °C) due to the exploitation of thermally stable TPB [237,250] fragment and the rigid carbazole [245] unit (**Table 4.9**). Moreover, di-carbazolyl-substituted compounds, ***p*-TPB-2Cz** and ***m*-TPB-2Cz**, display significantly higher T_{ID} (480 and 442 °C, respectively) comparing to their mono-substituted analogues. Interestingly, *para*-substituted TPB derivatives display T_{ID} at higher temperatures, than the *meta*-substituted ones. This observation can be attributed to the more efficient *para*-conjugation, which can stabilize more planar structures and inhibit intramolecular rotations, leading to higher T_{ID}.

Table 4.9. Thermal characteristics of the carbazolyl and cyano-substituted TPB derivatives

Compound	T_{ID} [a] [°C]	T_g [b] [°C]	T_{cr} [b] [°C]	T_m [b] [°C]
***p*-TPB-Cz**	419	228	274	326
***p*-TPB-2Cz**	480	210	320	382
***m*-TPB-Cz**	401	128	235	247
***m*-TPB-2Cz**	442	158	-	-
***p*-TPB-*m*-Cz**	422	152	205	290

[a] Determined by TGA. [b] Determined by DSC.

As the investigated compounds contain a prone to crystallization TPB fragment and bulky, but short *tert*-butyl groups, all of them, except for di-carbazolyl-substituted ***m*-TPB-2Cz**, were obtained after purification as white needle-like crystals. The absence of the crystalline form in ***m*-TPB-2Cz** can be explained by the sterical screening of the TPB core by two twisted carbazolyl fragments (see geometry optimization, **Fig. 4.20**), which results in the prevention of molecular packing. The glass-forming capabilities of the studied D-A molecules were assessed by performing DSC measurements (**Table 4.9**). The melting (T_m) in the first heating of DSC traces of ***p*-TPB-Cz** and ***p*-TPB-2Cz** was followed by the appearance of T_g / T_{cr} and T_g in cooling and T_g / T_m and T_g / T_{cr} /T_m during the second heating, proving the coexistence of amorphous and crystalline phases. In turn, the first heating scans of ***m*-TPB-Cz** and ***p*-TPB-*m*-Cz** indicated only endothermic melting peaks, whereas cooling resulted in the complete phase transformation to the glassy state (can be evidenced by the absence of T_{cr} and T_m, as well as the appearance of characteristic glass transition signals in the second heating scans). ***m*-TPB-2Cz** exhibited only T_g. All the target compounds displayed remarkably high T_g values ranging from 128 to 228 °C. A similar trend, compared to T_{ID}, can be observed for the glass transition temperatures: compounds featuring *para*-substitution show 52-100 °C higher T_g, than the *meta*-substituted ones. To conclude, the involvement of *meta*-conjugation leads to the formation of stable molecular glasses.

4.5.4. Optical and photophysical properties

UV/Vis and PL spectra of the compounds under consideration were accessed in the media of different rigidity, i.e. 10^{-5} M hexane solution, solid solution in Zeonex polymer and neat film, providing an opportunity to investigate the effect of

molecular conformations and packing on the optical characteristics (**Fig. 4.21 (b)**). The absorption spectra (hexane solutions) of the bipolar TPB derivatives range to ca. 360 nm, clearly featuring bands originating from the strongly allowed π–π* transitions of the benzonitrile fragment [285] (250-280 nm) and the sharp peaks at ca. 300 nm assigned to carbazole monomer excitations [222]. As expected, the bands at 300 nm are more expressed in ***p*-TPB-2Cz** and ***m*-TPB-2Cz**, comprising two carbazolyl units. The differences between the molecules with various substituent positions can be observed in the lower energy region. Well-resolved $S_0 \rightarrow S_1$ bands occur in the absorption of substituted TPBs due to the n–π* transitions within the carbazole units, being better expressed in *para*-conjugated molecules. This observation can be attributed to good electronic coupling and, hence, a certain degree of the CT character [286] between the donating and accepting parts of the molecule, in agreement with the slight HOMO/LUMO overlap (see section 4.5.2). The absorption of the neat films and solid solutions in polymer matrix maintains the features of solutions' spectra, though the bands were found to be less resolved in the solid state. Apparently, experimentally obtained UV/Vis spectra show some discrepancy with the calculated ones. Thus, no well-expressed ICT bands were observed in the experimental absorption, indicating that donating 3,6-di-*tert*-butyl-carbazolyl and accepting nitrile moieties are spatially separated by the twisted core TPB fragment.

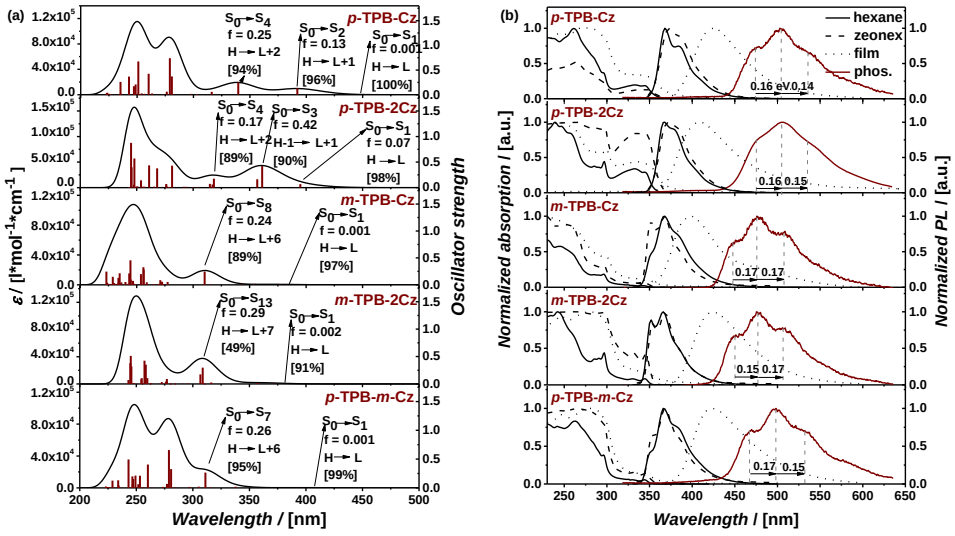

Fig. 4.21. a) Theoretically calculated UV/Vis spectra (TD-DFT B3LYP/6-31G(d) method in vacuum) and b) UV/Vis and PL (λ_{ex} = 310 nm) spectra of the carbazolyl and cyano-substituted TPB derivatives recorded for 10^{-5} M hexane solutions, solid solutions in Zeonex (1 wt.% of compound), deposited films and phosphorescence spectra recorded for the solid solution in Zeonex at 77K (delay 10 ms, integration time 50 ms), respectively

Upon the excitation at 310 nm all the differently carbazolyl and cyano-substituted TPB derivatives exhibited deep violet PL (λ_{max} = 368 nm) featuring vibronic structure both in solid and liquid solutions (**Fig. 4.21 (b)**). Maintenance of

vibronic mode in PL spectra of Zeonex solutions suggests, that intramolecular motions are restricted in the rigid medium. Interestingly, *meta*-carbazolyl-substituted derivatives, i.e. ***m*-TPB-Cz**, ***m*-TPB-2Cz** and ***p*-TPB-*m*-Cz**, display an additional band at 351 nm (more expressed in solid solutions PL), comparing to *para*-carbazolyl-substituted analogues. Evidently, this band appears due to the poor electronic coupling of the carbazole unit with the substituted core, which is caused by interrupted conjugation. While peaks at 351 and 368 nm can be assigned to the PL of locally excited carbazole unit [222], pronounced as a shoulder band at 387 nm clearly originates from the CT emission. In turn, PL of the deposited films of the TPB derivatives is by 32-56 nm red-shifted comparing to those of liquid and solid solutions. Broad profile, smeared out vibronic mode and long tail at lower energies indicate, that molecules in the thin layer are packed both in twisted and planar conformations, suggesting the possibility of long-living excited species formation as well.

Compounds with *para*-linkages, ***p*-TPB-Cz** and ***p*-TPB-2Cz**, exhibited remarkably high PLQYs (0.96 and 0.90, respectively) in hexane solutions, owing to efficient conjugation and slight HOMO/LUMO overlap, while the PL efficiency of ***m*-TPB-Cz**, ***m*-TPB-2Cz** and ***p*-TPB-*m*-Cz** is drastically quenched (η = 0.13-0.19), consistently with the theoretically calculated data (**Table 4.10**). While the PLQY of *para*-substituted compounds remained similar upon the incorporation into the rigid polymer matrix, PLQY of *meta*-substituted derivatives enhanced 2.5 times due to the restriction of intramolecular rotations. Interestingly, while PL efficiency of *para*-substituted molecules reduced significantly due to the π-π stacking in the neat films, comparing to hexane solutions, two-fold increase was observed for ***m*-TPB-Cz** and ***p*-TPB-*m*-Cz**, giving a hint of the possibility of the AIEE phenomenon. We can explain this observation by the restriction of intramolecular rotations [50] without the planarization of the molecular structure.

PL decay transients were accessed for the determination of the major relaxation pathways of the carbazolyl and cyano-substituted TPB derivatives in various media. The hexane solutions of all the compounds under consideration were found to follow single exponential decay with τ 2.44–4.39 ns (**Table 4.10**). Consistently with high PLQY values, *para*-substituted compounds ***p*-TPB-Cz** and ***p*-TPB-2Cz** exhibited shorter τ indicative of the facilitated $S_1 \rightarrow S_0$ transition, while their *meta*-substituted analogues displayed by ca. 1.5 ns longer decays. In turn, molecular suspensions in zeonex matrix can be best described by the biexponential mode. The decays of all the D–A TPB derivatives feature dominant long component, which could occur due to the triplet excited states contribution, which is consistent with the phosphorescence observed even at room temperature. Noteworthy, the deposited films of the target compounds can be described by the triple-exponential model with remarkably high values of the long component (up to 66 ns), giving a hint of the triplet state assistance as well.

All the differently carbazolyl and cyano-substituted TPB derivatives exhibited intense phosphorescence even at room temperature. For the sake of obtaining better resolved spectra phosphorescence was recorded at 77K as well (**Fig. 4.21 (b)**). The position and profile of the spectra suggest, that the triplet emission originates from

the carbazole locally excited states [257]. Three vibronic peaks with equal energy separation of 0.14-0.17 eV confirm the carbazole involvement in the $^3\pi\pi^*$ triplet T^1 state of this molecule [44]. The triplet energy values (**Table 4.10**) were found to be moderately high (2.68-2.82 eV). Noteworthy, ***m*-TPB-Cz** and ***m*-TPB-2Cz**, employing carbazole units in *meta*-positions, display by ca. 0.13 eV higher triplet energy, than other materials of the series, which can be attributed to the poorer electronic coupling of *meta*-linked carbazole to the central chromophore comparing to the *para*-connection [286].

Table 4.10. Photophysical characteristics of the carbazolyl and cyano-substituted TPB derivatives

Compound	10^{-5} Hexane solution		Neat film		Zeonex film		
	η^a	τ^b	η^a	τ^b	η^a	τ^b	$E_T{}^c$ [eV]
***p*-TPB-Cz**	0.96	2.44	0.30	2.51 [17.3%], 12.95 [43.05%], 44.48 [39.7%]	0.92	3.15 [28.6%], 6.44 [71.4%]	2.68
***p*-TPB-2Cz**	0.90	3.20	0.25	2.36 [40.6%], 8.40 [30.5%], 26.06 [28.9%]	0.97	1.96 [25.5%], 3.82 [74.5%]	2.68
***m*-TPB-Cz**	0.15	4.39	0.31	0.92 [18.6%], 5.31 [36.1%], 18.22 [45.3%]	0.36	2.49 [10.3%], 7.32 [89.7%]	2.81
***m*-TPB-2Cz**	0.19	4.29	0.22	2.33 [6.5%], 21.99 [28.3%], 66.11 [65.2%]	0.46	2.53 [4.0%], 6.95 [96.0%]	2.82
***p*-TPB-*m*-Cz**	0.13	4.06	0.29	1.49 [21.5%], 11.56 [21.3%], 50.37 [57.2%]	0.32	0.87 [3.20%], 7.09 [96.8%]	2.72

[a] PLQY estimated with the usage of the integrating sphere. [b] PL decay lifetimes (χ^2 in the range 1.00-1.20). [c] Determined from the half blue-edge onset of the phosphorescence spectra measured in Zeonex matrix at 77K.

Such advantages, as the D–A molecular architecture, well spatially separated HOMO and LUMO and the observation of phosphorescence in the synthesized compounds, give a hint of the possibility of DF occurance. There are two major mechanisms of the DF – TADF [48] and TTA [287] – which can take place depending on the peculiarities of the emitting molecule and the surrounding medium. Both of these mechanisms allow to convert triplet into emissive singlet states, and, hence, to enhance the quantum efficiency of the target devices. For the upconversion by the TADF mechanism to arise, a small splitting between the ^{1}CT and ^{3}LE, is desirable [44]. Since the position of phosphorescence is only slightly affected by the solvent polarity and the singlet emission of all the compounds under consideration in hexane solutions is peaked at ca. 367 nm and lacks the CT mode (**Fig. 4.21 (b)**), the necessity of investigating the solvatochromism [227] arose. For the sake of convenience, the investigation of DF only for ***p*-TPB-2Cz** is presented.

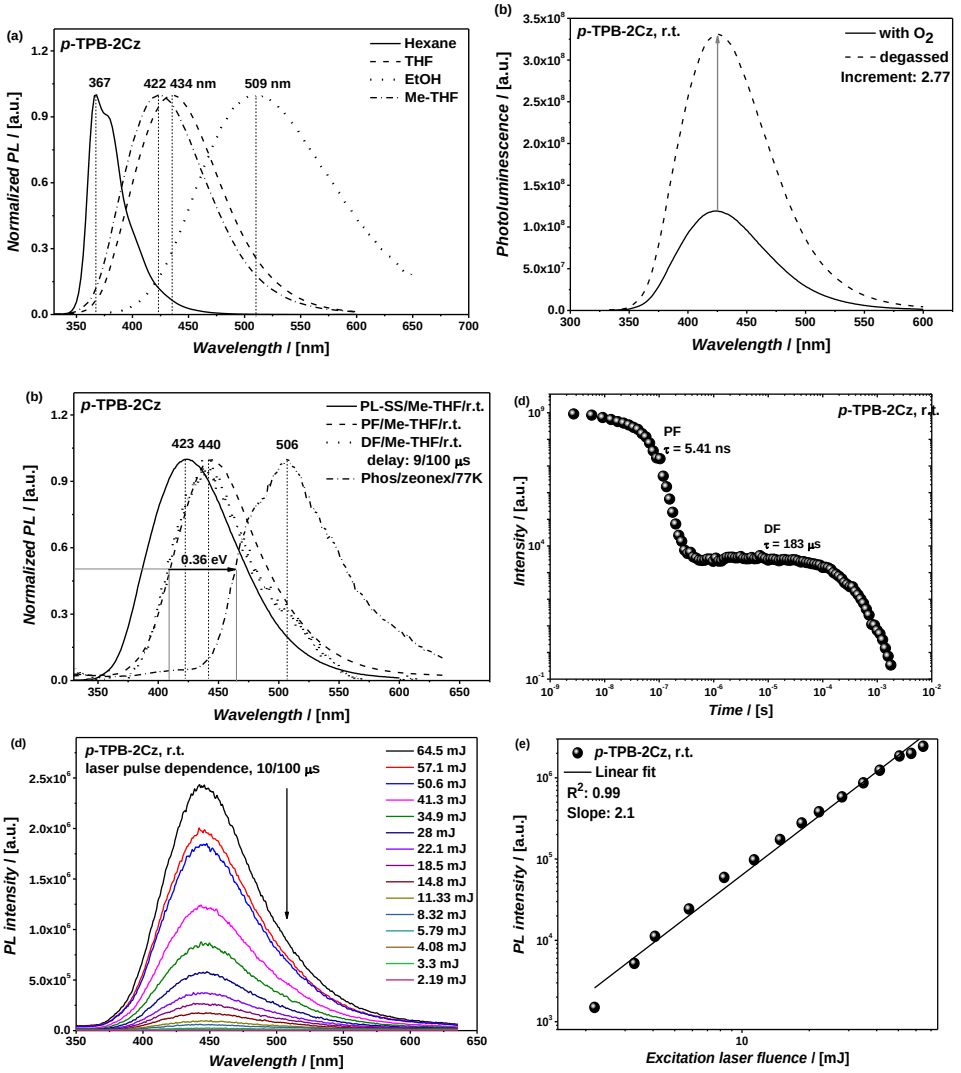

Fig. 4.22. (a) PL spectra of ***p*-TPB-2Cz** in various solvents; (b) SS PL spectra of oxygenated and degassed Me-THF solutions; (c) SS and time-resolved (Nd-YAG laser, λ_{ex} = 355 nm) PL spectra (d) PL decay lifetime curve; (e, f) dependence of the PL intensity on the excitation laser fluence (degassed solutions in Me-THF)

The PL spectra of the dilute solutions of ***p*-TPB-2Cz** in various solvents clearly bathochromically shift and gain a broad CT mode with the enhancement of solvent polarity (**Fig. 4.22 (a)**). As the PL intensity is drastically quenched in ethanol solutions, and THF lacks the ability to form transparent glass at low temperatures, Me-THF was chosen as the solvent for the further investigation. The contribution of the triplet excited states to the overall emission was determined by comparing the PL intensity in oxygen-saturated and degassed Me-THF solutions (**Fig. 4.22 (b)**). The 2.77-fold enhancement of CT emission upon the degassing, as well as a good match of the spectra obtained in non-degassed and degassed

solutions, prove that triplet excited states participate in the emission [46]. In turn, intense DF was observed in the time-resolved measurements of the degassed Me-THF solution (delay 9 μs, integration time 100 μs). The comparison of the steady-state (SS) and time-resolved (**Fig. 4.22 (c)**) spectra shows, that PF, recorded with short delay of 2 ns, as well as the DF, are by 17 nm bathochromically shifted, comparing to the SS emission, confirming the stabilization of the CT emission. The Me-THF solution of ***p*-TPB-2Cz** did not exhibit phosphorescence at room temperature, therefore phosphorescence of Zeonex film at 77K is presented for the calculation of ΔE_{ST}. Hence, the estimated ΔE_{ST} was found to be 0.36 eV. The PL decay transient (**Fig. 4.22 (d)**) shows that PF and DF follow clear exponential decay laws with the estimated lifetimes of 5.41 ns and 183 μs, respectively. Finally, for the determination of the mechanism of delayed emission the dependence of the ***p*-TPB-2Cz** PL intensity on the excitation laser fluence was recorded (**Fig. 4.22 (e, f)**). As expected, the PL intensity drops with the reduction of the laser fluence. The linear fit of the DF intensity dependence on the excitation dose characterized by slope 2 indicates the bimolecular origin of delayed emission, i.e. the triplet-triplet annihilation [44,251].

Similar experiments, as the one described above, were performed for all the materials of the series. Interestingly, only the compounds, bearing the accepting CN-groups in *para*-positions, i.e. ***p*-TPB-Cz**, ***p*-TPB-2Cz** and ***p*-TPB-*m*-Cz**, exhibited delayed emission *via* the TTA mechanism. The absence of DF in exclusively *meta*-substituted compounds, ***m*-TPB-Cz** and ***m*-TPB-2Cz**, originates from the poor electronic coupling between the chromophores, leading to the weak CT character. As the final benchmark, ΔE_{ST} is a medium-dependent parameter, and it is known, that in some molecules TADF and TTA mechanisms may coexist [44,46,288]. Therefore, the investigation of DF in other media, except for Me-THF, may prove successful.

4.5.5. Electrochemical and photoelectrical properties

All the investigated D–A compounds exhibit reversible oxidation and reduction processes in their CV scans regardless of the substituents' position, presenting proof of the electrochemical stability of the molecules (**Fig. 4.23 (a)**, **Table 4.11**). Similar values of half-wave oxidation ($E^{1/2}_{ox}$ 0.71 – 0.90 V) and reduction ($E^{1/2}_{red}$ -2.18 – -2.40 V) potentials suggest that carbazole [257] and benzonitrile [289] fragments are involved in anodic and cathodic processes, respectively. This observation is in agreement with the PCz localized HOMO and concentrated on cyano-biphenyl (for ***p*-TPB-2Cz** and ***m*-TPB-2Cz**) or dicyano-terphenyl (for ***p*-TPB-Cz**, ***m*-TPB-Cz**, ***p*-TPB-*m*-Cz**) fragments LUMO (see **Fig. 4.20**).

The approximations $IP_{SS} = |e|(4.8 + E_{ox}^{1/2})$ and $EA_{SS} = |e|(4.8 - E_{red}^{1/2})$ were involved for the elucidation of solid state *IP* and *EA*, respectively [203] (**Table 4.11**). The IP_{SS} values are moderately low for all the compounds of the series (5.51-5.70 eV). Evidently, involving *para*-conjugation ***p*-TPB-Cz** and ***p*-TPB-2Cz** display lower IP_{SS}, than *meta*-analogues, due to the more facilitated CT from HOMO to LUMO. EA_{SS} values are close (2.40-2.62 eV) for all the studied materials. Low EA_{SS}

indicates the weak electron-accepting strength of benzonitrile derivatives, which, however, proves to be advantageous for the blue-emitters design.

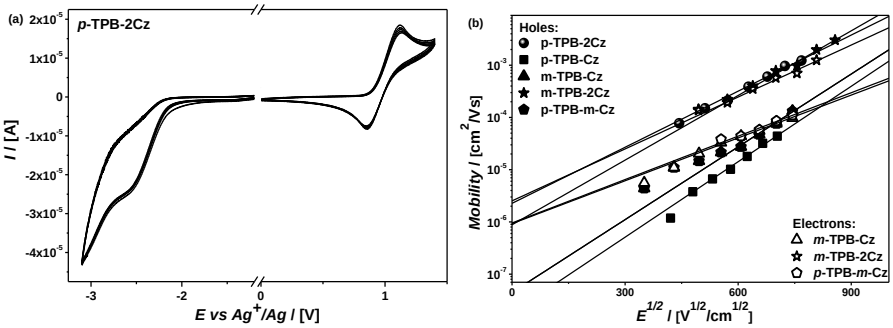

Fig. 4.23. (a) CV curves recorded for 10^{-3}M THF solutions and (b) electric field dependencies of the hole and electron drift mobility, measured by the TOF method at room temperature, of the carbazolyl and cyano-substituted TPB derivatives

Noteworthy, the experimentally estimated *IPs* and *EAs* are by ca. 0.4-0.7 eV higher, than the absolute values of E_{HOMO} and E_{LUMO}, obtained from DFT calculations. Obviously, the discrepancy between the theoretical and electrochemical data is a result of performing calculations lacking medium-related factors [266].

Table 4.11. Electrochemical and photoelectrical characteristics of the carbazolyl and cyano-substituted TPB derivatives

Compound	$E^{1/2}_{ox\ Fc+/Fc}$ [a] [V]	$E^{1/2}_{red\ Fc+/Fc}$ [a] [V]	IP_{SS} [b] [eV]	EA_{SS} [c] [eV]	$E_{g(CV)}$ [d] [eV]	IP_{EP} [e] [eV]
***p*-TPB-Cz**	0.71	-2.27	5.51	2.53	2.98	5.47
***p*-TPB-2Cz**	0.80	-2.24	5.60	2.56	3.04	5.36
***m*-TPB-Cz**	0.85	-2.38	5.65	2.42	3.23	5.51
***m*-TPB-2Cz**	0.90	-2.40	5.70	2.40	3.20	5.58
***p*-TPB-*m*-Cz**	0.90	-2.18	5.70	2.62	3.08	5.58

[a] Determined by CV in dilute THF solutions. [b] Estimated from the halfwave oxidation potential by using the relationship $IP_{SS} = |e|(4.8 + E_{ox\ Fc+/Fc}^{1/2})$. [c] Estimated from the halfwave reduction potential by using the relationship $EA_{SS} = |e|(4.8 - E_{red\ Fc+/Fc}^{1/2})$. [d] Calculated by using the equation $E_{g\ (CV)} = IP_{SS} - EA_{SS}$. [e] Determined from EP spectra.

The values of ionization potentials of solid layers IP_{EP} (**Table 4.11**) are slightly lower than those elucidated from CV, but, evidently, show the same tendency: *para*-conjugation leads to the lower *IP* and, hence, to the more facilitated hole injection.

4.5.6. Charge-transporting properties

In order to study the charge transporting properties of synthesized compounds, the TOF technique was used. In the ***m*-TPB-Cz** layer, the transit times for both holes and electrons were observed in the log-log scale indicating the ambipolar charge transport of this compound. A similar behaviour was observed for ***m*-TPB-2Cz** and ***p*-TPB-*m*-Cz**, however, only hole-transporting properties were obtained for ***p*-TPB-Cz** and ***p*-TPB-2Cz** (**Fig. 4.23(b)**). The shapes of the TOF current transients for holes and electrons were very similar for all the studied materials. In addition, the

transit times were not observed in the linear scale, showing dispersive charge transport of either holes or electrons. The hole and electron mobilities for ***p*-TPB-2Cz** and ***m*-TPB-2Cz** were found to be in the range from $7.8 \cdot 10^{-5}$ to $3.15 \cdot 10^{-3}$ cm^2/Vs at electric fields from $3.9 \cdot 10^5$ to $7.4 \cdot 10^5$ V/cm, while those for the other compounds were found to be lower approximately by one order of magnitude, falling in the range from $1.1 \cdot 10^{-6}$ to $1.4 \cdot 10^{-4}$ cm^2/Vs at electric fields from $1.1 \cdot 10^5$ to $5.6 \cdot 10^5$ V/cm. Relatively similar values for the electron and hole mobilities of ***m*-TPB-Cz**, ***m*-TPB-2Cz** and ***p*-TPB-*m*-Cz** were observed, leading to the balance of holes and electrons. The linear dependencies of hole and electron mobilities of the derivatives versus the square root of the electric field ($E^{1/2}$) with good agreement to Poole–Frenkel relationship $\mu = \mu_0 \cdot exp(\alpha \cdot E^{1/2})$ were obtained, as it had previously been observed for other organic amorphous semiconductors [290,291]. In turn, the field dependence of electron mobility for ***m*-TPB-Cz**, ***m*-TPB-2Cz** and ***p*-TPB-*m*-Cz** was found to be lower than that of the hole mobility. Apparently, the energetic disorder parameters could be different for holes and electrons in the molecular layers; yet, such differences lead to the differences in hole and electron mobility values as well as in the hole and electron field dependences [205].

4.5.7. Performance in organic light emitting diodes

In order to demonstrate the potential of the *para*-substituted compounds as emitters and the *meta*-substituted derivatives as hosts, fluorescent OLEDs with the architecture of ITO/CuI (8 nm)/TPD (10 nm)/**host: *p*-TPB-2Cz** (20%) (60 nm)/PBD (10 nm)/Ca (50 nm)/Al (200 nm) were prepared. In device A, commercially available hole-transporting mCP was used as the host matrix for the blue-emitting compound ***p*-TPB-2Cz**, while in device B the performance of newly synthesized ***m*-TPB-2Cz** was tested (**Fig. 4.24**). The electroluminescent spectra of devices A and B are peaked at the same position, as the PL of ***p*-TPB-2Cz** thin film. However, the EL spectrum of the device A contains a long-wavelength tail, which can probably be attributed to the excimers formation. Better energy levels matching in device B leads to the shifted to deeper blue region CIE coordinates of the device (**Table 4.12**). Current density–voltage–luminance curves of the blue OLEDs are shown in **Fig. 4.24 (e, f)**. The current density was increased threefold, while the turn-on voltage was decreased ca. 1.5 times by using ***m*-TPB-2Cz** as a host. However, the maximum brightness of device A was found to be higher than that of device B.

As the final benchmark, device B, utilizing ***m*-TPB-2Cz** as the host matrix for ***p*-TPB-2Cz**, demonstrated astonishingly high maximum EQE of 14.1 %, which can be assigned to the improved HOMO/LUMO and triplet energy levels of the host and the guest, the ambipolar charge transport of the host and the involvement of the triplet levels of emitter to the overall emission.

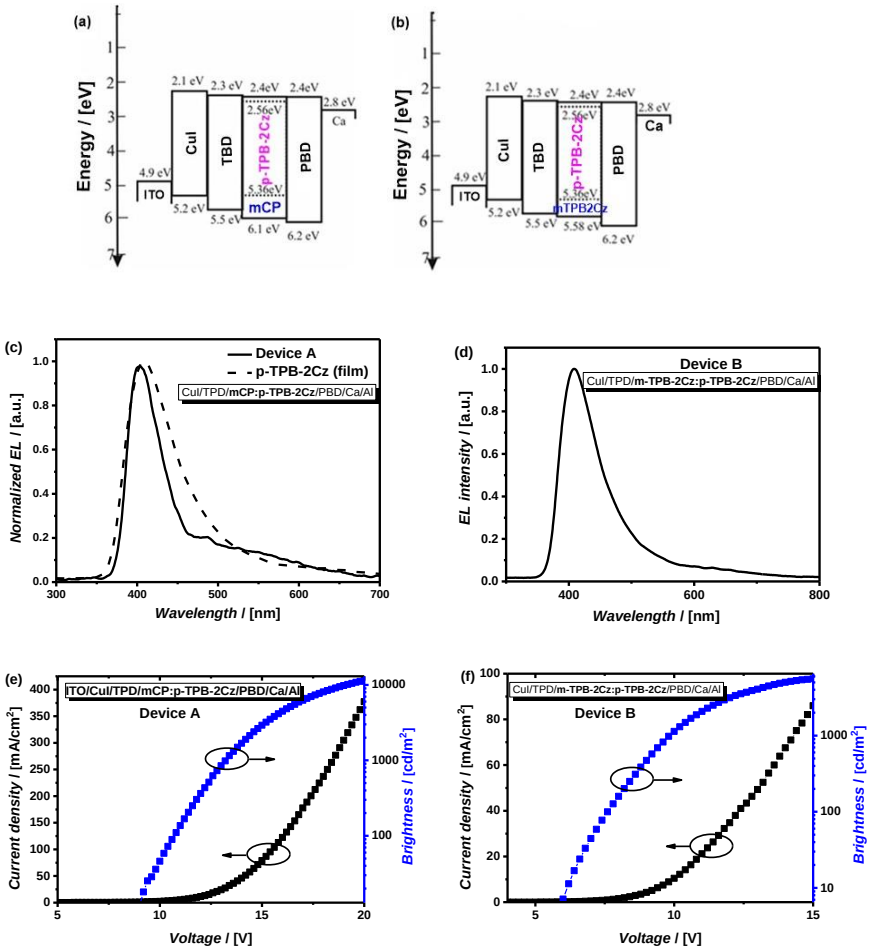

Fig. 4.24. (a, b) The energy levels of the materials; (c, d) electroluminescence spectra; (e, f) current density-voltage-luminance curves of devices A and B

Table 4.12. Electroluminescent properties of blue fluorescent devices A and B

Device	host	V_{on} [a] [V]	*Max. brightness* [b] [cd m^{-2}]	η_C [c] [cd A^{-1}]	η_P [d] [lm W^{-1}]	EQE_{max} [e] [%]	*CIE* [f] [x, y]
A	**mCP**	8.4	11450	3.7	0.85	3.5	0.25, 0.23
B	***m*-TPB-2Cz**	5.8	5500	11.1	4.20	14.1	0.22, 0.19

[a] Turn-on voltage. [b] Maximum brightness. [c] Maximum current efficiency. [d] Maximum power efficiency. [e] Maximum external quantum efficiency. [f] Color coordinates.

In conclusion, a series of bipolar TPB-based compounds, bearing carbazolyl and cyano-substituents in *para*- and *meta*-positions, was synthesized and characterized. The orientation of the substituents was found to affect greatly the properties of the compounds. Thus, the compounds involving *para*-conjugation, show higher T_{ID} and T_g, lower *IP*, exclusively hole transport and higher quantum efficiencies in non-polar media; while molecules with *meta*-linkage display an ability to form stable molecular glasses upon thermal annealing, ambipolar charge

transport, higher E_T and higher PLQY in the solid state. Interestingly, the compounds comprising accepting nitrile groups in the *para*-position, exhibit strong delayed fluorescence *via* triplet-triplet annihilation upconversion mechanism. A derivative with exclusively *para*-conjugation displayed good performance in OLED as a blue fluorescent emitter, while a compound with *meta*-linkages proved to be a successful host matrix in combination with a *para*-substituted guest. Thus, by varying the amount and position of electron donating and accepting substituents it is possible to construct promising emitters (*para*-substituted derivatives) and hosts (*meta*-substituted derivatives) for blue DF OLEDs and PhOLEDs, respectively.

4.6. Symmetrical and asymmetrical 1,4,5,8-naphthalenetetracarboxylic acid dianhydride derivatives

Currently, the main photovoltaic technologies are based on inorganic materials. OSCs are a promising source of alternative energy [292]. Lately, they have attracted much attention due to their advantages such as light weight, potential low cost, feasibility of large area fabrication [293,294] on flexible substrates [295]. According to their working principle, organic solar cells can be divided into two major classes: dye sensitized solar cells (DSSCs) [296] and heterojunction solar cells (HSCs) [297]. HSCs can be further differentiated by the production process: either solution processing or vacuum deposition. Vacuum processed small molecules are especially attractive for solar cells due to the well-defined molecular structure and monodisperse molecular weight as well as superior chemical purity via thermal gradient sublimation, and the possibility to easily deposit multilayer devices [298]. Recently, considerable efforts have been dedicated to the enhancement of the power conversion efficiencies of small molecule OSCs, involving the development of new electron donor materials [299] and improving the collection of charge carriers [300]. Another approach towards the improvement of OSC performance is design and preparation of prospective ETM. The standard material here is C_{60}, which has the disadvantage of parasitic absorption and does not allow a variation of the LUMO energy to fine tune the open circuit voltage of the cells. Various ETMs, such as BCP [301], TPBi [302] and Bphen [303] have been integrated into small molecule OSCs [304]. However, BCP, which found wide usage as an ETL in OLEDs [35] and OSCs [305], is denoted by such disadvantages, as thermal instability, and easy crystallization in the presence of moisture and at high temperatures [306]. The derivatives of naphthalenetetracarboxilic dianhydride are good candidates for the electron transporting layer in OPVs due to their high electron affinity, planar configuration, excellent electron transport and tunable optical and electrochemical properties [15].

In this chapter synthesis and the results of optical, electrochemical, photophysical, and computational studies of the two groups of 1,4,5,8-naphthalenetetracarboxylic dianhydride derivatives employing symmetrical and asymmetrical molecular architecture, are presented. The charge transport investigation and the performance of the compounds as ETMs in HJCs is reported as well. The materials presented here are denoted by excellent properties and some prove to be superior to the reference material C_{60}.

4.6.1. Synthesis

The chemical structures and the synthetic routes towards the symmetrical derivatives **ND1–ND4** are presented in **Schemes 4.9** and **4.10**. The synthesis of symmetric electron accepting compounds is a simple and efficient one-step procedure in which the commercially available 1,4,5,8-naphthalenetetracarboxylic dianhydride (NTCDA) is condensed with the appropriate primary aryl-amine in the presence of basic and high boiling pyridine. This method is clean and high yielding [307]. All the compounds **ND1**−**ND4** were obtained with yields of 79−97%. Compounds **ND1** [187], **ND2** and **ND3** [188] are prepared as model compounds for the direct comparison of the properties with other molecules of the series.

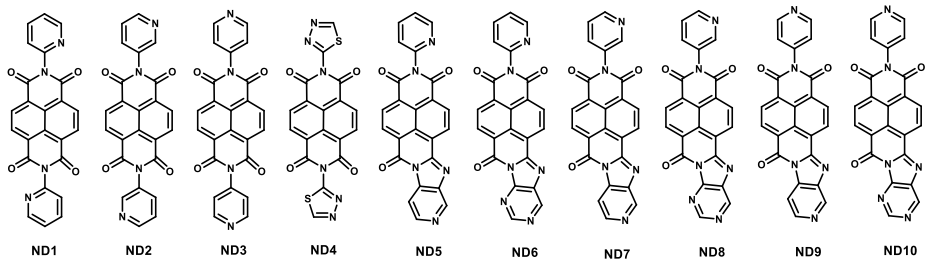

Scheme 4.9. Chemical structures of symmetrical and asymmetrical NTCDA derivatives

The synthetic strategy for obtaining the asymmetrical target materials **ND5**−**ND10** includes several steps (**Scheme 4.10**).

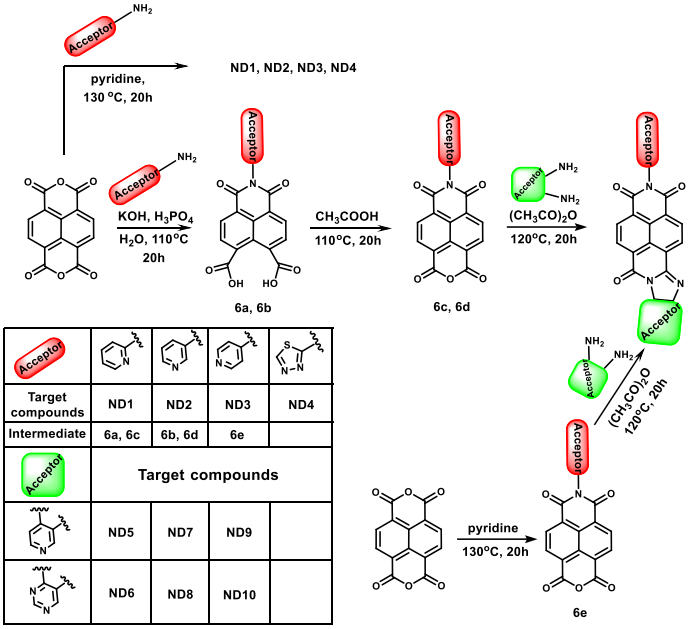

Scheme 4.10. Synthetic routes towards symmetrical and asymmetrical NTCDA derivatives

Intermediates **6a** and **6b** are prepared by the high-yield monofunctionalization through pH-controlled reaction of the primary amine with NTCDA [308]. The

further reaction with acetic anhydride generates the dissymmetric molecular components **6c** and **6d**. Compound **6e** was synthesized employing a similar condensation reaction as the symmetrical derivatives, since pH-controlled monofunctionalization of NTCDA by 4-aminopyridine resulted in a small yield of the target intermediate compound (unlike in the case of **6a** and **6b**). The final step of the asymmetric compounds synthesis involves the condensation reaction of the monosubstituted intermediates with the appropriate 1,2-diamine containing pyridinyl or pyrimidinyl moieties.

The synthesized compounds were purified by the two-step vacuum temperature gradient sublimation. All the molecules exhibit characteristic signals at 8.69–8.87 ppm in their ^{1}H NMR spectra, corresponding to the core protons of NTCDA derivatives [309], as well as the peaks in the range of 160.1–162.9 in ^{13}C spectra, characteristic for the carbons of the anhydride group. The signals in the weak field (9.12 –10.10 ppm) of the proton spectra of the asymmetric derivatives can be attributed to the protons of the pyridinyl and pyrimidinyl moieties condensed with the imidazole ring. The formation of the imidazole ring can also be proven by the presence of 181 ppm peaks in the carbon spectra of semiperinones, corresponding to the carbon of the amide group.

4.6.2. Theoretical investigation

The molecular structure of the NTCDA derivatives is determined by the rigid planar condensed core part [310] and the aromatic substituents located in the other plane. In case of symmetrical compounds **ND1−ND4,** the substituents of the imide part are attached almost orthogonally to the plane of the NTCDA core (**Fig. 4.25**).

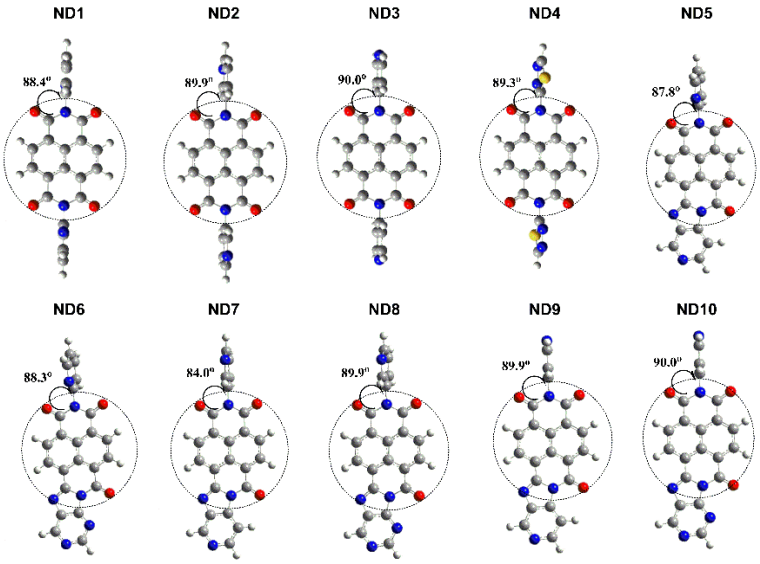

Fig. 4.25. The view on the DFT B3LYP/6-31G(d) optimal structures of NTCDA derivatives in vacuum

Exact perpendicular displacement of molecular parts is observed for **ND3**, containing a pyridin-4-yl fragment. What concerns the 1,3,4-thiadiazol-2-amine-substituted compound, **ND4**, the dihedral angle of 89.30° can be attributed to the carbonyl–sulfur repulsive interactions. The large angle between the core and the side units indicates weak conjugation between the parts of the molecules. Concerning the asymmetrical compounds **ND5**−**ND10**, their molecular skeleton is more planar than that of the symmetrical ones, due to the presence of the annulated imidazolyl ring. Interestingly, while comparing the pairs **ND5** and **ND6**, **ND7** and **ND8**, **ND9** and **ND10**, respectively, monofunctionalized with an appropriate pyridinamine, it can be observed that the dihedral angle between the planar and twisted aromatic parts is larger in the case of pyrimidinyl containing molecules, which could be explained by the higher electron-accepting strength of the pyrimidinyl moiety additionally increased by the carbonyl–nitrogen interactions.

Table 4.13. The theoretically calculated HOMO/LUMO energies, thermal and electrochemical characteristics of NTCDA derivatives

Compound	E_{HOMO} [a] [eV]	E_{LUMO} [a] [eV]	$E_{red\ Fc+/Fc}^{1/2}$ [b] [V]	EA_{SS} [c] [eV]	T_m [d] [°C]	T_{ID} [e] [°C]
ND1	-7.19	-3.59	-0.96	3.84	475	493
ND2	-7.21	-3.62	-0.93	3.87	442	470
ND3	-7.22	-3.63	-0.90	3.90	457	466
ND4	-7.37	-3.78	-0.65	4.15	–	415
ND5	-6.69	-3.67	-0.85	3.95	490	507
ND6	-6.85	-3.70	-0.70	4.10	442	449
ND7	-6.70	-3.68	-0.89	3.91	495	499
ND8	-6.86	-3.71	-0.76	4.04	458	461
ND9	-6.71	-3.69	-0.82	3.98	503	506
ND10	-6.87	-3.72	-0.82	3.98	403	413

[a] Calculated by DFT B3LYP/6-311G(d,p) approach for the DMF solution. [b] Determined by CV in 10^{-3} M DMF solutions from the first reduction wave. [c] Estimated from the half-wave potential $E_{red}^{1/2}$ by using the relation $EA_{SS} = |e|(4.8 + E_{red}^{1/2})$. [d] Determined by DSC. [e] Determined by TGA.

The values of theoretically calculated LUMO and HOMO energies of the studied molecules (**Table 4.13**) fall quite low in the energy scale indicative of the facilitated electron injection process in the compounds under consideration [311]. E_{LUMO} of **ND1**−**ND3** are close and comparable, while the E_{LUMO} of **ND4** is positioned much lower (-3.78 eV) due to the presence of 1,3,4-thiadiazolyl moiety, which is characterized by the higher accepting strength than the pyridinyl fragments. Apparently, asymmetrical compounds exhibit similar LUMO energies with the slightly lower ones found for **ND6**, **ND8** and **ND10**, bearing a pyrimidinyl unit in the condensed part.

4.6.3. Thermal properties

DSC scans, recorded for the NTCDA derivatives, revealed only melting points (except for **ND4**), indicating the crystalline state of the compounds upon the sublimation. The T_{ID} of the compounds **ND1**−**ND10** are rather high and range from 413 to 507 °C (**Table 4.13**). Symmetrical compounds **ND1**−**ND3**, containing a pyridinyl moiety, exhibit remarkably high T_{ID} with the highest value (493 °C) found

for **ND1**. The lowest T_{ID} of 415 °C was observed for **ND4**, probably, due to the decomposition of the thiadiazolyl unit. In turn, asymmetrical NTCDA derivatives, bearing a more thermally stable pyridinyl fragment in the condensed part, **ND5**, **ND7**, **ND9**, can be characterized by the higher values of the initial destruction temperature when compared to pyrimidinyl-containing members of the series. Interestingly, compounds **ND1** and **ND5**, derived from pyridin-2-amine, exhibit higher T_{ID}, when compared to other molecules under consideration, which can be explained by the additional stabilization of the –C=N− bond in the pyridine-2-yl fragment by the electron withdrawing NTCDA core.

4.6.4. Optical properties

All molecules exhibit good transparency in a wide range of the visible region and absorption in the near UV blue visible range.

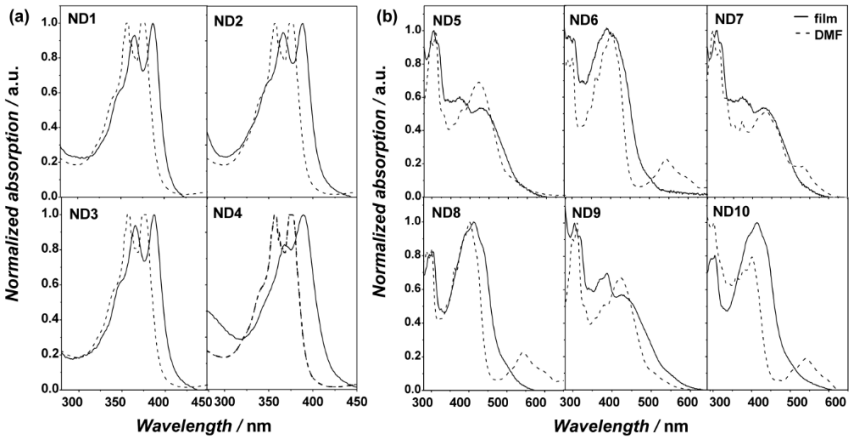

Fig. 4.26. UV/Vis spectra of 50 nm thin films and 10^{-5} M DMF solutions of (a) symmetrical; (b) asymmetric NTCDA derivatives

The symmetrical derivatives **ND1**−**ND4** (**Figure 4.26 (a)**) exhibit shapes of the spectra as it is common for NTCDA [312], showing a remarkably narrow absorption range. Evidently, the absorption of the symmetrical compounds does not depend strongly on the nature of the electron accepting moiety in the non-planar aromatic part. The dissymmetrical materials, i.e. **ND5**−**ND10**, absorb light at lower energies compared to the symmetrical molecules (**Fig. 4.26 (b)**). Thus, the rigid condensed imidazole part is responsible for the more efficient conjugation leading to the enhanced intermolecular interactions due to the π-stacking. All the semiperinones exhibit characteristic bands for the locally excited pyridine moiety in the non-planar part at 304 nm [313], as well as the located at the longer wavelengths (413−436 nm) peaks, which can be attributed to the n−π* transitions within the molecule [314]. The intensity of the n−π* transition bands is higher in the UV/Vis spectra of compounds having the pyrimidine moiety, **ND6**, **ND8** and **ND10**, due to the presence of additional nitrogen atom in the annulated part. These compounds show a remarkable blue shift in absorption spectra compared to those exploiting

pyridine in the condensed aromatic part, indicating a stronger electron accepting ability of the pyrimidine fragment. The occurrence of the peaks at 550 nm in the DMF solutions of **ND6**, **ND8** and **ND10** is observed, what can be attributed to the radical anions, which are stabilized in the solution, in contrast to the thin film [309]. The absorption spectra of the asymmetrical compounds show similar trends to those of symmetrical molecules: the red shift can be observed when comparing the spectra measured in thin films to those of DMF solutions, due to the aggregation effects. Moreover, only slight changes in the shape of the spectra and the position of bands is observed with the variation of linking topology (substitution through 2-, 3-, 4th position) of the twisted pyridinyl part.

As C_{60}, frequently used as an ETL in solar cells, exhibits parasitic absorption, referring to an optical absorption process not generating an electron/hole pair and competing with band-to-band absorption to decrease the photocurrent [15], it is useful to compare the absorptivity of the latter with that of the investigated NTCDA derivatives. A suitable electron transport material with a larger absorption onset aids to reduce the absorption in the doped layer to a higher density of the optical field in the photo-active layers hindering as well the exciton transfer from undoped C_{60} by the step in the energy gap width and reducing the quenching of excitons from the photo-active C_{60} layer. The absorption strength of the synthesized NTCDA derivatives is remarkably smaller than that of C_{60}. Thus, the intensity of the absorption bands of the symmetrical materials and **ND9** is by far lower than that of **ND10** and, moreover, C_{60}. However, the absorption onsets of **ND9** and **ND10** are higher than that of C_{60}. These observations suggest that ND compounds may show superior performance as ETLs in solar cells comparing to C_{60}.

4.6.5. Electrochemical properties

The redox behaviour of the compounds is examined in 10^{-3} M DMF solutions by using the CV method (**Table 4.13**). It should be noted that compounds **ND1**−**ND3** and **ND5**−**ND10**, containing pyridinyl moieties, linked through various topologies, show very similar behaviour when voltage is applied. All these molecules undergo two reversible one electron reductions, the first of which is the reduction of the neutral compound to a radical anion and the second one corresponds to the formation of a dianion, as it is common for many derivatives of NTCDA. On the contrary, the compound with the 1,3,4-thiadiazolyl moiety **ND4** shows multiple reversible reduction process, probably, due to the reduction of sulfur in 1,3,4-thiadiazolyl moiety [315].

The electron affinity is estimated by using the relationship $EA_{SS} = |e|(4.8 + E_{red}^{1/2})$ [203] (**Table 4.13**). The values of EA_{SS} fall in the range of 3.84 to 4.15 eV. These values make the compounds well suitable for the use in highly efficient fullerene based OSCs. The symmetrical derivatives of NTCDA substituted by various pyridine-amines, **ND1**−**ND3**, exhibit similar EA_{SS} values in the range of 3.84 to 3.90 eV, while the compound with the 1,3,4-thiadiazolyl fragment **ND4** shows the highest *EA* of 4.15 eV in this series, indicating a high accepting strength of this molecule. As for the dissymmetric target materials, those containing a pyridinyl fragment condensed with the imidazole ring (**ND5**, **ND7**, **ND9**) show similar EA_{SS}

values, while the molecules exploiting pyrimidine moiety (**ND6**, **ND8**), exhibit slightly higher values. Interestingly, the latter can be characterized by the highest EA_{SS} values of 4.10 and 4.04 eV, indicating the higher accepting ability of these molecules when compared to the one containing the pyridin-4-yl moiety (**ND10**). Moreover, it can be noted that compounds **ND9** and **ND10** exhibit similar values of EA_{SS}, irrespectively of their structural differences. In the CV scans no oxidation is observed, thus the ionization energy cannot be determined [230].

4.6.6. Charge-transporting and conducting properties

The electron mobility μ of the six selected compounds was determined by "potential mapping" (POEM) by thickness variation [154] in n-i-n electron-only devices (**Fig. 4.27 (a)**). The obtained mobility values range from 10^{-3} cm² Vs^{-1} for **ND7** and **ND9** down to 10^{-7} cm² Vs^{-1} in the case of **ND2** and **ND3**. In all the compounds, a pronounced field activation is observed, which is fitted to the Poole-Frenkel relation $\mu = \mu_0 \cdot \exp(\gamma \cdot F^{1/2})$ [316], yielding field activation coefficients in the range γ = (0.0043 .. 0.0098) (cm V^{-1})$^{1/2}$. In the case of **ND9**, the field dependence is only poorly resolved and cannot be directly fitted. From comparison to the other compounds, however, it is assumed that the Poole-Frenkel behaviour also applies to this material, provided that the physics of charge transport is similar in all the investigated compounds. Substituting the pyridinyl by the thiadiazolyl moiety in the symmetrical compounds has a strong positive effect on μ: the mobility in **ND4** is nearly two orders of magnitude higher than that in **ND2** and **ND3**.

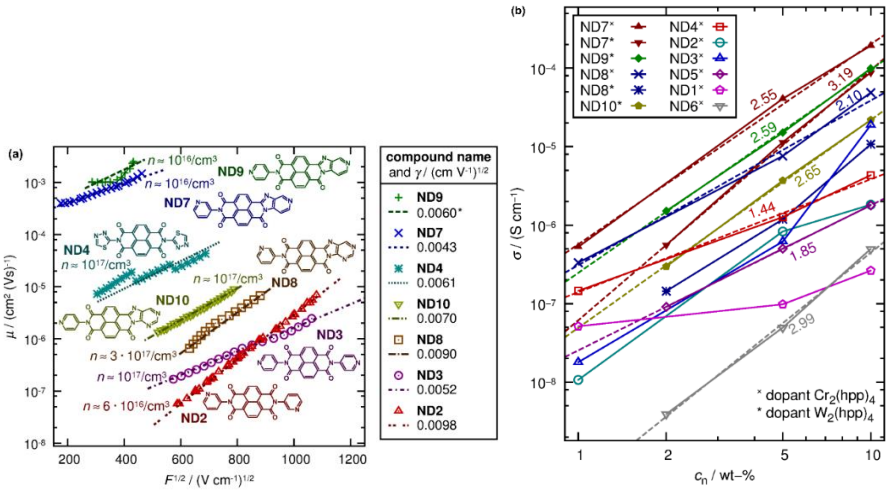

Fig. 4.27. (a) Electron mobility determined by POEM in electron-only devices, well resolving the absolute μ values and the Poole-Frenkel field activation coefficients γ (fits shown as lines) and (b) lateral conductivity σ of n-doped layers of NTCDA derivatives with varying doping concentration c. The data from **ND4**–**ND8** is fitted by power-law $\sigma \propto c^{\gamma}$ (dashed lines) with the resulting value for γ given next to each fit

An even stronger improvement of μ is achieved by annulating one pyridinyl ring, leading to asymmetric molecular structures: in compounds **ND7** and **ND9,** the highest electron mobilities in the range of 10^{-3} cm² Vs^{-1} are obtained which might

originate from an alternating brick-type [317]. The position of the nitrogen atom in the rotating pyridinyl ring does not have any significant influence on μ, as is can be seen when comparing **ND7** with **ND9**, **ND8** with **ND10**, or **ND2** with **ND3**. An additional nitrogen atom converting the annulated pyridinyl ring into pyrimidinyl, however, drastically reduces μ by three orders of magnitude, as observed in **ND8** compared to **ND7**. The additional nitrogen atom seems to largely inhibit the good orbital overlap in the stacking, leading to a mobility which is only slightly above the symmetrical pyridinyl substituted compounds **ND2** and **ND3**.

The conductivity of the investigated materials can be substantially enhanced by electrical n-doping (**Fig. 4.27 (b)**). Doping is tested with the established molecular dopants $Cr_2(hpp)_4$ and $W_2(hpp)_4$ in a concentration of 5 mol %. In compounds **ND1**−**ND8**, conductivity of $5 \cdot 10^{-8}$ S cm^{-1} (**ND6**) up to $4 \cdot 10^{-5}$ S cm^{-1} (**ND7**) can be achieved. The conductivity roughly scales with the mobility, suggesting the high-mobility materials as the most suitable candidates for the low-Ohmic doped transport layers in optoelectronic devices like solar cells.

4.6.7. Performance in bulk-heterojunction solar cells

Since the electrical properties of compounds with an asymmetrical molecular architecture prove to be more advantageous comparing to the symmetrical ones, the most promising materials **ND7** and **ND9**, as well as **ND10**, were tested as ETMs in the ETL of organic solar cells. For the device architecture, an n-i-p type [318] structure, based on a C_{60}/DCV5T-Me:C_{60} hybrid planar-bulk heterojunction, was chosen [319] (**Fig. 4.28 (a)**). The ETM is n-doped with 5 wt % and 10 wt % $W_2(hpp)_4$ and compared to the reference ETM C_{60} n-doped with 1 wt % and 5 wt % $W_2(hpp)_4$. The ETL has a thickness of 5 nm and is placed as the first layer on ITO, i.e. between the transparent bottom electrode and the C_{60} acceptor layer. The key parameters of the solar cells are summarized in **Fig. 4.28 (b)** and **Table 4.14**, showing that **ND9** outperforms C_{60} as an ETM for both doping concentrations. It is remarkable that it is the only material in this series, for which the increased doping concentration does not improve the device efficiency, indicating good transport properties and optimized energy levels at the same time. **ND7**, in comparison, is on a par with C_{60}, whereas **ND10** exhibits inferior performance. These differences can mainly be attributed to the lower mobility and conductivity of the latter two compounds leading to a reduced fill factor *FF*. The open-circuit voltage V_{OC} is approximately the same in all devices, confirming the general suitability of the transport levels. Comparing different doping concentrations, a higher c_n generally leads to a higher j_{SC}, which might be attributed to a higher built-in field in the intrinsic layers [320].

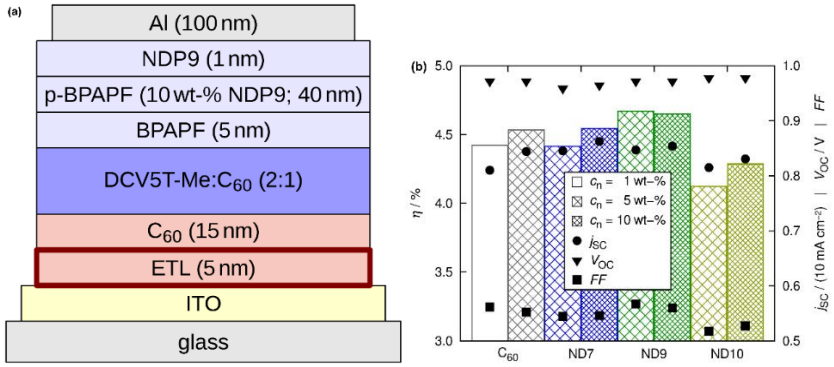

Fig. 4.28. (a) Illustration of the stack sequence of the high-performance test solar cells. (b) Performance of solar cells with C_{60}, **ND7**, **ND9**, and **ND10** as ETMs (columns)

As the final benchmark, the most promising material **ND9** is tested in comparison to n-C_{60} in a high performance device stack with a substrate-heated DCV5T-Me:C_{60} blend layer with the thickness of 40 nm. For both devices, the ETMs n-doped with 5 wt % $W_2(hpp)_4$ are used. The key parameters (**Table 4.14**) show that the solar cell with **ND9** has the power conversion efficiency of 7.9 % and outperforms the device with C_{60} (7.7 %) due to the improved fill factor (65.7 % vs 64.1 %). The short-circuit current density j_{SC} remains constant, indicating that the parasitic absorption of C_{60} is not significantly reduced by **ND9**. However, significant effects from parasitic absorption are not expected for such low ETL thickness.

Table 4.14. Key parameters of two solar cells with either C_{60} or **ND9** as ETM: power conversion efficiency η, fill factor *FF*, short-circuit current density j_{SC}, and opencircuit voltage V_{OC}

ETM	η [%]	*FF* [%]	j_{SC} [mA/cm^2]	V_{OC} [V]
C_{60}	7.7	64.1	12.5	0.96
ND9	7.9	65.7	12.5	0.96

In conclusion, two series of new high performance, easy to synthesize, electron transport materials based on NTCDA were developed and characterized. The obtained small molecules exhibit high thermal stability (T_{ID} in the range of 376–481 °C) and prove to be suitable for vacuum processed organic solar cells. The electrical properties are characterized by high conductivity (up to $4 \cdot 10^{-5}$ S cm^{-1}) and electron mobility (up to 10^{-3} cm^2 Vs^{-1}). The obtained symmetrical and asymmetrical compounds are optically superior compared to C_{60}, as they avoid parasitic absorption. The highest solar cell efficiency is obtained for **ND9** and exceeds the efficiency obtained for the standard material C_{60}. DFT calculations revealed the differences in geometry of the synthesized compounds. The comparison of the experimentally estimated electron affinities with the calculated LUMO energies revealed small differences and confirmed the similar dependencies of these parameters on the structural differences.

5. CONCLUSIONS

1. A series of blue-emitting star-shaped triazine-based molecules with fluorene side arms, linked through the linkages containing double, single, and triple bonds, were synthesized.

1.1. The compounds demonstrated excellent thermal stability (T_{ID} up to 402 °C), high fluorescence quantum yield values (0.50-0.70) and significant dependence on the solvent polarity.

1.2. The nature of the linking topology was found to have great influence on the geometry of the triazine derivatives, thus leading to the differences in optical, photophysical and photoelectrical characteristics.

1.3. Charge-transporting measurements revealed dispersive hole transport for the investigated compounds. The highest values of hole mobility (1.9×10^{-3} at the electric field of 1.15×10^{6} V/cm) were observed for the compound with ethenyl linkage.

2. Three star-shaped 1,3,5-triphenylbenzene derivatives with fluorene side arms, linked through the linkages containing double, single, and triple bonds, were synthesized.

2.1. The materials were found to emit light in the deep blue region with photoluminescence quantum efficiencies ranging from 0.40 to 0.54.

2.2. The compounds demonstrated high thermal stability (T_{ID} 422−434°C; T_g 55−75°C).

2.3. The derivatives demonstrated low dispersion hole transport and high hole mobilities. The highest hole mobility (2.4×10^{-3} $cm^2/V\cdot s$ at the electric field of 1×10^{5} V/cm) was observed for the ethenyl-bridged compound.

2.4. The variety in the characteristics was explained by the restriction of the intermolecular rotations in the star-shaped compounds, resulting from the differences in geometry.

3. Three boomerang-shaped compounds with various central units and bicarbazolyl side arms were designed and synthesized.

3.1. The bicarbazolyl group proved to be a stronger donor than the single carbazole fragment, by providing not only the lower ionization potential, but also the superior thermal and electrochemical stability.

3.2. Intense blue emission with the photoluminescence quantum yields reaching 0.93 and the triplet energies ranging from 2.44 to 2.68 eV were detected.

3.3. The highest hole mobility of 2.1×10^{-3} cm^2 V^{-1} s^{-1} at the electric field of 5.8×10^{5} Vcm^{-1} was exhibited by the derivative of 1,3,5-triphenylbenzene.

3.4. The compounds demonstrated moderately low *IP* values (5.45-5.50 eV).

4. Three donor-acceptor multichromophore fluorenone-based compounds were modelled and prepared.

4.1. The materials demonstrated superior thermal stability (T_{ID} up to 500 °C) and high glass transition temperatures (T_g up to 293 °C).

4.2. The compounds displayed ambipolar charge transport behaviour with balanced hole and electron mobility; the best results were determined for the 1,3,5-triphenylbenzene derivative (1.6×10^{-3} cm^2/Vs for holes and 2.8×10^{-3} cm^2/Vs for electrons at the electric field higher than 3.5×10^5 V/cm).

4.3. Dendritic fluorenone derivatives displayed high photoluminescence quantum yield (up to 0.90) in the non-polar media, quenched emission in the polar media and the AIEE feature. On the basis of experimental and theoretical results the mechanism of emission in the investigated materials was suggested.

5. Five bipolar 1,3,5-triphenylbenzene-based compounds, utilizing various substitution patterns (*para*- and *meta*-conjugation) to combine the carbazolyl donor and the nitrile acceptor were designed, characterized by theoretical approach and synthesized.

5.1. The materials revealed superior thermal characteristics (T_{ID} 401-480 °C; T_g 128-228 °C).

5.2. Moderately low ionization potential values (5.36-5.58 eV) were deduced for the compounds.

5.3. The orientation of the substituents was found to affect greatly the properties of the compounds. *Para*-conjugation resulted in higher T_{ID} and T_g, lower *IP*, exclusively hole transport and appearance of delayed fluorescence; the compounds with *meta*-linkage displayed ambipolar charge transport and higher triplet energies.

5.4. A derivative with exclusively *para*-conjugation displayed high performance in OLED as a blue fluorescent emitter, while a compound with *meta*-linkages proved to be a successful host matrix in combination with a *para*-substituted guest.

6. Two series of symmetrical and asymmetrical electron transport materials based on 1,4,5,8-naphthalenetetracarboxylic dianhydride were prepared.

6.1. High thermal stability (T_{ID} 413–507 °C) proved the materials to be suitable for vacuum processed organic solar cells.

6.2. Due to the reduction of parasitic absorption, the obtained symmetrical and asymmetrical compounds were shown to be optically superior compared to the standard electron transporting compound C_{60}.

6.3. Higher conductivity (up to $4 \cdot 10^{-5}$ S cm^{-1}) and electron mobility (up to 10^{-3} cm^2 Vs^{-1}) was demonstrated by the asymmetrical derivatives.

6.4. High electron affinity values (3.84-4.15 eV) were discovered in the compounds.

6.5. The most promising asymmetric compound, tested in a solar cell, showed a power conversion efficiency of 7.9 %, thus outperforming the device with C_{60} (7.7 %) due to an improved fill factor (65.7 % vs 64.1 %).

6. REFERENCES

1. TAKIMIYA, K. et al. π-Building Blocks for Organic Electronics: Revaluation of "Inductive" and "Resonance" Effects of π-Electron Deficient Units. *Chem. Mat.*[online]. 2014. vol. 26 (1), 587–593. Available from: http://pubs.acs.org/doi/abs/10.1021/cm4021063.

2. YANG, J. et al. Molecular Template Growth and Its Applications in Organic Electronics and Optoelectronics. *Chem. Rev.*[online]. 2015. vol. 115 (11), 5570–5603. Available from: http://pubs.acs.org/doi/abs/10.1021/acs.chemrev.5b00142.

3. WALLACE, J.U. - CHEN, S.H. Fluorene-based conjugated oligomers for organic photonics and electronics. *Adv. Polym. Sci*. 2008. vol. 212 (1), 145–186. .

4. WONG, K.-T. et al. Ter(9,9-diarylfluorene)s: Highly Efficient Blue Emitter with Promising Electrochemical and Thermal Stability. *J. Am. Chem. Soc.* [online]. 2002. vol. 124 (39), 11576–11577. Available from: http://pubs.acs.org/doi/abs/10.1021/ja0269587.

5. MATULAITIS, T. et al. Synthesis and properties of bipolar derivatives of 1,3,5-triazine and carbazole. *DyesPigments* [online]. 2016. vol. 127 45–58. Available from: http://linkinghub.elsevier.com/retrieve/pii/S0143720815004283.

6. ROQUET, S. et al. Triphenylamine−Thienylenevinylene Hybrid Systems with Internal Charge Transfer as Donor Materials for Heterojunction Solar Cells. *J. Am. Chem. Soc.* [online]. 2006. vol. 128 (10), 3459–3466. Available from: http://pubs.acs.org/doi/abs/10.1021/ja058178e.

7. JIANG, Y. et al. Multibranched triarylamine end-capped triazines with aggregation-induced emission and large two-photon absorption cross-sections. *Chem. Comm.*[online]. 2010. vol. 46 (26), 4689. Available from: http://xlink.rsc.org/?DOI=c0cc00803f.

8. LIU, Y. et al. Aggregation-Induced Emissions of Fluorenonearylamine Derivatives: A New Kind of Materials for Nondoped Red Organic Light-Emitting Diodes. *J. Phys. Chem. C* [online]. 2008. vol. 112 (10), 3975–3981. Available from: http://pubs.acs.org/doi/abs/10.1021/jp7117373.

9. AN, Z.-F. et al. Conjugated Asymmetric Donor-Substituted 1,3,5-Triazines: New Host Materials for Blue Phosphorescent Organic Light-Emitting Diodes. *Chem. Eur. J.* [online]. 2011. vol. 17 (39), 10871–10878. Available from: http://doi.wiley.com/10.1002/chem.201101118.

10. CHEN, H.-F. et al. 1,3,5-Triazine derivatives as new electron transport–type host materials for highly efficient green phosphorescent OLEDs. *J. Mater. Chem.*[online]. 2009. vol. 19 (43), 8112. Available from: http://xlink.rsc.org/?DOI=b913423a.

11. SU, S.-J. et al. Structure-Property Relationship of Pyridine-Containing Triphenyl Benzene Electron-Transport Materials for Highly Efficient Blue Phosphorescent OLEDs. *Adv.Funct. Mater.* [online]. 2009. vol. 19 (8), 1260–1267. Available from: http://doi.wiley.com/10.1002/adfm.200800809.

12. CHAN, K.L. et al. Understanding the Nature of the States Responsible for the Green Emission in Oxidized Poly(9,9-dialkylfluorene)s: Photophysics and Structural Studies of Linear Dialkylfluorene/Fluorenone Model Compounds. *Adv. Funct. Mater.* [online]. 2009. vol. 19 (13), 2147–2154. Available from: http://doi.wiley.com/10.1002/adfm.200801792.

13. LI, W. et al. Bipolar host materials for high-efficiency blue phosphorescent and delayed-fluorescence OLEDs. *J. Mater. Chem. C* [online]. 2015. vol. 3 (48), 12529–12538. Available from: http://xlink.rsc.org/?DOI=C5TC02997J.

14. NAKAGAWA, T. et al. Electroluminescence based on thermally activated delayed

fluorescence generated by a spirobifluorene donor–acceptor structure. *Chem. Comm.* [online]. 2012. vol. 48 (77), 9580. Available from: http://xlink.rsc.org/?DOI=c2cc31468a.

15. FERNANDO, R. et al. Tuning the Organic Solar Cell Performance of Acceptor 2,6-Dialkylaminonaphthalene Diimides by Varying a Linker between the Imide Nitrogen and a Thiophene Group. *J. Phys. Chem.C* [online]. 2014. vol. 118 (7), 3433–3442. Available from: http://pubs.acs.org/doi/abs/10.1021/jp411432a.

16. BERGGREN, M. et al. Organic materials for printed electronics. *Nat. Mater.* [online]. 2007. vol. 6 (1), 3–5. Available from: http://www.nature.com/doifinder/10.1038/nmat1817.

17. Embracing the organics world. *Nat. Mater.* [online]. 2013. vol. 12 (7), 591. Available from: http://www.nature.com/doifinder/10.1038/nmat3707.

18. The Special Issue on Organic Electronics. *Chem. Mater.* [online]. 2004. vol. 16 (23), 4381–4382. Available from: http://pubs.acs.org/doi/abs/10.1021/cm041000r.

19. TANG, C.W. - VANSLYKE, S.A. Organic electroluminescent diodes. *Appl. Phys. Lett.* [online]. 1987. vol. 51 (12), 913. Available from: http://scitation.aip.org/content/aip/journal/apl/51/12/10.1063/1.98799.

20. O'NEILL, M. - KELLY, S.M. Ordered Materials for Organic Electronics and Photonics. *Adv.Mater.* [online]. 2011. vol. 23 (5), 566–584. Available from: http://doi.wiley.com/10.1002/adma.201002884.

21. MESTA, M. et al. Molecular-scale simulation of electroluminescence in a multilayer white organic light-emitting diode. *Nat. Mater.* [online]. 2013. vol. 12 (7), 652–658. Available from: http://www.nature.com/doifinder/10.1038/nmat3622.

22. KELLEY, T.W. et al. Recent Progress in Organic Electronics: Materials, Devices, and Processes. *Chem. Mater.* [online]. 2004. vol. 16 (23), 4413–4422. Available from: http://pubs.acs.org/doi/abs/10.1021/cm049614j.

23. FORREST, S.R. - THOMPSON, M.E. Introduction: Organic Electronics and Optoelectronics. *Chem. Rev.* [online]. 2007. vol. 107 (4), 923–925. Available from: http://pubs.acs.org/doi/abs/10.1021/cr0501590.

24. ANTHONY, J.E. Functionalized Acenes and Heteroacenes for Organic Electronics. *Chem. Rev.* [online]. 2006. vol. 106 (12), 5028–5048. Available from: http://pubs.acs.org/doi/abs/10.1021/cr050966z.

25. LI, M. et al. Hexyl-Derivatized Poly(3,4-ethylenedioxyselenophene): Novel Highly Stable Organic Electrochromic Material with High Contrast Ratio, High Coloration Efficiency, and Low-Switching Voltage. *Adv. Mater.* [online]. 2009. vol. 21 (17), 1707–1711. Available from: http://doi.wiley.com/10.1002/adma.200802259.

26. WEN, L. et al. Synthesis and Characterization of New 2,3-Disubstituted Thieno[3,4- b]pyrazines: Tunable Building Blocks for Low Band Gap Conjugated Materials. *J. Org. Chem.* [online]. 2008. vol. 73 (21), 8529–8536. Available from: http://pubs.acs.org/doi/abs/10.1021/jo801632z.

27. TARKUC, S. et al. Tailoring the optoelectronic properties of donor–acceptor–donor type π-conjugated polymers via incorporating different electron-acceptor moieties. *Thin Solid Films* [online]. 2012. vol. 520 (7), 2960–2965. Available from: http://linkinghub.elsevier.com/retrieve/pii/S0040609011017743.

28. JOU, J.-H. et al. Approaches for fabricating high efficiency organic light emitting diodes. *J. Mater. Chem. C* [online]. 2015. vol. 3 (13), 2974–3002. Available from: http://xlink.rsc.org/?DOI=C4TC02495H.

29. KULKARNI, A.P. et al. Electron Transport Materials for Organic Light-Emitting

Diodes. *Chem. Mater.* [online]. 2004. vol. 16 (23), 4556–4573. Available from: http://pubs3.acs.org/acs/journals/doilookup?in_doi=10.1021/cm049473l.

30. SHIROTA, Y. - KAGEYAMA, H. Charge carrier transporting molecular materials and their applications in devices. *Chem. rev.* [online]. 2007. vol. 107 (4), 953–1010. [viewed2016-05-04]. . Available from: http://pubs.acs.org/doi/abs/10.1021/cr050143%2B.

31. KO, C.W. - TAO, Y.T. Bright white organic light-emitting diode. *Appl. Phys. Lett.* [online]. 2001. vol. 79 (25), 4234. Available from: http://scitation.aip.org/content/aip/journal/apl/79/25/10.1063/1.1425454.

32. LUNDIN, N.J. et al. Synthesis and Characterization of a Multicomponent Rhenium(I) Complex for Application as an OLED Dopant. *Angew. Chem. Int. Edit.*[online]. 2006. vol. 45 (16), 2582–2584. Available from: http://doi.wiley.com/10.1002/anie.200504532.

33. TAO, Y. et al. Organic host materials for phosphorescent organic light-emitting diodes. *Chem. Soc. Rev.* [online]. 2011. vol. 40 (5), 2943. Available from: http://xlink.rsc.org/?DOI=c0cs00160k.

34. LEE, T.-W. et al. Characteristics of Solution-Processed Small-Molecule Organic Films and Light-Emitting Diodes Compared with their Vacuum-Deposited Counterparts. *Adv. Funct. Mater.* [online]. 2009. vol. 19 (10), 1625–1630. Available from: http://doi.wiley.com/10.1002/adfm.200801045.

35. EARMME, T. - JENEKHE, S.A. High-performance multilayered phosphorescent OLEDs by solution-processed commercial electron-transport materials. *J. Mater. Chem.*[online]. 2012. vol. 22 (11), 4660. Available from: http://xlink.rsc.org/?DOI=c2jm14347j.

36. HOFMANN, S. et al. Engineering Blue Fluorescent Bulk Emitters for OLEDs: Triplet Harvesting by Green Phosphors. *Chem. Mater.* [online]. 2014. vol. 26 (7), 2414–2426. Available from: http://pubs.acs.org/doi/abs/10.1021/cm500602y.

37. LIU, W. et al. Novel Carbazol-Pyridine-Carbonitrile Derivative as Excellent Blue Thermally Activated Delayed Fluorescence Emitter for Highly Efficient Organic Light-Emitting Devices. *ACS Appl.Mater. Interfaces* [online]. 2015. vol. 7 (34), 18930–18936. Available from: http://pubs.acs.org/doi/10.1021/acsami.5b05648.

38. ADACHI, C. et al. Nearly 100% internal phosphorescence efficiency in an organic light-emitting device. *J. Appl. Phys.*[online]. 2001. vol. 90 (10), 5048. Available from: http://scitation.aip.org/content/aip/journal/jap/90/10/10.1063/1.1409582.

39. YEH, S.-J. et al. New Dopant and Host Materials for Blue-Light-Emitting Phosphorescent Organic Electroluminescent Devices. *Adv. Mater.* [online]. 2005. vol. 17 (3), 285–289. Available from: http://doi.wiley.com/10.1002/adma.200401373.

40. ADACHI, C. et al. High-efficiency organic electrophosphorescent devices with tris(2-phenylpyridine)iridium doped into electron-transporting materials. *Appl. Phys. Lett.* [online]. 2000. vol. 77 (6), 904. Available from: http://scitation.aip.org/content/aip/journal/apl/77/6/10.1063/1.1306639.

41. LAMANSKY, S. et al. Highly Phosphorescent Bis-Cyclometalated Iridium Complexes: Synthesis, Photophysical Characterization, and Use in Organic Light Emitting Diodes. *J. Am. Chem. Soc.* [online]. 2001. vol. 123 (18), 4304–4312. Available from: http://pubs.acs.org/doi/abs/10.1021/ja003693s.

42. LI, C.-L. et al. Yellow and Red Electrophosphors Based on Linkage Isomers of Phenylisoquinolinyliridium Complexes: Distinct Differences in Photophysical and Electroluminescence Properties. *Adv. Funct. Mater.* [online]. 2005. vol. 15 (3), 387–395.

Available from: http://doi.wiley.com/10.1002/adfm.200305100.

43. ZHENG, C.-J. et al. New Ambipolar Hosts Based on Carbazole and 4,5-Diazafluorene Units for Highly Efficient Blue Phosphorescent OLEDs with Low Efficiency Roll-Off. *Chem. Mater.*[online]. 2012. vol. 24 (4), 643–650. Available from: http://pubs.acs.org/doi/abs/10.1021/cm2036647.

44. DIAS, F.B. et al. Triplet Harvesting with 100% Efficiency by Way of Thermally Activated Delayed Fluorescence in Charge Transfer OLED Emitters. *Adv. Mater.* [online]. 2013. vol. 25 (27), 3707–3714. Available from: http://www.ncbi.nlm.nih.gov/pubmed/23703877.

45. UOYAMA, H. et al. Highly efficient organic light-emitting diodes from delayed fluorescence. *Nature* [online]. 2012. vol. 492 (7428), 234–238. Available from: http://www.nature.com/doifinder/10.1038/nature11687.

46. SANTOS, P.L. et al. Engineering the singlet–triplet energy splitting in a TADF molecule. *J. Mater. Chem. C* [online]. 2016. vol. 4 (17), 3815–3824. Available from: http://xlink.rsc.org/?DOI=C5TC03849A.

47. NOBUYASU, R.S. et al. Rational Design of TADF Polymers Using a Donor-Acceptor Monomer with Enhanced TADF Efficiency Induced by the Energy Alignment of Charge Transfer and Local Triplet Excited States. *Adv. Opt. Mater.* [online]. 2016. vol. 4 (4), 597–607. Available from: http://doi.wiley.com/10.1002/adom.201500689.

48. ZHANG, Q. et al. Design of Efficient Thermally Activated Delayed Fluorescence Materials for Pure Blue Organic Light Emitting Diodes. *J. Am. Chem. Soc.* [online]. 2012. vol. 134 (36), 14706–14709. Available from: http://pubs.acs.org/doi/abs/10.1021/ja306538w.

49. SAIGUSA, H. - LIM, E.C. Excited-State Dynamics of Aromatic Clusters: Correlation between Exciton Interactions and Excimer Formation Dynamics. *J. Phys. Chem.* [online]. 1995. vol. 99 (43), 15738–15747. Available from: http://pubs.acs.org/doi/abs/10.1021/j100043a010.

50. HONG, Y. et al. Aggregation-induced emission. *Chem. Soc. Rev.* [online]. 2011. vol. 40 (11), 5361. Available from: http://xlink.rsc.org/?DOI=c1cs15113d.

51. BÜNAU, G. V. J. B. Birks: Photophysics of Aromatic Molecules. Wiley-Interscience, London 1970. 704 Seiten. Preis: 210s. *Ber. Bunsen. Phys. Chem.* [online]. 1970. vol. 74 (12), 1294–1295. [viewed2016-05-30]. . Available from: https://www.mendeley.com/research/j-b-birks-photophysics-aromatic-molecules-wileyinterscience-london-1970-704-seiten-preis-210s/?utm_source=desktop&utm_medium=1.15.3&utm_campaign=open_catalog&userDocumentId=%7Bdccf38a9-cac7-4542-bdf7-4d0aa560c63a%7D.

52. WANG, J. et al. Alkyl and Dendron Substituted Quinacridones: Synthesis, Structures, and Luminescent Properties. *J. Phys. Chem. B* [online]. 2007. vol. 111 (19), 5082–5089. Available from: http://pubs.acs.org/doi/abs/10.1021/jp068646m.

53. NGUYEN, B.T. et al. Enhancing the Photoluminescence Intensity of Conjugated Polycationic Polymers by Using Quantum Dots as Antiaggregation Reagents. *Langmuir* [online]. 2006. vol. 22 (10), 4799–4803. Available from: http://pubs.acs.org/doi/abs/10.1021/la053399j.

54. LUO, J. et al. Aggregation-induced emission of 1-methyl-1,2,3,4,5-pentaphenylsilole. *Chem. Comm.* [online]. 2001. (18), 1740–1741. Available from: http://xlink.rsc.org/?DOI=b105159h.

55. HONG, Y. et al. Aggregation-induced emission: phenomenon, mechanism and applications. *Chem. Comm.* [online]. 2009. (29), 4332. Available from:

http://xlink.rsc.org/?DOI=b904665h.

56. MEI, J. et al. Aggregation-Induced Emission: The Whole Is More Brilliant than the Parts. *Adv. Mater.* [online]. 2014. vol. 26 (31), 5429–5479. Available from: http://doi.wiley.com/10.1002/adma.201401356.

57. MEI, J. et al. Aggregation-Induced Emission: Together We Shine, United We Soar! *Chem. Rev.* [online]. 2015. vol. 115 (21), 11718–11940. Available from: http://pubs.acs.org/doi/10.1021/acs.chemrev.5b00263.

58. ZHAO, Q. et al. Aggregation-induced phosphorescent emission (AIPE) of iridium(<scp>iii</scp>) complexes. *Chem. Commun.* [online]. 2008. (6), 685–687. Available from: http://xlink.rsc.org/?DOI=B712416C.

59. ZHOU, J. et al. From tetraphenylethene to tetranaphthylethene: structural evolution in AIE luminogen continues. *Chem. Comm.* [online]. 2013. vol. 49 (25), 2491. Available from: http://xlink.rsc.org/?DOI=c3cc00010a.

60. HU, R. et al. AIE macromolecules: syntheses, structures and functionalities. *Chem. Soc. Rev.* [online]. 2014. vol. 43 (13), 4494. Available from: http://xlink.rsc.org/?DOI=c4cs00044g.

61. CHEN, C.-T. et al. Doubly Ortho-Linked Quinoxaline/Diphenylfluorene Hybrids as Bipolar, Fluorescent Chameleons for Optoelectronic Applications. *J. Am. Chem. Soc.* [online]. 2006. vol. 128 (34), 10992–10993. Available from: http://pubs.acs.org/doi/abs/10.1021/ja062660v.

62. ZHU, Y. et al. New Ambipolar Organic Semiconductors. 1. Synthesis, Single-Crystal Structures, Redox Properties, and Photophysics of Phenoxazine-Based Donor−Acceptor Molecules. *Chem. Mater.* [online]. 2008. vol. 20 (13), 4200–4211. Available from: http://pubs.acs.org/doi/abs/10.1021/cm702212w.

63. CHOU, H.-H. - CHENG, C.-H. A Highly Efficient Universal Bipolar Host for Blue, Green, and Red Phosphorescent OLEDs. *Adv. Mater.* [online]. 2010. vol. 22 (22), 2468–2471. Available from: http://doi.wiley.com/10.1002/adma.201000061.

64. CHASKAR, A. et al. Bipolar Host Materials: A Chemical Approach for Highly Efficient Electrophosphorescent Devices. *Adv. Mater.* [online]. 2011. vol. 23 (34), 3876–3895. Available from: http://doi.wiley.com/10.1002/adma.201101848.

65. LAI, M.-Y. et al. Benzimidazole/Amine-Based Compounds Capable of Ambipolar Transport for Application in Single-Layer Blue-Emitting OLEDs and as Hosts for Phosphorescent Emitters. *Angew. Chem. Int. Edit.* [online]. 2008. vol. 47 (3), 581–585. Available from: http://doi.wiley.com/10.1002/anie.200704113.

66. DUAN, L. et al. Strategies to Design Bipolar Small Molecules for OLEDs: Donor-Acceptor Structure and Non-Donor-Acceptor Structure. *Adv. Mater.* [online]. 2011. vol. 23 (9), 1137–1144. Available from: http://doi.wiley.com/10.1002/adma.201003816.

67. KIM, D. et al. Design of Efficient Ambipolar Host Materials for Organic Blue Electrophosphorescence: Theoretical Characterization of Hosts Based on Carbazole Derivatives. *J. Am. Chem. Soc.* [online]. 2011. vol. 133 (44), 17895–17900. Available from: http://pubs.acs.org/doi/abs/10.1021/ja207554h.

68. MIYAURA, N. et al. A new stereospecific cross-coupling by the palladium-catalyzed reaction of 1-alkenylboranes with 1-alkenyl or 1-alkynyl halides. *Tetrahedron Lett.* [online]. 1979. vol. 20 (36), 3437–3440. Available from: http://linkinghub.elsevier.com/retrieve/pii/S0040403901954292.

69. CHINCHILLA, R. - NÁJERA, C. The Sonogashira Reaction: A Booming Methodology

in Synthetic Organic Chemistry †. *Chem. Rev.* [online]. 2007. vol. 107 (3), 874–922. Available from: http://pubs.acs.org/doi/abs/10.1021/cr050992x.

70. STILLE, J.K. The Palladium-Catalyzed Cross-Coupling Reactions of Organotin Reagents with Organic Electrophiles[New Synthetic Methods(58)]. *Angew. Chem. Int. Edit. Eng.* [online]. 1986. vol. 25 (6), 508–524. Available from: http://doi.wiley.com/10.1002/anie.198605081.

71. BELETSKAYA, I.P. - CHEPRAKOV, A. V. The Heck Reaction as a Sharpening Stone of Palladium Catalysis. *Chem. Rev.* [online]. 2000. vol. 100 (8), 3009–3066. Available from: http://pubs.acs.org/doi/abs/10.1021/cr9903048.

72. WEINGARTEN, H. Ullmann Condensation. *J. Org. Chem.* [online]. 1964. vol. 29 (4), 977–978. Available from: http://pubs.acs.org/doi/abs/10.1021/jo01027a529.

73. LI, J.J. *Name Reactions* [online]. Berlin, Heidelberg: Springer Berlin Heidelberg, 2009. ISBN 978-3-642-01052-1.

74. LIU, B. et al. A novel bipolar phenanthroimidazole derivative host material for highly efficient green and orange-red phosphorescent OLEDs with low efficiency roll-off at high brightness. *J. Mater. Chem. C* [online]. 2016. vol. 4 (10), 2003–2010. Available from: http://xlink.rsc.org/?DOI=C5TC04393J.

75. ZHU, M. et al. Highly efficient solution-processed green and red electrophosphorescent devices enabled by small-molecule bipolar host material. *J. Mater. Chem.* [online]. 2011. vol. 21 (25), 9326. Available from: http://xlink.rsc.org/?DOI=c1jm10987a.

76. TSAI, M.-H. et al. Highly Efficient Organic Blue Electrophosphorescent Devices Based on 3,6-Bis(triphenylsilyl)carbazole as the Host Material. *Adv. Mater.*[online]. 2006. vol. 18 (9), 1216–1220. Available from: http://doi.wiley.com/10.1002/adma.200502283.

77. HUANG, B. et al. A novel, bipolar host based on triazine for efficient solution-processed single-layer green phosphorescent organic light-emitting diodes. *DyesPigments* [online]. 2014. vol. 101 9–14. Available from: http://linkinghub.elsevier.com/retrieve/pii/S0143720813003422.

78. WAGNER, D. et al. Triazine Based Bipolar Host Materials for Blue Phosphorescent OLEDs. *Chem. Mater.* [online]. 2013. vol. 25 (18), 3758–3765. Available from: http://pubs.acs.org/doi/abs/10.1021/cm4023216.

79. KIM, M. et al. Molecular design of triazine and carbazole based host materials for blue phosphorescent organic emitting diodes. *Phys. Chem. Chem. Phys.* [online]. 2015. vol. 17 (20), 13553–13558. Available from: http://xlink.rsc.org/?DOI=C5CP01676B.

80. LIU, X.-K. et al. Novel bipolar host materials based on 1,3,5-triazine derivatives for highly efficient phosphorescent OLEDs with extremely low efficiency roll-off. *Phys. Chem. Chem. Phys.* [online]. 2012. vol. 14 (41), 14255. Available from: http://xlink.rsc.org/?DOI=c2cp41542a.

81. JEON, S.O. et al. Phenylcarbazole-Based Phosphine Oxide Host Materials For High Efficiency In Deep Blue Phosphorescent Organic Light-Emitting Diodes. *Adv. Funct. Mater.* [online]. 2009. vol. 19 (22), 3644–3649. Available from: http://doi.wiley.com/10.1002/adfm.200901274.

82. JEON, S.O. et al. External Quantum Efficiency Above 20% in Deep Blue Phosphorescent Organic Light-Emitting Diodes. *Adv. Mater.* [online]. 2011. vol. 23 (12), 1436–1441. Available from: http://doi.wiley.com/10.1002/adma.201004372.

83. CHANG, H.-H. et al. A new tricarbazole phosphine oxide bipolar host for efficient single-layer blue PhOLED. *Org. Electron.* [online]. 2011. vol. 12 (12), 2025–2032.

Available from: http://linkinghub.elsevier.com/retrieve/pii/S1566119911003077.

84. HSU, F.-M. et al. Phosphine-Oxide-Containing Bipolar Host Material for Blue Electrophosphorescent Devices. *Chem. Mater.* [online]. 2009. vol. 21 (6), 1017–1022. Available from: http://pubs.acs.org/doi/abs/10.1021/cm802199d.

85. HOLMES, R.J. et al. Efficient, deep-blue organic electrophosphorescence by guest charge trapping. *Appl. Phys. Lett.* [online]. 2003. vol. 83 (18), 3818. Available from: http://scitation.aip.org/content/aip/journal/apl/83/18/10.1063/1.1624639.

86. CHEN, D. et al. Nitrogen heterocycle-containing materials for highly efficient phosphorescent OLEDs with low operating voltage. *J. Mater. Chem. C* [online]. 2014. vol. 2 (45), 9565–9578. Available from: http://xlink.rsc.org/?DOI=C4TC01941E.

87. TANG, C. et al. A versatile efficient one-step approach for carbazole–pyridine hybrid molecules: highly efficient host materials for blue phosphorescent OLEDs. *Chem. Commun.* [online]. 2015. vol. 51 (9), 1650–1653. Available from: http://xlink.rsc.org/?DOI=C4CC08335K.

88. TAO, Y. et al. Dynamically Adaptive Characteristics of Resonance Variation for Selectively Enhancing Electrical Performance of Organic Semiconductors. *Angew. Chem. Int. Edit.* [online]. 2013. vol. 52 (40), 10491–10495. Available from: http://doi.wiley.com/10.1002/anie.201304540.

89. SU, S.-J. et al. Pyridine-Containing Bipolar Host Materials for Highly Efficient Blue Phosphorescent OLEDs. *Chem. Mater.* [online]. 2008. vol. 20 (5), 1691–1693. [viewed2016-03-14]. . Available from: http://dx.doi.org/10.1021/cm703682q.

90. MOTOYAMA, T. et al. An α-Carboline-containing Host Material for High-efficiency Blue and Green Phosphorescent OLEDs. *Chem. Lett.* [online]. 2011. vol. 40 (3), 306–308. Available from: http://joi.jlc.jst.go.jp/JST.JSTAGE/cl/2011.306?from=CrossRef.

91. KIM, S.J. et al. High-efficiency blue phosphorescent organic light-emitting diodes using a carbazole and carboline-based host material. *Chem. Commun.* [online]. 2013. vol. 49 (60), 6788. Available from: http://xlink.rsc.org/?DOI=c3cc42569j.

92. CHO, M.J. et al. New Bipolar Host Materials for Realizing Blue Phosphorescent Organic Light-Emitting Diodes with High Efficiency at 1000 cd/m 2. *ACS Appl. Mater. Interfaces* [online]. 2014. vol. 6 (22), 19808–19815. Available from: http://pubs.acs.org/doi/abs/10.1021/am505049h.

93. DENG, L. et al. Simple bipolar host materials incorporating CN group for highly efficient blue electrophosphorescence with slow efficiency roll-off. *J. Mater. Chem. C* [online]. 2013. vol. 1 (48), 8140. Available from: http://xlink.rsc.org/?DOI=c3tc31893a.

94. OH, C.S. et al. Molecular design of host materials for high power efficiency in blue phosphorescent organic light-emitting diodes doped with an imidazole ligand based triplet emitter. *J. Mater. Chem. C* [online]. 2016. vol. 4 (17), 3792–3797. Available from: http://xlink.rsc.org/?DOI=C5TC02595H.

95. PARTEE, J. et al. Delayed Fluorescence and Triplet-Triplet Annihilation in π -Conjugated Polymers. *Phys. Rev. Lett.* [online]. 1999. vol. 82 (18), 3673–3676. Available from: http://link.aps.org/doi/10.1103/PhysRevLett.82.3673.

96. CHAUDHURI, D. et al. Metal-Free OLED Triplet Emitters by Side-Stepping Kasha's Rule. *Angew. Chem. Int. Edit.* [online]. 2013. vol. 52 (50), 13449–13452. Available from: http://doi.wiley.com/10.1002/anie.201307601.

97. YAO, L. et al. Highly Efficient Near-Infrared Organic Light-Emitting Diode Based on a Butterfly-Shaped Donor-Acceptor Chromophore with Strong Solid-State Fluorescence and a

Large Proportion of Radiative Excitons. *Angew. Chem. Int. Edit.* [online]. 2014. vol. 53 (8), 2119–2123. Available from: http://doi.wiley.com/10.1002/anie.201308486.

98. CHOU, P.-Y. et al. Efficient delayed fluorescence via triplet–triplet annihilation for deep-blue electroluminescence. *Chem. Commun.* [online]. 2014. vol. 50 (52), 6869. Available from: http://xlink.rsc.org/?DOI=c4cc01851f.

99. TAO, Y. et al. Thermally Activated Delayed Fluorescence Materials Towards the Breakthrough of Organoelectronics. *Adv. Mater.* [online]. 2014. vol. 26 (47), 7931–7958. Available from: http://doi.wiley.com/10.1002/adma.201402532.

100. SUN, J.W. et al. Thermally Activated Delayed Fluorescence from Azasiline Based Intramolecular Charge-Transfer Emitter (DTPDDA) and a Highly Efficient Blue Light Emitting Diode. *Chem. Mater.*[online]. 2015. vol. 27 (19), 6675–6681. Available from: http://pubs.acs.org/doi/10.1021/acs.chemmater.5b02515.

101. YAMAGUCHI, S. - TAMAO, K. Silole-containing σ- and π-conjugated compounds. *Dalton Transactions* [online]. 1998. (22), 3693–3702. Available from: http://xlink.rsc.org/?DOI=a804491k.

102. TSAI, W.-L. et al. A versatile thermally activated delayed fluorescence emitter for both highly efficient doped and non-doped organic light emitting devices. *Chem. Commun.* [online]. 2015. vol. 51 (71), 13662–13665. Available from: http://xlink.rsc.org/?DOI=C5CC05022G.

103. TANAKA, H. et al. Dual Intramolecular Charge-Transfer Fluorescence Derived from a Phenothiazine-Triphenyltriazine Derivative. *J. Phys.Chem. C* [online]. 2014. vol. 118 (29), 15985–15994. Available from: http://pubs.acs.org/doi/abs/10.1021/jp501017f.

104. TANAKA, H. et al. Efficient green thermally activated delayed fluorescence (TADF) from a phenoxazine–triphenyltriazine (PXZ–TRZ) derivative. *Chem.Commun.* [online]. 2012. vol. 48 (93), 11392. Available from: http://xlink.rsc.org/?DOI=c2cc36237f.

105. HIRATA, S. et al. Highly efficient blue electroluminescence based on thermally activated delayed fluorescence. *Nat. Mater.*[online]. 2014. vol. 14 (3), 330–336. Available from: http://www.nature.com/doifinder/10.1038/nmat4154.

106. ENDO, A. et al. Efficient up-conversion of triplet excitons into a singlet state and its application for organic light emitting diodes. *Appl. Phys. Lett.* [online]. 2011. vol. 98 (8), 083302. Available from: http://scitation.aip.org/content/aip/journal/apl/98/8/10.1063/1.3558906.

107. CHANG, C.-H. et al. A dicarbazole–triazine hybrid bipolar host material for highly efficient green phosphorescent OLEDs. *J. Mater. Chem.* [online]. 2012. vol. 22 (9), 3832. Available from: http://xlink.rsc.org/?DOI=c2jm14686j.

108. SEREVIČIUS, T. et al. Enhanced electroluminescence based on thermally activated delayed fluorescence from a carbazole–triazine derivative. *Phys. Chem. Chem. Phys.* [online]. 2013. vol. 15 (38), 15850. Available from: http://xlink.rsc.org/?DOI=c3cp52255e.

109. KIM, M. et al. Stable Blue Thermally Activated Delayed Fluorescent Organic Light-Emitting Diodes with Three Times Longer Lifetime than Phosphorescent Organic Light-Emitting Diodes. *Adv. Mater.* [online]. 2015. vol. 27 (15), 2515–2520. Available from: http://doi.wiley.com/10.1002/adma.201500267.

110. HUANG, B. et al. Thermally activated delayed fluorescence materials based on 3,6-di-tert-butyl-9-((phenylsulfonyl)phenyl)-9H-carbazoles. *DyesPigments* [online]. 2014. vol. 111 135–144. Available from: http://linkinghub.elsevier.com/retrieve/pii/S0143720814002320.

111. WU, S. et al. High-efficiency deep-blue organic light-emitting diodes based on a

thermally activated delayed fluorescence emitter. *J. Mater. Chem. C* [online]. 2014. vol. 2 (3), 421–424. Available from: http://xlink.rsc.org/?DOI=C3TC31936A.

112. LEE, J. et al. Oxadiazole- and triazole-based highly-efficient thermally activated delayed fluorescence emitters for organic light-emitting diodes. *J. Mater. Chem. C* [online]. 2013. vol. 1 (30), 4599. Available from: http://xlink.rsc.org/?DOI=c3tc30699b.

113. ZHANG, Q. et al. Efficient blue organic light-emitting diodes employing thermally activated delayed fluorescence. *Nat. Photon.* [online]. 2014. vol. 8 (4), 326–332. Available from: http://www.nature.com/doifinder/10.1038/nphoton.2014.12.

114. ZHANG, Q. et al. Nearly 100% Internal Quantum Efficiency in Undoped Electroluminescent Devices Employing Pure Organic Emitters. *Adv. Mater.* [online]. 2015. vol. 27 (12), 2096–2100. Available from: http://doi.wiley.com/10.1002/adma.201405474.

115. JANKUS, V. et al. Highly Efficient TADF OLEDs: How the Emitter-Host Interaction Controls Both the Excited State Species and Electrical Properties of the Devices to Achieve Near 100% Triplet Harvesting and High Efficiency. *Adv. Funct. Mater.*[online]. 2014. Available from: http://doi.wiley.com/10.1002/adfm.201400948.

116. NEUMANN, M.G. et al. Photophysics and photoreactivity of substituted thioxanthones. *Faraday Transactions* [online]. 1997. vol. 93 (8), 1517–1521. Available from: http://xlink.rsc.org/?DOI=a607264j.

117. WANG, H. et al. Novel Thermally Activated Delayed Fluorescence Materials-Thioxanthone Derivatives and Their Applications for Highly Efficient OLEDs. *Adv. Mater.* [online]. 2014. vol. 26 (30), 5198–5204. Available from: http://doi.wiley.com/10.1002/adma.201401393.

118. MÉHES, G. et al. Enhanced Electroluminescence Efficiency in a Spiro-Acridine Derivative through Thermally Activated Delayed Fluorescence. *Angew. Chem. Int. Edit.* [online]. 2012. vol. 51 (45), 11311–11315. Available from: http://doi.wiley.com/10.1002/anie.201206289.

119. SHIH, P.-I. et al. Novel host material for highly efficient blue phosphorescent OLEDs. *J. Mater. Chem.* [online]. 2007. vol. 17 (17), 1692. Available from: http://xlink.rsc.org/?DOI=b616043c.

120. CHO, Y.J. et al. Cool and warm hybrid white organic light-emitting diode with blue delayed fluorescent emitter both as blue emitter and triplet host. *Scientific Reports* [online]. 2015. vol. 5 7859. Available from: http://www.nature.com/articles/srep07859.

121. CHO, Y.J. et al. The Design of Dual Emitting Cores for Green Thermally Activated Delayed Fluorescent Materials. *Angew. Chem.* [online]. 2015. vol. 127 (17), 5290–5293. Available from: http://doi.wiley.com/10.1002/ange.201412107.

122. HARADA, N. et al. Interchromophoric homoconjugation effect and intramolecular charge-transfer transition of the triptycene system containing a tetracyanoquinodimethane chromophore. *Perkin Transactions 2* [online]. 1989. (10), 1449. Available from: http://xlink.rsc.org/?DOI=p29890001449.

123. KAWASUMI, K. et al. Thermally Activated Delayed Fluorescence Materials Based on Homoconjugation Effect of Donor–Acceptor Triptycenes. *J. Am. Chem. Soc.* [online]. 2015. vol. 137 (37), 11908–11911. Available from: http://pubs.acs.org/doi/10.1021/jacs.5b07932.

124. TSENG, N.-W. et al. Deciphering mechanism of aggregation-induced emission (AIE): Is E–Zisomerisation involved in an AIE process? *Chem. Sci.* [online]. 2012. vol. 3 (2), 493–497. Available from: http://xlink.rsc.org/?DOI=C1SC00690H.

125. CHANG, Z. et al. Aggregation-enhanced emission and efficient electroluminescence of

tetraphenylethene-cored luminogens. *Chem. Commun.* [online]. 2013. vol. 49 (6), 594–596. Available from: http://xlink.rsc.org/?DOI=C2CC37928G.

126. LIU, Y. et al. Intermolecular Hydrogen Bonds Induce Highly Emissive Excimers: Enhancement of Solid-State Luminescence. *J. Phys. Chem. C* [online]. 2007. vol. 111 (17), 6544–6549. Available from: http://pubs.acs.org/doi/abs/10.1021/jp070288f.

127. ANANTHAKRISHNAN, S.J. et al. Offsetting the problem of charge trapping in white polymer light-emitting diodes using a fluorenone-based luminogen. *J. Mater. Chem. C* [online]. 2014. vol. 2 (42), 9035–9044. Available from: http://xlink.rsc.org/?DOI=C4TC01722F.

128. CHEN, L. et al. Rational Design of Aggregation-Induced Emission Luminogen with Weak Electron Donor–Acceptor Interaction to Achieve Highly Efficient Undoped Bilayer OLEDs. *ACS Appl. Mater. Interfaces* [online]. 2014. vol. 6 (19), 17215–17225. Available from: http://pubs.acs.org/doi/abs/10.1021/am505036a.

129. SHI, H. et al. The synthesis of novel AIE emitters with the triphenylethene-carbazole skeleton and para-/meta-substituted arylboron groups and their application in efficient non-doped OLEDs. *J. Mater. Chem. C* [online]. 2016. vol. 4 (6), 1228–1237. Available from: http://xlink.rsc.org/?DOI=C5TC04008F.

130. ZHAO, Z. et al. Tetraphenylethene: a versatile AIE building block for the construction of efficient luminescent materials for organic light-emitting diodes. *J. Mater. Chem.* [online]. 2012. vol. 22 (45), 23726. Available from: http://xlink.rsc.org/?DOI=c2jm31949g.

131. MU, G. et al. Constructing New n-Type, Ambipolar, and p-Type Aggregation-Induced Blue Luminogens by Gradually Tuning the Proportion of Tetrahphenylethene and Diphenylphophine Oxide. *J. Phys. Chem. C* [online]. 2014. vol. 118 (16), 8610–8616. Available from: http://pubs.acs.org/doi/abs/10.1021/jp501752a.

132. YUAN, W.Z. et al. Efficient Solid Emitters with Aggregation-Induced Emission and Intramolecular Charge Transfer Characteristics: Molecular Design, Synthesis, Photophysical Behaviors, and OLED Application. *Chem. Mater.* [online]. 2012. vol. 24 (8), 1518–1528. Available from: http://pubs.acs.org/doi/abs/10.1021/cm300416y.

133. CHAMPION, R.D. et al. Electronic Properties and Field-Effect Transistors of Thiophene-Based Donor-Acceptor Conjugated Copolymers. *Macromol. Rapid Commun.* [online]. 2005. vol. 26 (23), 1835–1840. Available from: http://doi.wiley.com/10.1002/marc.200500616.

134. DU, X. - WANG, Z.Y. Donor–acceptor type silole compounds with aggregation-induced deep-red emission enhancement: synthesis and application for significant intensification of near-infrared photoluminescence. *Chem. Commun.* [online]. 2011. vol. 47 (14), 4276. Available from: http://xlink.rsc.org/?DOI=c1cc00066g.

135. QIAN, G. - WANG, Z.Y. Near-Infrared Organic Compounds and Emerging Applications. *Chem. Asian J.* [online]. 2010. vol. 5 (5), 1006–1029. Available from: http://doi.wiley.com/10.1002/asia.200900596.

136. SINGH, G. et al. Carbazole-functionalized polyphenylene-decorated solid state emissive D–A–D molecules: reduced donor–acceptor interaction and enhanced emission in the solid state. *Phys. Chem. Chem. Phys.* [online]. 2015. vol. 17 (34), 22079–22089. Available from: http://xlink.rsc.org/?DOI=C5CP02234G.

137. SETAYESH, S. et al. Polyfluorenes with Polyphenylene Dendron Side Chains: Toward Non-Aggregating, Light-Emitting Polymers. *J. Am. Chem. Soc.* [online]. 2001. vol. 123 (5), 946–953. Available from: http://pubs.acs.org/doi/abs/10.1021/ja0031220.

138. GONG, X. et al. White Light Electrophosphorescence from Polyfluorene-Based Light-Emitting Diodes: Utilization of Fluorenone Defects. *J. Phys. Chem. B* [online]. 2004. vol. 108 (25), 8601–8605. Available from: http://pubs.acs.org/doi/abs/10.1021/jp040027v.

139. INAGI, S. et al. Electrochemical Tuning of the Optoelectronic Properties of a Fluorene-Based Conjugated Polymer. *Langmuir* [online]. 2010. vol. 26 (24), 18631–18633. Available from: http://pubs.acs.org/doi/abs/10.1021/la104099q.

140. ZHOU, X.-H. et al. Effect of Fluorenone Units on the Property of Polyfluorene and Oligofluorene Derivatives: Synthesis, Structure−Properties Relationship, and Electroluminescence. *Macromol.* [online]. 2006. vol. 39 (11), 3830–3840. Available from: http://pubs.acs.org/doi/abs/10.1021/ma0601262.

141. GRISORIO, R. et al. Influence of Keto Groups on the Optical, Electronic, and Electroluminescent Properties of Random Fluorenone-Containing Poly(fluorenylene-vinylene)s. *J. Phys. Chem. C* [online]. 2008. vol. 112 (50), 20076–20087. Available from: http://pubs.acs.org/doi/abs/10.1021/jp806879c.

142. SONG, P. - MA, F. Tunable Electronic Structures and Optical Properties of Fluorenone-Based Molecular Materials by Heteroatoms. *J. Phys. Chem. A* [online]. 2010. vol. 114 (5), 2230–2234. Available from: http://pubs.acs.org/doi/abs/10.1021/jp909594e.

143. SPANO, F.C. The Spectral Signatures of Frenkel Polarons in H- and J-Aggregates. *Acc. Chem. Res.*[online]. 2010. vol. 43 (3), 429–439. Available from: http://pubs.acs.org/doi/abs/10.1021/ar900233v.

144. SPANO, F.C. - SILVA, C. H- and J-Aggregate Behavior in Polymeric Semiconductors. *Annu. Rev. Phys. Chem.* [online]. 2014. vol. 65 (1), 477–500. Available from: http://www.annualreviews.org/doi/abs/10.1146/annurev-physchem-040513-103639.

145. ANANTHAKRISHNAN, S.J. et al. A solution processable fluorene–fluorenone oligomer with aggregation induced emission enhancement. *Chem. Commun.* [online]. 2013. vol. 49 (91), 10742. Available from: http://xlink.rsc.org/?DOI=c3cc46151c.

146. GAN, S. et al. Integration of aggregation-induced emission and delayed fluorescence into electronic donor–acceptor conjugates. *J. Mater. Chem. C* [online]. 2016. vol. 4 (17), 3705–3708. Available from: http://xlink.rsc.org/?DOI=C5TC03588K.

147. XU, S. et al. An Organic Molecule with Asymmetric Structure Exhibiting Aggregation-Induced Emission, Delayed Fluorescence, and Mechanoluminescence. *Angew. Chem. Int. Edit.* [online]. 2015. vol. 54 (3), 874–878. Available from: http://doi.wiley.com/10.1002/anie.201409767.

148. TSUBOI, Y. et al. Laser-Induced Shock Wave Can Spark Triboluminescence of Amorphous Sugars. *J. Phys. Chem. A* [online]. 2008. vol. 112 (29), 6517–6521. Available from: http://pubs.acs.org/doi/abs/10.1021/jp8002504.

149. XIE, Z. et al. White-Light Emission Strategy of a Single Organic Compound with Aggregation-Induced Emission and Delayed Fluorescence Properties. *Angew. Chem. Int. Edit.* [online]. 2015. vol. 54 (24), 7181–7184. Available from: http://doi.wiley.com/10.1002/anie.201502180.

150. MELLO, J.C. DE et al. An improved experimental determination of external photoluminescence quantum efficiency. *Adv. Mater.* [online]. 1997. vol. 9 (3), 230–232. Available from: http://doi.wiley.com/10.1002/adma.19970090308.

151. MIYAMOTO, E. et al. Ionization potential of organic pigment film by atmospheric photoelectron emission analysis. *Electrophotography* [online]. 1989. vol. 28 (4), 364–370. Available from: https://astp.jst.go.jp/modules/search/DocumentDetail/0387-

916X_28_4_Ionization+potential+of+organic+pigment+film+by+atmospheric+photoelectron+emission+analysis._N%252FA.

152. VAJIRAVELU, S. et al. Effect of substituents on the electron transport properties of bay substituted perylene diimide derivatives. *J. Mater. Chem.* [online]. 2009. vol. 19 (24), 4268. Available from: http://xlink.rsc.org/?DOI=b901847f.

153. GENEVIČIUS, K. et al. Charge transport in π-conjugated polymers from extraction current transients. *Thin Solid Films* [online]. 2002. vol. 403-404 415–418. Available from: http://linkinghub.elsevier.com/retrieve/pii/S0040609001015838.

154. WIDMER, J. et al. Electric potential mapping by thickness variation: A new method for model-free mobility determination in organic semiconductor thin films. *Org. Electron.* [online]. 2013. vol. 14 (12), 3460–3471. Available from: http://linkinghub.elsevier.com/retrieve/pii/S1566119913004114.

155. WIDMER, J. Charge transport and energy levels in organic semiconductors. *PhD Thesis* [online]. 2014. [viewed2016-05-30]. . Available from: http://www.qucosa.de/recherche/frontdoor/?tx_slubopus4frontend[id]=15491.

156. FALKENBERG, C. Optimizing Organic Solar Cells. *PhD Thesis* [online]. 2011. [viewed2016-05-30]. . Available from: http://www.qucosa.de/recherche/frontdoor/?tx_slubopus4frontend[id]=u.

157. COTTON, F.A. et al. Expeditious Access to the Most Easily Ionized Closed-Shell Molecule, W 2 (hpp) 4. *J. Am. Chem. Soc.* [online]. 2005. vol. 127 (31), 10808–10809. Available from: http://pubs.acs.org/doi/abs/10.1021/ja0535458.

158. MENKE, T. et al. In-situ conductivity and Seebeck measurements of highly efficient n-dopants in fullerene C60. *Appl. Phys. Lett.* [online]. 2012. vol. 100 (9), 093304. Available from: http://scitation.aip.org/content/aip/journal/apl/100/9/10.1063/1.3689778.

159. WALZER, K. et al. Highly Efficient Organic Devices Based on Electrically Doped Transport Layers. *Chem. Rev.* [online]. 2007. vol. 107 (4), 1233–1271. Available from: http://pubs.acs.org/doi/abs/10.1021/cr050156n.

160. FISCHER, A. et al. Self-heating effects in organic semiconductor crossbar structures with small active area. *Org. Electron.* [online]. 2012. vol. 13 (11), 2461–2468. Available from: http://linkinghub.elsevier.com/retrieve/pii/S1566119912003138.

161. FITZNER, R. et al. Correlation of π-Conjugated Oligomer Structure with Film Morphology and Organic Solar Cell Performance. *J. Am. Chem. Soc.*[online]. 2012. vol. 134 (27), 11064–11067. Available from: http://pubs.acs.org/doi/abs/10.1021/ja302320c.

162. FRISCH, M.J. et al. Gaussian 09, Revision E.01, Wallingford CT, Gaussian, Inc., 2009.

163. HARWOOD, L.M. - MOODY, C.J. *Experimental organic chemistry: principles and practice* [online]. [s.l.]: Oxford: Blackwell scientific, 1990. ISBN 0632020164 ; 0632020172 pbk.

164. GARCÍA, A. et al. New Building Block for C 3 Symmetry Molecules: Synthesis of s -Triazine-Based Redox Active Chromophores. *Org. Lett.*[online]. 2009. vol. 11 (23), 5398–5401. Available from: http://pubs.acs.org/doi/abs/10.1021/ol902203t.

165. HAYAMI, S. - INOUE, K. Structure and Magnetic Property of the Organic Triradical with Triazine Skeleton; 2,4,6-Tris{p-(N-oxy-N-tert-butylamino)phenyl}triazine. *Chem. Lett.* [online]. 1999. vol. 28 (7), 545–546. Available from: https://www.jstage.jst.go.jp/article/cl/28/7/28_7_545/_article.

166. KRUZINAUSKIENE, A. et al. Fluorene-based hydrazones and enamines as holetransporting materials for electrophotography. *J. Optoelectron. Adv. Mater.* [online].

2007. vol. 9 (9), 2857–2862. [viewed2016-05-30]. Available from: http://www.mendeley.com/research/fluorenebased-hydrazones-enamines-holetransporting-materials-electrophotography/.

167. KRUZINAUSKIENE, A. et al. Carbazolyl- and diphenylamino substituted fluorenes as hole transport materials. *Syn. Met.* [online]. 2007. vol. 157 (8-9), 401–406. Available from: http://linkinghub.elsevier.com/retrieve/pii/S0379677907000781.

168. KIM, S.W. et al. Synthesis and properties of new electroluminescent polymers possessing both hole and electron-transporting units in the main chain. *Polymer* [online]. 2002. vol. 43 (15), 4297–4305. Available from: http://linkinghub.elsevier.com/retrieve/pii/S0032386102002525.

169. CHO, D.H. et al. An Improved Synthesis of 1,4-Bis(3,4-dimethyl-5-formyl-2-pyrryl)butadiyne and 1,2-Bis(3,4-dimethyl-5-formyl-2-pyrryl)ethyne. *J. Org. Chem.* [online]. 1999. vol. 64 (21), 8048–8050. Available from: http://pubs.acs.org/doi/abs/10.1021/jo9909406.

170. BERGER, R. et al. New symmetrically substituted 1,3,5-triazines as host compounds for channel-type inclusion formation. *Cryst. Eng. Comm* [online]. 2012. vol. 14 (3), 768–770. Available from: http://xlink.rsc.org/?DOI=C2CE06034E.

171. SONNTAG, M. et al. Novel Star-Shaped Triphenylamine-Based Molecular Glasses and Their Use in OFETs. *Chem. Mater.* [online]. 2005. vol. 17 (11), 3031–3039. Available from: http://pubs.acs.org/doi/abs/10.1021/cm047750i.

172. PEARSON, J. M., Yanus, J. F. 2-Vinyl-(9-dicyanomethylene) fluorene and derivatives thereof. Patent US 3883488 A [online]. 1975. [viewed2016-05-30]. Available from: https://www.google.ch/patents/US3883488.

173. KOTHA, S. et al. Synthesis ofC3-Symmetric Nano-Sized Polyaromatic Compounds by Trimerization and Suzuki−Miyaura Cross-Coupling Reactions. *Eur. J. Org. Chem.* [online]. 2004. vol. 2004 (19), 4003–4013. [viewed2016-05-30]. . Available from: http://doi.wiley.com/10.1002/ejoc.200400257.

174. RAJWAR, D. et al. Synthesis and 2D self-assembly at the liquid-solid interface of end-substituted star-shaped oligophenylenes. *Cryst. Eng. Comm* [online]. 2012. vol. 14 (16), 5182. Available from: http://xlink.rsc.org/?DOI=c2ce25530h.

175. TUCKER, S.H. LXXIV.-Iodination in the carbazole series. *J. Chem. Soc. (Resumed)* [online]. 1926. vol. 129 (546), 546. Available from: http://xlink.rsc.org/?DOI=jr9262900546.

176. BEGINN, C. et al. Synthesis of poly(9-hexyl-3,6-carbazolyleneethynylene) and its model compounds. *Macromol. Chem. Phys.* [online]. 1994. vol. 195 (7), 2353–2370. Available from: http://doi.wiley.com/10.1002/macp.1994.021950706.

177. NEUGEBAUER, F.A. - FISCHER, H. tert.-Butyl-substituierte Carbazole. *Chem. Ber.* [online]. 1972. vol. 105 (8), 2686–2693. Available from: http://doi.wiley.com/10.1002/cber.19721050829.

178. PATI, P.B. - ZADE, S.S. Highly emissive triphenylamine based fluorophores for detection of picric acid. *Tetrahedron Lett.* [online]. 2014. vol. 55 (38), 5290–5293. Available from: http://linkinghub.elsevier.com/retrieve/pii/S0040403914012726.

179. SHI, L. et al. High performance aniline vapor detection based on multi-branched fluorescent triphenylamine-benzothiadiazole derivatives: branch effect and aggregation control of the sensing performance. *J. Mater. Chem.* [online]. 2012. vol. 22 (23), 11629. Available from: http://xlink.rsc.org/?DOI=c2jm30933e.

180. LIN, T.-C. et al. Synthesis and Characterization of Highly Soluble Two-Photon-

Absorbing Chromophores with Multi-Branched and Dendritic Architectures. *Eur. J. Org. Chem.* [online]. 2011. vol. 2011 (5), 912–921. Available from: http://doi.wiley.com/10.1002/ejoc.201001165.

181. YOU, J. et al. Starburst dendrimers consisting of triphenylamine core and 9-phenylcarbazole-based dendrons: synthesis and properties. *Org. Biomol. Chem.* [online]. 2012. vol. 10 (47), 9481. Available from: http://xlink.rsc.org/?DOI=c2ob26483h.

182. THIRION, D. et al. Violet-to-Blue Tunable Emission of Aryl-Substituted Dispirofluorene-Indenofluorene Isomers by Conformationally-Controllable Intramolecular Excimer Formation. *Chem. Eur. J.* [online]. 2011. vol. 17 (37), 10272–10287. Available from: http://doi.wiley.com/10.1002/chem.201100971.

183. DEWHURST, F. - SHAH, P.K.J. Iodination of fluorenone by N-iodosuccinimide. *J. Chem. Soc. C: Org.* [online]. 1969. (11), 1503. Available from: http://xlink.rsc.org/?DOI=j39690001503.

184. LYLE, R.E. et al. Acid Catalyzed Condensations. I. 1,3,5-Triarylbenzenes 1. *J. Am. Chem. Soc.* [online]. 1953. vol. 75 (23), 5959–5961. Available from: http://pubs.acs.org/doi/abs/10.1021/ja01119a053.

185. IYER, V.S. et al. From Hexa-peri-hexabenzocoronene to"Superacenes". *Angew. Chem. Int. Edit. Eng.* [online]. 1997. vol. 36 (15), 1604–1607. Available from: http://doi.wiley.com/10.1002/anie.199716041.

186. CHERCKA, D. et al. Pyrene based materials for exceptionally deep blue OLEDs. *J. Mater. Chem. C* [online]. 2014. vol. 2 (43), 9083–9086. Available from: http://xlink.rsc.org/?DOI=C4TC01801J.

187. SUGIMORI, G. et al. Anti-helicobacterial agents. Patent EP 1340755 A1 [online]. 2003. Japan. Available from: http://www.google.com/patents/EP1340755A1?cl=en.

188. KOSHKAKARYAN, G. et al. Alternative Donor−Acceptor Stacks from Crown Ethers and Naphthalene Diimide Derivatives: Rapid, Selective Formation from Solution and Solid State Grinding. *J. Am. Chem. Soc.* [online]. 2009. vol. 131 (6), 2078–2079. Available from: http://pubs.acs.org/doi/abs/10.1021/ja809088v.

189. LI, J.Y. et al. White-Light Emission from a Single-Emitting-Component Organic Electroluminescent Device. *Adv. Mater.* [online]. 2004. vol. 16 (17), 1538–1541. Available from: http://doi.wiley.com/10.1002/adma.200305838.

190. FARINOLA, G.M. - RAGNI, R. Electroluminescent materials for white organic light emitting diodes. *Chemical Society Reviews* [online]. 2011. vol. 40 (7), 3467. Available from: http://xlink.rsc.org/?DOI=c0cs00204f.

191. LING, M.M. - BAO, Z. Thin Film Deposition, Patterning, and Printing in Organic Thin Film Transistors. *Chem. Mater.* [online]. 2004. vol. 16 (23), 4824–4840. Available from: http://pubs.acs.org/doi/abs/10.1021/cm0496117.

192. ZHONG, H. et al. New Conjugated Triazine Based Molecular Materials for Application in Optoelectronic Devices: Design, Synthesis, and Properties. *J. Phys. Chem. C* [online]. 2011. vol. 115 (5), 2423–2427. Available from: http://pubs.acs.org/doi/abs/10.1021/jp109806m.

193. ROTHMANN, M.M. et al. Designing a bipolar host material for blue phosphorescent OLEDs: Phenoxy-carbazole substituted triazine. *Org. Electron.* [online]. 2011. vol. 12 (7), 1192–1197. Available from: http://linkinghub.elsevier.com/retrieve/pii/S1566119911001236.

194. ROTHMANN, M.M. et al. Donor-Substituted 1,3,5-Triazines as Host Materials for Blue Phosphorescent Organic Light-Emitting Diodes. *Chem. Mater.* [online]. 2010. vol. 22

(7), 2403–2410. Available from: http://pubs.acs.org/doi/abs/10.1021/cm9033879.

195. TOMKEVICIENE, A. et al. Impact of Linking Topology on the Properties of Carbazole Trimers and Dimers. *J. Phys. Chem. C* [online]. 2011. vol. 115 (11), 4887–4897. Available from: http://pubs.acs.org/doi/abs/10.1021/jp111333v.

196. KULKARNI, A.P. et al. High-Performance Organic Light-Emitting Diodes Based on Intramolecular Charge-Transfer Emission from Donor–Acceptor Molecules: Significance of Electron- Donor Strength and Molecular Geometry. *Adv. Funct. Mater.* [online]. 2006. vol. 16 (8), 1057–1066. Available from: http://doi.wiley.com/10.1002/adfm.200500722.

197. LI, H. et al. A modified Wittig polycondensation—to high-trans- and high-molecular weight PPVs. *Tetrahedron Lett.* [online]. 2004. vol. 45 (19), 3823–3826. Available from: http://linkinghub.elsevier.com/retrieve/pii/S0040403904005210.

198. KUKHTA, N.A. et al. Effect of linking topology on the properties of star-shaped derivatives of triazine and fluorene. *Syn. Met.* [online]. 2014. vol. 195 266–275. Available from: http://dx.doi.org/10.1016/j.synthmet.2014.06.019.

199. ZHOU, H.-X. - GILSON, M.K. Theory of Free Energy and Entropy in Noncovalent Binding. *Chem. Rev.* [online]. 2009. vol. 109 (9), 4092–4107. Available from: http://pubs.acs.org/doi/abs/10.1021/cr800551w.

200. LUO, M.-H. - CHEN, K.-Y. Asymmetric perylene bisimide dyes with strong solvatofluorism. *DyesPigments* [online]. 2013. vol. 99 (2), 456–464. Available from: http://linkinghub.elsevier.com/retrieve/pii/S0143720813002088.

201. KUCHERAK, O.A. et al. Fluorene Analogues of Prodan with Superior Fluorescence Brightness and Solvatochromism. *J. Phys. Chem. Lett.* [online]. 2010. vol. 1 (3), 616–620. Available from: http://pubs.acs.org/doi/abs/10.1021/jz9003685.

202. YAN, Y.-Q. et al. Effect of the Substitution Pattern on the Intramolecular Charge-Transfer Emissions in Organoboron-Based Biphenyls, Diphenylacetylenes, and Stilbenes. *Chem. Asian J.* [online]. 2013. vol. 8 (12), 3164–3176. Available from: http://doi.wiley.com/10.1002/asia.201300872.

203. KAAFARANI, B.R. et al. Bis(carbazolyl) derivatives of pyrene and tetrahydropyrene: synthesis, structures, optical properties, electrochemistry, and electroluminescence. *J. Mater. Chem. C* [online]. 2013. vol. 1 (8), 1638. Available from: http://xlink.rsc.org/?DOI=c2tc00474g.

204. AHN, T. et al. Blue Electroluminescent Polymers: Control of Conjugation Length by Kink Linkages and Substituents in the Poly(p -phenylenevinylene)-Related Copolymers. *Macromol.* [online]. 1999. vol. 32 (10), 3279–3285. Available from: http://pubs.acs.org/doi/abs/10.1021/ma981864w.

205. BORSENBERGER, P.M. et al. Charge transport in disordered molecular solids. *J. Chem. Phys.* [online]. 1991. vol. 94 (8), 5447. Available from: http://scitation.aip.org/content/aip/journal/jcp/94/8/10.1063/1.460506.

206. SHIN, H. et al. Synthesis and electroluminescence property of new hexaphenylbenzene derivatives including amine group for blue emitters. *Nanoscale Res. Lett.* [online]. 2013. vol. 8 (1), 421. Available from: http://nanoscalereslett.springeropen.com/articles/10.1186/1556-276X-8-421.

207. HUANG, J. et al. Bipolar anthracene derivatives containing hole- and electron-transporting moieties for highly efficient blue electroluminescence devices. *J. Mater. Chem.* [online]. 2011. vol. 21 (9), 2957. Available from: http://xlink.rsc.org/?DOI=c0jm03300f.

208. VERBOUWE, W. et al. Photoinduced Intramolecular Charge Transfer in

Diphenylamino-Substituted Triphenylbenzene, Biphenyl, and Fluorene. *J. Phys. Chem. A* [online]. 1997. vol. 101 (44), 8157–8165. Available from: http://pubs.acs.org/doi/abs/10.1021/jp970666o.

209. KREGER, K. et al. Combinatorial Development of Blue OLEDs Based on Star Shaped Molecules. *Adv. Funct. Mater.* [online]. 2007. vol. 17 (17), 3456–3461. Available from: http://doi.wiley.com/10.1002/adfm.200700223.

210. VERGADOU, V. et al. Self-Organization of Four Symmetric Tri-phenyl-benzene Derivatives. *Cryst. Growth Des.* [online]. 2006. vol. 6 (11), 2486–2492. Available from: http://pubs.acs.org/doi/abs/10.1021/cg060183m.

211. LIN, Z.-M. et al. Facile synthesis and optoelectronic properties of N,N-difluorenevinylaniline-based molecules. *New J. Chem.* [online]. 2012. vol. 36 (7), 1512. Available from: http://xlink.rsc.org/?DOI=c2nj40051k.

212. TOUR, J.M. Conjugated Macromolecules of Precise Length and Constitution. Organic Synthesis for the Construction of Nanoarchitectures. *Chem. Rev.* [online]. 1996. vol. 96 (1), 537–554. Available from: http://pubs.acs.org/doi/abs/10.1021/cr9500287.

213. MOORE, J.S. Shape-Persistent Molecular Architectures of Nanoscale Dimension. *Acc. Chem. Res.* [online]. 1997. vol. 30 (10), 402–413. Available from: http://pubs.acs.org/doi/abs/10.1021/ar950232g.

214. RONCALI, J. Synthetic Principles for Bandgap Control in Linear π-Conjugated Systems. *Chem. Rev.* [online]. 1997. vol. 97 (1), 173–206. Available from: http://pubs.acs.org/doi/abs/10.1021/cr950257t.

215. BRUNEL, J. et al. Propeller-Shaped Octupolar Molecules Derived from Triphenylbenzene for Nonlinear Optics: Synthesis and Optical Studies. *Chem. Mater.* [online]. 2003. vol. 15 (21), 4139–4148. Available from: http://pubs.acs.org/doi/abs/10.1021/cm030392j.

216. BEAVINGTON, R. et al. The Effect of Core Delocalization on Intermolecular Interactions in Conjugated Dendrimers. *Adv. Funct. Mater.* [online]. 2003. vol. 13 (3), 211–218. Available from: http://doi.wiley.com/10.1002/adfm.200390032.

217. XIA, H. et al. Synthesis and photophysical properties of triphenylamine-based dendrimers with 1,3,5-triphenylbenzene cores. *Tetrahedron Lett.* [online]. 2007. vol. 48 (33), 5877–5881. Available from: http://linkinghub.elsevier.com/retrieve/pii/S0040403907011495.

218. MEIER, H. et al. Guest-Host Systems of 1,3,5-Tristyrylbenzenes. *Z. Naturforsch. B Chem.* [online]. 2003. 775–781. [viewed2016-05-30]. Available from: https://www.mendeley.com/research/guesthost-systems-135tristyrylbenzenes-1/?utm_source=desktop&utm_medium=1.15.3&utm_campaign=open_catalog&userDocumentId=%7Bb4b1536a-37ae-4472-965c-50b3324aa383%7D.

219. CHATFIELD, D. CRAMER, C. J.: Essentials of Computational Chemistry: Theories and Models. *Theoretical Chemistry Accounts: Theory, Computation, and Modeling (Theoretica Chimica Acta)* [online]. 2002. vol. 108 (6), 367–368. Available from: http://link.springer.com/10.1007/s00214-002-0380-8.

220. ZHAN, C.-G. et al. Ionization Potential, Electron Affinity, Electronegativity, Hardness, and Electron Excitation Energy: Molecular Properties from Density Functional Theory Orbital Energies. *J. Phys. Chem. A* [online]. 2003. vol. 107 (20), 4184–4195. Available from: http://pubs.acs.org/doi/abs/10.1021/jp0225774.

221. GRISORIO, R. et al. Influencing the Spectral Stability and the Electroluminescence Behavior of New Blue-Emitting Bifluorene-Based Materials by the 7,7"-Functionalization of

the Core. *J. Phys. Chem. C* [online]. 2008. vol. 112 (17), 7005–7014. Available from: http://pubs.acs.org/doi/abs/10.1021/jp7102403.

222. KARPICZ, R. et al. Impact of intramolecular twisting and exciton migration on emission efficiency of multifunctional fluorene-benzothiadiazole-carbazole compounds. *J. Chem. Phys.* [online]. 2011. vol. 134 (20), 204508. Available from: http://scitation.aip.org/content/aip/journal/jcp/134/20/10.1063/1.3594047.

223. KHOTINA, I.A. et al. Phenylene dendrimers and novel hyperbranched polyphenylenes as light emissive materials for blue OLEDs. *J. Luminesc.*[online]. 2004. vol. 110 (4), 232–238. Available from: http://linkinghub.elsevier.com/retrieve/pii/S0022231304002534.

224. IIDA, A. - YAMAGUCHI, S. Intense solid-state blue emission with a small Stokes' shift: π-stacking protection of the diphenylanthracene skeleton. *Chem. Commun.* [online]. 2009. (21), 3002. Available from: http://xlink.rsc.org/?DOI=b901794a.

225. CUI, X. et al. Perylene-Derived Triplet Acceptors with Optimized Excited State Energy Levels for Triplet–Triplet Annihilation Assisted Upconversion. *J. Org. Chem.* [online]. 2014. vol. 79 (5), 2038–2048. Available from: http://pubs.acs.org/doi/abs/10.1021/jo402718e.

226. FANG, Z. et al. Tuning two-photon absorption cross-sections for triphenylamine derivatives. *RSC Adv.* [online]. 2013. vol. 3 (39), 17914. Available from: http://xlink.rsc.org/?DOI=c3ra42789g.

227. REICHARDT, C. *Solvents and Solvent Effects in Organic Chemistry* [online]. Weinheim, FRG: Wiley-VCH Verlag GmbH & Co. KGaA, 2002. 534 p. ISBN 3527306188.

228. HAPIOT, P. et al. Comparative Study of the Oxidation of Fluorene and 9,9-Disubstituted Fluorenes and Their Related 2,7-Dimers and Trimer. *Chem. Mater.* [online]. 2005. vol. 17 (8), 2003–2012. Available from: http://pubs.acs.org/doi/abs/10.1021/cm048331o.

229. TIGREROS, A. et al. Influence of acetylene-linked π-spacers on triphenylamine–fluorene dye sensitized solar cells performance. *Sol. Energ. Mat. Sol. Cells* [online]. 2014. vol. 121 61–68. Available from: http://linkinghub.elsevier.com/retrieve/pii/S0927024813005564.

230. BREDAS, J.-L. Mind the gap! *Mater. Horiz.* [online]. 2014. vol. 1 (1), 17–19. Available from: http://xlink.rsc.org/?DOI=C3MH00098B.

231. BAHETI, A. et al. Simple Triarylamine-Based Dyes Containing Fluorene and Biphenyl Linkers for Efficient Dye-Sensitized Solar Cells. *J. Phys. Chem. C* [online]. 2009. vol. 113 (20), 8541–8547. Available from: http://pubs.acs.org/doi/abs/10.1021/jp902206g.

232. REGHU, R.R. et al. Air stable electron-transporting and ambipolar bay substituted perylene bisimides. *J. Mater. Chem.* [online]. 2011. vol. 21 (21), 7811. Available from: http://xlink.rsc.org/?DOI=c1jm11091h.

233. BALDO, M.A. et al. Highly Efficient Phosphorescent Emission from Organic Electroluminescent Devices. *Nature* [online]. 1998. vol. 395 (6698), 151–154. Available from: http://www.nature.com/doifinder/10.1038/25954.

234. HOLMES, R.J. et al. Blue organic electrophosphorescence using exothermic host–guest energy transfer. *Appl. Phys. Lett.* [online]. 2003. vol. 82 (15), 2422. Available from: http://scitation.aip.org/content/aip/journal/apl/82/15/10.1063/1.1568146.

235. JAROSZ, T. et al. Advances in Star-Shaped π-Conjugated Systems: Properties and Applications. *Macromol. Rapid Commun.* [online]. 2014. vol. 35 (11), 1006–1032. Available from: http://doi.wiley.com/10.1002/marc.201400061.

236. LUKEŠ, V. et al. Charged States of 1,3,5-Triazine Molecules as Models for Star-shaped Molecular Architecture: A DFT and Spectroelectrochemcial Study. *J. Phys. Chem. B* [online]. 2011. vol. 115 (13), 3344–3353. Available from: http://pubs.acs.org/doi/abs/10.1021/jp111297y.

237. KUKHTA, N.A. et al. Structure–property relationships of star-shaped blue-emitting charge-transporting 1,3,5-triphenylbenzene derivatives. *DyesPigments* [online]. 2015. vol. 117 122–132. Available from: http://linkinghub.elsevier.com/retrieve/pii/S014372081500056X.

238. KWON, O. et al. Aromatic Amines: A Comparison of Electron-Donor Strengths. *J. Phys.l Chem. A* [online]. 2005. vol. 109 (41), 9346–9352. Available from: http://pubs.acs.org/doi/abs/10.1021/jp054334s.

239. REGHU, R.R. et al. Glass forming donor-substituted s-triazines: Photophysical and electrochemical properties. *Dye Pigments* [online]. 2013. vol. 97 (3), 412–422. Available from: http://linkinghub.elsevier.com/retrieve/pii/S0143720813000211.

240. SIMOKAITIENĖ, J. et al. Synthesis, photophysical and photoelectrical properties of glass-forming phenothiazinyl- and carbazolyl-substituted ethylenes. *J. Optoelectron. Adv. Mater.*[online]. 2006. vol. 8 (2), 876–882. Available from: http://dspace.vgtu.lt/handle/1/345.

241. MICHINOBU, T. et al. Band-gap tuning of carbazole-containing donor–acceptor type conjugated polymers by acceptor moieties and π-spacer groups. *Polymer* [online]. 2008. vol. 49 (1), 192–199. Available from: http://linkinghub.elsevier.com/retrieve/pii/S0032386107010816.

242. LAMBERT, C. et al. Electronic Coupling in Tetraanisylarylenediamine Mixed-Valence Systems: The Interplay between Bridge Energy and Geometric Factors. *J. Am. Chem. Soc.* [online]. 2005. vol. 127 (23), 8508–8516. Available from: http://pubs.acs.org/doi/abs/10.1021/ja0512172.

243. KU, J.-M. et al. Time-Dependent Density Functional Theory Study on Cyclopentadithiophene-Benzothiadiazole-Based Push-Pull-Type Copolymers for New Design of Donor Materials in Bulk Heterojunction Organic Solar Cells. *Bull. Korean Chem. Soc.* [online]. 2012. vol. 33 (3), 1029–1036. Available from: http://koreascience.or.kr/journal/view.jsp?kj=JCGMCS&py=2012&vnc=v33n3&sp=1029.

244. QU, J. et al. Synthesis and properties of polyacetylenes carrying N-phenylcarbazole and triphenylamine moieties. *Polymer* [online]. 2006. vol. 47 (19), 6551–6559. Available from: http://linkinghub.elsevier.com/retrieve/pii/S0032386106008883.

245. JUSTIN THOMAS, K.R. et al. Light-Emitting Carbazole Derivatives: Potential Electroluminescent Materials. *J. Am. Chem. Soc.* [online]. 2001. vol. 123 (38), 9404–9411. Available from: http://pubs.acs.org/doi/abs/10.1021/ja010819s.

246. GUIN, M. et al. A π-stacked phenylacetylene and 1,3,5-triazine heterodimer: a combined spectroscopic and ab initio investigation. *Phys. Chem. Chem. Phys.* [online]. 2009. vol. 11 (47), 11207. Available from: http://xlink.rsc.org/?DOI=b911640k.

247. TAO, Y.-M. et al. Synthesis and characterization of efficient luminescent materials based on 2,1,3-benzothiadiazole with carbazole moieties. *Syn. Met.* [online]. 2011. vol. 161 (9-10), 718–723. Available from: http://dx.doi.org/10.1016/j.synthmet.2011.01.020.

248. MARINI, A. et al. What is Solvatochromism? *J. Phys. Chem. B* [online]. 2010. vol. 114 (51), 17128–17135. Available from: http://pubs.acs.org/doi/abs/10.1021/jp1097487.

249. SONNTAG, M. - STROHRIEGL, P. Novel 2,7-Linked Carbazole Trimers as Model Compounds for Conjugated Carbazole Polymers. *Chem. Mater.* [online]. 2004. vol. 16 (23),

4736–4742. Available from: http://pubs.acs.org/doi/abs/10.1021/cm040142i.

250. KUKHTA, N.A. et al. Effect of the Nature of the Core on the Properties of the Star-Shaped Compounds Containing Bicarbazolyl Moieties. *J. Phys. Chem. C* [online]. 2016. vol. 120 (2), 1208–1217. Available from: http://pubs.acs.org/doi/abs/10.1021/acs.jpcc.5b10570.

251. ALBRECHT, C. Joseph R. Lakowicz: Principles of fluorescence spectroscopy, 3rd Edition. *Analytical and Bioanalytical Chemistry* [online]. 2008. vol. 390 (5), 1223–1224. Available from: http://link.springer.com/10.1007/s00216-007-1822-x.

252. KERSTING, R. et al. Femtosecond site-selective probing of energy relaxing excitons in poly(phenylenevinylene): Luminescence dynamics and lifetime spectra. *J. Chem. Phys.* [online]. 1997. vol. 106 (7), 2850. Available from: http://scitation.aip.org/content/aip/journal/jcp/106/7/10.1063/1.473094.

253. SEREVIČIUS, T. et al. Photophysical properties of 2-phenylanthracene and its conformationally-stabilized derivatives. *DyesPigments* [online]. 2013. vol. 98 (2), 304–315. Available from: http://linkinghub.elsevier.com/retrieve/pii/S0143720813000685.

254. REICHARDT, C. Solvatochromic Dyes as Solvent Polarity Indicators. *Chem. Rev.* [online]. 1994. vol. 94 (8), 2319–2358. Available from: http://pubs.acs.org/doi/abs/10.1021/cr00032a005.

255. LIPPERT, E. Dipolmoment und Elektronenstruktur von angeregten Molekülen. *Zeit. Naturforsch. A* [online]. 1955. vol. 10 (7), 541–545. Available from: http://www.degruyter.com/view/j/zna.1955.10.issue-7/zna-1955-0707/zna-1955-0707.xml.

256. MATAGA, N. et al. Solvent Effects upon Fluorescence Spectra and the Dipolemoments of Excited Molecules. *Bull. Chem. Soc. Japan* [online]. 1956. vol. 29 (4), 465–470. Available from: http://joi.jlc.jst.go.jp/JST.Journalarchive/bcsj1926/29.465?from=CrossRef.

257. BRUNNER, K. et al. Carbazole Compounds as Host Materials for Triplet Emitters in Organic Light-Emitting Diodes: Tuning the HOMO Level without Influencing the Triplet Energy in Small Molecules. *J. Am. Chem. Soc.* [online]. 2004. vol. 126 (19), 6035–6042. Available from: http://pubs.acs.org/doi/abs/10.1021/ja049883a.

258. BERNIUS, M.T. et al. Progress with Light-Emitting Polymers. *Adv. Mater.* [online]. 2000. vol. 12 (23), 1737–1750. Available from: http://doi.wiley.com/10.1002/1521-4095(200012)12:23<1737:AID-ADMA1737>3.0.CO;2-N.

259. THOMPSON, B.C. et al. Soluble Narrow Band Gap and Blue Propylenedioxythiophene-Cyanovinylene Polymers as Multifunctional Materials for Photovoltaic and Electrochromic Applications. *J. Am. Chem. Soc.* online]. 2006. vol. 128 (39), 12714–12725. Available from: http://pubs.acs.org/doi/abs/10.1021/ja061274a.

260. WU, W. et al. π-Conjugated molecules with fused rings for organic field-effect transistors: design, synthesis and applications. *Chem. Soc. Rev.* [online]. 2010. vol. 39 (5), 1489–1502. Available from: http://xlink.rsc.org/?DOI=B813123F.

261. LA TORRE, G. DE et al. Role of Structural Factors in the Nonlinear Optical Properties of Phthalocyanines and Related Compounds. *Chem. Rev.* [online]. 2004. vol. 104 (9), 3723–3750. Available from: http://pubs.acs.org/doi/abs/10.1021/cr030206t.

262. HUANG, T.-H. et al. Investigation on the linear and nonlinear optical properties of fluorenone-based linear conjugated oligomers: The influence of π-spacer. *J. Photochem. Photobiol. A: Chem.* [online]. 2013. vol. 261 41–45. Available from: http://linkinghub.elsevier.com/retrieve/pii/S101060301300172X.

263. FISHER, A.L. et al. Efficient Deep-Blue Electroluminescence from an Ambipolar

Fluorescent Emitter in a Single-Active-Layer Device. *Chem. Mater.* [online]. 2011. vol. 23 (7), 1640–1642. Available from: http://pubs.acs.org/doi/abs/10.1021/cm103314t.

264. BÜRGI, L. et al. High-Mobility Ambipolar Near-Infrared Light-Emitting Polymer Field-Effect Transistors. *Adv. Mater.* [online]. 2008. vol. 20 (11), 2217–2224. Available from: http://doi.wiley.com/10.1002/adma.200702775.

265. KUDER, J.E. Fluorenone Derivatives as Electron Transport Materials. *J. Electrochem. Soc.* [online]. 1978. vol. 125 (11), 1750. Available from: http://jes.ecsdl.org/cgi/doi/10.1149/1.2131288.

266. METRI, N. et al. Processable Star-Shaped Molecules with Triphenylamine Core as Hole-Transporting Materials: Experimental and Theoretical Approach. *J. Phys. Chem. C* [online]. 2012. vol. 116 (5), 3765–3772. Available from: http://pubs.acs.org/doi/abs/10.1021/jp2098872.

267. LIN, B.C. et al. Reorganization Energies in the Transports of Holes and Electrons in Organic Amines in Organic Electroluminescence Studied by Density Functional Theory. *J. Phys. Chem. A* [online]. 2003. vol. 107 (26), 5241–5251. Available from: http://pubs.acs.org/doi/abs/10.1021/jp0304529.

268. MALAGOLI, M. - BRÉDAS, J.L. Density functional theory study of the geometric structure and energetics of triphenylamine-based hole-transporting molecules. *Chem. Phys. Lett.* [online]. 2000. vol. 327 (1-2), 13–17. Available from: http://linkinghub.elsevier.com/retrieve/pii/S0009261400007570.

269. ESTRADA, L.A. et al. Revisiting Fluorenone Photophysics via Dipolar Fluorenone Derivatives. *J. Phys. Chem. A* [online]. 2011. vol. 115 (24), 6366–6375. Available from: http://pubs.acs.org/doi/abs/10.1021/jp200507j.

270. BARONAS, P. et al. High-triplet-energy carbazole and fluorene tetrads. *J. Luminesc.* [online]. 2016. vol. 169 256–265. Available from: http://linkinghub.elsevier.com/retrieve/pii/S0022231315300375.

271. YOSHIHARA, K. Spectroscopic Properties of the Lower-Lying Excited States of Fluorenone. *J. Chem. Phys.* [online]. 1966. vol. 45 (6), 1991. Available from: http://scitation.aip.org/content/aip/journal/jcp/45/6/10.1063/1.1727883.

272. GIRIBABU, L. - SUDHAKAR, K. Photoinduced intramolecular reactions in triphenylamine–corrole dyads. *J. Photochem. Photobiol. A: Chem.* [online]. 2015. vol. 296 11–18. Available from: http://linkinghub.elsevier.com/retrieve/pii/S1010603014003992.

273. KUKHTA, N.A. et al. Impact of the conjugation length and ground state aggregation on the absorption spectra of fluorenone-based compounds. [online]. 2016. (In preparation).

274. KUKHTA, N.A. et al. Design, synthesis and characterization of the ambipolar butterfly-shaped fluorenone derivatives. [online]. 2016. (In preparation).

275. YUAN, M.-S. et al. Fluorenone Organic Crystals: Two-Color Luminescence Switching and Reversible Phase Transformations between π–π Stacking-Directed Packing and Hydrogen Bond-Directed Packing. *Chem. Mater.* [online]. 2014. vol. 26 (7), 2467–2477. Available from: http://pubs.acs.org/doi/abs/10.1021/cm500441r.

276. AN, B.-K. et al. Enhanced Emission and Its Switching in Fluorescent Organic Nanoparticles. *J. Am. Chem. Soc.* [online]. 2002. vol. 124 (48), 14410–14415. Available from: http://pubs.acs.org/doi/abs/10.1021/ja0269082.

277. CHEN, J. et al. Aggregation-Induced Emission of cis , cis -1,2,3,4-Tetraphenylbutadiene from Restricted Intramolecular Rotation. *J. Phys. Chem. A* [online]. 2004. vol. 108 (37), 7522–7526. Available from:

http://pubs.acs.org/doi/abs/10.1021/jp048475q.

278. RECHE, I. et al. The role of cations in the reduction of 9-fluorenone in bis(trifluoromethylsulfonyl)imide room temperature ionic liquids. *New J. Chem.* [online]. 2014. vol. 38 (10), 5030–5036. Available from: http://xlink.rsc.org/?DOI=C4NJ01200C.

279. YANG, X. et al. Recent advances of the emitters for high performance deep-blue organic light-emitting diodes. *J. Mater. Chem. C* [online]. 2015. vol. 3 (5), 913–944. Available from: http://xlink.rsc.org/?DOI=C4TC02474E.

280. KIM, S.H. et al. Highly efficient deep-blue emitting organic light emitting diode based on the multifunctional fluorescent molecule comprising covalently bonded carbazole and anthracene moieties. *J. Mater. Chem.* [online]. 2011. vol. 21 (25), 9139. Available from: http://xlink.rsc.org/?DOI=c1jm11111f.

281. HUNG, W.-Y. et al. A new benzimidazole/carbazole hybrid bipolar material for highly efficient deep-blue electrofluorescence, yellow–green electrophosphorescence, and two-color-based white OLEDs. *J. Mater.Chem.* [online]. 2010. vol. 20 (45), 10113. Available from: http://xlink.rsc.org/?DOI=c0jm02143a.

282. CHA, J.-R. et al. New efficient fused-ring spiro[benzoanthracene-fluorene] dopant materials for blue fluorescent organic light-emitting diodes. *New J. Chem.* [online]. 2015. vol. 39 (5), 3813–3820. Available from: http://xlink.rsc.org/?DOI=C5NJ00143A.

283. KOELSCH, C.F. - WHITNEY, A.G. THE ROSENMUND-von BRAUN NITRILE SYNTHESIS 1. *J. Org. Chem.* [online]. 1941. vol. 06 (6), 795–803. Available from: http://pubs.acs.org/doi/abs/10.1021/jo01206a002.

284. MEE, S.P.H. et al. Stille Coupling Made Easier—The Synergic Effect of Copper(I) Salts and the Fluoride Ion. *Angew. Chem. Int. Edit.* [online]. 2004. vol. 43 (9), 1132–1136. Available from: http://doi.wiley.com/10.1002/anie.200352979.

285. HIRT, R.C. - HOWE, J.P. The Ultraviolet Absorption Spectrum of Benzonitrile Vapor. *J. Chem. Phys.*[online]. 1948. vol. 16 (5), 480. Available from: http://scitation.aip.org/content/aip/journal/jcp/16/5/10.1063/1.1746920.

286. BAGNICH, S.A. et al. Triplet energies and excimer formation in meta- and para-linked carbazolebiphenyl matrix materials. *Phil. Trans. R. Soc. A* [online]. 2015. vol. 373 (2044), 20140446–20140446. Available from: http://rsta.royalsocietypublishing.org/cgi/doi/10.1098/rsta.2014.0446.

287. SINGH-RACHFORD, T.N. - CASTELLANO, F.N. Photon upconversion based on sensitized triplet–triplet annihilation. *Coord. Chem. Rev.* [online]. 2010. vol. 254 (21-22), 2560–2573. Available from: http://linkinghub.elsevier.com/retrieve/pii/S0010854510000093.

288. JANKUS, V. et al. Generating Light from Upper Excited Triplet States: A Contribution to the Indirect Singlet Yield of a Polymer OLED, Helping to Exceed the 25% Singlet Exciton Limit. *Adv. Sci.* [online]. 2016. vol. 3 (1), n/a–n/a. Available from: http://doi.wiley.com/10.1002/advs.201500221.

289. ROMANIN, A.M. et al. Electrode reduction mechanism of aromatic nitriles in aprotic solvents. *J. Electroanalyt.Chem.Interfac. Electrochem.* [online]. 1978. vol. 88 (2), 175–185. Available from: http://linkinghub.elsevier.com/retrieve/pii/S0022072878802654.

290. BORSENBERGER, P.M. - SHI, J. Hole Transport in a Vapor Deposited Phenylenediamine Molecular Glass. *Physic. Status Solidi (b)* [online]. 1995. vol. 191 (2), 461–469. Available from: http://doi.wiley.com/10.1002/pssb.2221910219.

291. MIMAITE, V. et al. Can hydrogen bonds improve the hole-mobility in amorphous organic semiconductors? Experimental and theoretical insights. *J. Mater. Chem. C* [online].

2015. vol. 3 (44), 11660–11674. Available from: http://xlink.rsc.org/?DOI=C5TC02534F.

292. BLOKING, J.T. et al. Solution-Processed Organic Solar Cells with Power Conversion Efficiencies of 2.5% using Benzothiadiazole/Imide-Based Acceptors. *Chem. Mater.* [online]. 2011. vol. 23 (24), 5484–5490. Available from: http://pubs.acs.org/doi/abs/10.1021/cm203111k.

293. DOU, L. et al. Tandem polymer solar cells featuring a spectrally matched low-bandgap polymer. *Nat. Photon.* [online]. 2012. vol. 6 (3), 180–185. Available from: http://www.nature.com/doifinder/10.1038/nphoton.2011.356.

294. SMALL, C.E. et al. High-efficiency inverted dithienogermole–thienopyrrolodione-based polymer solar cells. *Nat. Photon.* [online]. 2011. vol. 6 (2), 115–120. Available from: http://www.nature.com/doifinder/10.1038/nphoton.2011.317.

295. RIEDE, M. et al. Small-molecule solar cells—status and perspectives. *Nanotech.* [online]. 2008. vol. 19 (42), 424001. Available from: http://stacks.iop.org/0957-4484/19/i=42/a=424001?key=crossref.6adeaf5f3d376dec41154d3accd8b862.

296. LI, B. et al. Review of recent progress in solid-state dye-sensitized solar cells. *Sol. En. Mater. Sol. Cells* [online]. 2006. vol. 90 (5), 549–573. Available from: http://linkinghub.elsevier.com/retrieve/pii/S0927024805001479.

297. GÜNES, S. et al. Conjugated Polymer-Based Organic Solar Cells. *Chem. Rev.* [online]. 2007. vol. 107 (4), 1324–1338. Available from: http://pubs.acs.org/doi/abs/10.1021/cr050149z.

298. PFUETZNER, S. et al. Improved bulk heterojunction organic solar cells employing C[sub 70] fullerenes. *Appl. Phys. Lett.* [online]. 2009. vol. 94 (22), 223307. Available from: http://scitation.aip.org/content/aip/journal/apl/94/22/10.1063/1.3148664.

299. STEINBERGER, S. et al. A-D-A-D-A-Type Oligothiophenes for Vacuum-Deposited Organic Solar Cells. *Org. Lett.* [online]. 2011. vol. 13 (1), 90–93. Available from: http://pubs.acs.org/doi/abs/10.1021/ol102603n.

300. LEONG, W.L. et al. Differential Resistance Analysis of Charge Carrier Losses in Organic Bulk Heterojunction Solar Cells: Observing the Transition from Bimolecular to Trap-Assisted Recombination and Quantifying the Order of Recombination. *Adv. En. Mater.* [online]. 2011. vol. 1 (4), 517–522. Available from:doi.wiley.com/10.1002/aenm.201100196.

301. WANG, S. et al. High efficiency organic photovoltaic cells based on a vapor deposited squaraine donor. *Appl. Phys. Lett.* [online]. 2009. vol. 94 (23), 233304. Available from: http://scitation.aip.org/content/aip/journal/apl/94/23/10.1063/1.3152011.

302. LEE, J.-H. et al. A high performance transparent inverted organic light emitting diode with 1,4,5,8,9,11-hexaazatriphenylenehexacarbonitrile as an organic buffer layer. *J. Mater. Chem.* [online]. 2012. vol. 22 (30), 15262. Available from: http://xlink.rsc.org/?DOI=c2jm32438e.

303. SCHULZE, K. et al. Efficient Vacuum-Deposited Organic Solar Cells Based on a New Low-Bandgap Oligothiophene and Fullerene C60. *Adv. Mater.* [online]. 2006. vol. 18 (21), 2872–2875. Available from: http://doi.wiley.com/10.1002/adma.200600658.

304. LIN, H.-W. et al. Pyridine-based electron transporting materials for highly efficient organic solar cells. *J. Mater. Chem. A* [online]. 2013. vol. 1 (5), 1770–1777. Available from: http://xlink.rsc.org/?DOI=C2TA00253A.

305. PLACENCIA, D. et al. Organic Photovoltaic Cells Based On Solvent-Annealed, Textured Titanyl Phthalocyanine/C 60 Heterojunctions. *Adv. Funct. Mater.* [online]. 2009. vol. 19 (12), 1913–1921. Available from: http://doi.wiley.com/10.1002/adfm.200801723.

306. PEUMANS, P. et al. Small molecular weight organic thin-film photodetectors and solar cells. *J. Appl. Phys.* [online]. 2003. vol. 93 (7), 3693. Available from: http://scitation.aip.org/content/aip/journal/jap/93/7/10.1063/1.1534621.

307. BHOSALE, S. V et al. Chemistry of naphthalene diimides. *Chem. Soc. Rev.* [online]. 2008. vol. 37 (2), 331–342. Available from: http://xlink.rsc.org/?DOI=B615857A.

308. ULRICH, S. et al. Metallo-Controlled Dynamic Molecular Tweezers: Design, Synthesis, and Self-Assembly by Metal-Ion Coordination. *Eur. J. Inorg. Chem.* [online]. 2010. vol. 2010 (13), 1913–1928. Available from: http://doi.wiley.com/10.1002/ejic.200901262.

309. AJAYAKUMAR, M.R. - MUKHOPADHYAY, P. Naphthalene-bis-hydrazimide: radical anions and ICT as new bimodal probes for differential sensing of a library of amines. *Chem. Commun.* [online]. 2009. (25), 3702. Available from: http://xlink.rsc.org/?DOI=b903097b.

310. ORTIZ, R.P. et al. Rational Design of Ambipolar Organic Semiconductors: Is Core Planarity Central to Ambipolarity in Thiophene-Naphthalene Semiconductors? *Chem. Eur. J.* [online]. 2012. vol. 18 (2), 532–543. Available from: http://doi.wiley.com/10.1002/chem.201101715.

311. GAWRYS, P. et al. Effect of N-Substituents on Redox, Optical, and Electronic Properties of Naphthalene Bisimides Used for Field-Effect Transistors Fabrication. *J. Phys. Chem. B* [online]. 2010. vol. 114 (5), 1803–1809. Available from: http://pubs.acs.org/doi/abs/10.1021/jp908931w.

312. LEE, S.K. et al. Electrochemistry, Spectroscopy and Electrogenerated Chemiluminescence of Perylene, Terrylene, and Quaterrylene Diimides in Aprotic Solution. *J. Am. Chem. Soc.* [online]. 1999. vol. 121 (14), 3513–3520. Available from: http://pubs.acs.org/doi/abs/10.1021/ja984188m.

313. PRON, A. et al. Triarylamine Substituted Arylene Bisimides as Solution Processable Organic Semiconductors for Field Effect Transistors. Effect of Substituent Position on Their Spectroscopic, Electrochemical, Structural, and Electrical Transport Properties. *J. Phys. Chem. C* [online]. 2011. vol. 115 (30), 15008–15017. Available from: http://pubs.acs.org/doi/abs/10.1021/jp202553h.

314. TOZLU, C. et al. Photoresponsive n-channel organic field effect transistor based on naphthalene bis-benzimidazole with divinyltetramethyl disiloxane-bis (benzo-cyclobutene) gate insulator. *Sens. Actuators A: Phys.* [online]. 2010. vol. 161 (1-2), 46–52. Available from: http://linkinghub.elsevier.com/retrieve/pii/S0924424710002438.

315. KUKHTA, N.A. et al. New Electron Transport Materials for High Performance Organic Solar Cells: Synthesis and Properties of Symmetrical and Asymmetrical 1,4,5,8-Naphthalenetetracarboxylic Dianhydride Derivatives. *Adv. Electron. Mater.* [online]. 2016. vol. 2 (5). Available from: http://doi.wiley.com/10.1002/aelm.201600047.

316. FRENKEL, J. On Pre-Breakdown Phenomena in Insulators and Electronic Semi-Conductors. *Phys. Rev.* [online]. 1938. vol. 54 (8), 647–648. Available from: http://link.aps.org/doi/10.1103/PhysRev.54.647.

317. DENG, P. et al. Naphthoylene(trifluoromethylbenzimidazole)-dicarboxylic acid imides for high-performance n-type organic field-effect transistors. *Chem. Commun.* [online]. 2012. vol. 48 (20), 2591. Available from: http://xlink.rsc.org/?DOI=c2cc17272k.

318. MAENNIG, B. et al. Organic p -i- n solar cells. *Appl. Phys. A: Mater. Sci. Process.*[online]. 2004. vol. 79 (1), 1–14. Available from: http://link.springer.com/10.1007/s00339-003-2494-9.

319. MEERHEIM, R. et al. Highly efficient organic multi-junction solar cells with a thiophene based donor material. *Appl. Phys. Lett.* [online]. 2014. vol. 105 (6), 063306. Available from: http://scitation.aip.org/content/aip/journal/apl/105/6/10.1063/1.4893012.

320. SIEBERT-HENZE, E. et al. Electroabsorption studies of organic p-i-n solar cells: Increase of the built-in voltage by higher doping concentration in the hole transport layer. *Org. Electron.* [online]. 2014. vol. 15 (2), 563–568. Available from: http://linkinghub.elsevier.com/retrieve/pii/S1566119913005405.

7. LIST OF PUBLICATIONS ON THE SUBJECT OF THE THESIS

1. Kukhta, Nadzeya A.; Simokaitiene, Jurate; Volyniuk, Dmytro; Ostrauskaite, Jolita; Grazulevicius, Juozas Vidas; Juska, Gytis; Jankauskas, Vygintas. Effect of linking topology on the properties of star-shaped derivatives of triazine and fluorene // Synthetic Metals. 2014, vol. 195, p. 266-275.
2. Kukhta, Nadzeya A.; Volyniuk, Dmytro; Peciulyte, Laura; Ostrauskaite, Jolita; Juska, Gytis; Grazulevicius, Juozas Vidas. Structure–property relationships of star-shaped blue-emitting charge-transporting 1,3,5-triphenylbenzene derivatives // Dyes and Pigments. 2015, vol. 117, p. 122–132.
3. Kukhta, Nadzeya A.; Volyniuk, Dmytro; Grazulevicius, Juozas Vidas; Juska, Gytis. Effect of the nature of the core on the properties of the star-shaped compounds containing bicarbazolyl moieties // Journal of Physical Chemistry C. 2016, vol. 120, iss. 2, p. 1208–1217.
4. Data, Przemyslaw; Zassowski, Pawel; Lapkowski, Mieszyslaw; Grazulevicius, Juozas Vidas; Kukhta, Nadzeya A.; Reghu, Renji R. Electrochromic behaviour of triazine based ambipolar compounds // Dyes and Pigments. 2016, vol. 192, p. 283–295.
5. Kukhta, Nadzeya A.; Zeika, Olaf; Widmer, Johannes; Koerner, Christian; Meerheim, Rico; Petrich, Annette; Behrnd, Norwid-Rasmus; Leo, Karl; Grazulevicius, Juozas Vidas. New electron transport materials for high performance organic solar cells: synthesis and properties of symmetrical and asymmetrical 1,4,5,8-naphthalenetetracarboxylic dianhydride derivatives // Advanced Electronic Materials. 2016, vol. 2, iss. 5, DOI: 10.1002/aelm.201600047.

8. LIST OF PRESENTATIONS AT THE INTERNATIONAL CONFERENCES

1. N. A. Kukhta, J. Simokaitienė, J.V. Gražulevičius. New bipolar dendritic materials having 2,4,6-triphenyl-1,3,5-triazine core for optoelectronic applications // BPS-2012: Baltic Polymer Symposium 2012/ September 19-22, 2012 Liepaja, Latvia: list of posters and participants, abstract, practical information, p. 69.
2. N. A. Kukhta, J. Simokaitienė, J. V. Gražulevičius. New bipolar dendritic materials having 2,4,6-triphenyl-1,3,5-triazine core for optoelectronic applications // Physical and Technological Problems of Radio Engineering Devices, Telecommunication, Nano- and Microelectronics/ October 25-27,

2012, Chernivtsi, Ukraine: list of posters and participants, abstract, practical information, p. 190.

3. N.A. Kukhta, J. Ostrauskaite, V. Jankauskas, J. Grazulevicius. Synthesis and properties of triphenylamine-based star-shaped compounds // ICEPOM-9: 9th International Conference on Electrical Processes in Organic Materials/ May 20-24, 2013, Lviv, Ukraine: list of posters and participants, abstract, practical information, p.152.
4. N. A. Kukhta, J. Simokaitienė, J. Ostrauskaite, J. V. Gražulevičius. Synthesis and properties of the star-shaped compounds with fluorene side arms and the different cores // ECME 2013: 12th European Conference on Molecular Electronics/ September 3-7, 2013, London, Great Britain: list of posters and participants, abstract, practical information, p. 96.
5. N. A. Kukhta, J. Simokaitienė, J. Ostrauskaite, J. V. Gražulevičius. The influence of the linking topologies on the properties of the dendrimers with different cores and fluorene side arms // BPS-2013: Baltic Polymer Symposium 2013/ September 18-20, 2013, Trakai, Lithuania: list of oral presentations, abstract, practical information, p. 44.
6. N. A. Kukhta, J. Ostrauskaite, D. Volyniuk, J. V. Grazulevicius. Synthesis and characterization of bicarbazolyl-end-capped boomerang-shaped molecules // BOS-2014: Balticum Organicum Syntheticum 2014/ July 6-9, 2014, Vilnius, Lithuania: list of posters and participants, abstract, practical information, p. 155.
7. N. A. Kukhta, J. Ostrauskaite, D. Volyniuk, J. V. Grazulevicius. The influence of the nature of the core on the properties of the boomerang-shaped compounds containing bicarbazolyl moieties // BPS-2014: Baltic Polymer Symposium 2014/ September 24-26, 2014, Laulasmaa, Estonia: list of oral presentations, abstract, practical information, p. 26.
8. N. A. Kukhta, D. Volyniuk, J. V. Grazulevicius. Improving of the thermal stability of the ambipolar multichromophore fluorenone-based compounds // BPS-2015: Baltic Polymer Symposium 2015/ September 16-18, 2015, Sigulda, Latvia: list of oral presentations, abstract, practical information, p. 32.
9. N. A. Kukhta, J. V. Grazulevicius, D. Volyniuk. Development of the efficient deep-blue organic emitters based on cyano-substituted 1,3,5-triphenylbenzene: design, synthesis and investigation of properties // Electronic processes in organic and inorganic materials (ICEPOM–10) / May 22-27, 2016, Ternopil, Ukraine: list of oral presentations, abstract, practical information, p. 106.
10. N. A. Kukhta, J. V. Grazulevicius, D. Volyniuk, A. P. Monkman. The impact of the substitution pattern on the properties of multifunctional deep-blue emitters // Organic Semiconductors / September 22-25, 2016, Dubrovnik, Croatia: list of poster presentations, abstract, practical information, p. 79.

9. ACKNOWLEDGEMENTS

Dr. Jolita Ostrauskaitė, Department of Polymer Chemistry and Technology, Kaunas University of Technology, is greatly acknowledged for the supervision of my Doctoral research.

Prof. Habil. dr. Juozas Vidas Gražulevičius, Department of Polymer Chemistry and Technology, Kaunas University of Technology, is sincerely thanked for the consultations, support and useful advices during my Doctoral research.

PhD student Tomas Matulaitis is whole-heartedly thanked for the support, faith, appreciation, valuable advices, consultations and ideas, and creation of friendly working atmosphere.

Prof. Karl Leo (Dresden University of Technology, Germany) is greatly acknowledged for the supervision of my internship in Dresden.

Prof. Gjergji Sini (University of Cergy-Pontoise, France) is greatly thanked for sharing vast knowledge in theoretical calculations, helpful discussions and consultations, as well as for enthusiastically supporting new ideas.

Dr. Olaf Zeika (Dresden University of Technology, Germany) is kindly acknowledged for the supervision, support and useful advices in synthesis during my internship in Dresden.

Dr. Johannes Widmer and dr. Norwid-Rasmus Behrnd (Dresden University of Technology, Germany) are sincerely thanked for kind attitude, friendship and sharing knowledge in the field of solar cells.

Dr. K. Ivaniuk (Lviv Polytechnic University, Ukraine) is kindly thanked for the preparation of OLEDs.

Dr. Jūratė Simokaitienė is greatly thanked for friendship and mentoring my scientific work upon entering Kaunas University of Technology, useful advices in synthesis and systematization of results.

Dr. Ramūnas Lygaitis is kindly acknowledged for friendship, support, valuable academic discussions and advice.

Dr. Laura Pečiulytė is thanked for helping in DSC and TGA measurements.

Dr. Dmytro Volyniuk is thanked for the estimation of charge carrier mobility of the synthesized compounds.

Dr. Ina Liutvinienė is greatly acknowledged for the help with UV/Vis, PL and IR measurements.

Marytė Krenevičienė and dr. Greta Ragaitė are greatly thanked for quickly and accurately preforming NMR spectra.

Dr. Mykola Bezuglyi, Sandra Korychenska, Eglė Stanislovaitytė, PhD students Yan Daniliv, Iryna Hladka and Galyna Sych are sinserely thanked for support, valuable advices and pleasant work atmosphere.

All the colleagues of the research group are most sincerely thanked for help and friendly working atmosphere.

My family and friends are whole-heartedly thanked for the immeasurable support and advice during my Dortoral research.

UDK 547-3 + 621.315.5](043.3)

SL344. 2016-10-31, 21,5 leidyb. apsk. l. Tiražas 10 egz. Užsakymas 406. Išleido Kauno technologijos universitetas, K. Donelaičio g. 73, 44249 Kaunas Spausdino leidyklos „Technologija“ spaustuvė, Studentų g. 54, 51424 Kaunas